



VO₂ nanostructures for dynamically tunable nanophotonic devices

Jimmy John

► To cite this version:

Jimmy John. VO₂ nanostructures for dynamically tunable nanophotonic devices. Micro and nanotechnologies/Microelectronics. Université de Lyon, 2020. English. NNT : 2020LYSEI044 . tel-03070633

HAL Id: tel-03070633

<https://theses.hal.science/tel-03070633>

Submitted on 15 Dec 2020

HAL is a multi-disciplinary open access archive for the deposit and dissemination of scientific research documents, whether they are published or not. The documents may come from teaching and research institutions in France or abroad, or from public or private research centers.

L'archive ouverte pluridisciplinaire **HAL**, est destinée au dépôt et à la diffusion de documents scientifiques de niveau recherche, publiés ou non, émanant des établissements d'enseignement et de recherche français ou étrangers, des laboratoires publics ou privés.



INSA

N°d'ordre NNT : 2020LYSEI044

THÈSE de DOCTORAT DE L'UNIVERSITÉ DE LYON

Opérée au sein de :

l'INSA LYON

Ecole Doctorale ED 160

Électronique, Électrotechnique et Automatique

Spécialité de doctorat : Électronique, micro et nanoélectronique, optique
et laser

Soutenue publiquement le 30/06/2020, par :

Jimmy JOHN

VO₂ nanostructures for dynamically tunable nanophotonic devices

Devant le jury composé de :

TORTAI Jean-Hervé	Maître de Conférences HDR	Rapporteur
BERNAL Maria-Pilar	Directrice de Recherche CNRS	Rapporteur
KILDERS SANCHIS Pablo	Professeur des Universités	Rapporteur
JOURLIN Yves	Professeur des Universités	Examinateur
CALLARD Ségolène	Professeur des Universités	Examinateur
OROBTCOUK Régis	Maître de conférences HDR	Directeur de thèse
CUEFF Sébastien	Chargé de recherche CNRS	Co-Directeur de thèse

TABLE OF CONTENTS

Acknowledgments	v
List of Tables	xii
List of Tables	xii
List of Figures	xiii
List of Figures	xiii
Résumé	xxi
0.1 Part 1: Guide d'onde modulateur hybride VO ₂ /Si	xxi
0.1.1 Introduction	xxi
0.1.2 La photonique sur silicium: Avantages et inconvénients	xxii
0.1.3 Oxyde de Vanadium (VO ₂): Introduction et science de la modulation	xxiii
0.1.4 Caractérisation du VO ₂	xxvi
0.1.5 Modulateur guide d'onde hybride VO ₂ /Silicium: Conception et principe de fonctionnement	xxx
0.1.6 Simulation, fabrication et résultat	xxxiii
0.2 Part 2: Résonances multipolaires accordable par design utilisant des nanocristaux de VO ₂	xxxvii
0.2.1 Introduction	xxxvii

0.2.2	Théorie de Mie et extraction des paramètres effectifs des nanocristaux de VO ₂	xxxvii
0.2.3	Discussion et perspectives futures	xl
0.2.4	Conclusion	xliii
0.3	Part 3: Méasurfaces à base de VO ₂ pour la nanophotonique accordable en espace libre	xlv
0.3.1	Introduction	xlv
0.3.2	Méasurface de VO ₂ pour la génération de couleur structurelle accordable	xlvi
0.3.3	Méasurface de VO ₂ pour une absorption totale accordable.	xlix
Chapter 1: Introduction and Background	1
1.1	Context	1
1.2	Theoretical aspects on insulator-metal transitions	4
1.2.1	Band Theory	5
1.2.2	Mott insulators and Mott Transition Mechanism	6
1.2.3	Peierls Transition Mechanism	9
1.3	Vanadium oxides and its transition theory	11
1.3.1	Vanadium oxide	11
1.3.2	Crystallographic structure of Vanadium oxide	11
1.3.3	Electronic Band structures of Vanadium oxide	15
1.3.4	Discussion on Vanadium oxide transition	16
1.4	Organization of the manuscript	17
Chapter 2: Structural and Optical characterization of VO₂ thin-films	20

2.1	Introduction	20
2.2	VO_2 growth technique and deposition	20
2.3	Structural Characterization	22
2.3.1	XRD characterization and Results	22
2.3.2	Reciprocal space mapping (RSM)	28
2.3.3	Transmission electron microscopy (TEM) characterization	31
2.4	Spectroscopic ellipsometry: Measurements and analysis	35
2.4.1	Working Principle	35
2.4.2	I_s and I_c parameters	36
2.5	Optical permittivity modeling of VO_2	37
2.5.1	Oscillators model and dispersion function for VO_2	38
2.5.2	Extension to Multiple oscillators	41
2.6	Optical modelling and characterization of extracted data	42
2.6.1	Discussion	50
2.7	Conclusion	51
Chapter 3:	VO_2 based active optical modulator: design, fabrication and experimental results	52
3.1	Introduction on Silicon photonics	52
3.1.1	Electro-optic modulators	53
3.1.2	Hybrid integration of functional materials on Silicon for efficient modulators	54
3.2	Optical Waveguides: Theory and coupling mechanisms	56
3.2.1	Optical waveguide theory	56

3.2.2	Poynting Vector	59
3.3	VO ₂ -based waveguide modulator: Design and Working principles	61
3.3.1	Codirectional Coupling	65
3.3.2	Symmetric and Anti-symmetric field pattern	67
3.4	Simulation study and Numerical Analysis	71
3.4.1	2D Mode Solver	71
3.4.2	Finite difference method	76
3.4.3	Simulation Results	79
3.5	Fabrication	87
3.5.1	Discussion	90
3.5.2	Use of this modulator as a partial power transfer	91
3.6	Conclusion	93
Chapter 4:	Multipolar Resonances with Designer Tunability Using VO₂ Phase-Change Materials	95
4.1	Introduction	95
4.2	Mie theory for wavelength-scale particles	96
4.3	VO ₂ Nanocrystals: Theory	98
4.4	VO ₂ Nanocrystals: Fabrication and Characterization	101
4.4.1	Fabrication	101
4.4.2	Characterization	101
4.5	Effective parameter retrieval of VO ₂ Nanocrystals	106
4.5.1	Derivation of the expressions for effective permittivity and permeability	106
4.5.2	Modelling the effect of interactions between nanoparticles	109

4.5.3	Modelling the polydispersity in size distribution of nanoparticles . . .	113
4.5.4	Discussion on the results and parameter retrieval of the system . . .	115
4.6	Tunable multipolar resonances based on VO ₂ -NCs system: Future Perspective	116
4.6.1	Discussion	116
4.6.2	Perspective towards designer metamaterial	118
4.6.3	Conclusions	121
Chapter 5: VO₂ based metasurfaces for tunable free-space nanophotonics . . .		123
5.1	VO ₂ metasurface for tunable structural color.	125
5.1.1	Introduction	125
5.1.2	Color perception	127
5.1.3	RGB color space	129
5.1.4	All dielectric tunable structural color generation	131
5.1.5	Tunable color generation using VO ₂	136
5.1.6	Discussion and future perspectives	143
5.2	VO ₂ metasurface for tunable perfect absorption	144
5.2.1	Concept	144
5.2.2	Metasurface Design and Simulation	148
5.2.3	Metasurface Fabrication	149
5.2.4	Metasurface Characterization	150
5.2.5	Conclusions and outlook	154
Chapter 6: Conclusion and future perspectives		156

Appendix A: Additional Waveguide theory	161
A.1 Boundary Conditions	161
A.2 Total internal Reflection	162
A.3 Optical Waveguide and transmission analysis	164
A.4 TE mode	166
A.5 TM mode	170
A.6 Coupled mode theory	171
Appendix B: Energy transfer and mode matching method	175
B.1 Mode Matching Method	175
B.1.1 Mode matching at an Interface	176
B.1.2 Interface matrix	179
B.2 Layer Matrix	180
B.2.1 Generalization for N interfaces	181
References	201

LIST OF TABLES

2.1	Parameters for Reactive Sputtering Technique for the growth of VO ₂ thin-films on quartz.	22
3.1	Power transfer simulation calculated around the core area of the waveguide. 80% of the input power is calculated at the central area of the core, rest is dissipated at the edges of the waveguide.	85
3.2	Geometric parameters for VO ₂ waveguide modulator.	86

LIST OF FIGURES

1	Indice de réfraction et coefficient d'absorption extraits de VO ₂ en fonction de la température. Cette extraction est basée sur un fit de données ellipsométriques, où l'on arrive à un accord entre les données optiques et expérimentales	xxix
2	Vue schématique du modulateur hybride actif basé sur la transition de phase isolant-métal du VO ₂	xxxii
3	Variation spectrale de l'amplitude de modulation de l'indice de réfraction effectif (Δn_{eff} et Δk_{eff}) du métamatériaux pour la taille des NCs sélectionnés. Graphique du bas : Figure de mérite ($FOM = \Delta n_{eff}/\Delta k_{eff}$) de la plateforme VO ₂ -NCs pour différentes tailles de nanocristaux et comparé au FOM pour une couche mince VO ₂	xlii
1.1	(a) Splitting of a normal band into upper and lower Hubbard band due to electron correlations. (b) Bandwidth controlled metal-insulator transition. Changing the bandwidth W could induce a metal-insulator transition. (c) and (d) Oxide Mott insulators could be categorized into two types based on the relative position of the oxygen band and Hubbard bands. (c)Mott-Hubbard insulator where the oxygen p-band lies under the lower Hubbard band; and (d) charge-transfer insulator where oxygen p-band is in between the lower Hubbard band and upper Hubbard band. This figure is reproduced from Ref.[97, 98]	8
1.2	Schematic illustration of a Peierls transition. Energy versus density of states a) for a 1D lattice of equally spaced atoms and b) for a dimerized 1D lattice. The horizontal dotted line represents the Fermi energy c) The changes in the lattice across the Peierls transition. The dotted lines represent the original atomic position and the solid sphere represents the perturbed state.	10

1.3 (a) Crystal structure of VO ₂ in its metallic phase. It has a rutile structure with small atoms being vanadium and large atoms being oxygen. (b) The cation-cation interaction further splits the t _g and e _g orbitals. Crystal structure of (c) metallic rutile phase and (d) insulating monoclinic phase of VO ₂ viewing form the b axis. (e) Proposed band structure of the metallic and insulating phase based on the Goodenough and Mott pictures, respectively.	14
2.1 Experimental phase diagram of VOx. This image has been adapted from [116, 117]	21
2.2 Relation between tetragonal structure (high-temperature, black lines) and monoclinic (low-temperature, dashed blue lines) unit cells. This image has been adapted from [125]. Below table shows the dimensions of the unit cell of VO ₂ at both its state [125].	23
2.3 XRD of VO ₂ on Si, home-made deposition (Reactive ion sputtering).	24
2.4 XRD of VO ₂ on Al ₂ O ₃ , home-made deposition (Reactive ion sputtering).	25
2.5 VO ₂ on SiO ₂ home-made (failed deposition).	26
2.6 Transverse XRD and peak shift observed during the transition of VO ₂ indicating the structural transition.	27
2.7 XRD intensity peak shift and width increase showing structural changes in the crystalline structure of VO ₂ during the temperature induced phase transition.	28
2.8 RSM on VO ₂ on Al ₂ O ₃ as a function of temperature. We observe the gradual shift in in-plane parameter.	29
2.9 In-plane and out-of-plane Lattice parameter shift as a function of temperature	30
2.10 TEM cross section reveals the presence of additional native oxide layer in between the VO ₂ layer and Si substrate.	32
2.11 EELS and TEM cross of the intermediate layer for Sample 1 (VO ₂ 100nm) reveals that at the interface of SiOx we observe 2-3 nm of V(3 ⁺) or V(2 ⁺) reduction V atoms.	32
2.12 SAED pattern VO ₂ deposited on sapphire indexed as a monoclinic structure on the growth direction.	33

2.13 (a) SAED surface plane analysis and (b) TEM cross section for Sample (VO ₂ 25nm) on Al ₂ O ₃ revealing the interface of substrate and thin film. (c) EELS cross section of intermediate layer	34
2.14 HORIBA-Jobin Yvon UVISEL Ellipsometry setup	36
2.15 Linkam THMSEL350V Heating stage temperature controller	37
2.16 Optical model: Layer by layer modelling of VO ₂ on SiO ₂	38
2.17 Fitting the optical model and experimental data.	43
2.18 Thermal evolution of refractive index of VO ₂ extracted from the optical models after the fit.	44
2.19 Fit parameter values obtained for both the states of VO ₂	46
2.20 Varying parameters of VO ₂ ellipsometric models calculated as a function of temperature.	47
2.21 Band structure of the a. Insulating and b. Metallic VO ₂	48
2.22 Evolution of refractive index as a function of temperature on VO ₂ /Al ₂ O ₃ . .	49
2.23 Thermal hysteresis loop of VO ₂ at $\lambda = 1200\text{nm}$	50
3.1 Schematic view of the active PCM modulator based on vanadium dioxide insulator-metal phase transition: Top Figure : VO ₂ is insulating, wave propagation is unaltered. Figure below shows when VO ₂ is metallic, the wave diverts its path of propagation into the adjacent waveguide leveraging the absorption of VO ₂	62
3.2 Evolution of the effective indices in the guide to guide coupler versus the width of the waveguide with the VO ₂ layer.	63
3.3 Refractive index distribution of the coupled waveguide and electric field of subsequent waveguides. The width of the VO ₂ /Si waveguide is adjusted to manipulate the effective index in order to match the bus waveguide effective index.	64
3.4 Schematics for mode coupling between two dissimilar waveguides.	66
3.5 Schematics for symmetric and anti-symmetric super modes in directional couplers	68

3.6	Schematics for π order phase between symmetric and anti-symmetric mode leading to co directional mode coupling.	69
3.7	Variation of L_c versus the gap between the two coupled waveguides.	70
3.8	Basic Finite Difference Method	77
3.9	Finite Difference Method	77
3.10	Finite difference scheme discretization of VO_2 waveguide modulator.	78
3.11	Top simulation view of wave propagation and modulation in the proposed device when VO_2 is insulating and when it is metallic (with and without loss). .	81
3.12	Efficient coupling of VO_2 waveguide modulator.	82
3.13	Evolution of the output power (P_{out}) versus the variation of the refractive index of the VO_2 layer.	83
3.14	Evolution of the output power (P_{out}) versus the variation of the wavelength with losses.	84
3.15	Schematic cross-sectional view of the coupler section in the optical device as simulated with light modulation as function of transition in VO_2	85
3.16	Intensity of the guided mode as a function of position along the device.	87
3.17	Fabrication steps involved for the realization of VO_2 modulator	88
3.18	SEM image of patterned hard mask before the first ICP etching.	89
3.19	SEM image of patterned hard mask after ICP etching.	90
3.20	Simulation for VO_2 waveguide modulator as partial power filter using the intermediate state of VO_2 transitions.	92
3.21	Gradual power variation in the bus waveguide (Core 1) as function of changing refractive index.	93
4.1	Real and imaginary part of the dielectric permittivity ϵ of a VO_2 thin-film in the Vis/NIR range as a function of temperature.	99

4.2	Calculated absorption efficiency of VO_2 spheres with radius 50 nm in their a) insulating and b) metallic states embedded in quartz. With colored lines are represented the dipolar electric a_1 (red), dipolar magnetic b_1 (yellow), quadrupolar electric a_2 (light blue) and quadrupolar magnetic b_2 (dark blue) contributions to Q_{abs}	100
4.3	VO_2 NCs TEM image (top) and sketch (bottom)	102
4.4	Evolution of ellipsometric parameters I_s and I_c measured as a function of temperature. The accuation was performed on VO_2 NC at an incident angle of 65°	103
4.5	Thermal Hysteresis loop of VO_2 NCs.	104
4.6	Dynamic optical measurements of the VO_2 NCs IMT. The rate of temperature ramp is 1° per minute. The initial stating temperature was 23°C	105
4.7	3D representation of optical stacks for VO_2 NC embedded in fused silica.	105
4.8	Fitting (solid line) and experimental measurements(circles) of the ellipsometric parameters I_s (blue) and I_c (red) for both states of VO_2 -NCs: a) metallic and b) insulating for a VO_2 -NCs for size of $R = 35\text{nm}$ and a filling-factor $f = 0.18$. (incident angle: 55°).	109
4.9	Scheme of the analyzed system: dimer formed by spheres ($R = 25\text{nm}$) separated by a gap and illuminated with x – (left) and y –polarized beams (right). With arrows are represented the polarization of the illuminating beam (E, blue arrow) and the wave vector (k, red arrow).	110
4.10	Absorption cross-section C_{abs} of VO_2 dimers in its metallic phase ($R = 35\text{ nm}$) when illuminated with (a) x- (b) y- and (c) 45° polarizations (4.9) for different interparticle distances (gaps). As an inset in (a) and (b) is indicated the maximum spectral shift between the interacting and non-interacting (dashed black lines) dimer. In (c) the spectral shift $\Delta\lambda$ is represented as a function of the gap.	111
4.11	Absorption cross-section C_{abs} of VO_2 dimers in its insulating phase ($R = 35\text{ nm}$) when illuminated with (a) x- (b) y- and (c) 45° polarizations (4.9) for different interparticle distances (gaps). As an inset in (a) and (b) is indicated the maximum spectral shift between the interacting and non-interacting (dashed black lines) dimer. In (c) the spectral shift $\Delta\lambda$ is represented as a function of the gap.	113

4.12 Absorption cross-section C_{abs} spectra for the reference monodisperse system ($R = 35$ nm, black line) and others with (a) symmetric and (c) asymmetric distribution of NC sizes. Size distribution of the (b) symmetric and (d) asymmetric systems. With the light dotted line is represented the size of the monodisperse distribution.	114
4.13 a) Effective dielectric function (ϵ_{eff}), b) magnetic permeability (μ_{eff}), and c) real and d) imaginary parts of the effective refractive index ($m_{eff} = n_{eff} + ik_{eff}$) of a slab of quartz with VO_2 spheres with radius $R = 35$ nm and a filling fraction $f = 0.18$ in their insulating (low temperature) and metallic (high temperature) states.	116
4.14 Variation of effective optical parameters for different sizes of nanocrystals in both states of VO_2 a) and b) n_{eff} and k_{eff} for insulating VO_2 with a filling fraction $f = 0.18$. c) and d) n_{eff} and k_{eff} for metallic VO_2 . e) and f) represent the amplitude of modulation of the effective refractive index of the metamaterial as a function of NCs size. e) Δn_{eff} and f) Δk_{eff}	117
4.15 Spectral variation of the amplitude of modulation of the effective refractive index (Δn_{eff} and Δk_{eff}) of the metamaterial for selected NCs size. Bottom graph: Figure of Merit ($FOM = \Delta n_{eff}/\Delta k_{eff}$) of the VO_2 -NCs platform for different sizes of nanocrystals and compared to the FOM for a VO_2 thin-film.	119
4.16 Calculated absorption cross-section efficiency Q_{abs} of NCs of different sizes in their insulator and metallic states embedded in quartz. With colored lines are represented the dipolar electric a_1 (red), dipolar magnetic b_1 (yellow), quadrupolar electric a_2 (light blue) and quadrupolar magnetic b_2 (dark blue) contributions to Q_{abs}	120
 5.1 Normalized response spectra of human cones, to monochromatic spectral stimuli, with wavelength given in nanometers [213].	128
5.2 The chromaticity diagram of the CIE 1931 color space. The curved outer limit is the spectral locus, with wavelengths shown in nanometers. The colors your monitor displays in this image are specified using sRGB, so colors outside the sRGB range are not displayed correctly. This diagram shows the maximum saturated vivid colors that can be perceived by human eyes.	129
5.3 This the D65 sunlight spectrum simulated by D series daylight simulator by CIE standard. It cover the whole visible spectrum and the roughness shows the various points of absorption and diffusion by earth's atmosphere. This figure is taken from [215]	130

5.4	TiO ₂ nanostructures and the constituent color reproduction with varying dimensional parameters	132
5.5	Real and simulated image based on structural color of TiO ₂	134
5.6	TiO ₂ D65 white reference and the variation of color and L value as the function FF and a.	135
5.7	The structural color reproduction by VO ₂ in semiconductor state.	138
5.8	The structural color reproduction by VO ₂ in metallic state.	139
5.9	VO ₂ nano structure color gamut comparison	139
5.10	TiO ₂ metasurface fabricated on VO ₂ thin film deposited on SiO ₂	140
5.11	TiO ₂ nanostrutures on VO ₂ , the color switch observed at both the states of VO ₂	141
5.12	Photographs of TiO ₂ nano pillars viewed at (a) normal incident and (b) at an angle. For the images (c) and (d) we observe the different structural colors at different angles, as they are highly sensitive to angle.	142
5.13	a) Design concept: a silicon meta-atom is embedded into glass/PMMA surrounding with a buried thin VO ₂ layer. VO ₂ thickness: 25 nm, Si disk height: 240 nm, disk radius: 270 nm, square lattice period: 800 nm, PMMA layer thickness: 400 nm and b) Electron microscope image of the fabricated Si-VO ₂ metasurface prior to the PMMA coating. c) Functionality concept: at low temperatures, the metasurface reflects light at a designed wavelength, and d)at high temperature the light is absorbed by the metasurface.	147
5.14	EM simulation study on absorption, transmission and reflection as a function of Si nano disk diameter, with a period of 830nm and VO ₂ is insulating. The red dotted circle shows perfect absorption (transmission is near 0) region due ED and MD overlap and black dotted circle shows the split in the dipole overlap.	148
5.15	EM simulation study on absorption, transmission and reflection as function of Si nano disk diameter, with a period of 830nm and VO ₂ is Metallic. The red dotted circle shows disappearance of the MD when VO ₂ becomes metallic but we keep a strong absorption.	149

5.16 EM simulation study on absorption, transmission and reflection of Si nano disk diameter 540nm scanned as function of temperature, with a period of 830nm. The dotted line shows the wavelength of interest $1.55 \mu m$, for our tunable near-perfect absorption device.	149
5.17 Device sketch of the a-Si metasurface on VO_2 thin films. The layers are defined as: a. PMMA, b. a-Si nano disks, c. SiO_2 protective layer, d. VO_2 thin film and e. SiO_2 substrate layer	150
5.18 I_s and I_c values as a function of temperature at the final stage of the fabrication of the metasurfaces. Analysing the figure, we see the effect of VO_2 transition, suggesting successful completion of all the stages of fabrication.	152
5.19 Reflection measurements versus temperature of the metasurface. We observe a perfect absorption at 1550 nm when the phase of VO_2 is metallic. And we also observe the tunability and reversibility as due to temperature induced phase modulation of VO_2	153
5.20 Experimental results on the tunable reflection of the Si- VO_2 metasurface. (a) Reflection spectra for two temperature points: $40^\circ C$ (a dielectric phase of VO_2) and $80^\circ C$ (a metallic phase of VO_2). (b) Reflection contrast between the two temperature points. (c) Reversible temperature tuning of the metasurface reflection at 1550 nm wavelength exhibiting a hysteresis-like behavior.	154
A.1 Transmitted wave characteristics in total internal reflection (TIR), the direction of propagation in z direction.	163
A.2 Schematics of 1-D planar waveguide and 2-D rectangular planar waveguide .	165
A.3 Planar mirror waveguide with reflective metal surface on the boundary and the index variation map as function of x-axis value.	167
A.4 Symmetric step-index planar waveguide structure and the index variation map as function of x-axis value.	169
A.5 Overlap of transverse evanescent field between two adjacent parallel symmetric slab waveguide structure and the index variation map of guide as function of x-axis value.	172
B.1 a) Structure to model. b) Decomposition of the structure to be modeled into elementary straight wave guides.	175

B.2 Schematic diagram of the calculation of reflection and transmission coefficients at an interface in the case of an incident wave equal to (a). $a_n^{1,+}$ and (b) $a_n^{2,-}$.	176
B.3 Relationship between the amplitudes of electromagnetic waves at an interface.	180

RÉSUMÉ

0.1 Part 1: Guide d'onde modulateur hybride VO₂/Si

0.1.1 Introduction

Les communications optiques, internet, la détection, l'informatique, les applications de type "machine learning" ou "cloud computing" font l'objet d'une demande toujours croissante en termes de bande passante et de débit de données. Pour les communications sur puce, les solutions électroniques existantes basées sur des semi-conducteurs et des technologies CMOS sont actuellement mises à rude épreuve et sollicitées à leur limite maximale. La vitesse maximale de la nouvelle connexion mobile 5G est de 10 Gbits/s. Lorsque la vitesse dépasse les normes 5G de 10 Gbits/s, les technologies actuelles d'interconnexions métalliques transportant le courant entre puces déforment et atténuent fortement le signal de données en raison de la résistance parasite, de l'inductance et de la capacité de la piste métallique.

Afin de combler l'écart avec la demande croissante de données, l'industrie se tourne de plus en plus vers la photonique silicium pour relever ce défi. C'est pourquoi la photonique silicium est en passe de devenir une base essentielle pour la prochaine génération de systèmes de communication et les interconnexions basées sur le transport d'information par la lumière. L'utilisation de la lumière comme vecteur d'information est une stratégie connue depuis longtemps. Elle a été largement utilisée pour les communications à grande distance grâce au développement de la technologie des fibres en silice, pour lesquelles la transmission optique présente de très faibles pertes. Cela a, en soi, révolutionné la dynamique de la demande actuelle de données, qui ne cesse d'augmenter. En fait, la fibre optique est devenue de plus en plus populaire pour les réseaux de communication à courte distance, en raison de sa large bande passante et de son débit élevé. Ces différents avantages des communications optiques paraissent tout à fait prometteurs pour surmonter le goulet d'étranglement lié aux

limites des interconnexions métalliques auquel est confrontée l'industrie technologique actuelle.

Rien ne va plus vite que la lumière. L'avantage clair des communications basées sur la lumière est donc la vitesse et la bande passante. Grâce à la richesse des recherches dans ce domaine, il est de plus en plus possible d'intégrer des circuits photoniques et électroniques sur la même puce. Les technologies photoniques basées sur le silicium sont en passe de devenir la norme pour répondre à la demande actuelle de données. Cependant, la vitesse de transmission des données dépend de la rapidité avec laquelle un dispositif peut contrôler ou moduler la lumière.

0.1.2 La photonique sur silicium: Avantages et inconvénients

Les dispositifs fonctionnels classiques de la photonique silicium sur puce comme les modulateurs, les filtres, les guides d'ondes et les commutateurs, sont largement utilisés pour les technologies intégrées depuis un certain temps. Avec tous leurs avantages, nos dispositifs actuels basés sur la lumière sont cependant considérés comme encombrants (quelques centaines de micromètres) par rapport aux interconnexions métalliques et autres composants microélectroniques de la génération actuelle. Même si la technologie actuelle permet des interconnexions électriques à une architecture de 10 nm [1], la demande de données a créé un goulot d'étranglement en ce qui concerne la poursuite de la miniaturisation de leurs composants électroniques pour les raisons déjà mentionnées ci-dessus.

Cette incompatibilité de taille entre les composants photoniques et l'architecture électronique a été au centre de nombreuses recherches récentes. La majorité d'entre elles comprennent l'utilisation de matériaux alternatifs en conjonction avec des dispositifs à base de silicium pour amplifier les capacités de dispositifs hybrides. Cette hybridation de matériaux avec le silicium est nécessaire à cause des limites du Silicium pour la photonique. Comme le dispositif photonique est conçu pour être suffisamment petit pour être intégré sur une puce, on suppose que sa fonctionnalité devrait être comparable à celle des circuits

électroniques de la génération actuelle. Même si le silicium est à la base du développement de la photonique, la structure cristallographique du matériau lui-même l'empêche d'avoir des propriétés intrinsèques de modulation électro-optique. C'est pourquoi la réalisation de modulateurs photoniques en silicium a soit nécessité l'utilisation de structures résonantes (par exemple, des résonateurs en anneau et des nanocavités de cristaux photoniques) [2, 3] soit des configurations non résonantes telles que les interféromètres de type Mach-Zehnder [4].

Dans la première partie de cette thèse, nous étudierons le développement de nouveaux modulateurs/commutateurs hybrides combinés avec un nouveau matériau, l'oxyde de vanadium, conçus pour fonctionner aux longueurs d'onde des communications optique, avec pour objectif de réduire les dimensions, la consommation d'énergie et les pertes d'insertion ainsi que d'augmenter l'indice de modulation (modulateurs) et la fréquence de fonctionnement.

0.1.3 Oxyde de Vanadium (VO_2): Introduction et science de la modulation

Introduction

Le dioxyde de vanadium (VO_2) appartient à la classe des oxydes métalliques corrélés qui présentent une transition de phase métal-isolant (IMT). Cette transition de phase du VO_2 peut être obtenue par l'application d'un champ électrique ($E = 10^5 \text{ Vcm}^{-1}$) [5], par injection de porteurs ($n_e \approx 10^{18} \text{ cm}^{-3}$ [5]), par voie optique [6], impulsions térahertz [7] et chauffage thermique (au-delà de $T_c \approx 340 \text{ K}$ à la pression standard) [5]. D'autre part, la nature sous-jacente de cette IMT est qu'elle est suivie d'une transformation structurelle, entraînant par la suite un changement drastique des propriétés électriques et optiques du matériau. L'IMT du VO_2 et ses différents oxydes sont connues depuis quelques décennies. Les IMT induites thermiquement ont été étudiées pour la première fois par Morin [8] en 1959. Plusieurs oxydes de vanadium intermédiaires et un certain nombre d'autres oxydes de métaux de transition possèdent cette propriété, mais le VO_2 est le plus intéressant d'un point de vu pratique, car sa température de transition est de loin la plus proche des températures ambiantes, ce qui

signifie qu'il est plus facilement accessible pour une application à température proche de la température ambiante.

Théorie

Le vanadium est un métal de transition de configuration électronique $[Ar]3d^34s^2$. Il présente donc différents états d'oxydation et compte plus de dix états stables différents, dont l'oxyde monovalent VO et l'oxyde mixte comme V_8O_{15} , figure: 2.1. La plupart de ces oxydes présentent des transitions réversibles entre semi-conducteurs et métaux, ce qui est contraire à l'état prédict par la théorie des bandes. En général, cette transition pour les oxydes est déclenchée par un stimulus externe et elle se manifeste généralement par un changement radical de structure, suivi d'une variation drastique des propriétés optiques et électriques. Le déclenchement peut être de nature diverse comme la température, la pression et les champs électromagnétiques (EM) [9, 10, 11].

La raison pour laquelle la théorie des bandes ne parvient pas à prédire la nature du VO_2 , est que la théorie générale des bandes [12] est basée sur différentes hypothèses quant aux matériaux étudiés. Ces hypothèses ne prennent pas en compte la corrélation électron-électron et la corrélation électron-réseau. En outre, le VO_2 est connu pour être un matériau polymorphe, c'est-à-dire qu'il existe dans différentes structures crystallographiques: $VO_2(A)$, $VO_2(B)$, $VO_2(M1)$ et $VO_2(R)$ [13]. Il n'est donc pas facile d'expliquer la théorie complexe qui sous-tend la transition de VO_2 . De nombreux débats existent sur les différents mécanismes de transition majoritaires au sein du VO_2 [14, 15].

Mott, dans son étude sur l'oxyde de nickel (NiO), a découvert que, selon la théorie, le NiO était censé être métallique mais qu'expérimentalement il se révélait être isolant. A partir de cette observation, Mott a théorisé que certains matériaux, censés être métalliques selon la théorie des bandes, étaient en fait isolants à cause d'interactions électron-électron supplémentaires au sein de leur structure. En suivant cette théorie, il a suggéré que, si un électron se déplace de son site d'origine vers un nouveau site déjà rempli, il subira une

répulsion coulombienne. Et si l'énergie de répulsion est supérieure à l'énergie de l'électron entrant, cet électron restera alors lié à son site initial, limitant ainsi sa liberté de mouvement. Ce phénomène d'interaction des électrons conduit à la division de la bande initiale à moitié remplie en deux bandes séparées. Cette interaction électron-électron, négligée dans la théorie des bandes, est connue sous le nom de corrélation électronique.

Au contraire, Rudolf Peierls [16] dans ses recherches, a étudié un réseau 1-D d'atomes en chaîne disposés périodiquement et a postulé qu'une déformation structurelle peut créer des perturbations périodiques dans la chaîne du réseau. Selon le théorème de Bloch, ces perturbations peuvent modifier la structure de bande en couplant à la fois l'électron et le phonon, introduisant ainsi des transitions isolant-métal (IMT) dans les systèmes 1-D. Le phénomène découvert a été nommé Distorsion de Peierls. La transition structurelle peut ainsi être attribuée à une distorsion de Peierls due au déplacement du réseau [14]. Des études récentes suggèrent cependant qu'une IMT du VO₂ pourrait également se faire sans distorsion de Peierls [17].

De nombreux débats existent quant aux différents mécanismes physiques qui gouvernent les propriétés uniques de ces matériaux fortement corrélés et notamment sur les mécanismes majoritairement responsables de la transition isolant-métal. [18, 19, 20, 21, 15]. En effet, dans le cas du VO₂, la présence d'une transition à la fois structurelle et électronique complique la modélisation théorique. Une des questions fréquemment posée dans les recherches est de savoir si la force motrice de la transition est due aux changements de symétrie structurelle favorisant la localisation des électrons ou si la transition structurelle est motivée par de fortes corrélations électrons-électrons. Ou s'il s'agit plutôt d'une combinaison des deux mécanismes. En d'autres termes: l'IMT du VO₂ est-elle une transition de Mott, une transition de Peierls, ou un mélange de ces deux phénomènes? Même si la réponse exacte à cette question ne fait pas encore l'objet d'un consensus scientifique, nous montrerons dans les sections suivantes que nous pouvons exploiter l'IMT de nombreuses manières différentes, en induisant l'accordabilité des matériaux dans les dispositifs nanophotoniques. La théorie

détaillée est expliquée dans le chapitre 1.

0.1.4 Caractérisation du VO₂

Afin de réaliser un dispositif actif, nous devons analyser les caractéristiques structurelles et optiques du VO₂ en fonction des différentes techniques de dépôt et du substrat. En raison des différentes stœchiométries stables et complexes des phases de VO₂, comme le montre la figure 2.1, le dépôt de VO₂ en couche minces n'est pas une tâche simple. Ce qui rend la caractérisation structurelle encore plus difficile. En outre, on observe que même une petite variation du rapport oxygène/vanadium et de sa structure de liaison, affecte les caractéristiques de la couche mince, influençant ainsi les propriétés optiques et la transition de phase du VO₂ [22, 23, 24]. Et toute impureté non identifiée, que ce soit dans le système V-O ou dans les phases stoechiométriques, entraîne généralement une modification de la dispersion optique et des caractéristiques de commutation. Comme la fabrication est complexe, chaque échantillon ainsi fabriqué peut présenter des dispersions optiques différentes. Il est donc extrêmement important de procéder à une caractérisation précise de chaque couche mince pour en extraire les propriétés optiques nécessaires à la conception des dispositifs.

Dans notre laboratoire, nous avons utilisé la technique de dépôt par pulvérisation réactive assistée par magnétron pour la croissance de couches minces VO₂. Le système de pulvérisation est un AC450 de chez Alliance Concept. Les détails du système et de la technique de dépôt sont donnés dans le chapitre 2. De plus, nous avons reçu des échantillons de VO₂ déposés sur les substrats Si, SiO₂, Al₂O₃ et SOI, de S. Ramanathan de l'université de Purdue (USA). Le VO₂ déposé a été analysé structurellement à l'aide de techniques telles que XRD, RSM et TEM, puis analysé optiquement à l'aide de l'ellipsométrie spectroscopique. Les résultats sont détaillés au chapitre 2. L'importance de cette caractérisation est que ces échantillons seront utilisés comme base pour la réalisation de dispositifs VO₂ hybrides mentionnés ci-dessus. Par conséquent, sur la base de cette caractérisation optique, nous

extrayons les valeurs des propriétés du matériau, comme les changements de l'indice de réfraction en fonction de la température, qui sera un paramètre d'entrée important pour la conception des dispositifs. Afin d'extraire les propriétés optiques, nous avons caractérisé les couches minces de VO₂ par ellipsométrie spectroscopique. Il s'agit d'une technique optique utilisée pour mesurer l'amplitude spectrale tan(ψ) et la phase (Δ) de la lumière réfléchie, qui sont liées aux propriétés optiques et à la microstructure de l'échantillon étudié. Dans le cas d'un ellipsomètre à modulation de phase, comme celui que nous utilisons, nous ne mesurons pas directement les angles ellipsométriques ψ et Δ mais nous mesurons plutôt des fonctions de ψ et Δ . Définies comme :

$$Is = \sin(2\psi) \cdot \sin(\Delta)$$

$$Ic = \sin(2\psi) \cdot \cos(\Delta)$$

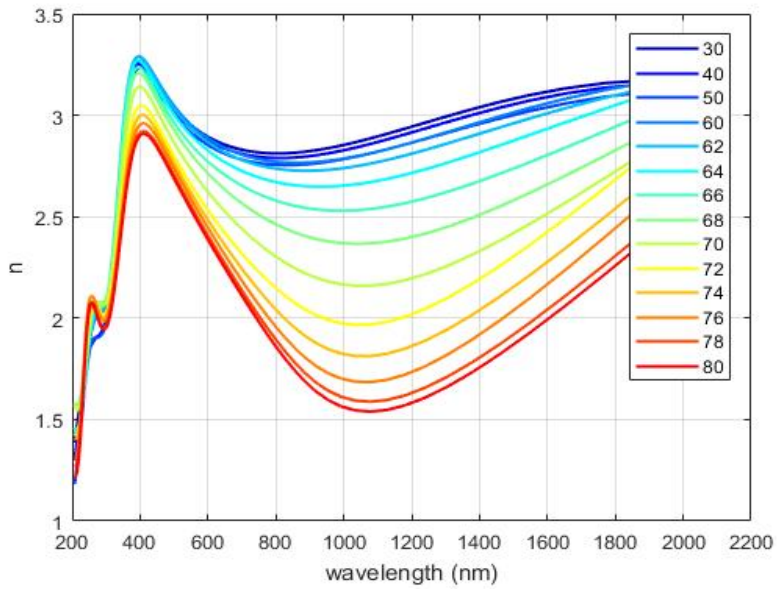
Ces fonctions trigonométriques Is et Ic sont directement liées à ψ et Δ . L'indice de réfraction analysé de VO₂ à l'état d'isolant (en dessous de T_c) est de $3,243 + 0,25367i$, et il passe à $2,02 + 2,9393i$ pour l'état métallique à une longueur d'onde de $1,55 \mu\text{m}$ (au-dessus de T_c) [25]. L'approche ellipsométrique extensive est expliquée en détail dans la section sur l'ellipsométrie du chapitre 2.

Nous pouvons résumer que les étapes impliquées dans le calcul des propriétés optiques de VO₂ en utilisant l'ellipsométrie comme première étape sont la collecte des valeurs Is et Ic par ellipsométrie, après quoi nous créons (simulons) le modèle optique pour l'échantillon en question (VO₂ sur SiO₂) en utilisant une formule de dispersion pour tous les matériaux constituant chaque couche individuellement.

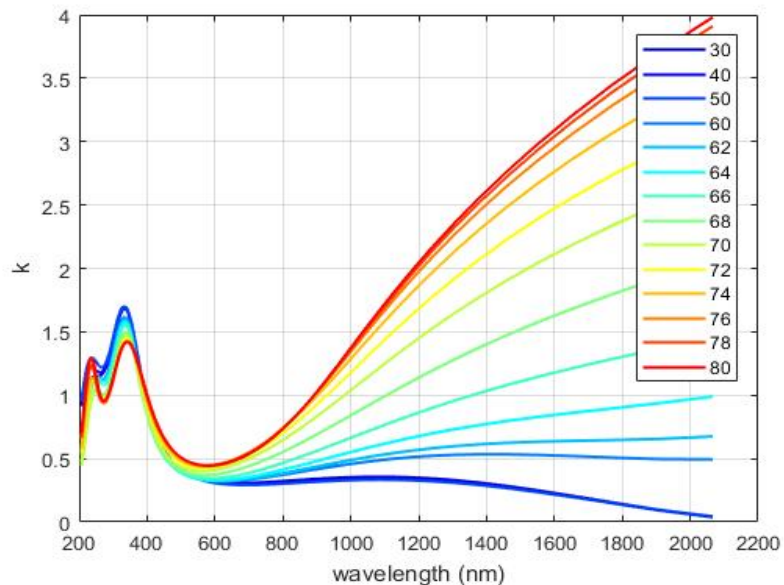
Pour VO₂, nous utilisons un modèle d'oscillateur dit "3TL" pour modéliser la dispersion du VO₂, où 3TL représente trois oscillateurs de Tauc-Lorentz. Le modèle théorique Tauc-Lorentz [26] a été développé par Jellison et Modine en 1996. Ils ont modélisé la fonction diélectrique complexe en utilisant la densité d'états joints de Tauc et l'oscillateur de Lorentz.

La somme de trois oscillateurs Tauc-Lorentz, chacun correspondant à des transitions interbandes dans le matériau [27], a été utilisée pour modéliser les propriétés optiques du VO₂. C'est-à-dire en utilisant trois oscillateurs Tauc-Lorentz pour des valeurs d'énergie faibles à élevées, partageant une bande interdite optique Tauc commune [28]. Pour décrire les propriétés optiques de VO₂ à l'état métallique, un modèle Drude [28] est ajouté au modèle de dispersion Tauc-Lorentz afin de prendre en compte la contribution des électrons libres. Pour plus de détails, nous renvoyons le lecteur au chapitre 2.

Comme le montre la figure 2.17, nous voyons que nous obtenons un très bon accord entre les paramètres Is/Ic ellipsométriques mesurés expérimentalement et le modèle optique simulé décrit ci-dessus, avec un bon facteur d'ajustement $\chi^2 = 0,59$. Sur la base de ces ajustements, nous arrivons à un accord entre les données optiques et expérimentales. Cet ajustement indique l'évolution du comportement métallique et ainsi l'émergence d'électrons libres dans l'échantillon lorsque nous faisons varier la température. Cela suggère l'ajout du modèle de Drude à l'oscillateur de Tauc-Lorentz. Dans notre cas, nous mesurons l'émergence du comportement métallique à 68°C, comme observé sur la figure 2.18.



(a) Extracted n as function of temp



(b) Extracted k as function of temp

Figure 1: Indice de réfraction et coefficient d'absorption extraits de VO₂ en fonction de la température. Cette extraction est basée sur un fit de données ellipsométriques, où l'on arrive à un accord entre les données optiques et expérimentales

0.1.5 Modulateur guide d'onde hybride VO₂/Silicium: Conception et principe de fonctionnement

Préambule et motivation

Dans le cadre des efforts visant à faire progresser les performances des modulateurs en Si, différentes équipes de recherche ont étudié des modulateurs à guide d'ondes basés sur des architectures hybrides utilisant des semi-conducteurs III-V et du LiNbO₃ (niobate de lithium) [29] intégrés sur silicium pour étendre sa capacité de modulation.

Contrairement aux larges changements optiques observés dans le VO₂, ces technologies tirent principalement parti des petites variations de l'indice de réfraction du milieu de guidage en réponse au changement de densité de charge, généralement induit par une tension. Cette petite variation de l'indice de réfraction peut entraîner une modulation >5dB pour une seule longueur d'onde pour une fréquence de modulation supérieure à >10 GHz [30]. Cependant, ces modulateurs classiques à cavité ou à structure interférométrique ont généralement des dimensions linéaires dépassant quelques dizaines de microns avec une gamme spectrale limitée. De même, les modulateurs à base de LiNbO₃ qui utilisent le schéma type "Mach-Zehnder" ont des dimensions plus importantes. Par exemple, les modulateurs composés (InGaAlAs/InAlAs/AlGaN) ont des performances équivalentes à celles des modulateurs à base de LiNbO₃, mais ils nécessitent une plus grande distance de couplage (quelques centaines de microns) en raison de leur modulation d'absorption limitée et du chevauchement modal [31].

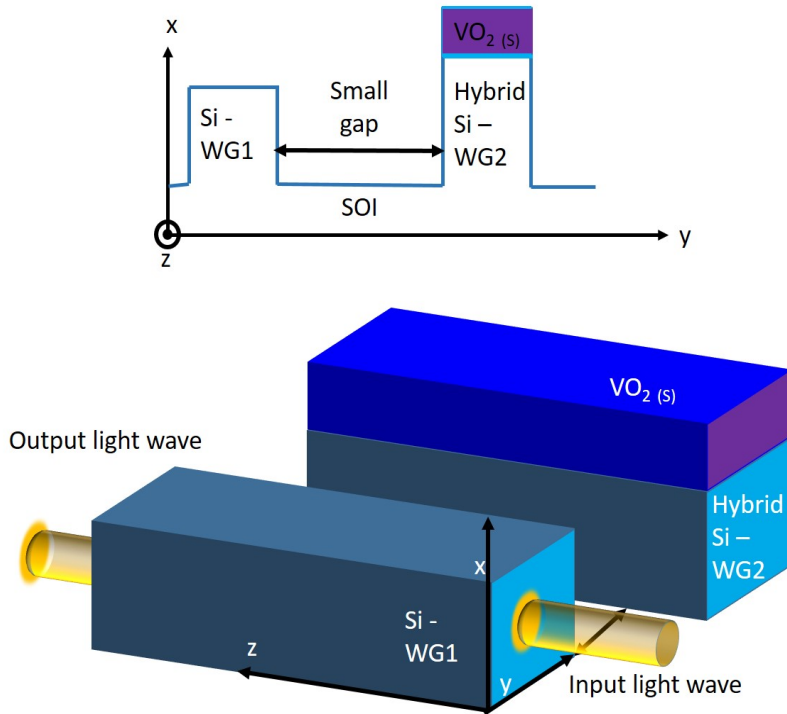
Idéalement, en termes d'énergie requise, un modulateur typique d'une empreinte de $1\mu m^2$ aura une consommation d'énergie de plusieurs ordres de grandeur supérieure à celle d'un dispositif de taille similaire basé sur VO₂ [32] avec une vitesse de commutation observée en régime sub-nanoseconde [33]. Compte tenu de toutes les propriétés intéressantes du VO₂ présentées dans le chapitre 2, il s'agit à ce jour d'un matériau très intéressant pour obtenir une accordabilité efficace dans les dispositifs photoniques.

Les modulateurs en espace libre basés sur le VO₂ ont déjà fait l'objet de démonstrations

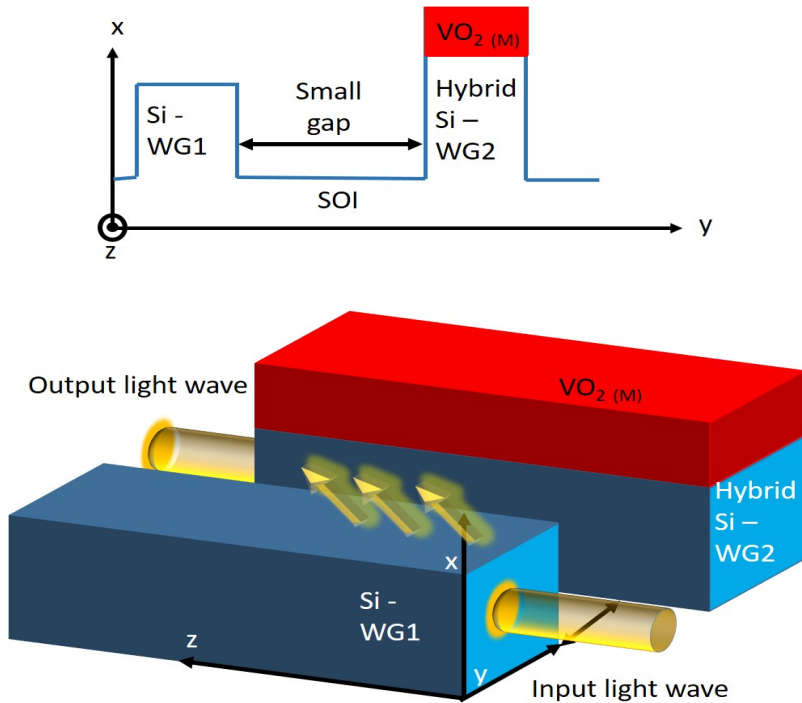
dans les gammes de longueurs d'onde infrarouge [34] et visible [35], via des transitions induites par la chaleur. Compte tenu des propriétés du matériau, les dispositifs basés sur le VO₂ sont souvent confrontés à de grandes pertes d'insertion et d'absorption, ce qui rend difficile leur mise en cascade dans un système intégré. Ces pertes d'absorption les rendent inutilisables pour des applications futures. Dans le cadre de cette thèse, nous avons mis au point une stratégie qui permet d'exploiter pleinement l'accordabilité de l'indice de réfraction sans que la forte absorption affecte les performances du dispositifs. Nous prévoyons de créer un modulateur intégré à guide d'ondes basé sur le VO₂ compatible CMOS qui utilise les pertes d'absorption du VO₂ comme un avantage.

Stratégie de conception

Nous passons maintenant à la conception du dispositif optique, dont la théorie a été formulée en détail dans le chapitre 3. Le design du guide d'onde modulateur hybride VO₂/Si proposé est basé sur les composants de type coupleur directionnel, conformément à la théorie des modes couplés. La stratégie de conception repose sur un patch de VO₂ intégré sur un guide Si, dont les dimensions sont conçues afin d'optimiser la modulation. Le schéma de la figure: 3.1, montre le patch de VO₂ conçu sur un guide d'onde hybride en Si, qui est placé stratégiquement à proximité du guide d'onde bus en Si. Le principe est le suivant: lorsque le VO₂ est isolant, le signal optique se propage dans le guide d'onde bus sans se coupler au guide d'onde hybride VO₂/Si. Puis lorsque le VO₂ est porté dans sa phase métallique, l'indice effectif du mode guidé dans le guide d'onde hybride se modifie et remplit les conditions pour le couplage directionnel. S'ajoute à cela les pertes optiques induites par le VO₂, permettant ainsi l'absorption totale du mode optique, et ainsi la modulation du signal dans le guide d'onde bus. Même si d'autres groupes ont déjà proposé des modulateurs plasmoniques basés sur le VO₂ avec une architecture différente, le dispositif que nous proposons va au-delà des anciens dispositifs proposés en terme de fonctionnalité et d'intégration. [36, 37, 38].



(a) Le VO_2 est isolant, la propagation des ondes est inaltérée et reste dans Si-WG1.



(b) Le VO_2 est métallique, l'onde dévie son chemin de propagation dans le guide d'onde adjacent et est absorbée par le VO_2 .

Figure 2: Vue schématique du modulateur hybride actif basé sur la transition de phase isolant-métal du VO_2

Le dispositif hybride proposé permet un nouveau type de modulateur compact qui peut être facilement intégré dans l'infrastructure photonique actuelle basée sur le Si et pourrait tirer parti de la transition rapide du VO₂. Les simulations électromagnétiques indiquent des géométries de dispositif de 600 μm de longueur avec un patch de modulation VO₂ de 300 μm avec un espace entre les guides d'ondes de 500 nm pour obtenir une plus grande profondeur de modulation. En outre, elle montre que la structure du dispositif basée sur le guide d'ondes peut être utilisée pour exploiter les états intermédiaires de VO₂ afin d'agir comme un filtre de puissance et de sonder davantage les propriétés fondamentales de la transition.

0.1.6 Simulation, fabrication et résultat

Simulation

La simulation du dispositif nécessite des moyens numériques pour calculer et analyser les modes des guides d'ondes dans la structure. Dans notre cas, nous utilisons la méthode des différences finies pour discréteriser le modulateur de manière à pouvoir calculer l'évolution des composantes électriques et magnétiques du champ électromagnétique en chaque point afin de pouvoir prédire avec précision le comportement de la lumière à l'intérieur et aux limites de la structure de guidage. Les informations importantes requises pour analyser le modulateur par calcul sont les propriétés du matériau, qui ont été extraites précédemment à l'aide des techniques de caractérisation optique. L'explication détaillée de la théorie de simulation est donnée dans le chapitre 3, où les méthodes de discréterisation et le solveur de mode conçu en interne sont également expliqués.

Grâce à la simulation numérique, nous avons pu calculer les dimensions souhaitées du guide d'onde bus Si et du guide d'onde hybride ainsi que leur espacement. Les dimensions obtenues, comme mentionné dans le paragraphe précédent, sont de la plus haute importance car le couplage de la lumière du guide d'ondes bus au guide d'ondes hybride est très sensible à l'espace entre les guides d'ondes. Il est également important de faire correspondre les

modes effectifs et les conditions de couplage pour les deux guides d'ondes, de sorte que les conditions de propagation dans les deux guides soient identiques. Dans tous les calculs, nous nous sommes basés sur un film mince de VO₂ sur SOI. Nous avons calculé la largeur correcte du guide d'ondes hybride de sorte que l'indice effectif des deux guides d'ondes soit identique lorsque le VO₂ est dans sa phase métallique.

En outre, dans notre cas, la cartographie de la grille en termes de schéma de différences finies a été réalisée de telle sorte que nous discrétonissons plus finement les zones proches de la limite de deux interfaces et sans utiliser de moyennage de l'indice de réfraction à la frontière contrairement aux outils du commerce, de manière à calculer plus précisément les champs E et H. Les schémas pour lesquels nous avons effectué cette discrétonisation sont donnés dans la figure 3.10. L'ensemble du système est discrétonisé en neuf couches verticalement sur l'axe des x et en six sections sur l'axe horizontal des y. Cela permet d'obtenir des valeurs plus précises en termes de l'indice effectif et des conditions d'orthogonalité entre mode de l'ordre de 10⁻¹⁵ par opposition à 10⁻⁷ pour les outils commerciaux. Le seul inconvénient est que le calcul est un processus intensif qui prend plus de temps lorsqu'une partie imaginaire de l'indice de réfraction est ajoutée.

Fabrication

Nous cherchons par la suite à fabriquer la structure simulée précédemment. La première étape vers la réalisation du dispositif hybride VO₂/Si est l'étape de lithographie définissant les deux structures de guide d'ondes. Afin de définir la structure, le motif a été exposé sur une résine ZEP 520A à l'aide d'un système de lithographie par faisceau électronique et ensuite développé. Le masque a été fabriqué en interne et toute la procédure de lithographie a été réalisée par P. Rojo-Romeo. Après avoir défini le motif, nous avons effectué une imagerie MEB Fig3.18, afin de vérifier le transfert du motif et nous avons observé un transfert parfait du motif et une distinction précise des intervalles entre les guides d'ondes. L'étape suivante a consisté à effectuer une gravure par RIE-ICP (Inductively Coupled Plasma Etching (ICP))

en utilisant un mélange d'Ar et de Cl₂ à température ambiante. La formulation de la recette de gravure a été faite en interne et la procédure de gravure a été réalisée par C. Chevalier. Après la procédure de gravure, nous avons effectué une observation MEB afin de visualiser le motif gravé. L'observation MEB a révélé que contrairement à ce qui était attendu, il y avait de multiples imperfections suite à l'étape de gravure.

En comparaison directe avec les images MEB avant (fig:3.18) et après (fig:3.19), nous observons un mauvais état général de la surface de l'échantillon. Comme nous pouvons presque distinguer les différents guides d'ondes, on peut supposer que le problème est soit lié à des restes de résine ou soit des résidus de masque dur sur la surface supérieure des guides d'ondes. Ce qui indique que le processus doit avoir été incomplet, entraînant des résidus de résine, ou que la gravure a pu endommager le masque métallique (atteignant le VO₂), contrairement à ce qui était prévu, en raison de la faible vitesse de gravure de la région couverte par le masque dur.

Résultats et discussion

Contrairement à ce que l'on attendait, le masque métallique et la résine ont été complètement gravés, ce qui a entraîné un effet résiduel sur la surface. Afin de récupérer le dispositif, il est nécessaire d'analyser l'échantillon en profondeur et de comprendre la composition chimique de la topographie de la surface. Cela permettrait d'identifier la composition du matériau en surface, qui nous éclairerait sur les problèmes liés à la gravure. Deuxièmement, une étude topographique par AFM pourrait nous donner des informations sur la rugosité. Après la caractérisation, nous pourrions procéder à une nouvelle gravure et à un nouveau processus de nettoyage afin d'éventuellement réussir à finaliser le dispositif. D'autre part, nous pourrions utiliser une technique de dépôt et de fabrication alternatives, par le biais d'une approche dite de lift-off pour permettre le dépôt de VO₂ uniquement sur les guides d'ondes déjà patternés, évitant ainsi l'étape de gravure qui est problématique.

Plus loin dans le chapitre, j'ai également montré un nouveau concept pour l'application

du modulateur guide d'ondes, comme filtre de puissance, en exploitant les différentes étapes de transition de VO₂. Cette application est particulièrement utile dans le domaine des réseaux neuronaux, dans le but de développer un réseau neuronal tout optique (AONN). Cet AONN est un réseau complexe de dispositifs multifonctionnels fonctionnant en synergie pour fournir un calcul similaire à ceux ayant lieu au sein des neurones. Notre modulateur VO₂ pourrait être utilisé comme une "weight bank" optique qui est un composant de l'AONN.

Le modulateur à guide d'ondes hybride VO₂/Si, s'il est fabriqué avec succès, peut être un composant prometteur pour les futurs systèmes optiques intégrés. Les simulations pour les modulateurs montrent que, par rapport aux modulateurs classiques, un simple déclencheur (optique, électrique ou thermique) peut avoir un impact profond sur les valeurs de transmission dans le guide d'ondes du bus. Contrairement aux dispositifs VO₂ basés sur une absorption élevée, cette architecture de dispositif peut être mise en cascade avec de faibles pertes d'absorption.

0.2 Part 2: Résonances multipolaires accordable par design utilisant des nanocristaux de VO₂

0.2.1 Introduction

Dans cette partie, nous étudions les propriétés de nanocristaux de VO₂ implantés dans de la silice fondu. Nous y démontrons expérimentalement que les résonances multipolaires des nanocristaux (NC) de VO₂ peuvent être accordées dynamiquement grâce à la transition isolant-métal du VO₂. En utilisant à la fois la théorie de Mie et la théorie du milieu effectif de Maxwell-Garnett, nous retrouvons l'indice de réfraction complexe du milieu effectif composé d'une couche de VO₂-NCs immersés dans du SiO₂ et nous montrons qu'un tel métamatériaux présente une accordabilité optique distincte par rapport à du VO₂ non structuré. Mais surtout, nous montrons dans ce qui suit que cette approche métamatériaux permet de concevoir des métamatériaux composites accordables présentant une modulation de l'indice de réfraction sans extinction induite, ou en d'autres termes un métamatériaux à changement de phase à extinction induite nulle. La section suivante explique la théorie, suivie des techniques de fabrication et de caractérisation des VO₂-NC.

0.2.2 Théorie de Mie et extraction des paramètres effectifs des nanocristaux de VO₂

Théorie de Mie

Nous commençons par analyser les propriétés de particules sphériques diélectriques lorsqu'elles sont illuminées par une onde électromagnétique et en particulier, nous étudions la diffusion (scattering) correspondante de manière à évaluer les composantes magnétiques et électriques. La complexité de l'analyse de la diffusion augmente considérablement lorsque la taille de l'objet s'approche de la longueur d'onde de l'onde incidente. Dans notre cas le rayon sphérique était de 50 nm. Dans une telle situation, nous ne pouvons plus supposer que le champ est constant à l'intérieur de l'objet: l'"approximation aux grandes longueurs d'onde" cesse de s'appliquer et les effets de retard doivent être pris en compte. Par conséquent,

pour calculer le champ diffusé par un objet de forme arbitraire, il faudrait une approche numérique. Un problème aussi complexe peut cependant être simplifié si l'objet est une sphère. En 1908, Mie a trouvé une solution exacte à ce problème, en calculant le champ diffusé comme une solution en série [39]. L'idée était d'étendre les champs électriques et magnétiques en termes d'harmoniques sphériques vectorielles. Ensuite, les fonctions de champs peuvent être représentées dans une combinaison linéaire de termes qui sont les produits de fonctions séparables des trois coordonnées sphériques.

Nous avons calculé numériquement le coefficient de diffusion en nous basant sur le formalisme de Lorenz-Mie pour la diffusion et l'absorption de la lumière par des petites particules [40]. En traçant ainsi les coefficients de diffusion calculés, nous avons observé que, quel que soit l'état de VO₂, en dessous de 700 nm, la réponse électromagnétique est dominée par la réponse dipolaire électrique (DE) et la réponse dipolaire magnétique (DM), avec une petite contribution du terme quadrupolaire électrique (QE). comme le montre la figure 4.2.

Extraction des paramètres effectifs des nanocristaux de VO₂

Avant de se pencher sur les méthodes d'extraction de l'indice de réfraction effectif du milieu composite, nous avons analysé les propriétés structurales et de transition des VO₂ NCs intégrés dans la silice. Nous avons appliqué les mêmes tactiques d'ellipsométrie que celles mentionnées au chapitre 3 pour extraire les propriétés physiques inhérentes à l'échantillon. Selon les résultats, (qui sont expliqués en détail au chapitre 4), nous observons les changements de propriétés des matériaux comme on peut s'y attendre d'un matériau à changement de phase. Pour les mesures expérimentales d'ellipsométrie, un modèle optique multicouche a été créé (similaire au chapitre 2) qui comprend quatre couches, comme le montre la figure 4.7. (i) une couche mince de SiO₂, (ii) la couche effective VO₂-NCs + SiO₂, (iii) une couche intermédiaire contenant des inclusions et des impuretés de vanadium et (iv) un substrat semi-infini de SiO₂. Ce modèle à quatre couches est justifié par les observations

TEM des sections transversales de l'échantillon. Nous utilisons un fichier de dispersion de référence pour le SiO₂ (Palik : [41]).

Afin d'extraire l'indice de réfraction effectif numérique, nous utilisons l'approximation du milieu effectif (EMA) de Maxwell-Garnet assistée par la théorie de Mie. Ce mélange des théories de Mie et de Maxwell-Garnett (Mie-MG-EMA), nous permet de calculer une permittivité diélectrique effective (ϵ_{eff}) et une perméabilité magnétique (μ_{eff}) qui sont directement déterminées par les coefficients dipolaires de Mie électrique a_1 et magnétique b_1 respectivement. Ainsi, l'ajout de la théorie de Mie dans les calculs de milieux effectifs nous permet de tenir compte des effets de taille qui ont été ignorés par l'approximation électrostatique dans l'EMA classique de Maxwell-Garnett. Nous avons ainsi pu obtenir des formules analytiques permettant le calcul des valeurs de ϵ_{eff} , de μ_{eff} et ainsi de l'indice de réfraction complexe effectif en fonction de la taille des NCs et du facteur de remplissage. Ces formules analytiques ont ensuite été utilisées pour fitter les données expérimentales mesurées par ellipsométrie.

La procédure de fit des mesures expérimentales de l'ellipsométrie a été la suivante: (détails dans le chapitre 4), les épaisseurs respectives de la couche supérieure SiO₂, de la couche d'inclusion VO₂-NCs et de la couche d'inclusion V ont été définies comme des paramètres d'ajustement libre, dans le modèle multicouche présenté sur la figure 4.7. Aucune des dispersions de la matière n'a été fittée, nous avons plutôt modifié la taille et la densité des VO₂-NCs dans notre modèle Mie-Maxwell Garnett pour ajuster les fits aux mesures. Comme il pourrait exister une corrélation entre les épaisseurs et la permittivité des films absorbants, nous ajustons simultanément les deux séries de mesures pour VO₂ isolant et VO₂ métallique et nous lions les différentes épaisseurs. Cela signifie que le fit final donnera les mêmes épaisseurs pour les différentes couches, quelle que soit la phase de VO₂-NCs. La seule différence entre les deux modèles réside dans la dispersion des VO₂-NCs.

Dans la figure 4.8, nous montrons les fits optimisés avec les données expérimentales.

Nous obtenons une bonne correspondance globale entre le modèle et les mesures pour une taille de VO₂-NCs de $R = 35\text{nm}$ et un facteur de remplissage $f = 0,18$. En particulier, les fits sont presque parfaits dans la gamme UV/Vis mais une légère divergence apparaît dans le proche infrarouge.

Cet écart entre le modèle et les données expérimentales peut être expliqué par les quelques interactions interparticulaires possibles qui n'ont pas été prises en compte par l'approximation de Mie-MG-EMA. Dans le chapitre 4, nous essayons d'expliquer et d'étudier en détail les deux phénomènes physiques potentiellement responsables de cet écart entre calcul et expérience, à savoir l'interaction électromagnétique entre les particules et un degré de polydispersité potentiellement non négligeable dans la distribution de taille des VO₂-NCs.

0.2.3 Discussion et perspectives futures

Dans ce chapitre, nous avons pu constater un accord qualitatif remarquable entre les mesures et les calculs, malgré les approximations mentionnées ci-dessus. Nous avions également souligné le fait que ce modèle simple est capable de reproduire correctement les principales caractéristiques de la réponse optique pour les deux états de VO₂ en changeant simplement la dispersion de VO₂ entre isolant et métallique. Ce que l'on peut effectivement observer sur la figure 4.2, est que les calculs reproduisent bien le premier pic dans le visible, qui est une combinaison de résonances dipolaires électriques et magnétiques, et le second pic dans le proche infrarouge qui est une résonance plasmonique. Cette dernière n'est présente que lorsque le VO₂ est métallique, c'est à dire lorsque la partie réelle de la permittivité est négative. Il s'agit donc d'une résonance accordable dynamiquement.

Le modèle Mie-MG-EMA nous permet ainsi de reproduire par calcul les principales caractéristiques spectrales des métamatériaux basés sur VO₂-NC. Nous pouvons ainsi prédire les propriétés optiques attendues des VO₂-NC de tailles arbitraires. Nous montrons ci-dessous comment ce modèle peut être utilisé pour concevoir des métamatériaux accordables

avec des propriétés adaptées pour des gammes de longueurs d'onde souhaitées. La figure 4.14 montre l'évolution calculée des valeurs n_{eff} et k_{eff} des VO₂-NCs dans leurs états isolants et métalliques pour différentes dimensions de NCs. Nous avons ensuite tracé Δn_{eff} et Δk_{eff} , qui sont définis comme $\Delta n_{eff} = n_{eff,isolant} - n_{eff,mettallique}$ et $\Delta k_{eff} = k_{eff,isolant} - k_{eff,mettallique}$ et qui représentent l'amplitude de modulation de l'indice de réfraction effectif et du coefficient d'extinction effectif, respectivement. Avec cette figure, nous pouvons identifier des régions spécifiques de la taille en fonction de la longueur d'onde pour lesquelles la commutation de VO₂ se traduit soit par un indice de réfraction accordable, soit par un coefficient d'extinction accordable.

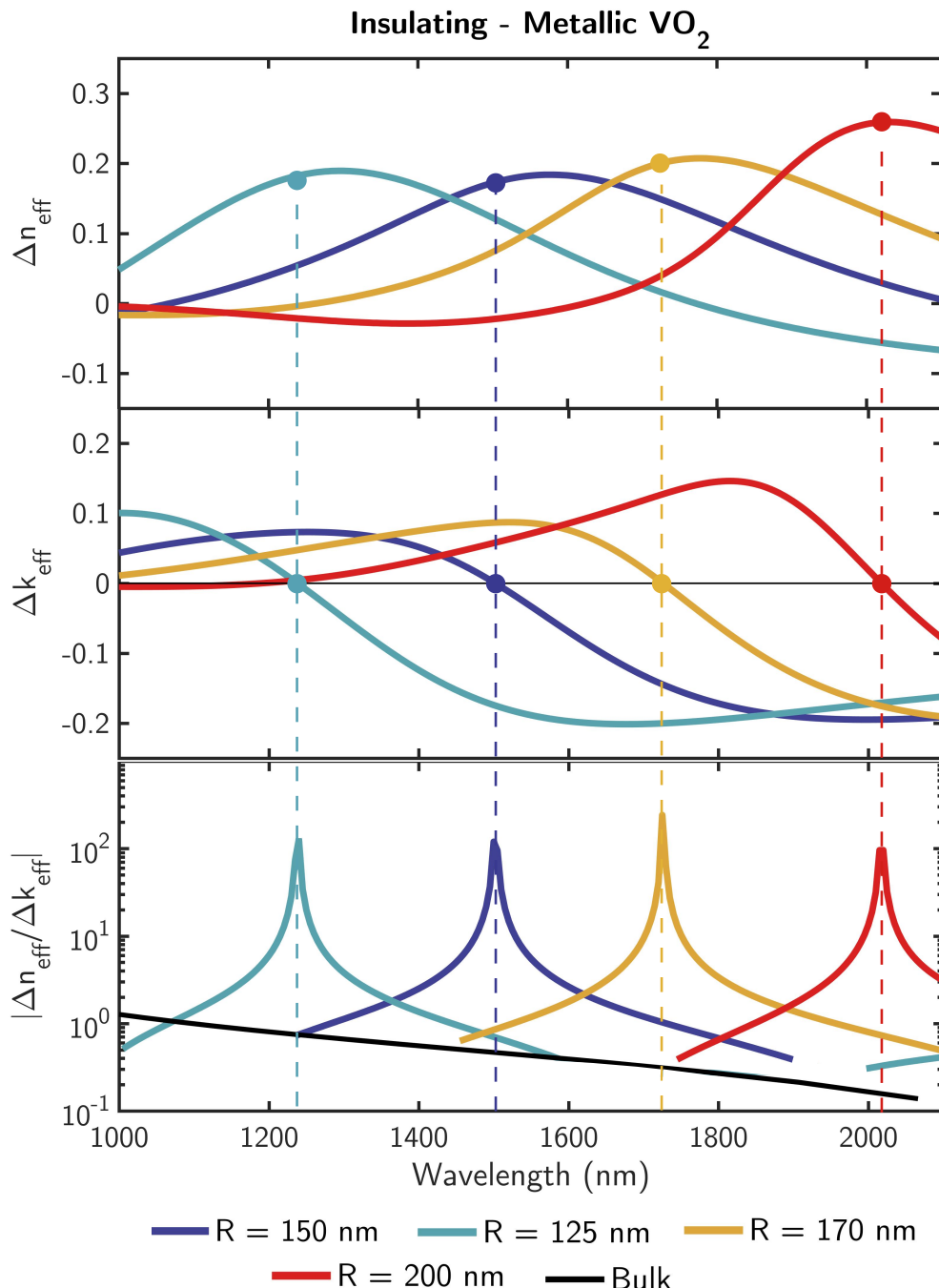


Figure 3: Variation spectrale de l'amplitude de modulation de l'indice de réfraction effectif (Δn_{eff} et Δk_{eff}) du métamatériaux pour la taille des NCs sélectionnés. Graphique du bas : Figure de mérite ($FOM=\Delta n_{eff}/\Delta k_{eff}$) de la plateforme VO₂-NCs pour différentes tailles de nanocristaux et comparé au FOM pour une couche mince VO₂.

Il est intéressant de noter qu'en traçant les valeurs Δn_{eff} et Δk_{eff} calculées pour quelques tailles sélectionnées de VO₂-NCs (comme le montre la figure 4.15), nous avons

observé qu'autour du maximum Δn_{eff} atteint pour chaque taille de NCs, nous avons simultanément $\Delta k_{eff}=0$. Ce qui signifie que cette plateforme de métamatériaux à changement de phase permet d'obtenir par design une accordabilité dynamique de l'indice de réfraction sans modifier l'absorption optique, figure 3.

De plus, cet ajustement de l'indice de réfraction à "perte induite nulle" peut être conçu pour se produire dans toute la gamme du proche infrarouge en sélectionnant spécifiquement une taille appropriée de NCs. Cet effet ne peut pas être obtenu avec des films minces de matériaux à changement de phase et souligne l'utilité de les modifier par une approche type métamatériaux. Nous notons également que l'effet inverse peut être exploité, à savoir, proche du maximum Δk_{eff} , nous pouvons avoir simultanément une valeur Δn_{eff} négligeable. Cette plate-forme peut donc être utilisée pour contrôler activement l'absorption sans modifier l'indice de réfraction du milieu (par exemple, pour R=95nm à $\lambda=1500\text{nm}$, on obtient $\Delta k_{eff}=-0,2$ et $\Delta n_{eff}=0$), comme le montre la figure 4.16.

0.2.4 Conclusion

En conclusion, nous avons démontré une plateforme active basée sur des VO₂-NCs intégrés dans du SiO₂ sous forme de nano-inclusions sphériques qui permettent d'exploiter l'IMT du VO₂ pour accorder et commuter des modes multipolaires dans le visible et le proche infrarouge. Contrairement aux couches minces de VO₂ non patternées, cette approche métamatériaux permet d'adapter l'indice de réfraction complexe et l'accordabilité des matériaux à changement de phase. En effet, nous avons montré qu'en ajustant la taille des VO₂-NCs, ce système peut être exploité comme un métamatériaux à changement de phase dont les propriétés de modulation d'indice de réfraction et d'absorption sont ajustables par design. Dans une perspective scientifique plus large, les résultats présentés dans ce chapitre aident à définir un nouveau système permettant d'étudier les interactions accordables entre les nanoparticules et les interférences accordables entre les résonances multipolaires. Nous l'envisageons comme un banc d'essai pour la modulation dynamique de la diffusion de la

lumière, les effets Kerker accordables et le contrôle actif de la directivité de la lumière.

0.3 Part 3: Mésasurfaces à base de VO₂ pour la nanophotonique accordable en espace libre

0.3.1 Introduction

Le domaine des métamatériaux et des mésasurfaces connaît une croissance considérable. Cela est dû aux limites des matériaux et structures naturels où l'interaction et l'accordabilité sont limitées par la diffraction et sont principalement régis par l'indice de réfraction et non par la structure. Sauf dans certains cas, comme celui du papillon Morpho, où les nanostructures complexes de ses ailes reproduisent une couleur bleue vibrante. Ce phénomène a motivé les scientifiques à comprendre et à reproduire une telle couleur vibrante en laboratoire en utilisant des matériaux naturels.

Cette limitation des matériaux naturels est surmontée en créant essentiellement des matériaux artificiels qui peuvent se comporter de manière similaire à un milieu naturel ou même présenter des propriétés supérieures à ces matériaux. Cette catégorie de matériaux ou de dispositifs fabriqués par l'homme est connue sous le nom de métamatériaux (où méta signifie "au-delà" en grec). Afin d'obtenir les interactions souhaitées avec la lumière, les constituants de ces métamatériaux, appelés méta-atomes (généralement plus petits que la longueur d'onde de la lumière), sont définis par l'utilisateur et sont conçus et disposés de telle sorte qu'un effet moyen se produise en termes de diffusion et d'interférence avec les ondes lumineuses. La propriété ou la réponse globale des métamatériaux dépend des structures unitaires individuelles, mais surtout des propriétés physiques, de la disposition et de l'orientation de la ou des méta-structures/méta-atomes. Par conséquent, en ajustant les dimensions et arrangements de ces méta-atomes, il est possible de développer de nouveaux matériaux, possédant des propriétés uniques qui ne sont pas naturellement disponibles dans la nature. De tels travaux ont conduit par exemple au développement de matériaux à indice de réfraction négatif [42, 43, 44], de matériaux à indice zéro [45, 46, 47], de "capes d'invisibilité" (optical cloaking) [48, 49] et imagerie sub-diffraction [50, 51].

Dans cette section, nous nous concentrerons davantage sur les métasurfaces 2D, qui présentent un phénomène similaire à celui attendu des métamatériaux, mais dont les épaisseurs sont de l'ordre d'une fraction de la longueur d'onde et sont donc relativement plus simple à fabriquer. En outre, les métasurfaces permettent de fabriquer des composants plats qui peuvent être intégrés presque partout. Cela permet de réduire considérablement les dimensions des composants optiques (les composants en optique classique reposent sur l'accumulation de la phase optique pendant la propagation, ce qui nécessite, par exemple, d'avoir des surfaces courbes pour les lentilles). Contrairement à l'optique classique, où la lumière traverse un milieu d'un indice de réfraction particulier pour modifier son trajet, les métamatériaux permettent de manipuler l'indice de réfraction du milieu par le biais de nanostructures pour obtenir le contrôle du front d'onde souhaité. Jusqu'à présent, la plupart des métasurfaces démontrées expérimentalement sont statiques après fabrication et, par conséquent, leurs applications sont pour le moment limitées. [52, 53].

Notre travail vise donc à conférer de l'accordabilité aux métasurfaces en exploitant la transition isolant-métal du VO₂. Pour cela, nous cherchons à moduler dynamiquement les résonances de structures de dimensions sous-longueurs d'onde. En utilisant cette stratégie de contrôle de la résonance, nous proposons d'abord une modulation de couleurs structurelles au sein de nanostructures de TiO₂ sur un film mince de VO₂, créant ainsi un champ d'application futur pour les affichages de couleurs structurelles accordables. Nous démontrons également la manipulation de résonances de Mie électriques et magnétiques induites par l'IMT du VO₂, supportée par des nano-piliers de silicium, qui permettent d'obtenir une modulation de transmission de l'ordre de trois ordres de grandeur à $\lambda = 1555\text{nm}$.

0.3.2 Métasurface de VO₂ pour la génération de couleur structurelle accordable

Introduction

La couleur structurelle est un champ de recherche dont l'origine a été inspirée par la couleur bleue vibrante des ailes du papillon Morpho. La couleur structurelle pourrait

être une technologie alternative aux technologies d'affichage actuelles car la majorité de ces technologies utilisent soit des LCD (écrans à cristaux liquides) soit des LED (diodes électroluminescentes) dont les dimensions sont plus grandes que la longueur d'onde de fonctionnement, ce qui limite la taille des pixels et des dispositifs. En outre, la plupart du temps, lorsque nous voulons produire de la couleur, nous utilisons des pigments pour l'affichage visuel, qu'ils soient statiques (affiches, peintures murales, imprimantes, etc.) ou dynamique, comme les écrans à cristaux liquides. Les colorants synthétiques sont coûteux à produire, plus difficiles à recycler et nuisibles à l'environnement. En outre, ils se décomposent et ne sont pas stables, ils manquent de résolution, ce qui limite encore leur champ d'application. C'est pourquoi, dans la recherche d'un remplacement approprié, les chercheurs ont accordé une attention considérable à la coloration structurelle. Un exemple célèbre de couleur structurelle peut être observé dans la nature : la couleur bleue métallique des ailes du papillon Morpho. Le papillon Morpho nous a permis de réaliser qu'il existe une autre façon de produire des couleurs sans aucun colorant ni pigment, en disposant simplement des matériaux transparents dans une structure périodique [54] façonnant l'interférence entre la lumière incidente et la lumière réfléchie. Cependant, la haute qualité des couleurs structurelles que présente la nature nécessite des structures compliquées et volumineuses [55, 56] qui rendent la taille de la structure beaucoup plus grande que la longueur d'onde [57].

La technologie des écrans est très utile à l'humanité. Il est donc très important de comprendre comment l'homme perçoit les couleurs. Dans le chapitre 5, nous avons expliqué en détail la perception des couleurs et la carte des couleurs RGB (Red Green Blue), qui sont très importantes pour comprendre et représenter les différentes couleurs sous forme numérique.

Génération de couleurs structurelles accordables par des structures diélectriques

Le type de matériau utilisé classifie la métasurface et son interaction. Par exemple, les nanostructures métalliques utilisent les plasmons de surface (une interaction collective entre les électrons libres et le photon) (SP) [58] pour piloter la réponse optique des méta-structures métalliques ; d'où le nom de métasurface plasmonique [59, 60]. Des recherches récentes ont démontré expérimentalement des métasurfaces plasmoniques permettant de contrôler la polarisation, l'amplitude et la phase du rayonnement électromagnétique [61, 62]. Celles-ci ont joué un rôle essentiel dans divers domaines d'application tels que les lentilles plates [63], les hologrammes [64], les coupleurs directionnels [65] etc.

Dans les métamatériaux diélectriques, les résonances supportées sont une combinaison de dipôles électriques et magnétiques, autrement appelées résonances de Mie. La théorie de Mie est une solution analytique des équations de Maxwell pour la diffusion du rayonnement électromagnétique par des particules de toute taille (également appelée diffusion de Mie). Cela a permis de comprendre que l'utilisation d'un matériau diélectrique à indice de réfraction élevé nous permet de contrôler à la fois le dipôle électrique et magnétique contrairement au seul dipôle électrique dans un système de matériau plasmonique. L'amélioration de la réponse magnétique provoquée par l'interaction de la lumière incidente avec des particules de taille similaire à la longueur d'onde peut permettre de concevoir des filtres de couleur qui utilisent différentes résonances de Mie avec des multipôles d'ordre supérieur. [66]

De même, nous pouvons ajuster davantage les propriétés optiques des métasurfaces en utilisant des effets collectifs grâce au couplage entre les résonateurs avec une catégorie de résonance plus générale appelée résonance de Fano [67]. Elle utilise l'interférence entre la lumière rayonnée et réfléchie de manière constructive ou destructive. Ce phénomène a été étudié par Fano et al [68]. Cette théorie de la résonance peut être utilisée pour générer une couleur structurelle par interférence entre la lumière directement réfléchie et le mode de résonance guidée sur une structure de surface. Puisque les réponses électromagnétiques de ces structures ne sont pas seulement régies par les permittivités complexes du matériau,

mais aussi par la géométrie dans laquelle elles existent. Par conséquent, pour créer une reproduction précise des couleurs, il est essentiel de déterminer les mécanismes de couplage de la surface avec la lumière extérieure et de pouvoir les concevoir de manière à obtenir les propriétés souhaitées. Ce type de résonance nous donne la flexibilité nécessaire pour le choix du matériau, l'extensibilité pour la fabrication à grande échelle et une faible dépendance angulaire.

Dans notre cas, nous avons démontré à l'aide de simulations, deux stratégies uniques pour mettre en œuvre l'accordabilité en créant une couleur structurelle accordable. Notre première stratégie consiste à utiliser des nano-structures cylindriques de TiO₂ sur des films minces de VO₂, de telle sorte que pendant la transition, la résonance fano de la couleur structurelle est modulée, ce qui entraîne un léger décalage dans l'interférence de l'onde incidente et de l'onde rayonnée. Ce qui conduit à un changement de couleur de manière collective. Alors que la seconde stratégie implique la mise en œuvre directe de nanocylindres de VO₂, où la transition IMT du VO₂ affecte à la fois les résonances de Mie et les résonances de Fano. Les résultats de la simulation dans les deux cas sont présentés en détail au chapitre 5. Le résultat sur l'implémentation des nanostructures de VO₂ montre des résultats prometteurs par rapport à la structure en couche mince et pourrait être un avantage pour les futures technologies d'affichage colorés basées sur des structures accordables.

0.3.3 Métasurface de VO₂ pour une absorption totale accordable.

Introduction

Les absorbants parfaits utilisant des structures de type métamatériaux ont gagné en popularité ces dernières années. Un absorbant parfait est un dispositif dans lequel tout le rayonnement incident est absorbé à la fréquence de fonctionnement. Les premières applications des absorbants électromagnétiques (EM) ont été l'exploitation furtive dans la gamme des opérations RADAR ou micro-ondes/ondes radio, réduisant la section transversale du radar [69, 70]. Plus récemment, les absorbants EM sont utilisés pour réduire les interférences en

absorbant les rayonnements EM parasites. Le contrôle de l'absorbance de la lumière joue un rôle majeur dans nos industries photoniques actuelles et peut avoir un fort impact dans la collecte de l'énergie solaire [71, 72], les bolomètres ainsi que les capteurs chimiques et biologiques. Les métamatériaux sont conçus pour modifier les valeurs de μ et ϵ de telle sorte que leur impédance corresponde à celle de l'espace libre, créant ainsi un milieu transparent et sans réflexion. Cela peut s'avérer très avantageux pour créer des filtres parfaits et limiter les pertes. Malgré la croissance des métasurfaces statiques basées sur la résonance de Mie, les rendre accordables reste un problème majeur. Ces dernières années, des efforts considérables ont été déployés pour mettre au point des dispositifs nanophotoniques accordables constitués de nanostructures métalliques couplées à divers matériaux à changement de phase tels que GeSbTe et VO₂ [73, 74, 75], mais les nanostructures accordables entièrement diélectriques restent largement inexplorées. Dans cette section, nous démontrons la stratégie de conception d'un absorbant parfait à métasurface accordable basé sur le VO₂, composé de résonateurs en Si, supportant à la fois des modes de Mie électriques et magnétiques.

Principe et théorie de conception des absorbants parfait

Contrairement à la section précédente, nous nous concentrons ici sur l'accordabilité du VO₂ dans le spectre des télécommunications (proche infrarouge) [76, 77]. Dans une nanoparticule diélectrique, une résonance magnétique de Mie provient d'une excitation d'un mode électromagnétique particulier dans la particule. Cette excitation se produit lorsque la longueur d'onde effective de la lumière à l'intérieur de la particule devient comparable à la taille de la particule, présentant un courant de déplacement circulaire du champ électrique [78, 79]. La capacité d'exciter simultanément les réponses électriques et magnétiques au sein d'une nanoparticule est d'un grand intérêt pour diverses applications et donne un autre degré de liberté pour ajuster la réponse d'un métamatériaux par conception [80, 78]. Il a également été démontré que les emplacements spectraux des résonances dipolaires électriques et magnétiques d'un résonateur diélectrique peuvent être ajustés en faisant varier la géométrie

du résonateur de manière à obtenir les propriétés de diffusion souhaitées. Milton Kerker a étudié ce phénomène en 1983 et a révélé qu'il est possible d'obtenir un rayonnement de champ asymétrique avec une diffusion arrière nulle (zero back scattering) ou une diffusion avant nulle (zero forward scattering) en combinant correctement les dipôles électriques et magnétiques des particules magnéto-diélectriques. Selon la première condition de Kerker, lorsque $\mu = \epsilon$, l'onde incidente subit une diffusion vers l'arrière nulle (ZBS). Alors que pour une diffusion avant nulle (ZFS), μ et ϵ doivent satisfaire la condition $\epsilon = \frac{(4-\mu)}{2\mu-1}$, soit la deuxième condition de Kerker.

Dans notre travail, nous assemblons des nano résonateurs Si spécialement conçus en réseaux périodiques bidimensionnels fabriqués sur un film mince VO₂. Le principe est le suivant : lorsque VO₂ est isolant, les résonances ED et MD se chevauchent et nous remplissons ainsi les conditions de Kerker et obtenons une diffusion arrière nulle. Comme le VO₂ est partiellement absorbant même à l'état isolant, la majeure partie de la lumière est absorbée et nous obtenons donc un absorbant quasi parfait. D'autre part, lorsque VO₂ devient métallique, la résonance MD disparaît et la condition Kerker n'est plus remplie. Cependant, comme l'absorption du VO₂ augmente largement, nous maintenons toujours un régime d'absorption quasi-parfait, mais décalé spectralement en raison de la modulation de l'indice de réfraction du VO₂. L'état de phase de la couche VO₂ définit donc l'interaction entre la lumière incidente et deux modes de résonance et contrôle la position spectrale de l'absorption parfaite. Il est possible d'approcher un régime d'absorption parfaite cohérente réduisant la réflexion des métasurfaces de plus de deux ordres de grandeur à une longueur d'onde de 1555 nm. Le concept proposé est illustré dans la figure : 5.13. La fabrication d'un tel échantillon est une tâche fastidieuse car il y a de multiples empilements de couches soigneusement ajustées, déposées et gravées. Nous avons mesuré et caractérisé l'échantillon plusieurs fois au cours de sa fabrication pour nous assurer que l'échantillon reste intact et que son fonctionnement peut être répété sur de nombreux cycles. Toutes les étapes importantes sont mentionnées en détail dans le chapitre 5.

Finalement, nous avons caractérisé le dispositif ainsi fabriqué et démontré, pour la première fois à notre connaissance, des métasurfaces hybrides silicium/VO₂ présentant des résonances de Mie accordables dynamiquement. En jouant sur le recouvrement spectral des ED et MD et en tirant parti de la transition de phase du VO₂, nous avons démontré expérimentalement une modulation de la réflexion de deux ordres de grandeur à $\lambda = 1550\text{nm}$. Par la suite, nous avons également démontré que la réponse optique de la métasurface présente un comportement d'hystérésis et pourrait donc être utilisée comme mémoire non volatile.

Conclusion

Cette partie correspond au chapitre 5 de la thèse. Nous y avons démontré deux types de métasurfaces activement accordables en espace libre, exploitant la propriété de transition du VO₂. Le concept qui sous-tend les deux démonstrations est similaire, mais le spectre d'application peut être varié. Nous avons utilisé des matériaux diélectriques structurés en métasurfaces et présentant des résonances ED et MD accordables permettant de contrôler le chemin de diffusion du rayonnement et son absorption. Dans un cas, ce principe permet de moduler les résonances de manière à générer des couleurs structurelles; dans l'autre cas, il permet de créer un absorbant parfait avec un avantage d'accordabilité grâce au VO₂. Ceci montre l'impact potentiel du VO₂ et ses différentes domaines d'applications possibles.

CHAPTER 1

INTRODUCTION AND BACKGROUND

1.1 Context

Information has become the most valuable commodity in the world. This drive to the new information age has been propelled by the ability to transmit information faster, at the speed of light. This erupted the need for finer researches on controlling the information carriers more efficiently. Starting from Erbium-doped optical fibers for long haul communication, the photonic research has grown exponentially to the point where light has become a major information carrier for increasingly short distances communication. The exponential growth of telecommunication space and easy access to smart devices fueled the technological industry to be highly competitive, innovative and perceptive to exponential advancements. This increased data demand has led to the implementation of optical fibers and transceivers inside data centres interconnecting the servers, while putting intense researches into integrating optical components directly onto micro-scale chipsets.

The current generation chipsets are based on copper interconnects between the chips and within the chips components. These metallic interconnects are limited by the latency and bandwidth due to parasitic resistance and capacitance of the material. This has paved the way for silicon photonics as an emerging field using light for optical interconnection. Silicon has been the backbone for the microelectronic industry, making silicon photonics CMOS compatible, which is an industrial standard. Even though the current technology allows electrical interconnects at 10 nm architecture [1], the demand has created a bottleneck in regard with further miniaturisation of their electronic components, making it difficult in predicting and controlling the logic operations in nanoscale components. On the other hand, shifting towards photonics (relying on speed of light) can appear as an endless resource,

although it comes with a fair share of drawbacks. But if utilized properly, it may satisfy the increasing industrial data demand for decades. This has motivated the researches to invest in the field, making photonics technologies a foundation for the universal global data communications [81]. The ever increasing data bandwidth, falling power consumption requirements, and low cost margins of on-chip optical interconnects [82] have paved the way for photonic components to be the new integrated platform for the information age [83].

However, a complete shift to photonic devices integration in microelectronic chips is difficult, as the current optical components (lasers, modulators) are substantially larger compared to their electronic counterpart (transistor gates). Although researchers have demonstrated integrated on-chip photonic functional devices, the size remains comparatively large by industrial chip-architectural standards. With increased size comes increased costs and power consumption. Therefore, without further innovation, this subsequent mismatch in size proportions prevents the further integration of photonics components with electronic chips. This has lead to exponential increase in researches and technology for alternative technologies combining, for example electro-optic materials and plasmonics for realising new and functional devices with increased modulation index (modulators), frequency of operation as well as reduced footprints, energy consumption and insertion losses.

There are two main methods that are actively researched to create efficient photonic devices. First, by using the appropriate materials for each specific functionalities in an optical system (e.g. III-V materials for lasers, LiNbO_3 for modulators, etc.) [29] and second, by creating nanostructured materials, to increase light-matter interaction and control propagation [36, 37, 38]. For the purpose of having an efficient control over the flow of light, there is a need for utilizing modern techniques to enhance light-matter interactions. With that intention, the potential of nanophotonics for tailoring light-matter interaction at the nanoscale has gained considerable attention in recent years [84, 85, 66, 86]. It was made possible by a wealth of research in characterization and nano-fabrication techniques, understanding novel materials with unique properties and utilizing them in efficient and

sometimes unnatural ways [87, 85].

Engineering materials to accurately manipulate light has been at the forefront of most of the recent technological advancement in optics [66, 85]. And in particular, there is a current strong interest in the structural engineering of materials through nanopatterning in order to modify or impart abrupt changes to the phase and amplitude of incident light over deep-subwavelength length scales. Such exotic optical scattering properties were found to occur in natural microstructures such as the wings of morpho-butterfly, which became an inspiration for controlling light-matter interaction through engineering the structure and arrangement of matter. In that spirit, the field of metamaterials was then created to go beyond what is naturally existing ('meta' means 'beyond' in greek). In order to achieve the desired interactions with light, the constituents of these metamaterials, called meta-atoms (usually smaller than wavelength of light), are user defined and are designed and arranged such that an averaged effect is encountered in terms of scattering and interference with light waves. The unique optical properties of metamaterials are derived from engineering their multipolar resonances in subwavelength structures. Therefore, knowledge of the underlying behavior of these multipolar resonances is essential for a variety of metamaterial applications [88, 89].

Approaching the standard of the current technological industry, Si is still the backbone of all advancement primarily due to the existing infrastructure and knowledge base for Si processing residing in the microelectronics industry. The crystallographic structure of Silicon prevents it to have intrinsic electro-optic modulation properties, hence realizing Si photonic tunable devices has either required the use of resonant structures (e.g., ring resonators and photonic crystal nanocavities) [2, 3] or large footprints in non-resonant Mach-Zehnder interferometer configurations [4]. Although current technology enables us to have a good light-matter interaction, the devices are still passive in terms of modulation parameters. Nothing goes faster than the speed of light, however our ability to send information depends highly on how fast can we modulate this light.

Keeping the trend, this thesis aims to examine the introduction of additional tunability, leveraging the unique properties of VO₂ as a driving mechanism for integrated photonic and metamaterial applications. We propose new types of actively tunable devices with improved or extended modulation capabilities, tackling the drawbacks of material absorption and keeping the standard size and energy consumption to the minimum. The following section will be the introduction to the unique insulator-metal transition (IMT) of VO₂, explaining the types of transition and their associated physical theory.

1.2 Theoretical aspects on insulator-metal transitions

Vanadium is a transition metal with electronic configuration [Ar]3d³4s². It therefore has various oxidation states and have more than ten different stable states including single valent oxide, VO₂ and mixed valent oxide like V₈O₁₅ Fig.2.1. Most of these oxides exhibit reversible semiconductor to metal transitions, which is contrary to the state predicted by band theory [12]. Generally this transition for the oxides are triggered by an external stimulus and they are usually manifested as a drastic change of structure as well as in their optical and electrical properties. The trigger can be of various nature like temperature, pressure, doping and electromagnetic fields [9, 10, 11]. This class of material has been of great interest for researchers and engineers, not only for applications perspectives but also for understanding the complex physics at play in these intriguing materials.

In solid-state physics, the electronic band theory provides a general framework for materials, classifying them generally into metal or insulator, based on whether their electronic band is partially or completely filled. Metals can be defined as materials with partially filled electronic band and finite density of state at the Fermi level, thus it is able to conduct electricity even with slight input, whereas insulators have completely filled valence band, a zero density of states at the Fermi level and an empty conduction band. This powerful approach was found to be invalid for certain kind of materials like VO₂ or NiO [90, 91]. Indeed, VO₂ and some other complex materials involve complex physics for which it is

necessary to introduce other concepts in addition to band theory. In the following sections, we will try to explain the reason why, starting with band theory, followed by its limitations and then introduce additional concepts, explaining the behaviour in correlated materials.

1.2.1 Band Theory

Band theory is the basis for behaviour and classification for practically everyday materials. The equations that define the theory are based on a model described by the conventional non-relativistic Schrodinger equation, which is given by

$$i\hbar \cdot \left(\frac{\delta}{\delta t} \right) \psi = \psi \mathcal{H}$$

where :

- \mathcal{H} is the Hamiltonian,
- ψ is the wavefunction,

\mathcal{H} , the Hamiltonian in terms of quantum mechanics, can be described as the total energy operator of a system (in terms of components of momentum and coordinates of space and time). Solving the Schrodinger's equation can give us insight on the energy band distribution and thus help us to understand and classify the material. But it is difficult to solve Schrodinger's equation for a system of large values of particles. Therefore, for simplification, a number of assumptions are usually made. One of which is the Born-Oppenheimer approximation [92, 93], which separates the total wavefunction of a solid (ψ) into the wavefunction of electron (ψ_e) and nuclei (ψ_n).

According to the Hartree-Fock approximation [94, 95], the wavefunction of a collective system having N number of electrons can be represented by one determinant having the spin and position of all electrons in defined direction, representing them as a summation in terms of each single-electron wave functions. Therefore, keeping the symmetry of the system, the Hartree-Fock method determines the set of spin orbitals which minimize the energy and give us the best single determinant function. The assumption therefore implies that electrons

are treated independently in classical theory, which means that the electrostatic potential experienced by each electron comes from the nucleus and the averaged distribution of other electrons, leading to consistency in their behaviour. This mean-field theory forms the basis of the classical band theory. However, the classical band theory completely disregards the interaction between the electrons, including Pauli's exclusion principle (spin-electron pairing). And instead implies the correlation between electrons is substituted by repulsion of each electron with an average electron cloud.

1.2.2 Mott insulators and Mott Transition Mechanism

Mott, in his study [90] found that Nickel Oxide (NiO), that was supposed to be metallic by the classical band theory, was interestingly insulating. He postulated that, for those materials which were expected to be metallic but were insulating in reality, were experiencing an additional electron-electron interactions within their lattice structure. Based on his theory, it is considered that, if an electron jumps from its initial site to a new site that has already been filled, it will undergo a Coulombic repulsion. If the energy of repulsion is higher than the energy of the incoming jumping electron, then this latter will be bound to their initial site, constricting their freedom of movement. This electron interaction phenomenon leads to splitting of the original single half-filled band into two subsequent bands. As identified, this is contrary to the fact that isolated atom arrays are not conducting because it neglects the Coulombic interaction between electrons. This neglected electron-electron interaction is known as electron correlation.

This inter-particle correlation and splitting of energy bands is the heart of the quantum mechanics analytics. Similar to the Kronig Penny interacting potential-well problem, where we discretize the original band into multiple bands because of the increased interaction by nearby energy systems. Like in the case for two interacting well problem, analytical solution gives us two solutions where the original energy band splits into one higher energy band and one lower energy bands. Which is similar when electrons face large enough

Coulombic repulsion \mathbf{U} , the electron correlation effectively splits the single half filled bands in two: one containing electrons occupying the site, called a full lower band (lower Hubbard band, LHB) and an empty higher band, known as upper higher band (upper Hubbard band, UHB). The magnitude of the coulomb repulsion \mathbf{U} is the energy experienced between the jumping electron and the electron that are already present at the lattice position, which dictates the overall proportion of band splitting. This model is known as the Hubbard model [96] and the materials that experience such strong electron correlations are referred to as "Mott insulators". The competition between the carrier localisation and delocalisation can drive a transition between the metallic and insulating states, a phenomenon also known as "Insulator-to-Metal Transition" (IMT).

Most transition metal oxides (partially filled $4d$, $4f$, $5f$ orbitals) should behave as metals according to band theory. But because of electron correlation and the band splitting, they act as Mott insulators. There are different ways to induce phase transition, one such way is to manipulate the delocalisation energy by introducing stress. Compressing lattice constants by an external stress can modify the bandwidth (W) leading to bandwidth-induced IMT. Another way is by manipulating the Coulombic repulsion energy \mathbf{U} by doping carriers charges, hence reducing the repulsion energy. In some cases like temperature driven transitions, both the bandwidth and carrier-induced mechanisms come into play. The density of states with varying relative magnitude of Coulomb repulsion (\mathbf{U}) to bandwidth (W) is shown in Figure 4b(1.1).

Additionally, in strongly correlated oxides, oxygen orbitals also play an important role in dictating the transition property of the material. Following the assumption that there are no hybridization between the transition metal $3d$ band and the oxygen $2p$ band ($O2p$), it is possible to categorize transition metal oxides based on the relative level of $O2p$ band [97, 98]. The first category is a Mott-Hubbard type, where the $O2p$ level is under the lower Hubbard band. And the second category is a charge transfer type, where the $O2p$ lies in between two Hubbard bands Figures (1.1 c and d). It is realistically seen that conducting

electrons hop through transition metals in Mott-Hubbard insulator whereas jumping occurs between metal and oxygen atom in a charge-transfer insulator.

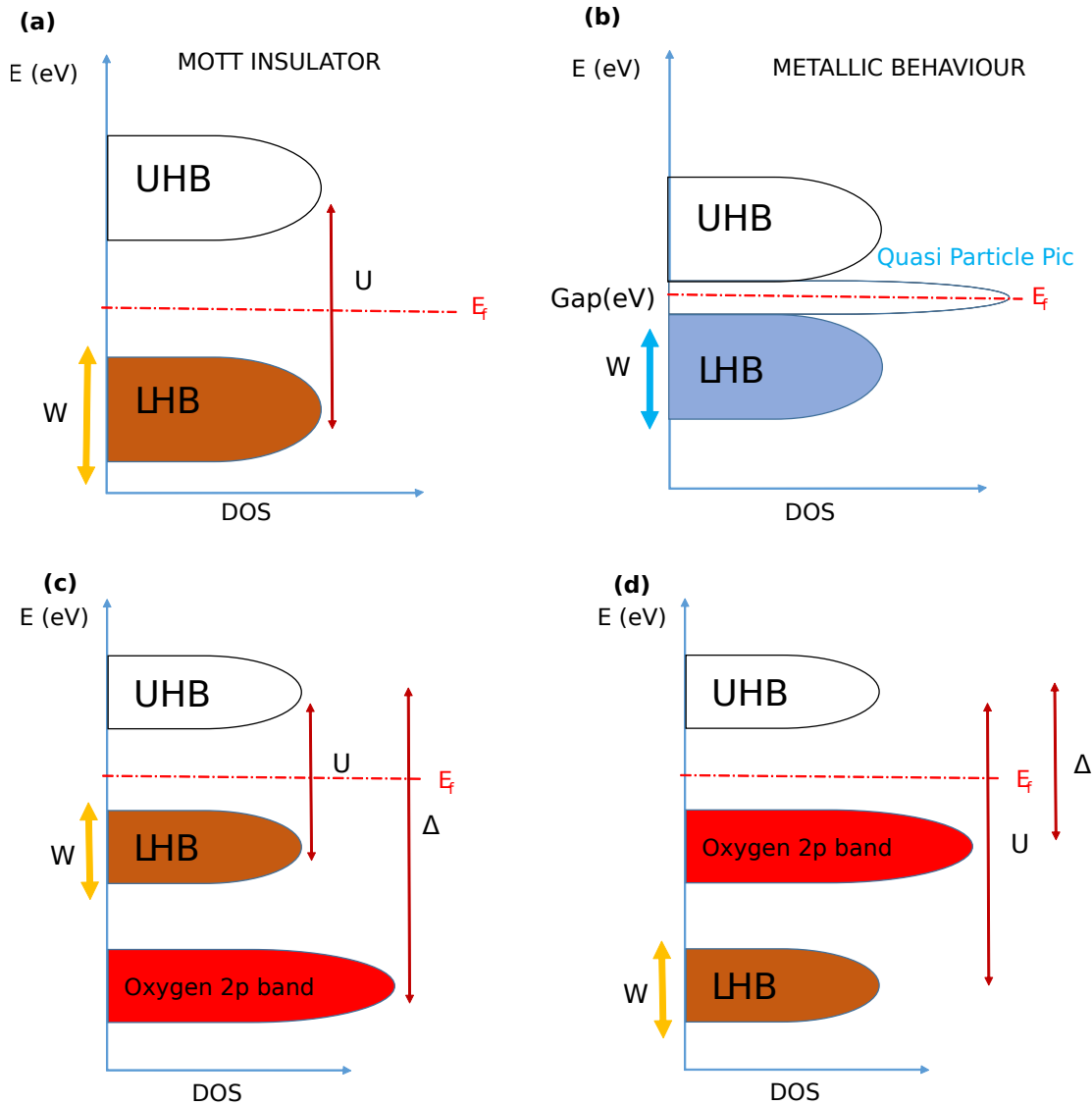


Figure 1.1: (a) Splitting of a normal band into upper and lower Hubbard band due to electron correlations. (b) Bandwidth controlled metal-insulator transition. Changing the bandwidth W could induce a metal-insulator transition. (c) and (d) Oxide Mott insulators could be categorized into two types based on the relative position of the oxygen band and Hubbard bands. (c) Mott-Hubbard insulator where the oxygen p-band lies under the lower Hubbard band; and (d) charge-transfer insulator where oxygen p-band is in between the lower Hubbard band and upper Hubbard band. This figure is reproduced from Ref.[97, 98]

1.2.3 Peierls Transition Mechanism

Rudolf Peierls [16] studied a 1-D lattice of periodically arranged chain of atoms and postulated that a structural deformation can create periodic perturbations in the lattice chain. Keeping in regard with Bloch theorem, this perturbation can manipulate the band structure by coupling both electrons and phonons, thus introducing an IMT in 1-D systems. The discovered phenomenon was coined after his name: the *Peierls Transition*.

In order to picture the Peierls transition, we imagine a periodic string of 1D atoms with atomic space "a". The periodicity of the crystal produces an energy bandgap at the edges of the brillion zone $k = \frac{\pi}{a}$. Now if we introduce a small distortion, say Δ , that propagates along the lattice, periodically perturbing the atoms and thus doubling the periodicity, it therefore opens up new band gaps at $k = \frac{\pi}{2a}$, leading to available electronics state.

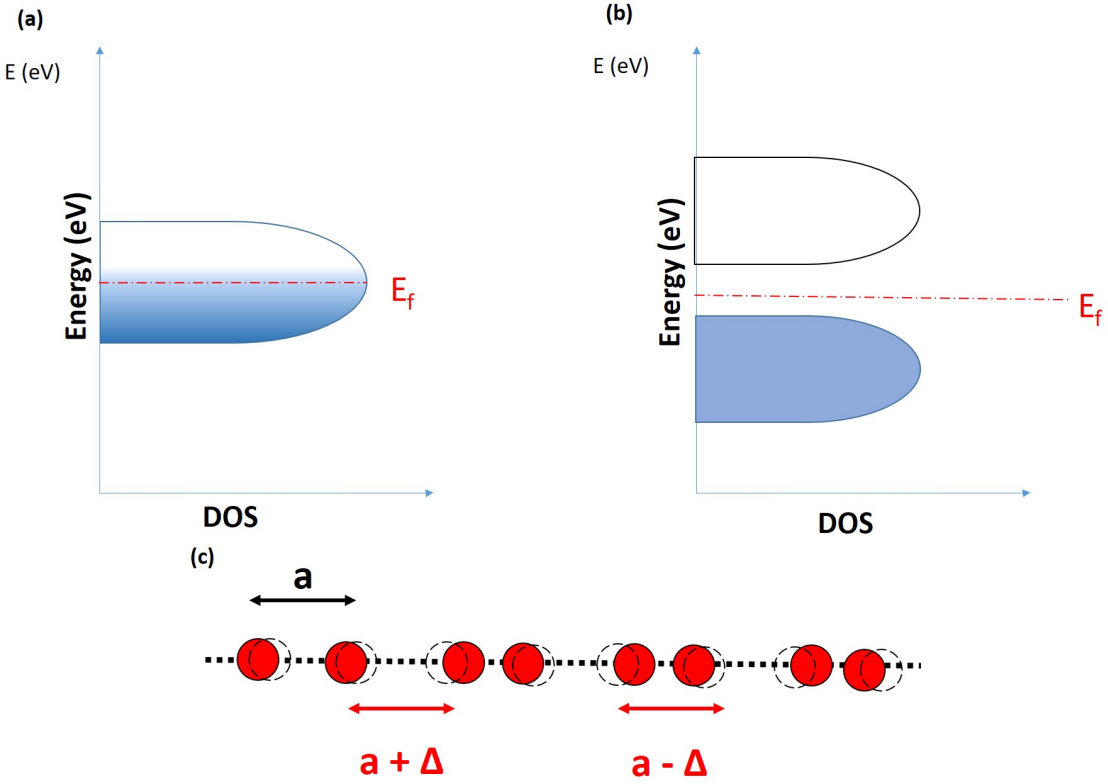


Figure 1.2: Schematic illustration of a Peierls transition. Energy versus density of states a) for a 1D lattice of equally spaced atoms and b) for a dimerized 1D lattice. The horizontal dotted line represents the Fermi energy c) The changes in the lattice across the Peierls transition. The dotted lines represent the original atomic position and the solid sphere represents the perturbed state.

In order to attain equilibrium and to counter this instability, the ions tend to loose energy by rearranging or distorting the lattice. This lattice distortion leads to introduction of smaller band gaps than that of the materials. So if, the energy saved from the band gap is larger than the elastic energy thus generated by lattice distortion, the rearrangement will be initiated. This periodically modulating position of atoms and the lattice potential leads to band gap openings at the Fermi surface, increasing the overall stability of the whole system. Therefore, overlooking atomic vibrations, Peierls [99] showed that a small perturbation Δ , can dominate the total energy of the system. This can be seen as a mechanism of IMT, where the perturbed state has additional bandgaps, so it is the insulating state, while the unperturbed has the fermi level in a partially filled band, so it is the metallic state. In the following sections we will analyze the interplay between the Peierls distortion and other

degrees of freedom and later we discuss how this theory can explain some of the physical properties of VO_2 .

1.3 Vanadium oxides and its transition theory

1.3.1 Vanadium oxide

VO_2 comes under the class of correlated metal oxides that has an insulator-metal phase transition (IMT) [5]. This transition in VO_2 can be achieved using applied electric fields ($E = 10^5 \text{ Vcm}^{-1}$) [5], injected carrier densities ($n_e \approx 10^{18} \text{ cm}^{-3}$ [5]), optical [6], terahertz pulses [7] and thermal heating (beyond $T_c \approx 340 \text{ K}$ at standard pressure) [5]. This IMT is concomitant with a structural transformation, subsequently leading to an adverse change in material's electrical and optical properties. The IMT of VO_2 and its various oxides have been a known fact for a few decades. Thermally-induced IMT was first studied by Morin [8] in 1959. Several intermediate vanadium oxides and a number of other transition metal oxides possess this property, but VO_2 is of the most practical importance, as its transition temperature is closest by far to the ambient temperatures, meaning it is more easily accessible for near room temperature application.

1.3.2 Crystallographic structure of Vanadium oxide

VO_2 represents a classic case for correlated electron materials. It is known to be a polymorphic material, that is, it exists in $\text{VO}_2(\text{A})$, $\text{VO}_2(\text{B})$, $\text{VO}_2(\text{M1})$ and $\text{VO}_2(\text{R})$ [13]. Therefore, it is not easy to explain the complex theory behind the transition of VO_2 , as the simple band theory of solids fails to predict its state. As explained before, different physical mechanisms could be responsible for an IMT, and more specifically the Mott transition and the Peierls transition mechanisms. The debate over which one is the prominent transition mechanism has been going on for a long time [14, 15]. On par with Mott, it could be that the electron correlation is the key factor for the transition behaviour. But the experimentally verified structural transition can be credited to a Peierls transition [14] due to lattice displacement.

There have been some recent study suggesting an IMT of VO_2 without Peierls distortion [17].

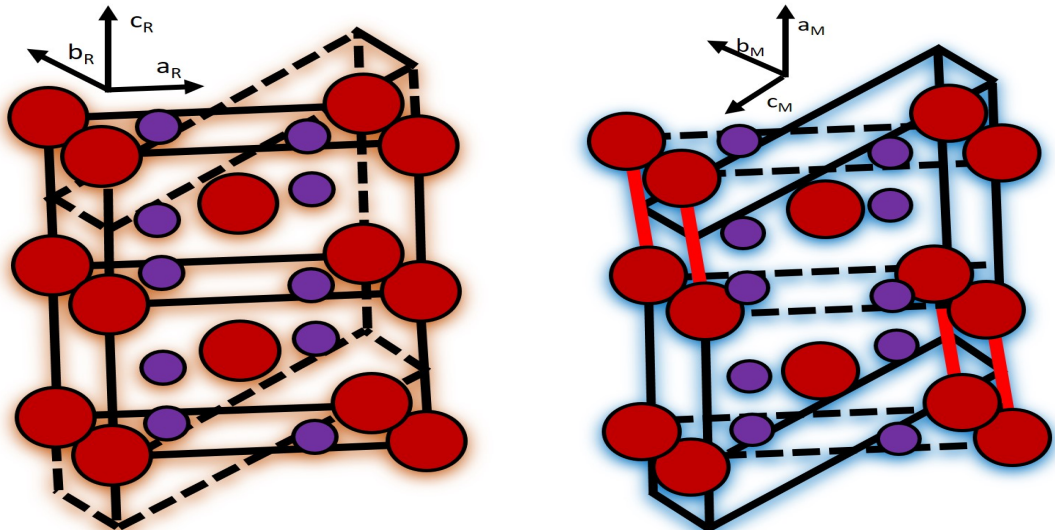
In a single crystal form, at room temperature Vanadium dioxide is semiconducting, with a monoclinic structure, having lattice constants $a = 5.75\text{\AA}$ $b = 4.53\text{\AA}$, $c = 5.38\text{\AA}$ and a band gap of 0.6 eV [100]. Upon heating above the transition temperature, the resistivity decreases about 4 to 5 orders of magnitude, indicating a metallic conductivity. This phenomenon is the starting point of puzzling physics: the conductivity of this material is strongly enhanced when we heat it. As we describe in the following, this electronic property changes is also accompanied by a structural change [101].

In this new metallic phase, vanadium dioxide crystallizes into a rutile structure (referred to as R phase from body-centered tetragonal) with lattice constant $a = b = 4.53\text{\AA}$, $c = 2.87\text{\AA}$ as shown in figure: 1.3a. The Vanadium atoms occupy the vertices and the center of the tetragonal unit cell. Each of which is surrounded by six oxygen atoms sitting at the centre of an octahedron made of neighbouring oxygen atoms. Along the c axis, these octahedron share their edges with their neighboring octahedron within the (001) plane 1.3b.

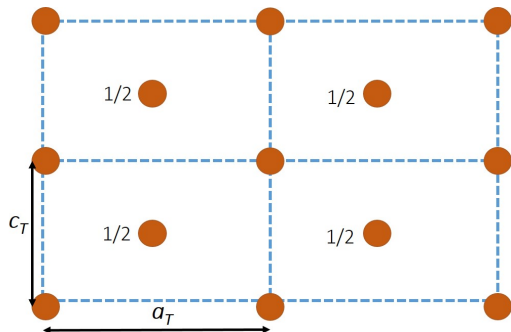
While crossing the transition temperature back into the insulating state, the dimerization of vanadium atoms occurs along the original rutile c axis and the tilt of the dimer is with respect to the rutile c axis, while the oxygen atoms roughly stay at the same positions, represented in the figure 1.3 c and d. At the body center of the unit cell is the vanadium atom with the c coordinate equal to $\frac{1}{2}$, because of the dimer formation. So the overall contribution of V in a crystal is $\frac{1}{2}$ as the two original vanadium atoms in the dimer become non-equivalent.

Hence, the new unit cell in the insulating phase of VO_2 must be twice as large as the original rutile primitive unit cell to include both vanadium atoms of the dimer. The tilt of the dimers leads to vanadium atoms being displaced away from the rutile c axis and also out from rutile plane. The tilting and dimerization depreciates the crystal symmetry and the crystal system transitions from tetragonal to monoclinic. These phases related cell system

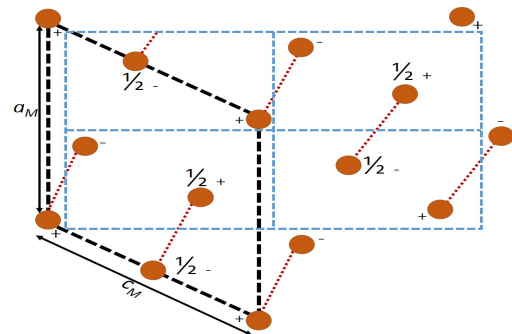
i.e. insulating phase cell to metallic phase cell are related by the edge vector of the lattice relations: $\vec{a}_{M1} = 2\vec{c}_R$, $\vec{b}_{M1} = \vec{b}_R$, $\vec{c}_{M1} = \vec{a}_R - \vec{c}_R$.



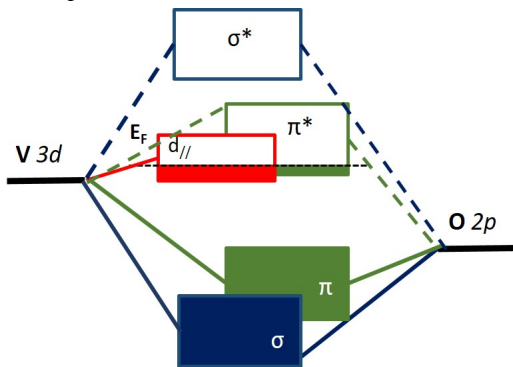
(a) VO_2 rutile crystal structure



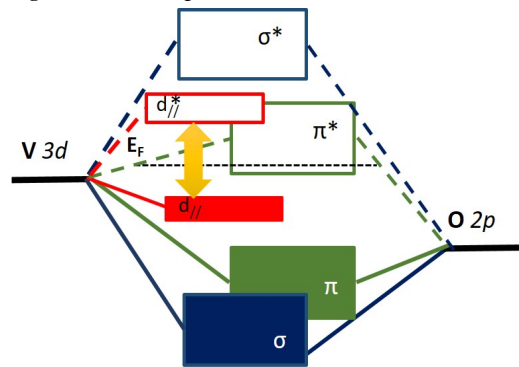
(b) VO_2 monoclinic crystal structure



(c) b_R axis view of lattice arrangement in Metallic (d) b_M axis view of lattice arrangement in Insulating rutile phase



(e) Band structure of the metallic.



(f) Band structure of the insulating.

Figure 1.3: (a) Crystal structure of VO_2 in its metallic phase. It has a rutile structure with small atoms being vanadium and large atoms being oxygen. (b) The cation-cation interaction further splits the t_g and e_g orbitals. Crystal structure of (c) metallic rutile phase and (d) insulating monoclinic phase of VO_2 viewing from the b axis. (e) Proposed band structure of the metallic and insulating phase based on the Goodenough and Mott pictures, respectively.

As people might see and extrapolate, the change in crystal structure can lead to change in the electronic band structure and thus act as a Peierls mechanism for the metal-insulator transition. Imada studied that the drastic change in conductivity across the metal to insulator transition could either be due to the vanishing free carrier density or the divergence of the effective mass of electrons [102], which corresponds to a change in the carrier density or carrier mobility, respectively [103].

In vanadium dioxide, it was observed that the conductivity change is specifically due to the change in the carrier density but the carrier mobility is almost unchanged. Hall measurements as measured on both single crystal and thin film VO_2 , show that the majority carriers are electrons in both phases and the carrier density increases from $\sim 10^{18} \text{ cm}^{-3}$ to $\sim 10^{23} \text{ cm}^{-3}$ from the Insulating to the metallic phase [104, 105]. Whereas, the carrier mobility stays at a roughly constant value of $\sim 0.1 \text{ cm}^2/\text{V.s}$ across the transition. Coming down to asking the central and main question in VO_2 , we want to understand whether the transition is due to electron-lattice interaction (Peierls transition), electron-electron correlation (Mott transition), or a collaborated Peierls-Mott transition [91, 106, 107]. This question is under debate even to this day. In the next section we discuss the proposed transition mechanisms and corresponding electronic band structures.

1.3.3 Electronic Band structures of Vanadium oxide

We can understand the electronic structure and conductivity in rutile phase, simply by discussing the metal t_{2g} orbital of VO_2 [108], which fall into the one-dimensional $d_{||}$ band, and the isotropically dispersing e_g^π bands, since vanadium has a d^1 electron configuration in VO_2 . Therefore in order to understand why t_{2g} splitting happens, we can take a look at the distance between V - V atoms (vanadium - vanadium) along the a , b , and c axis (axis pointers). In the monoclinic phase, we observe that the V - V distance is less along the c axis as compared to a or b direction, because of the lattice distortion. This smaller distance can initiate electron-electron correlation, leading to an imbalanced energy system. The electronic

energy of the orbitals which are pointing along the c axis are lower as compared to others' because of this cation - cation interaction. Therefore this orbital is almost one-dimensional and directed along the c axis (rutile) and, it is called the $d_{//}$ orbital. On the contrary, the other two t_{2g} orbitals are isotropic and known as the π^* band. It has also been suggested that this V-V dimer leads to the transition from high temperature localised rutile state to a localised monoclinic state.

In rutile metallic phase, the $d_{//}$, and the π^* orbitals in figure 1.3e, broaden and overlap to form the electronic band. The band structure as shown in figure 1.3 is generally accepted for the representation of the metallic phase, but exact band structures which includes the Fermi level, the bandwidth, and the offset between $d_{//}$ and π^* band are not well characterized. It has been estimated that the total bandwidth of $d_{//}$ and π^* bands is $\sim 2\text{eV}$ and the Fermi level is located at 0.6 eV above the minimum of conduction band [105, 109]. An interesting point to note here is that because of the quasi one dimensional character of the $d_{//}$ band, conductive anisotropy can be observed in VO_2 . The measured conductivity, parallel along the rutile c axis is larger than along the perpendicular a axis at room temperature. This conductivity difference is not too large, but, it is probably due to contribution from the π^* band.

1.3.4 Discussion on Vanadium oxide transition

The tilting of the vanadium pairs causes a shifting of the π^* band. Collectively this causes a band gap opening, following Peierls transition. To be noted, these above discussions are solely based on how the structural changes can modify the band structure and for simplicity we have disregarded the electron-electron correlation. On the other hand, Mott et al., explained the Metal-to-Insulator transition in terms of electron correlation [106]. It was discussed that in the Insulating phase, the $d_{//}$, band splits into two Hubbard bands because of electron correlation. When transformed into the metallic phase, the π^* band is energetically lowered and becomes partially filled. Thus the electrons in the π^* band could

overwhelm and overpower the electron correlation in the $d_{\parallel\parallel}$ band and fuse the two Hubbard bands into a single band.

With all the researches in the previous decades that focused on understanding the properties of the IMT in VO_2 [91, 106, 107], it came to a stale mate conclusion that the transition is a combined effect of lattice distortion and Coulomb correlation [109, 110, 111, 112, 113]. However, the observation of different other phases of VO_2 under doping and stress have further complicated the interpretation [114, 115] since neither Mott nor Peierls mechanism could alone explain the wide range of phenomenon in VO_2 .

The discussion concerning the physics behind these unique properties have always been a dilemma and is still been debated [18, 19, 20, 21, 15]. Reasoning to the presence of both structural and electronic transitions provides complications in theoretical modelling. In fact, the question still remains whether the driving force behind the transition is due to the changes in the structural symmetry favouring electron localization or whether the structural transition is driven by strong electron-electron correlations or a combination of both the mechanisms. Even though the exact physics is not completely understood, we will show in this thesis that we can exploit the IMT in many different ways, to induce a much needed optical tunability in nanophotonic devices.

1.4 Organization of the manuscript

My aim in this thesis is to study the unique physical properties of VO_2 (Vanadium dioxide) and devise a strategy leveraging the IMT in order to induce a tunability factor in functional photonics devices). One of the challenge is to exploit this unique property of VO_2 even though it comes with its fair share of disadvantages like high absorption which prevents the cascading of VO_2 based functional devices in an integrated manner. Therefore the main objectives of my thesis are to:

1. Study thoroughly the optical properties of VO_2 in all its states ranging from insulator to metal as well as all intermediate states;

2. Design devices that leverage the IMT while still circumventing the optical absorption;
3. Nanostructure VO₂ in a way that mitigates the optical losses;
4. Design devices that exploit both the refractive index modulation and absorption modulation (color printing and tunable absorber).

Overall, my thesis aims to demonstrate that we can design and fabricate an efficient hybrid VO₂-based platform for different fields of photonics (guided optics, metamaterials and metasurfaces) overcoming its limitations and find an efficient way to have an additional control over the light.

The Organisation of chapters is as follows:

- **Characterization of VO₂:** Chapter 2 presents the structural analysis of the VO₂ thin films fabricated in this thesis. We characterize the thin film's structural properties at both its states. Followed by optical characterization of the thin film investigating its electrical and optical properties. The samples under investigation here will be the basis for the the devices that will be theorised and demonstrated in the following chapters.
- **VO₂ based waveguide modulator:** Chapter 3 illustrates the design strategy and fabrication methodologies used in realising hybrid VO₂ based waveguide modulators. Which is a device that is used to modulate an optical signal by varying several characteristics of the input light such as the amplitude, the phase or the polarization. The active switching dynamics is presented in form of compact CMOS compatible integrated VO₂ photonic device that can manipulate light efficiently.
- **VO₂ nanocrystals:** We demonstrate in chapter 4 the dynamic control of multipolar resonances accommodated by VO₂ nanocrystals and successfully retrieve the complex refractive index of the effective medium using Mie extended Maxwell-Garnett theory. In addition we demonstrate a further scope for designer tunable materials showing

distinct optical tunability compared to unpatterned VO₂. Thus opening up a new degree of freedom to design low-loss phase-change metamaterials with designer optical tunability and actively controlled light scattering properties.

- **VO₂ metasurfaces:** In Chapter 5, we investigate various methods of dynamic control of light interaction with metasurfaces. We try to introduce tunability factor leveraging the insulator to metal transition of VO₂ in order to dynamically tune the resonances of sub-wavelength scattering structures. We further design and demonstrate possible applications in the field of structural color generation and tunable perfect absorbers.

CHAPTER 2

STRUCTURAL AND OPTICAL CHARACTERIZATION OF VO₂ THIN-FILMS

2.1 Introduction

The fabrication of VO₂ thin-films is a difficult task. Owing to various stable and complex phases of vanadium oxide as shown in figure 2.1, it is difficult to fabricate a perfectly stoichiometric VO₂ layer. It is observed that even a small variation in the oxygen-to-vanadium ratio and in the bonding structure, affects the thin-film characteristics and is comparable to introducing defects and doping, hence influencing the phase transition properties of VO₂ [22, 23, 24]. Additionally, any unidentified impurity, either in V-O system or stoichiometric phases usually lead to modifications in the optical dispersion and switching characteristics. Since the fabrication is complex, each samples thus fabricated may end up having different optical dispersions. This in turn makes the structural characterization even more challenging. Therefore, it is extremely important to perform accurate characterization to extract the optical properties that are needed to design devices.

2.2 VO₂ growth technique and deposition

Synthesis of VO₂ can be achieved via both chemical and physical methods such as, sol-gel method [118], molecular beam epitaxy [119], chemical vapour deposition [120] but the most common is the sputtering technique[121]. The advantage of sputtering process are film uniformity and size scalability of the sample substrate. Thin film growth of VO₂ using sputtering was first demonstrated at Bell laboratory in 1967 by Fuls, Hensler and Ross [122].

For our case, we utilized magnetron assisted reactive sputtering deposition technique, for the growth of VO₂ thin films. The sputtering system is an AC450 by alliance concept. The deposition of VO₂ thin-films in our laboratory at INL was led by B. Vilquin. The deposition

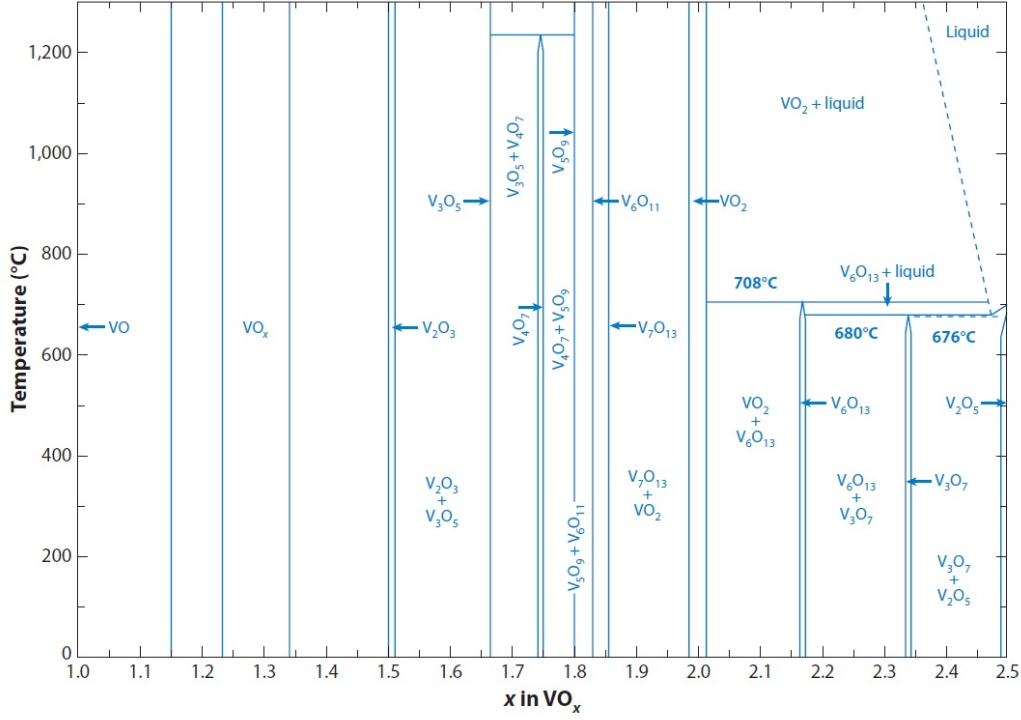


Figure 2.1: Experimental phase diagram of VO_x . This image has been adapted from [116, 117]

recipe for VO_2 has been standardized on many experimental trials and characterizations. In the initial study, we manipulated the temperature of deposition (Room temperature and at 550°C) and the concentration of O₂ in the chamber. Since the target used was V₂O₅, the standard procedure based on a previous study [123] suggests using only Ar gas or Ar + H₂ gas to maintain the partial pressure, but here we modified the concentration of O₂ to 2%. Later some samples were subjected to post deposition annealing at 550°C and Ar concentration was fixed at 50 sccm (Standard Cubic Centimeters per Minute) for the procedure. Following the deposition trials, to understand the crystallinity of deposited materials, we performed XRD to analyze the thin-film structural properties and phase of VO_2 . The following successful recipe is shown in the table 2.1. In addition to this home-made VO_2 , the majority of the VO_2 thin-films forming the basis of my research have been provided by the Ramanathan group from Purdue university (USA).

Temperature	550°C
Flow rate Ar gas	50 sccm
Flow rate O ₂ gas	2%
RF power	200 W
Rate of Deposition	2 nm/min
Rapid Annealing	10min
Annealing Temp	550°C

Table 2.1: Parameters for Reactive Sputtering Technique for the growth of VO₂ thin-films on quartz.

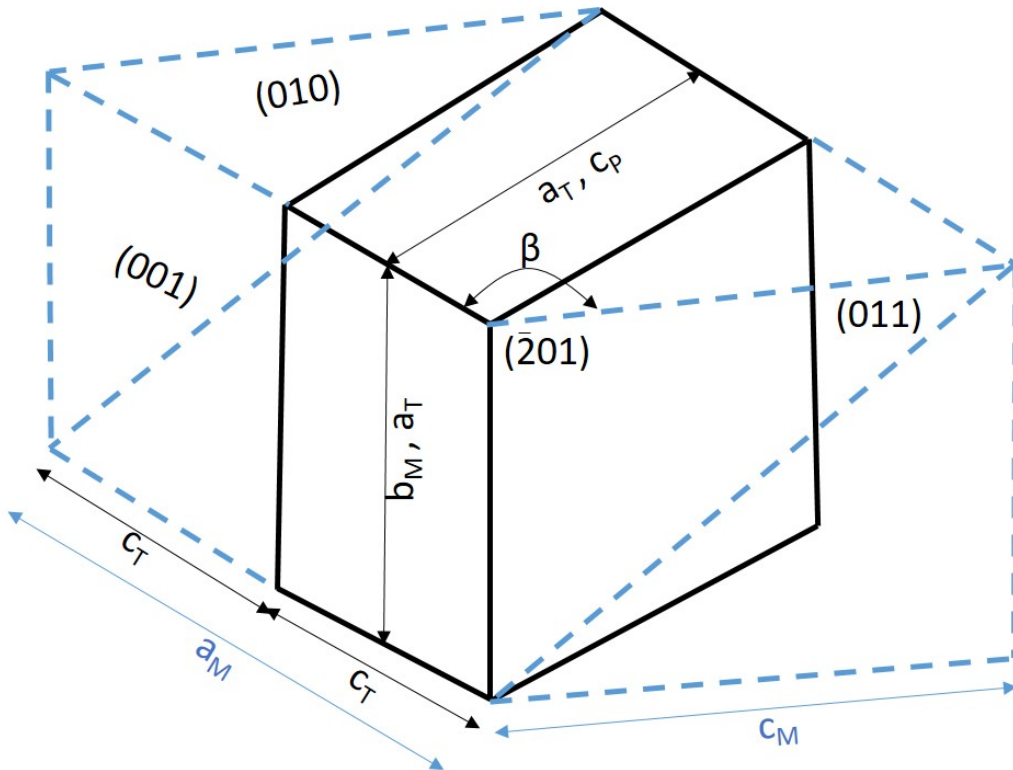
2.3 Structural Characterization

2.3.1 XRD characterization and Results

X-Ray diffraction (XRD) is a nondestructive analysis for thin film materials in order to identify the film's crystallinity and the strain between the film and the substrate. In XRD a collimated monochromatic x-ray beam is directed on a sample at a known angle and the intensity of the reflected beam is measured by a detector. The intensity and position of the reflected beam is an indication of the crystallographic arrangement of atoms. For example, at particular angles, we see a strong constructive interference if the planes of atoms are parallel in the crystal lattice and offer a constructive phase difference. The working principle of XRD is governed by Bragg's law which is given by $n\lambda = 2dsin\theta$, where λ is the wavelength, d is the atomic lattice spacing and θ is the diffraction angle. The sample is generally rotated at θ angles and reflection at each angle is recorded. The magnitude of the reflection provides information about the form factor of atoms (higher intensity for heavier element) and their arrangement in the lattice. Therefore, the angle and magnitude of reflection enable measuring the material's crystallographic structure, strain between the layers, the degree of crystallinity and the orientation of its phases [124].

The figure below (Fig. 2.2) shows the crystallographic structure of VO₂'s unit cell at both

its states. The knowledge of the crystallographic orientation is important, so to understand the growth direction and the crystallographic plane orientation of the thin-film. Furthermore, the growth direction and crystallographic orientation of materials partially dictate the overall property of the deposited medium.

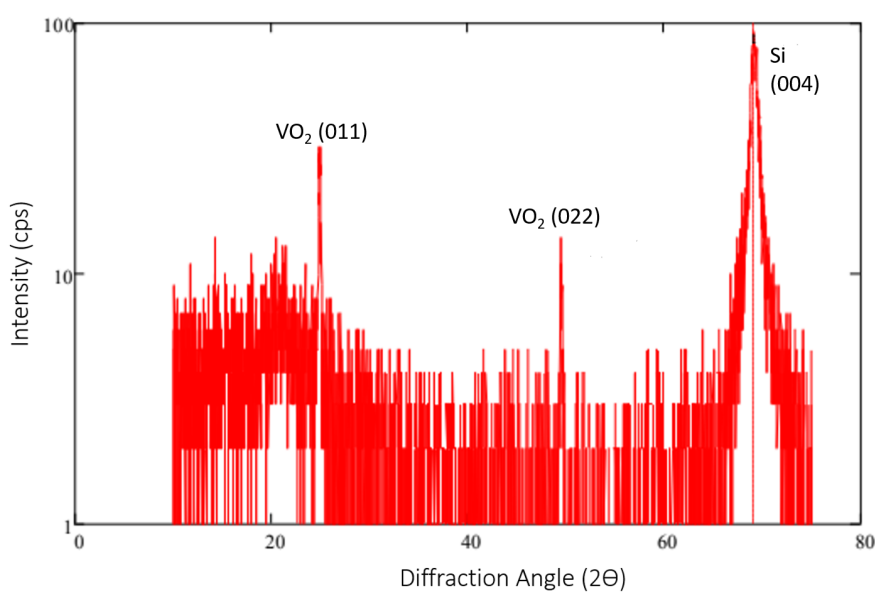


MONOCLINIC		TETRAGONAL	
a_M	5.743 Å	a_T	4.53 Å
b_M	4.517 Å	c_T	2.87 Å
c_M	5.375 Å		
c_P	4.53 Å		
β	122.61°		

Figure 2.2: Relation between tetragonal structure (high-temperature, black lines) and monoclinic (low-temperature, dashed blue lines) unit cells. This image has been adapted from [125]. Below table shows the dimensions of the unit cell of VO₂ at both its state [125].

We performed a so-called $\theta - 2\theta$ scan, that enables both the incident beam and the

detector to rotate simultaneously, to collect specular reflection and form a 2θ based intensity results. Since the Bragg's condition is only satisfied by certain combinations of θ and d-spacing, the intensity versus 2θ provides a quantitative measurement of the crystallinity of the material. The x-ray diffraction pattern for a VO_2 thin-film grown at INL is displayed in the figure 2.3. Analysing the pattern we observe intensity peaks measured along 2θ . From the position and the amplitude of the diffraction peaks, we can identify the surface crystallographic orientation, in this case we measure the (011) plane of VO_2 from the first order reflection. This indicates that (011) face could be parallel to the c axis (C_m - C_p plane). Identifying (022) face reflections, can suggest that the b-axis is perpendicular to the a-c plane, both suggesting monoclinic phase [126, 125]. Thus we can identify the crystallinity in the growth direction.



27

Figure 2.3: XRD of VO_2 on Si, home-made deposition (Reactive ion sputtering).

Similarly below we display the XRD measurements of a VO_2 thin-film on Al_2O_3 . The two intensity peaks show the proper grain boundaries and lattice orientation of VO_2 growth direction [127]. Enabling us to confirm the success of the homemade deposition technique

and recipe for epitaxial growth of VO_2 . The intensity peaks and its width provides us with useful information regarding the samples. The peak representing VO_2 (having a lattice orientation of 020) can be seen at the 2θ value of 40° suggesting a monoclinic phase.

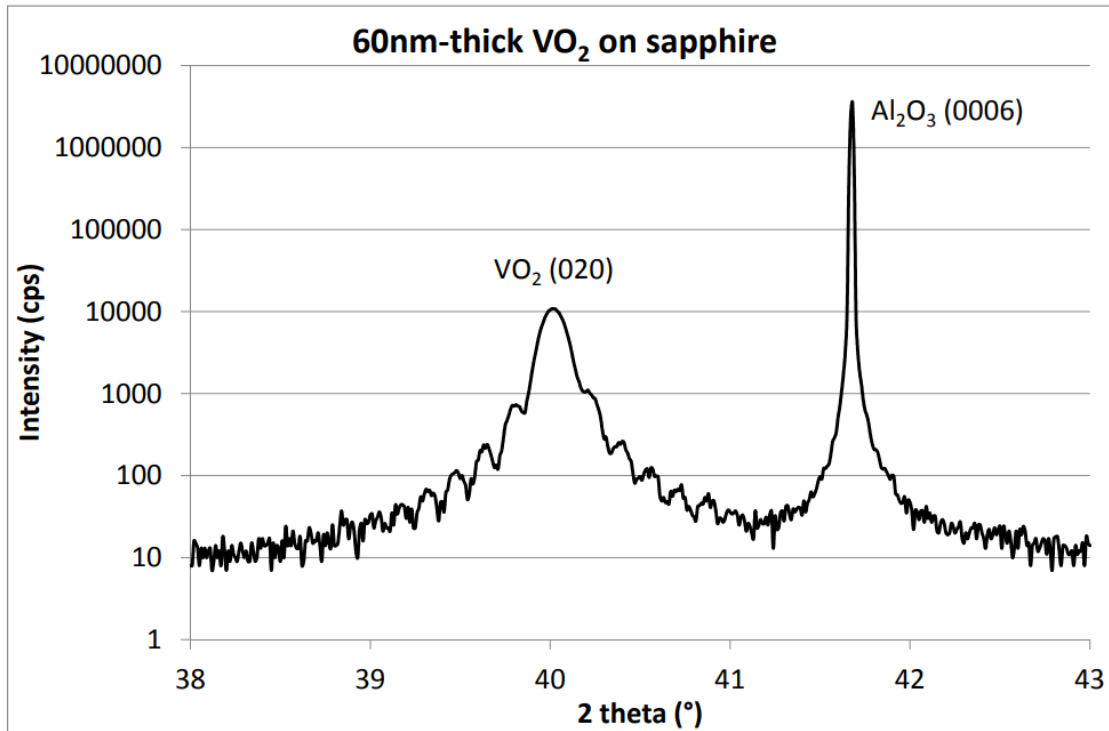


Figure 2.4: XRD of VO_2 on Al_2O_3 , home-made deposition (Reactive ion sputtering).

The peak intensity provides a qualitative estimation of the crystalline quality of the film: a high peak intensity indicates a good crystalline structure. The contrary is shown in figure 2.5, which shows multiple peaks indicating multiple crystallinity in different orientations.

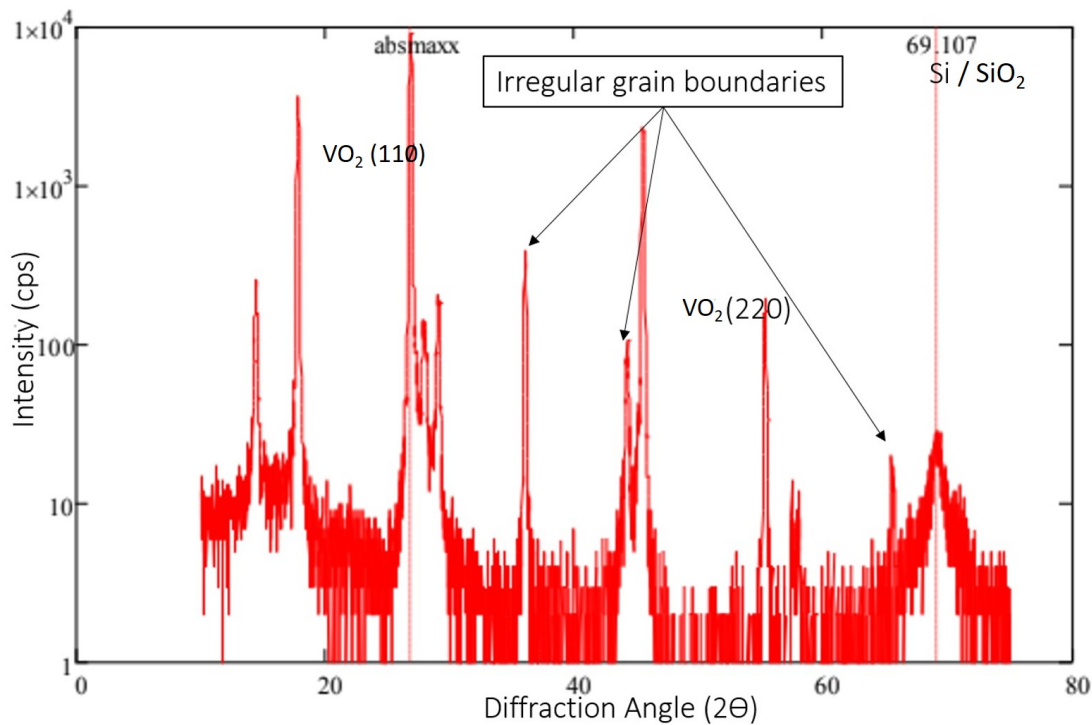
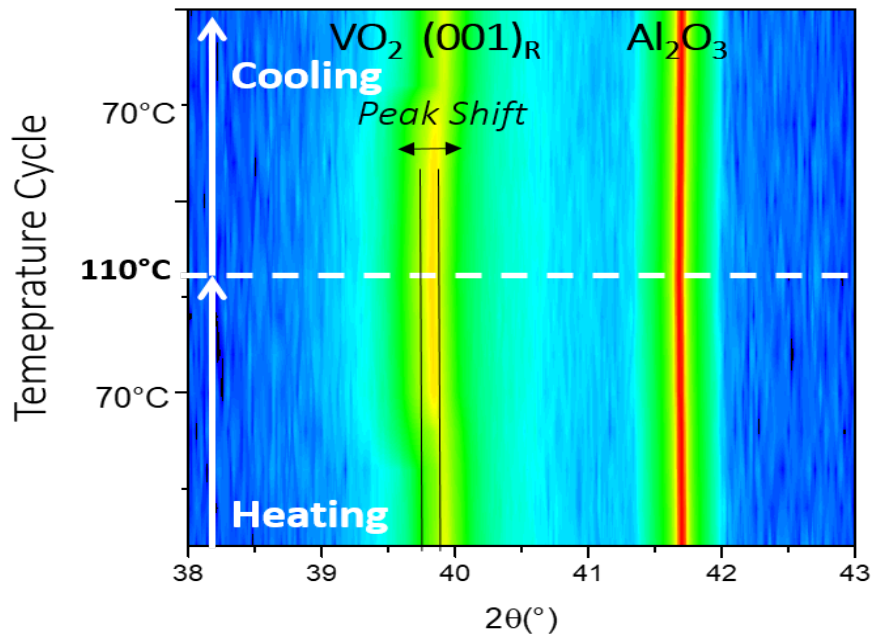
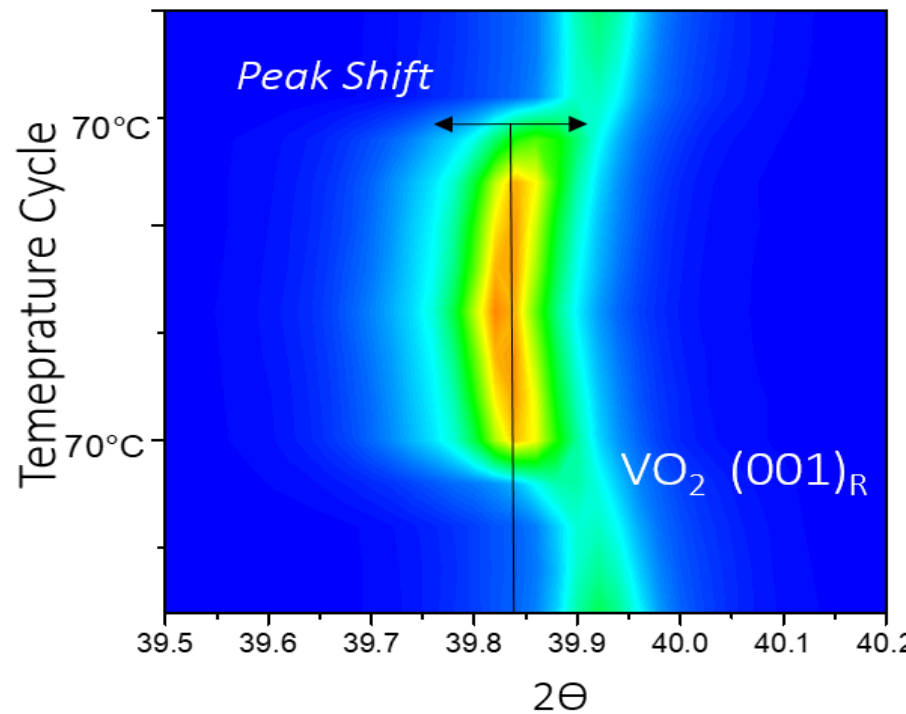


Figure 2.5: VO_2 on SiO_2 home-made (failed deposition).

Further, since we know that the IMT of VO_2 is accompanied by a crystallographic change from a monoclinic structure to a tetragonal structure, we try to map the crystallographic transformation by performing XRD measurements as a function of temperature. Therefore in order to obtain information on the structural changes involved in the phase transition of VO_2 , we performed XRD on the sample around the $(100)_R$ oriented VO_2 sample. The $\theta - 2\theta$ temperature scans were performed in two cycles, heating cycle from 40°C to 110°C and cooling cycle from 110°C to 40°C to map out the variance in intensity peak of VO_2 due to crystallographic structural change during the phase transition. The following XRD measurements were taken by José Penuelas a member of our INL lab.



(a) Transverse XRD on $\text{VO}_2/\text{Al}_2\text{O}_3$ sample. We can observe the peak shift in relation with the temperature change.



(b) Peak shift indicates change in the crystalline structure thus indicating structural change.

Figure 2.6: Transverse XRD and peak shift observed during the transition of VO_2 indicating the structural transition.

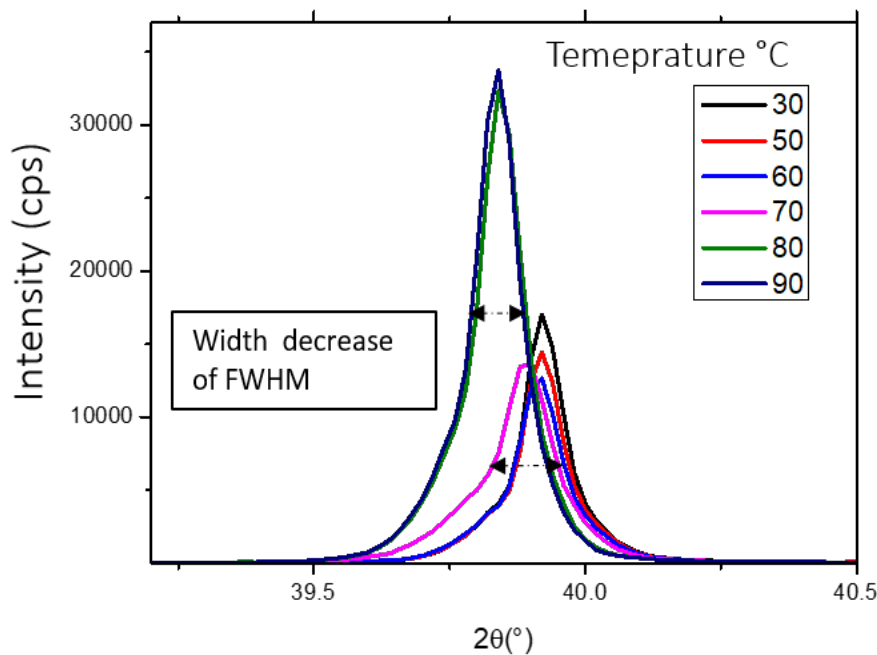


Figure 2.7: XRD intensity peak shift and width increase showing structural changes in the crystalline structure of VO_2 during the temperature induced phase transition.

In the above figures (2.6, 2.7) we observe that, as the phase transition happens in VO_2 thin-film, there is a structural change, as indicated by the change in width and shift in intensity peak in transverse XRD. This gives the indication for changes in the bond length and the gradual structural transformation as expected from a VO_2 thin-film.

2.3.2 Reciprocal space mapping (RSM)

The concept of reciprocal lattice is to give a visual representation on the phenomenon of diffraction. RSM is technically a $\theta - 2\theta$ scan calculated as a function of ω , ψ and ϕ , which are the angles of rotation of sample stage at x, y and z axis respectively. At certain diffraction conditions we can map 3-D diffraction patterns from thin-films and single crystals and represent them in the form of reciprocal lattice. This freedom of rotation in RSM can be utilised to measure the in - plane and out-of-plane lattice parameters of thin-films.

We performed RSM measurements of symmetric reflection of VO_2 in order to determine

the *in-plane* and *out-of-plane* lattice parameters. As discussed in the previous chapter, because of the quasi one dimensional character of the $d_{//}$ band in the rutile structure, there is an anisotropic conductivity parallel along the c axis in contrary to along other a and b axis-es at room temperature. Therefore we performed RSM to investigate and characterize this structural anisotropy. The principle for the characterisation is similar to XRD, measuring several $\theta - 2\theta$ scan for a different tilt of the sample in the ω direction. The difference in scan is that, it was performed as a function of temperature at 30°C, 50°C, 70°C and 90°C. Such an experiment should lead to very interesting information, as we should be able to observe the structural changes for both the *in-plane* and *out-of-plane* lattice parameters shift during the phase transition.

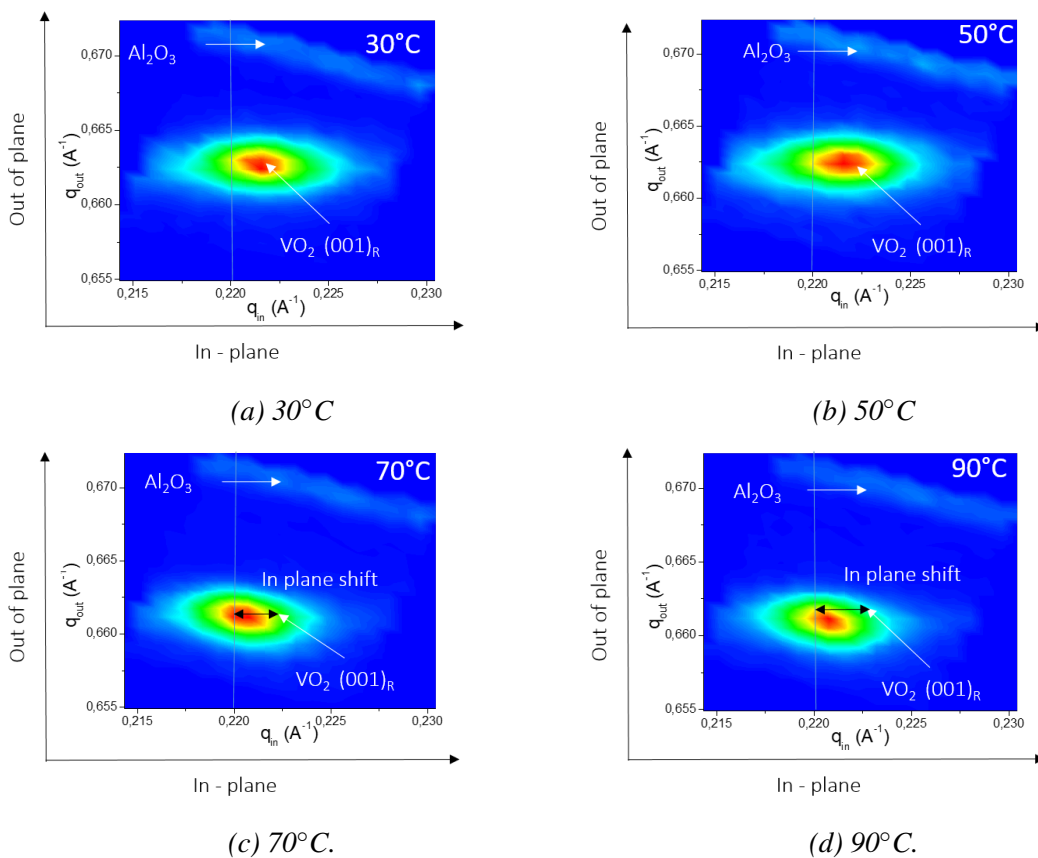


Figure 2.8: RSM on VO_2 on Al_2O_3 as a function of temperature. We observe the gradual shift in *in-plane* parameter.

From the above figure 2.8 we observe the shift in the *in-plane* lattice parameters of

the thin-film. We can further understand from the figure below 2.9, the evolution of change in both the *in – plane* and *out – of – plane* lattice parameters of the VO₂ thin-film as a function of temperature. Evaluating this in-plane and out-plane change gives interesting insight on the anisotropy of VO₂ and its structural evolution upon the IMT.

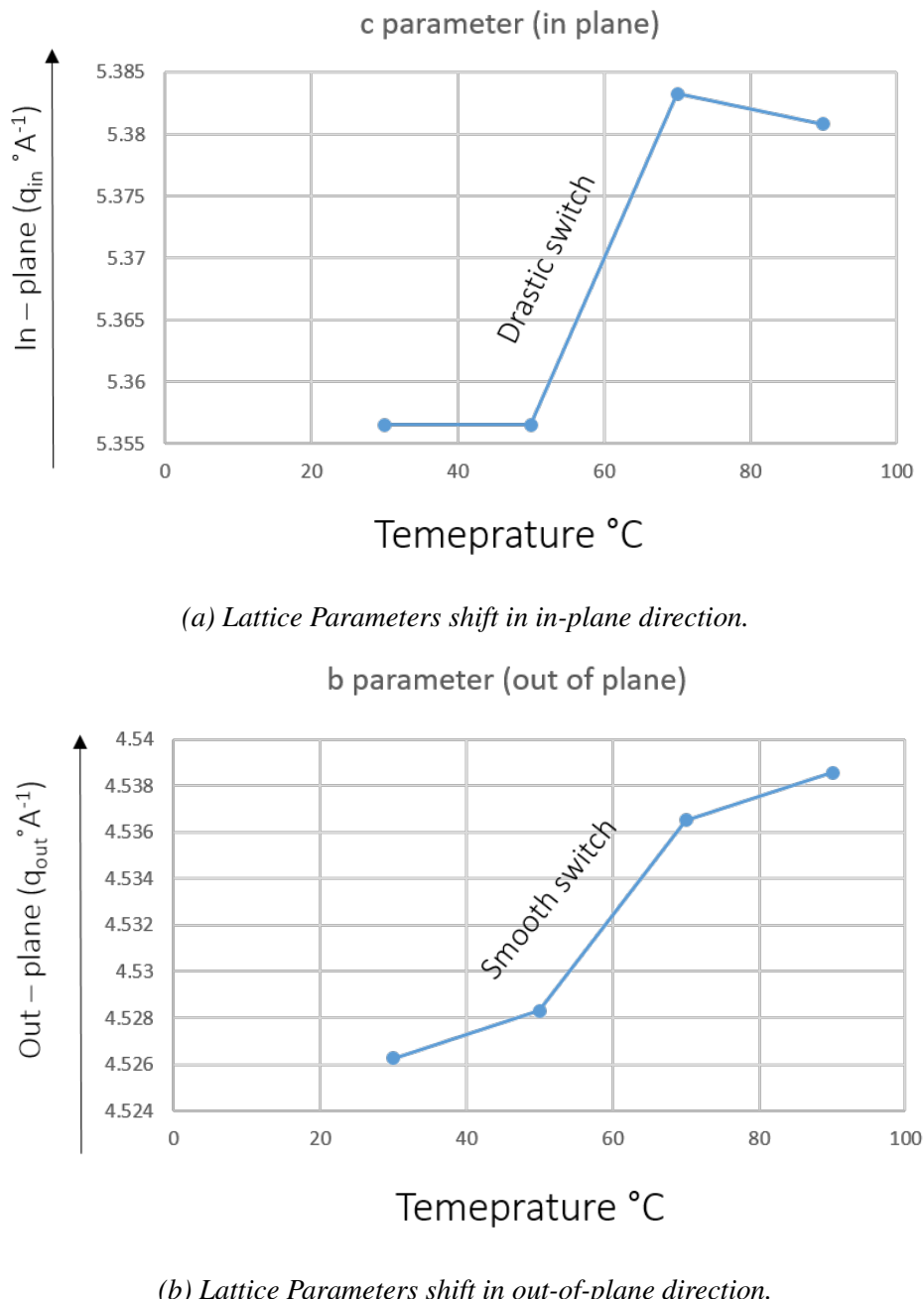


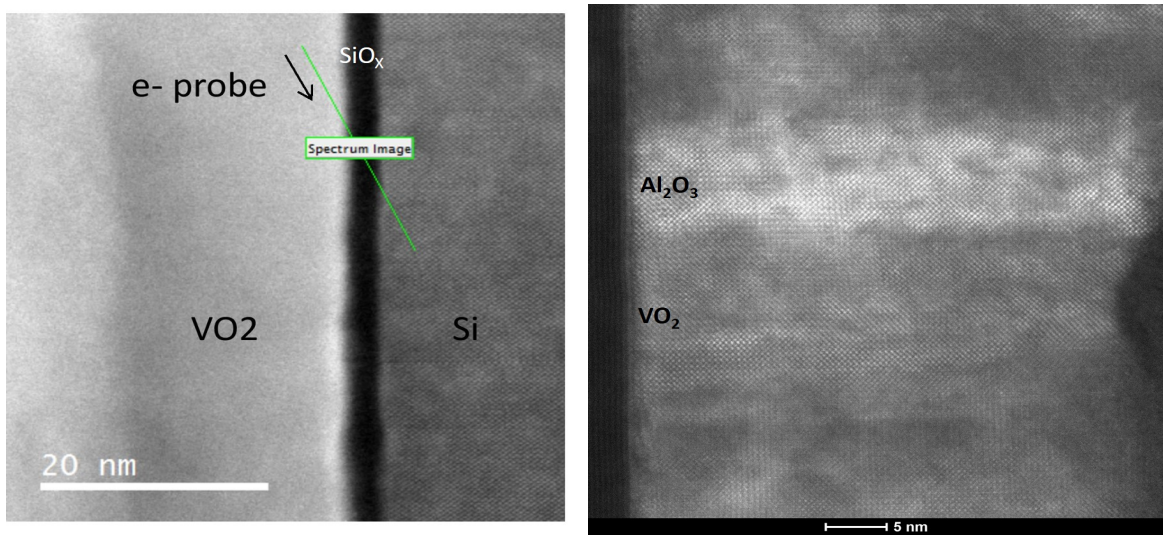
Figure 2.9: In-plane and out-of-plane Lattice parameter shift as a function of temperature

2.3.3 Transmission electron microscopy (TEM) characterization

Transmission electron microscopy (TEM) is a powerful tool for microstructure characterization. It enables imaging a material with a sub-nanometer precision providing direct insights into a material system down to the atomic scale. Additionally, as compared to commonly used surface analysis technique like SEM (scanning electron microscope) and AFM (atomic force microscope), TEM enables analyzing internal and small size microstructures along with cross-section and plan-view.

TEM analysis was performed on two samples for VO₂ on Si (Thickness = 50 and 100nm respectively) and VO₂ on Al₂O₃ (sapphire) of thickness 25nm. The samples were polished and prepared for the cross section analysis using focused ion beam (preparation was done by Solène Brottet). All the TEM measurements and analysis were performed by Matthieu Bugnet from the MATEIS laboratory. The figures 2.10 shows the cross section TEM images for VO₂ on Si and on Al₂O₃ samples and we can observe the individual atomic arrangements for each materials. The good homogeneous growth of VO₂ thin layer is clearly visible and further we notice the presence of an additional layer, presumably a native oxide in between the thin layer and the substrate material when VO₂ is grown on Si. We further perform EELS (Electron energy loss spectroscopy) measurements on the cross section to understand the nature of this intermediate layer.

The EELS analysis as shown in figure (2.11) reveals the presence of an interfacial layer of VO_x between VO₂ and SiO₂. Due to multi phase of VO_x, reduced layer could create strain and could create a variation in the optical properties and effect the transition conditions (similar to doping and defects). In terms of device perspective, this can cause abnormality in device performance for any sensitive applications. As per EELS fig 2.13b for the VO₂ on Al₂O₃, we observe that the intermediate layer and the top layer have similar chemical and structural compositions, suggesting uniformity in growth.



(a) Sample 1: VO_2 on Si

(b) Sample 1: VO_2 on Al_2O_3

Figure 2.10: TEM cross section reveals the presence of additional native oxide layer in between the VO_2 layer and Si substrate.

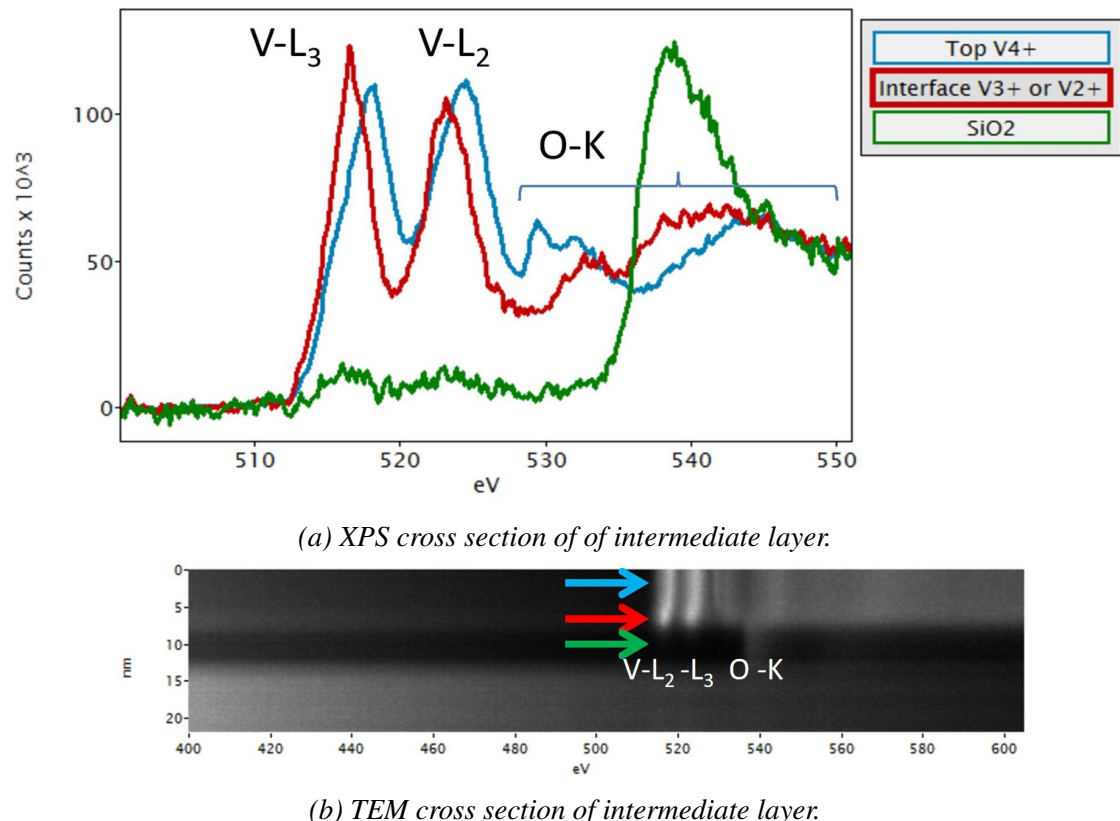


Figure 2.11: EELS and TEM cross of the intermediate layer for Sample 1 (VO_2 100nm) reveals that at the interface of SiO_x we observe 2-3 nm of V^{3+} or V^{2+} reduction V atoms.

In addition, we performed SAED (selected area electron diffraction) in order to closely observe the orientation of the atoms in their lattice structure. Analysing SAED of VO_2 on sapphire, we observe the diffraction patterns that are related to crystal lattice being observed. The bright spots on the figure 2.12 corresponds to the crystal plane of VO_2 . The spacing between the spots is inversely related to the distance between atomic planes and here we observed the monoclinic lattice arrangement of VO_2 .

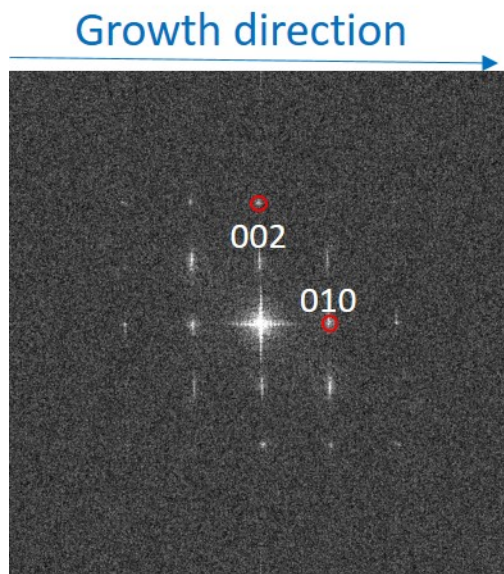
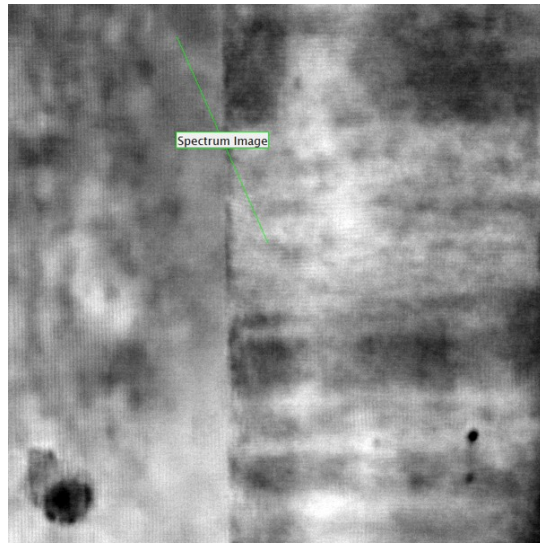
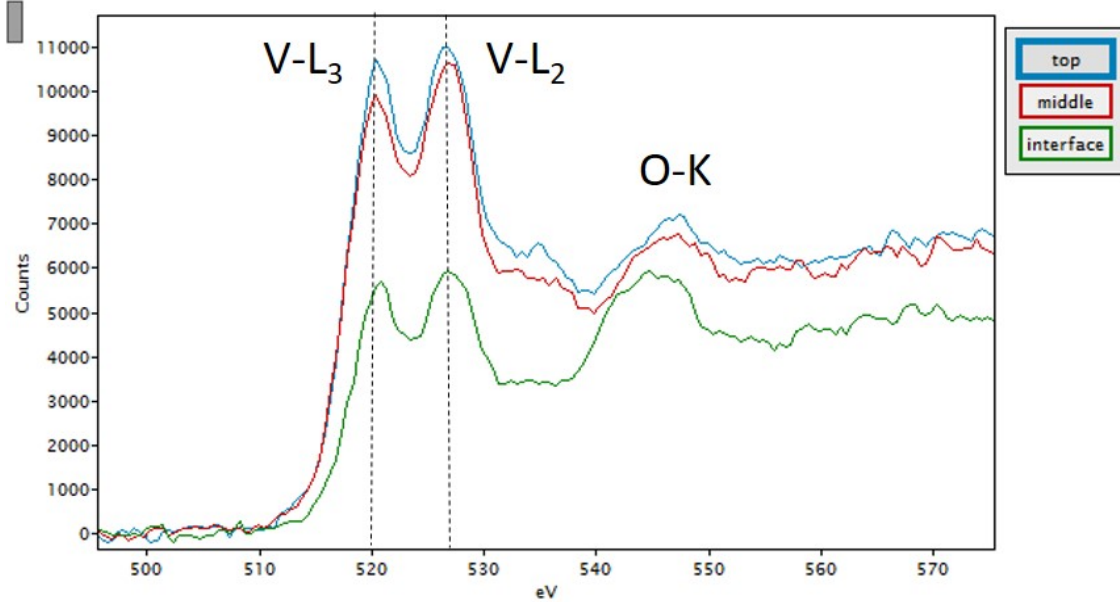


Figure 2.12: SAED pattern VO_2 deposited on sapphire indexed as a monoclinic structure on the growth direction.



(a) TEM cross section of intermediate layer.



(b) EELS cross section of intermediate layer.

Figure 2.13: (a) SAED surface plane analysis and (b) TEM cross section for Sample (VO_2 25nm) on Al_2O_3 revealing the interface of substrate and thin film. (c) EELS cross section of intermediate layer

In conclusion, these structural characterizations, performed on VO_2 thin-films, indicate that they present the correct stoichiometry and structures. We note the presence of an undesired oxide layer at the interface between the VO_2 and the Silicon substrate. This undesired layer seems to have negligible effects on the crystallographic growth, as we measure the structural change as expected from a VO_2 thin film with correct stoichiometry.

This structural analysis will serve as a basis for optical characterization and will help creating an optical model to mimic the optical properties of VO₂. We now want to deeply characterize and analyze the optical properties of these VO₂ thin-films.

2.4 Spectroscopic ellipsometry: Measurements and analysis

The ellipsometric characterization was performed using a Jobin Yvon-UVISEL spectroscopic ellipsometer combined with a heating cell. The device is composed of a Xenon source, a polarizer, an analyser, and a monochromator that disperses and redirects the reflected light to different photo-detectors. The ellipsometer UVISEL is capable to continuously cover the spectral range from 250 to 2100 nm.

2.4.1 Working Principle

Spectroscopic ellipsometry is an optical technique used to measure the spectral amplitude $\tan(\psi)$ and phase (Δ) of the reflected light, which are related to the optical properties and microstructure of the sample under study. The enabling principle of ellipsometry is that p- and s- polarized light reflect differently.

$$R_p \neq R_s$$

With ellipsometry, we measure the complex reflectivity ratio of p- and s- polarized light and reports the result generally in ellipsometric units ψ and Δ ,

$$\frac{R_p}{R_s} = \tan(\psi)e^{i\Delta}$$

where $\tan(\psi)$ is the magnitude of the ratio of Fresnel reflection coefficients and Δ is the phase difference. Spectroscopic ellipsometry therefore measures the change of phase and polarization of light, which enables the determination of the sample's complex dielectric function (ϵ) [128].

2.4.2 Is and Ic parameters

In the case of phase-modulated ellipsometer, like the one we use, we do not measure the ellipsometric angles ψ and Δ directly, but instead we measure functions of ψ and Δ . Defined as:

$$Is = \sin(2\psi) \cdot \sin(\Delta)$$

$$Ic = \sin(2\psi) \cdot \cos(\Delta)$$

These trigonometric functions Is and Ic are directly related to ψ and Δ . They depend on the measurement conditions, in our case these above equations are only valid for the situation when the analyzer is at 45° and the modulator at 0° . Throughout this work, we directly fit the theoretical models to the Is and Ic values.

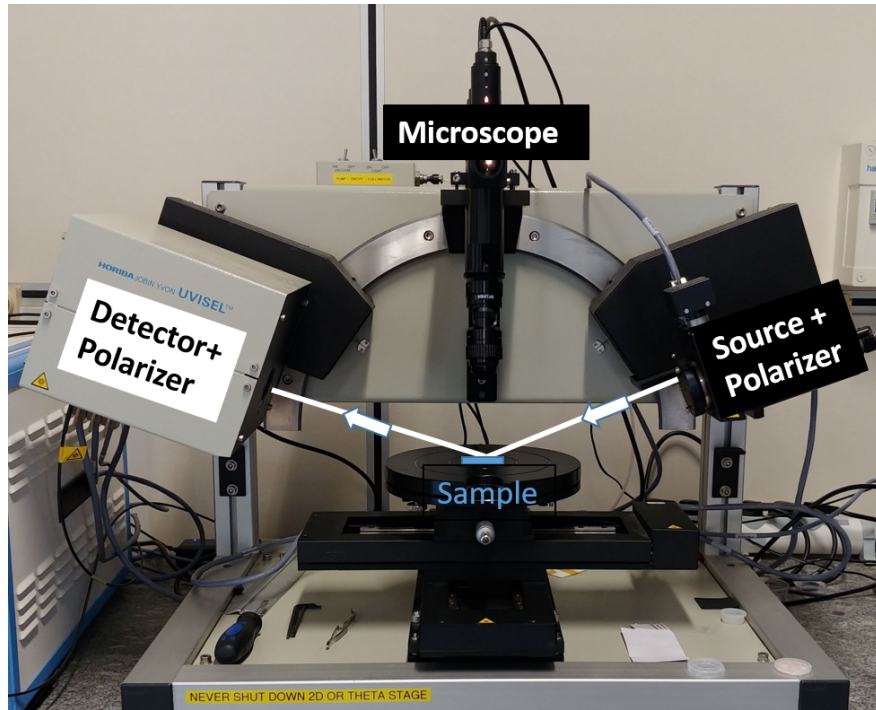


Figure 2.14: HORIBA-Jobin Yvon UVISEL Ellipsometry setup

An optical model that describes the sample structure where each layer refers to a given

material is used to compare calculated and experimental data. Therefore fitting the calculated and the experimental data can provide us with the complex dielectric functions of thin-films. The precision on the fit is determined by the fitted parameters, associated errors, and measure of χ^2 which represents the goodness of the fit.

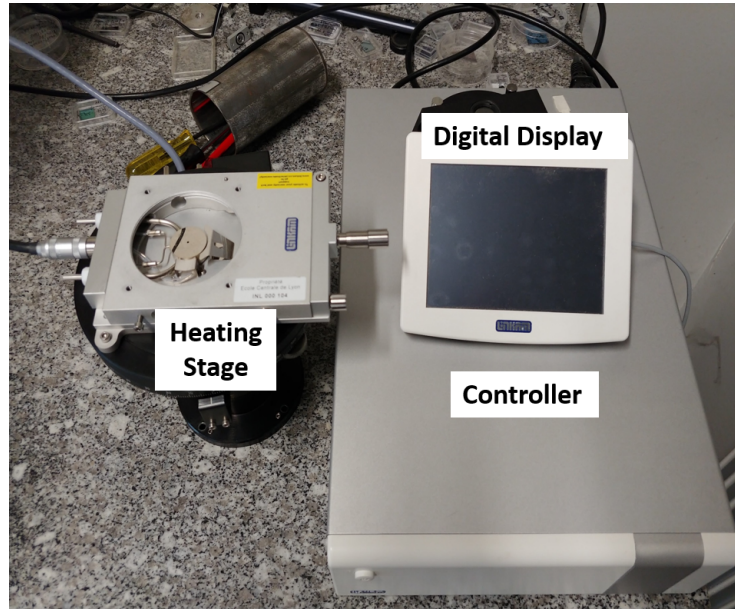


Figure 2.15: Linkam THMSEL350V Heating stage temperature controller

2.5 Optical permittivity modeling of VO₂

The acquired ellipsometric parameters I_s and I_c of the thin-film of VO₂ have been collected for angles varying from 55° - 75° over a spectrum range of 260 - 2100 nm. In order to unambiguously extract the correct optical dispersions of the thin-films, a multi-fit procedure is performed, i.e. fitting the measurements performed at two different incident angles simultaneously. The acquisition was carried out in a range of temperatures from 35°C to 80°C using a digitally controlled heat cell (Linkam THMSEL350V). The substrate (SiO₂) response was modeled using dispersion formula by Malitson *et al*[129].

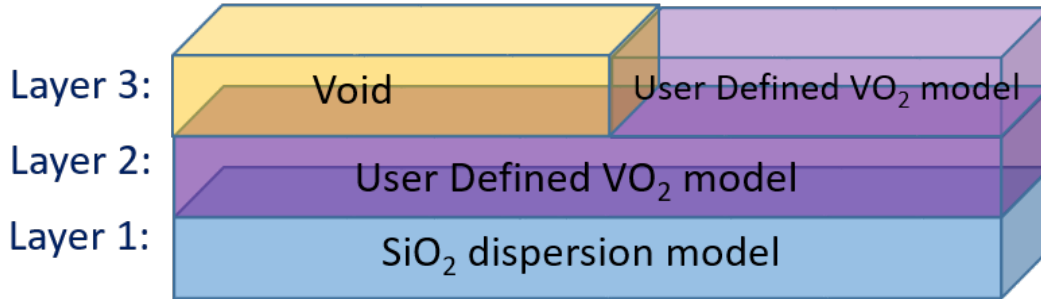


Figure 2.16: Optical model: Layer by layer modelling of VO₂ on SiO₂.

Knowing the unique nature of VO₂, it exhibits complex structural changes upon the transition, making it quite difficult to establish a unique dielectric function for all phases. The IMT behaviour of VO₂ makes it harder to theorise the optical model specially at the intermediates stages of transition. An analytical representation for their different optical responses is therefore required to establish a correlation between nano film structure and its optical properties. In order to model the complex permittivity of VO₂, we have used a Tauc-Lorentz model with three oscillators and an additional Drude model for the metallic state, as explained in details in the next sections. Fig. 2.16 shows the ellipsometric multi-layer model composed of three layers: the top layer (Layer 3) is the roughness layer (VO₂ model + Void), expressed by an effective medium approximation (EMA) with Bruggeman formula [130]. Layer 2 is the VO₂ thin-film and Layer 1 is the substrate. The model is then subject to free fit using least-squares curve fitting thanks to the Levenberg - Marquardt (LM) algorithm.

2.5.1 Oscillators model and dispersion function for VO₂

Depending on the properties of materials, the frequently utilized dispersion functions for transparent or weakly absorbing films include Cauchy and Lorentz oscillator as well as Amorphous, New Amorphous, and Tauc-Lorentz models for semi-transparent materials (dielectrics, polymers and semiconductors absorbing in the VIS/FUV), and Drude model for metals. A sum of three Tauc-Lorentz oscillators was used to model the optical properties of

VO_2 . Each of which corresponding to inter-band transitions in the material [27], sharing a common Tauc optical bandgap [28]. To describe the optical properties of VO_2 at the metallic state, a Drude model [28] is added to the Tauc-Lorentz dispersion model in order to take the contribution of free electrons into account.

The Tauc-Lorentz theoretical model [26] was developed by Jellison and Modine in 1996. They came up with the complex dielectric function using a Tauc joint density of states and the Lorentz oscillator, given by:

$$\tilde{\epsilon}_{TL} = \epsilon_{r,TL} + i \cdot \epsilon_{i,TL} = \epsilon_{r,TL} + i \cdot (\epsilon_{i,T} \times \epsilon_{i,L})$$

In this equation, the imaginary part of the dielectric function $\epsilon_{i,TL}$, is given by the product of imaginary part of Tauc's dielectric function $\epsilon_{i,T}$ with the Lorentz one $\epsilon_{i,L}$. While taking the approximation of parabolic bands the Tauc's dielectric function describes the interband transition above the band edge. The obtained equation is:

$$\epsilon_{i,T}(E > E_g) = A_T \cdot \left(\frac{E - E_g}{E} \right)^2$$

where :

- A_T is the Tauc coefficient,
- E is the photon energy,
- E_g is the optical band gap,

The imaginary part of Tauc's dielectric function gives the response of the material caused by inter-band mechanisms only. Therefore $\epsilon_{i,T}(E \leq E_g) = 0$. The imaginary part of the Lorentzian oscillator model is given by :

$$\epsilon_{i,L}(E) = \frac{A_L \cdot E_0 \cdot C \cdot E}{(E^2 - E_0^2) + C^2 \cdot E^2}$$

where:

- A_L is the strength of the $\epsilon_{2,TL}(E)$ peak,
- C is the broadening term of the peak,
- E_0 is the peak central energy,

Therefore by evaluating these two functions, Jellison set up a new equation to express the imaginary part as an amalgam of both [28], i.e.

$$\epsilon_{i,TL}(E) = \epsilon_{i,L} \times \epsilon_{i,T} = \begin{cases} \left(\frac{1}{E}\right) \frac{A \cdot E_0 \cdot C \cdot (E - E_g)^2}{(E^2 - E_0^2)^2 + C^2 \cdot E^2}, & \text{for } E > E_g \\ 0, & \text{for } E \leq E_g \end{cases}$$

where: $A = A_T \times A_L$

Now the real part of the $\epsilon_{r,TL}$ is derived from the equation of ϵ_i using the Kramers-Kronig integration. Which is given by:

$$\epsilon_r(E) = \epsilon_r(\infty) + \frac{2}{\pi} \cdot P \cdot \int_{E_g}^{\infty} \frac{\xi \cdot \epsilon_i(\xi)}{\xi^2 - E^2} d\xi$$

where: ξ is the integration energy parameter (Cauchy's residue theorem analytics) and 'P' denotes Cauchy's principal values.

To take into account the effects of free carriers on a material's optical properties, we use the Drude model, that is given by:

$$\epsilon = \frac{(\omega_p)^2}{-(\omega)^2 + i\Gamma_D \omega}$$

Where, ω_p is the plasma frequency, ω is the frequency of the incident electromagnetic field and Γ_D (in eV) is the collision frequency (damping factor), which increases the broadening of absorption tail. The damping effect is due to the absorption and collision processes of free carriers.

2.5.2 Extension to Multiple oscillators

In the case where multi-transitions occur in the measured wavelength range, we generally use the multiple Tauc Lorentz (TL) model, which is the sum of several single-TL terms [131]. Increasing the number of oscillators thus increase the number of parameters that can be altered to model the permittivity of a material. To model the transition and the intermediate phases of VO₂, we use a combination of 3 Tauc Lorentz oscillators.

So the equation for the real and imaginary parts of the permittivity ϵ_r and ϵ_i are given by:

$$\epsilon_{i,TL}(E) = \epsilon_{i,L} \times \epsilon_{i,T} = \begin{cases} \sum_{i=1}^N \left(\frac{1}{E}\right) \frac{A_i \cdot E_i \cdot C_i \cdot (E - E_g)^2}{(E^2 - E_i^2)^2 + C_i^2 \cdot E^2}, & \text{for } E > E_g \\ 0, & \text{for } E \leq E_g \end{cases}$$

$$\epsilon_r(E) = \epsilon_r(\infty) + \sum_{i=1}^N \frac{2}{\pi} \cdot P \cdot \int_{E_g}^{\infty} \frac{\xi \cdot \epsilon_i(\xi)}{\xi^2 - E^2} d\xi$$

Where N denotes the number of oscillator used (3 in our case).

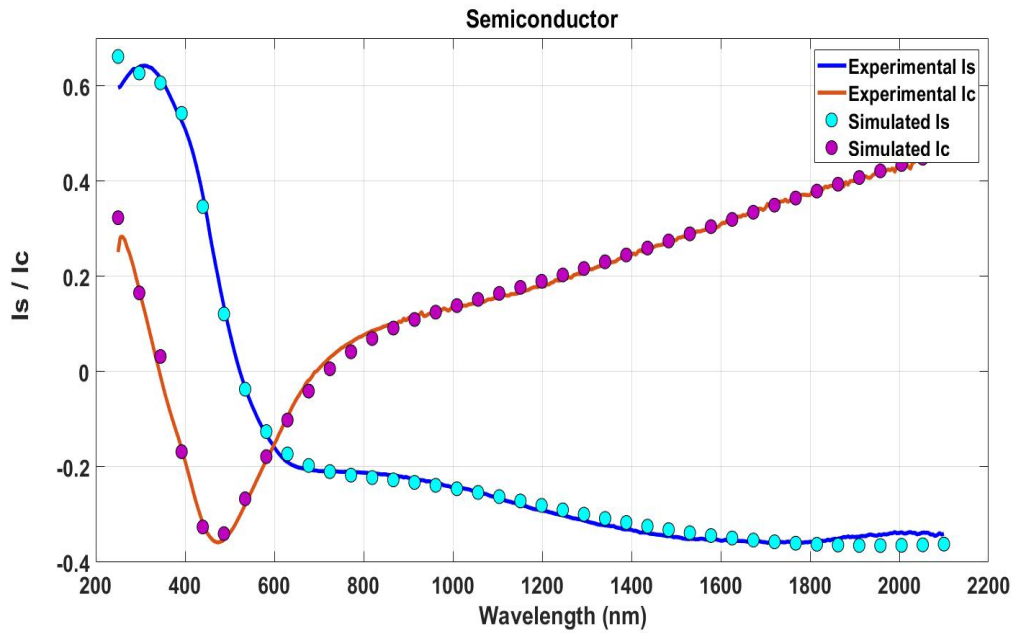
- ϵ_r parameter is linked to the real part of the dielectric function.
- $\epsilon_r(\infty) = \epsilon_\infty$ is the high frequency dielectric constant. This parameter prevents the ϵ_∞ from converging to zero for energies below the band gap $\epsilon_\infty > 1$.
- A_i (in eV) express the strength of the i^{th} absorption, and i refers to the number of oscillators.
- C_i (in eV) is the term related to the broadening ; it is a damping coefficient linked to the FWHM of the i^{th} peak of absorption.
- E_g (in eV) is the optical band gap energy.
- E_i (in eV) denotes the energy of maximum transition probability or the energy position of the peak of absorption. Always $E_g < E_i$

As compared to other models, the TL model can reflect more correct optical responses of matter, especially the sub-gap (mainly below E_g , sometimes below $E_{0,TL}$) refractive index, providing an insight into the electronic structure and the transitions within the material.

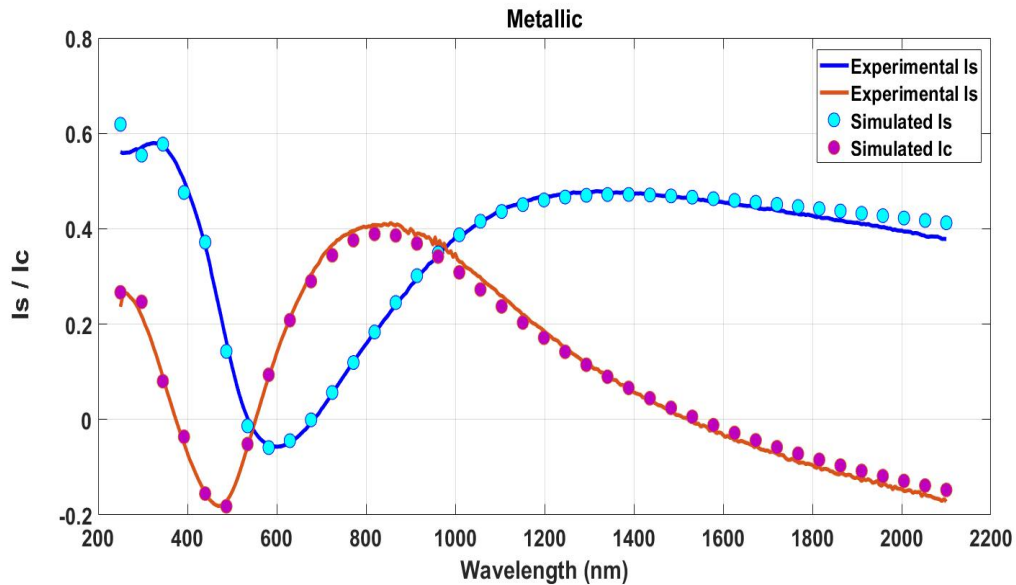
2.6 Optical modelling and characterization of extracted data

As we have learned from previous section, we can summarise that we first collect I_s and I_c values using ellipsometry, following which we create (simulate) the optical model for the sample in question (VO_2 on SiO_2) using dispersion formula for all materials constituting each layers, individually. For, VO_2 we use 3TL to model the correct dispersion in semiconductors state and 3TL + Drude model for the metallic state. As displayed in figure 2.17 we obtain a very good agreement between the experimentally measured ellipsometric parameters I_s/I_c and the simulated optical model described above, with a good fit factor $\chi^2 = 0.59$. These fits confirm the evolution of the material towards a metallic state as we vary the temperature. In our case, we experienced the emergence of metallic behaviour at 58°C , as observed in the figure 2.18.

Additionally, we fit the two phases of VO_2 model simultaneously using a bound multi-model fit. Where we correlated or bind the physical parameters of both low temperature and high temperature models of VO_2 like the thickness, model compositions and roughness. This binding technique enable us to remove correlations between thickness and permittivity in these absorbing films, thus allowing an unambiguous extraction of the optical data.

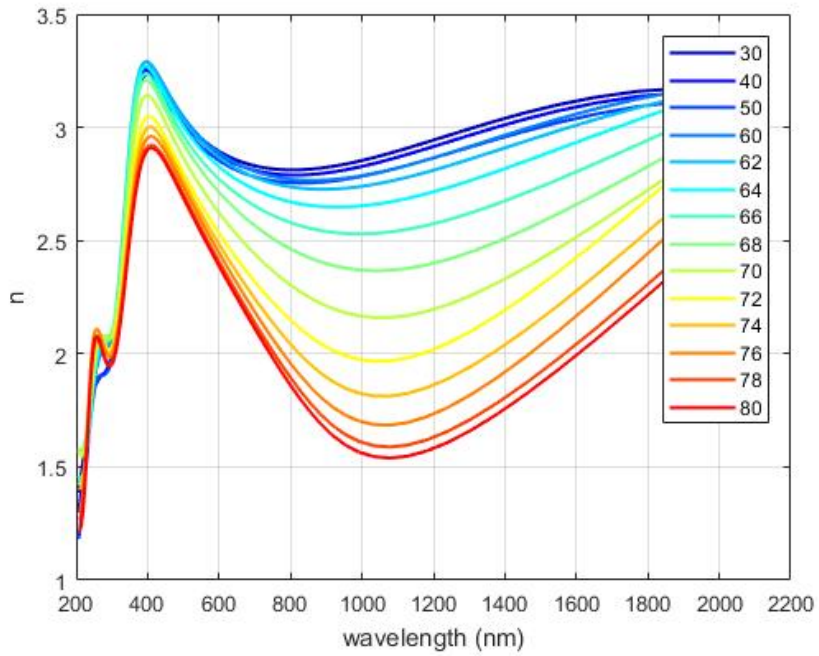


(a) Experimental and simulated I_s/I_c parameters for semiconductor state of VO_2

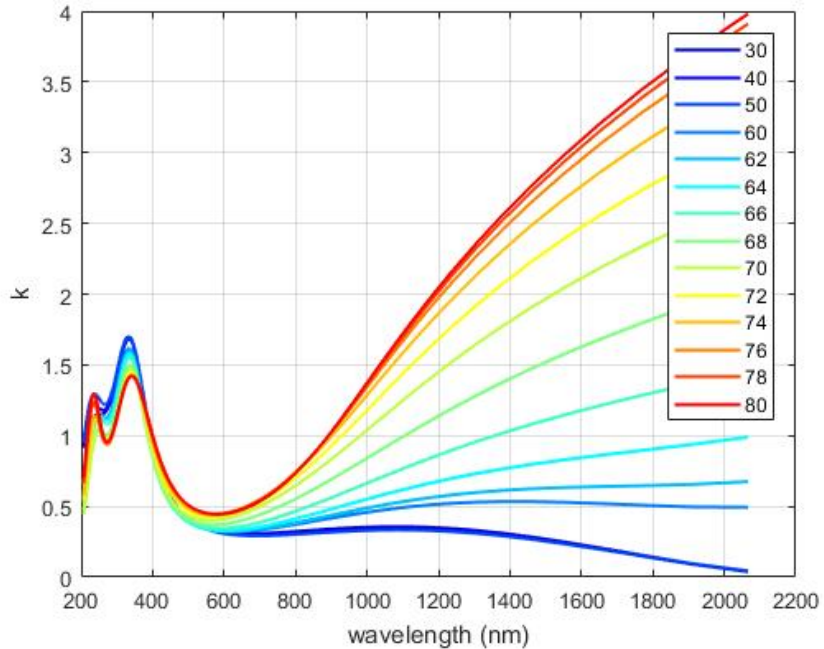


(b) Experimental and simulated I_s/I_c parameters for metallic state.

Figure 2.17: Fitting the optical model and experimental data.



(a) Evolution of real value of refractive index.



(b) Evolution of imaginary value of refractive index

Figure 2.18: Thermal evolution of refractive index of VO_2 extracted from the optical models after the fit.

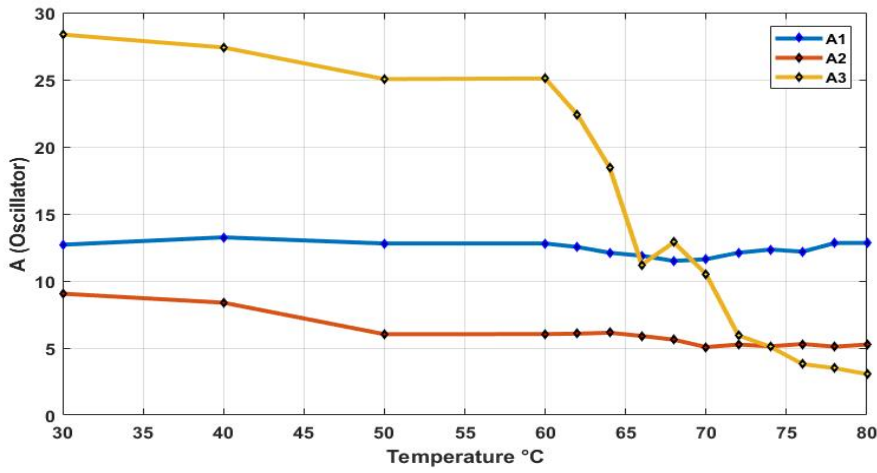
We now calculate the dispersion values from VO_2 models (Figure: 2.18) and observe

the evolution of its optical properties as a function of temperature. As the temperature is increased, there is almost no change in absorbance (imaginary part of the refractive index) in the visible region, except a small increase in absorbance from 440 to 520 nm, relating to the interband transitions between the oxygen $2p$ bands and the vanadium $3d$ bands as we discussed in chapter 1, fig: 2.21.

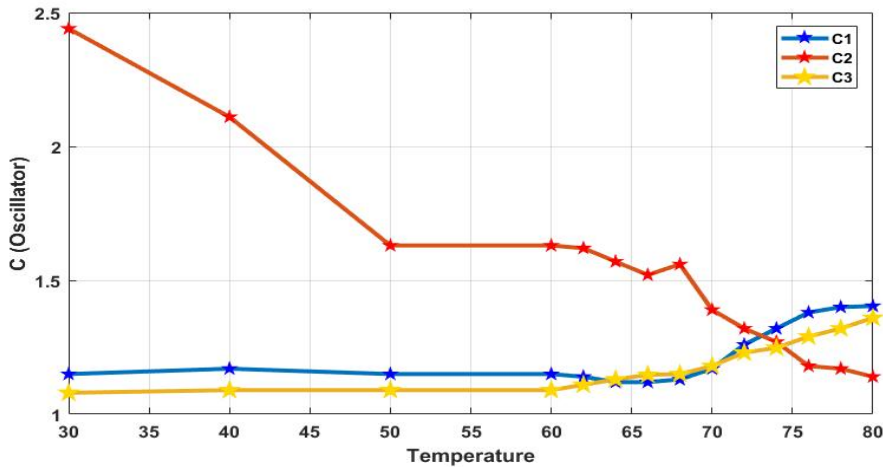
From the figure: 2.20, the first oscillator dominates the optical values in the visible range. The A1 (Amplitude of absorption of the oscillator) and C1 (damping coefficient) coefficients have a slight increase at the higher temperatures. Which can cause a slight increase in the absorption k in the visible range. The second oscillator below the transition is the primary factor for weak absorption in the near IR region. The third oscillator has no effect below the transition but above the transition temperature it affects the optical constants. In the table 2.19, we present the fit parameters and associated values, as extracted from the fits to spectroscopic ellipsometry measurements on VO_2 thin-films.

VO ₂ state 1: Semiconductor		VO ₂ state 2: Metallic	
Fit Parameters	Values	Fit Parameters	Values
ε_∞	1.944	ε_∞	1.421
Eg (eV)	0,535	Eg (eV)	0,06
3 x Tauc-Lorentz Oscillator Values			
A ₁ (eV)	13.48	A ₁ (eV)	14.63
E ₁ (eV)	3.53	E ₁ (eV)	3.069
C ₁ (eV)	1.477	C ₁ (eV)	1.662
A ₂ (eV)	15.89	A ₂ (eV)	44.51
E ₂ (eV)	5.85	E ₂ (eV)	6.02
C ₂ (eV)	2.57	C ₂ (eV)	5.10
A ₃ (eV)	29.58	A ₃ (eV)	1.646
E ₃ (eV)	0.49	E ₃ (eV)	0.46
C ₃ (eV)	1.05	C ₃ (eV)	3.10
Drude values			
ω	--	ω (eV)	3.872
Γ	--	Γ (eV)	0.654

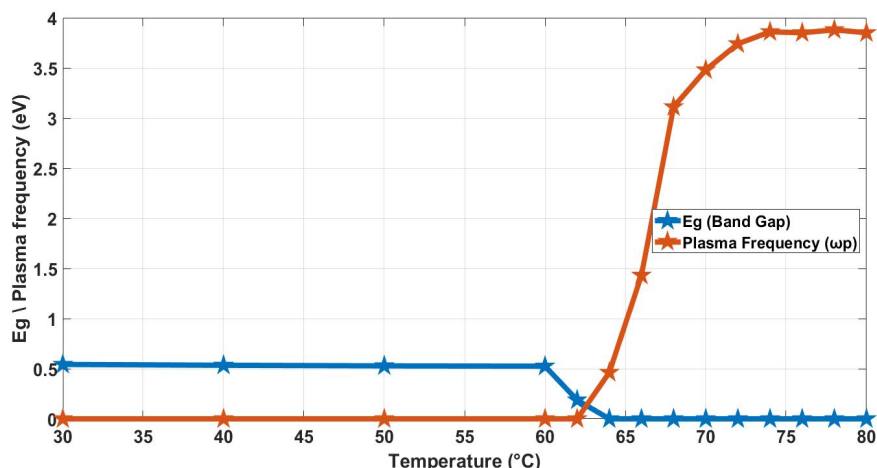
Figure 2.19: Fit parameter values obtained for both the states of VO₂.



(a) Evolution of A (absorption strength value in 3TL) as a function of Temperature.



(b) Evolution of C (damping coefficient for FWHM in 3TL) as a function of Temperature.



(c) Evolution of plasma frequency (increasing metallic character) and the closing of the band gap (decreasing insulating behaviour) as function of Temperature.

Figure 2.20: Varying parameters of VO_2 ellipsometric models calculated as a function of temperature.

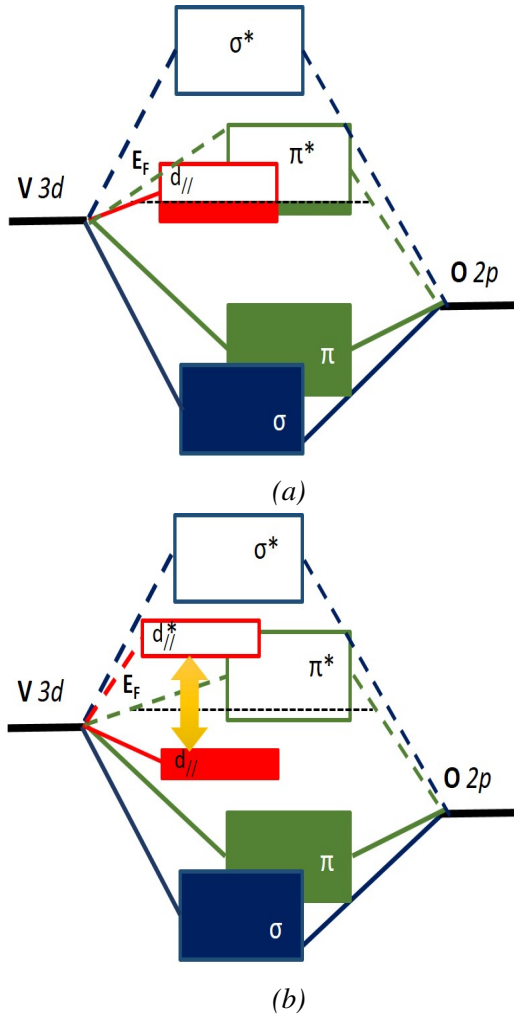
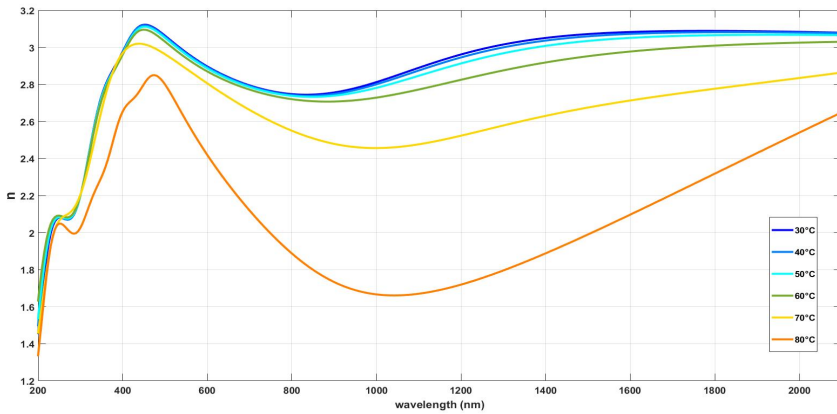
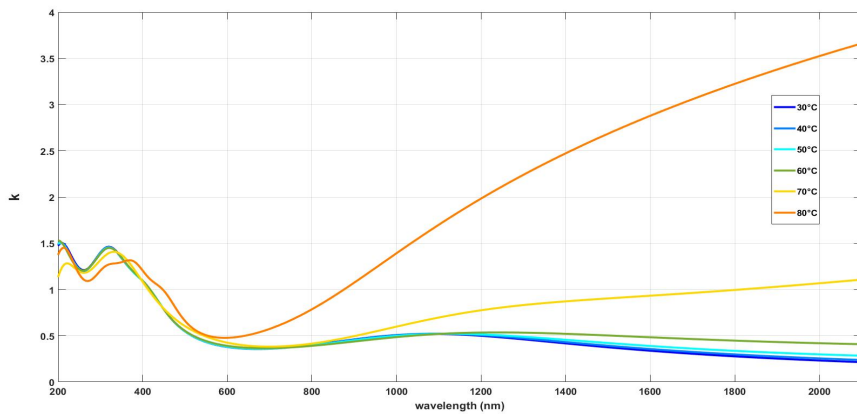


Figure 2.21: Band structure of the a. Insulating and b. Metallic VO_2 .

The absorbance increase seen in the IR region comes from free-carriers absorption, characteristics in VO_2 . Therefore the trend is that the spectral absorbance monotonically increases with wavelength and temperature variation. Similar extraction of evolution of optical property of VO_2 deposited on Al_2O_3 is shown in figure 2.22.



(a) Evolution of real value of refractive index.



(b) Evolution of imaginary value of refractive index

Figure 2.22: Evolution of refractive index as a function of temperature on $\text{VO}_2/\text{Al}_2\text{O}_3$.

Another unique feature of VO_2 is the thermal hysteresis (See Figure 2.23). As it shifts its crystal structure from monoclinic to rutile during the transition, it acquires a semi-stable state and therefore it shows a delay in transiting back to its original state once the trigger is removed, thus showing the presence of a memory effect in the form of hysteresis.

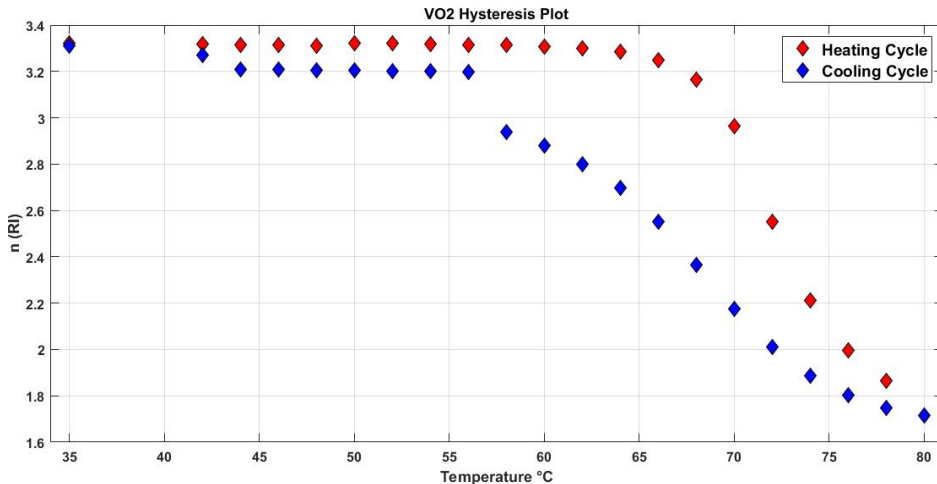


Figure 2.23: Thermal hysteresis loop of VO_2 at $\lambda = 1200\text{nm}$

2.6.1 Discussion

Ellipsometry has always been a powerful tool in investigating structural and optical properties of functional dielectric materials for a wide spectral range. The interest of ellipsometry is not only limited in measuring optical properties but also to have fundamental insights on the physics behind the IMT. Studying the doping effects, straining of VO_2 and its effects on crystallographic transition has given us new outlook in understanding the transition mechanism. Additional to physics, it has also enabled the researches to track the changes in the optical and electrical properties for the transition metals as a function of temperature.

Using this technique we were able to understand and extract the optical parameters of thin-films of VO_2 . The first steps included the data acquisition in terms of ellipsometric parameters for different temperature values. With first hand analysis of the extracted data, we were able to identify the transition property of VO_2 thin-film sample under observation. Following the optical modeling of the thin-film structure, we were able to model the optical properties of VO_2 analytically using a Tauc-Lorentz model with three oscillators and an additional Drude model for the metallic phase of the transition. This has helped to establish and validate the correlation between the theory of transition and experimental data.

This acquisition of optical properties from VO_2 thin-films is fundamental for understand-

ing the influence of the substrate and the thickness on the optical properties. We will see in the next chapters that this step is crucial to provide inputs to simulate, design and realise VO₂ based functional devices, which is the basis for this thesis.

2.7 Conclusion

In this chapter we thoroughly studied the structural and optical properties of VO₂ thin-films deposited in different laboratories. As mentioned before, there are multiple variations for the oxides of Vanadium, hence it is critical to control the environment and the condition for the growth of VO₂ during deposition. With further characterisation using XRD we observe the crystallinity of the deposited VO₂ and structural changes associated with it. This was followed by the optical characterization of the VO₂ thin-films, in order to measure their optical properties. Using ellipsometry, we extracted the optical dispersion of the materials and mapped its evolution as a function of temperature. Further, the thermal hysteresis of VO₂ coupled with the thermal evolution of its optical properties confirms the good quality of VO₂ thin-films, consistently with previous researches [132]. The optical dispersion of VO₂ thus extracted will be utilised as the primary input for the design, development and application of tunable nano-devices in the forth coming chapters.

CHAPTER 3

VO₂ BASED ACTIVE OPTICAL MODULATOR: DESIGN, FABRICATION AND EXPERIMENTAL RESULTS

3.1 Introduction on Silicon photonics

In this data driven world using light as the information carrier, Silicon-based photonics has become a promising technology for on-chip photonics. The success of Silicon as a standard platform is due to its compatibility to monolithically integrated electronics devices. Driven by the industrial demand, high purity silicon is now readily available in large quantities, including the ability to pattern nanoscale ($< 10nm$) features on silicon devices at a large scale [133]. Thus making Si, an industrial standard and a natural candidate for integrated photonics.

Adding to its success, Silicon On Insulator (SOI) architecture has become a technological advancement that has propelled Si-based integrated photonics. This structure of Silicon layer on SiO₂ buried oxide has enabled the fabrication of low-loss Silicon waveguides, taking advantage of the naturally available large refractive index contrast between Si and SiO₂, achieving high optical confinement in sub-micron dimensions [134]. Contrary to most expensive systems like III-V based semiconductors, the economics incentive of SOI platform has been the main driver behind exploring silicon platform for on-chip integrated photonics.

Wavelength division multiplexing (WDM) has enabled the transmittance of many signals through an optical waveguide, using monolithically integrated scalable silicon on-chip component. Thus WDM allows for much broader bandwidth density compared to electronic interconnects, with a speed demonstrated at 100Gb/s fiber coupled transceiver [135]. In addition to the clear advantages of Silicon for efficient waveguiding and multiplexing

functionalities, there is a need for more than just passive waveguide components.

A complete and scalable on-chip monolithically integrated photonic system requires various additional components like light sources, modulators, detectors, routers etc. In fact, each of these components represent a field of intense research pushing the limits of device performance and miniaturization while still keeping the size and cost of the devices low [136, 137, 138]. In terms of the limitations in optical properties and tunability factor for silicon there have been an active push to integrate new materials to create hybrid devices based on SOI platform [139, 140, 141, 142, 143].

3.1.1 Electro-optic modulators

The most important component for optical communication in a photonic link is an electro-optic modulator. Even though nothing travels faster than light, the real speed at which information can be carried by light is the speed at which we can modulate or control it. The speed of data-communication on-chip is therefore governed by the response time of our modulators. By definition, an optical modulator is a device that is used to modulate an optical signal by varying several characteristics of the input light such as the amplitude, the phase or the polarization. There have been a large amount of research dedicated to the demonstration of high efficiency optical modulators, with many different phenomena being used, including carrier depletion in silicon waveguide modulators [144], optical pumping induced Pauli blocking in graphene [145], and thermally, electrically and optically induced phase changes and metal-insulator transitions [146, 147]. Within the standard of the current technological industry, Si is still the backbone of all advancement, primarily due to the existing infrastructure and knowledge base for Si processing residing in the microelectronics industry.

The crystallographic structure of Silicon prevents it to have intrinsic electro-optic modulation properties. Hence, realizing Si photonic modulators has either required the use of resonant structures (e.g., ring resonators and photonic crystal nanocavities) [2, 3] or large

footprints in non-resonant Mach-Zehnder interferometer configurations [4]. Therefore this chapter aims to examine integrated photonic applications utilizing the transition of VO₂ as a driving mechanism for a new type of active optical modulator. But before that, we briefly review the state-of-the-art in terms of functional materials integration on Silicon for optical modulation.

3.1.2 Hybrid integration of functional materials on Silicon for efficient modulators

Contrary to the large optical changes observed in VO₂, the silicon photonics technologies primarily take advantage of small changes in the refractive index of the guiding medium (silicon) in response to the change in charge density, typically induced by a voltage. Even though, this small variation in the refractive index can result in a modulation of >5dB for a single wavelength in excess of modulation frequency greater than >10 GHz [30]. However these classical cavity based or interferometric modulator structure usually have linear dimensions exceeding few tens of micron with limited spectral range. In the effort towards the advancement in optical hybridization of Si modulators, researchers have looked into Si-based waveguide modulators utilizing III-V semiconductors and LiNbO₃ (Lithium niobate) [29] to extend its modulation capacity. Similarly, LiNbO₃ based modulators that employs MZI scheme (Pockel's effect), offers several advantages, like purely linear electro-optic response, no free carrier absorption loss, a simpler fabrication process, and higher bandwidths [148], nevertheless they are larger in dimensions. On the other hand, compound modulators (InGaAlAs/InAlAs/AlGaN), have performance capability matching LiNbO₃ modulators but they require longer coupling distance (few hundred microns) because of their limited absorption modulation and modal overlap [31].

In theory, we can assume the switching energy for a standard modulator with a footprint of $1\mu m^2$ will be a few orders of magnitude greater than the energy required by a VO₂ device of similar size [32] with a switching speed observed at 10 ns [33]. With meticulous device design the power requirement could be further reduced. Given all the attractive properties of

VO_2 reviewed in the previous chapters, it is a very interesting material for achieving active tunability in photonic devices.

VO_2 based free space modulators have already been demonstrated both in infrared [34] and visible [35] range wavelengths, both utilizing thermal induced transitions. Given the material's property and the devices' designs proposed so far, VO_2 based devices are often plagued by large insertion and absorption losses, making it difficult to cascade them in an integrated system. This absorption loss make them not viable for future applications. Here, we strategized a design that can fully exploit the refractive index tuning without suffering from the high absorption. We plan to create an integrated VO_2 based waveguide modulator that circumvent the absorption losses of VO_2 by using it as an advantage, and for future CMOS compatibility it is designed on a SOI platform.

In this chapter we demonstrate a design strategy that relies on a patch of VO_2 meticulously designed for modulation, leveraging the high absorption in the metallic phase of VO_2 . Other groups have previously proposed VO_2 -based plasmonic modulators but with a different architecture [36, 37, 38, 149]. Our simple structure will be compact in terms of architectural standpoint and could be easily be integrated to the current Si based photonic infrastructure and could leverage the fast transition of VO_2 . Aided by the electromagnetic simulations we determine the device geometries required to achieve the deeper modulation depth and also show the waveguide based device structure can be utilised to leverage the intermediate states of VO_2 to act as power filter and further probe the fundamental transition properties.

In the following section, we provide a comprehensive review on the physics involved with optical waveguiding and mode coupling mechanisms. We then explain in detail our design strategy and the simulation study for the VO_2 -based waveguide modulator device.

3.2 Optical Waveguides: Theory and coupling mechanisms

When we talk about integrated photonics or integrated optics, we usually refer to optical circuits that guide light, realised on a chip. It is very similar to electronic circuits integrated in modern chipsets. In the next section we present the theory of waveguiding and understand the coupling mechanisms which are relevant to understand the different concepts used in this chapter.

3.2.1 Optical waveguide theory

The basic component of an integrated optical circuit is a waveguide that confines light and provides a path for its propagation. A typical integrated dielectric waveguide comprises a rectangular core with a refractive index (n_c) higher than the one of the surrounding cladding or surface (n_s). Therefore, when the condition for total internal reflection ($n_c > n_s$) is met, we observe an optical guiding along the length of the waveguide, in the direction defined as z-axis such that x- and y- axis are the width and height of the waveguide core, respectively. The majority of the characteristics of waveguiding by dielectric waveguides can be understood through ray optics [150]. Ray optics has its own limitation as it cannot predict the propagation characteristics when the light confinement is of the order or comparable to the wavelength of light. Therefore to get a complete picture of light guiding we have to take into account the wave nature of light [151], hence the wave theory. This can be achieved by solving Maxwell's equations [151, 152] given the specific geometry of the guiding structures and understanding the characteristics of the modes.

For solving the general case of Maxwell's equation in 1D, we consider a homogeneous, linear, isotropic, charge free, dielectric medium. Inside the linear material we define the electromagnetic wave characteristics using Maxwell's equation, where electric field is defined as **E** (volts per metre), the magnetic field as **H** (ampere per metre), the electric flux density as **B** (ampere per square meter) and the current density **J**. In that case, Maxwell's

equations are as follows;

$$\nabla \times E = -\frac{\partial B}{\partial t} \quad (3.1)$$

$$\nabla \times H = -\frac{\partial D}{\partial t} + J \quad (3.2)$$

$$\nabla \cdot B = 0 \quad (3.3)$$

$$\nabla \cdot D = 0 \quad (3.4)$$

Where 3.4 is Gauss's law in differential form and the constitutive relations are given below,

$$D = \epsilon \cdot E \quad (3.5)$$

$$B = \mu \cdot H \quad (3.6)$$

Solving for the curl of equation 3.1 with certain assumption and variable separation method, we end up with the complete solution for the wave characteristics of light in 1D, The electric field (E) evolution of the wave in time and in the direction of propagation is shown as,

$$E(z, t) = E_0 e^{i(\omega t - kz)} \quad (3.7)$$

Provided the direction of propagation is fixed as +z direction, we observe that the light wave is a plane wave at a given time (t) and a constant z value. The ω represents the oscillating nature of electromagnetic (EM) wave propagating in Z direction with a phase

velocity given by $\frac{\omega}{k} = v_p$, where k is the angular wave number.

Similarly solving for the three dimensional case (3D), we can write the EM field equations as,

$$E(x, y, z, t) = E_o e^{i(\omega t - k_x x - k_y y - k_z z)} = E_o e^{i(\omega t - \vec{k} \cdot \vec{r})} \quad (3.8)$$

$$H(x, y, z, t) = H_o e^{i(\omega t - \vec{k} \cdot \vec{r})} \quad (3.9)$$

where, $k^2 = k_x^2 + k_y^2 + k_z^2$ and $\vec{r} = x\hat{x} + y\hat{y} + z\hat{z}$ such that k_x, k_y, k_z can assume any value provided there is no restriction on the direction of propagation.

Further solving for understanding the transverse property of the propagating EM field in z direction, we take the divergence of Maxwell's equations 3.4 and 3.3, we find that the solution of these equations showed no longitudinal component. Hence the wave is purely transverse: the E and H components of the wave lie in the $x - y$ plane and no component exists in the z direction. In order to find the relationship between the E and H component, we solve 3.1 with a condition such that the field is expressed as $E_{x,y,z} = E_{ox,y} e^{j(\omega t - \beta z)}$. Solving for the E component (E_{ox}) in the x direction, we get the following solution for H component;

$$H_{ox} = 0 \quad (3.10)$$

$$H_{oy} = \frac{k}{\omega \mu} E_{ox} \quad (3.11)$$

$$B_o = \frac{k}{\omega} E_o = \frac{E_o}{v_p} \quad (3.12)$$

where v_p is the phase velocity, which is the speed of light (c) in free space. Therefore, in a linearly polarised wave the amplitude of the electric component E_o is much higher

compared to the magnetic component B_0 .¹

3.2.2 Poynting Vector

In order to calculate the energy associated with the electromagnetic wave we take the divergence of $\vec{E} \times \vec{H}$, because if we compare the S.I units of \vec{E} is $\frac{\text{volts(V)}}{\text{Metre(m)}}$ and \vec{H} is $\frac{\text{ampere's(A)}}{\text{Metre(m)}}$. So divergence will give $\frac{\text{Power(V.A)}}{\text{Area(m}^2)}$, which is technically an intensity. Therefore, if we take the entire cross sectional area then from divergence theorem [153] we get the power using the equation;

$$\int_v \text{div}(\vec{E} \times \vec{H}) dv \quad (3.13)$$

So we use Maxwell's equations 3.2 and 3.1 to calculate the divergence of $\vec{E} \times \vec{H}$ as shown,

$$\nabla \cdot (\vec{E} \times \vec{H}) = \vec{H} \cdot (\vec{E} \times \vec{H}) - \vec{E} \cdot (\vec{E} \times \vec{H}) \quad (3.14)$$

Substituting from Maxwell's equation,

$$\nabla \cdot (\vec{E} \times \vec{H}) = -\mu \vec{H} \cdot \frac{\partial \vec{H}}{\partial t} - \vec{J} \cdot \vec{E} - \epsilon \vec{E} \cdot \frac{\partial \vec{E}}{\partial t} \quad (3.15)$$

Rearranging the terms we get,

$$\nabla \cdot (\vec{E} \times \vec{H}) = -\frac{\partial}{\partial t} \left[\frac{1}{2} \mu \vec{H}^2 + \frac{1}{2} \epsilon \vec{E}^2 \right] - \vec{J} \cdot \vec{E} \quad (3.16)$$

Where, $\frac{1}{2} \mu \vec{H}^2$ represents the density of the energy stored in the magnetic field, $\frac{1}{2} \epsilon \vec{E}^2$ is the density of the energy stored in the electric field and $\vec{J} \cdot \vec{E}$ represents joule loss per unit volume. Now if we represent $\vec{E} \times \vec{H}$ as \vec{S} and u as $\frac{1}{2} \mu \vec{H}^2 + \frac{1}{2} \epsilon \vec{E}^2$, we can rewrite the

¹That is why cones and rods in our eyes are sensitive to the electric field of the incoming light.

equation while integrating over all volume as:

$$\int_v \vec{\nabla} \cdot \vec{S} dv = -\frac{\partial}{\partial t} \int_v u dv - \int_v \vec{J} \cdot \vec{E} dv \quad (3.17)$$

Rearranging the terms,

$$\int_s \vec{S} \cdot ds = -\frac{\partial}{\partial t} \int_v u dv - \int_v \vec{J} \cdot \vec{E} dv \quad (3.18)$$

Where $\int_s \vec{S} \cdot ds$ represents the flux of \vec{S} through the closed surface S enclosing the volume v . Which are equal to $[-\frac{\partial}{\partial t} \int_v u dv]$, the rate of decrease of energy stored in EM field and $[\int_v \vec{J} \cdot \vec{E} dv]$, the rate of Joule loss, respectively. Therefore, conclusively we can say that \vec{S} is the energy per unit time per unit surface area, or the power per unit area. The direction of which is perpendicular to E and H field i.e. the z- direction. So we can say that power propagates on the direction of propagation of light and it is denoted by \vec{S} Poynting vector. The intricate theory for the boundary conditions and coupled mode theory are given in the Appendix A.1.

3.3 VO₂-based waveguide modulator: Design and Working principles

The principle design strategy relies on the optical power sharing, in accordance with the directional coupler theory. According to this theory, when two waveguides having similar propagation constant are in close proximity, they tend to share the power of input light between them considering a modal overlap of each waveguide. By carefully designing the distance between the waveguides and the length of the coupling region, it is possible to couple any desired fraction of the light from one waveguide to the other. The spacing between the waveguides is designed such that the evanescent tail of the mode in either of the waveguide penetrates the other waveguide, and thus the wave from one guide gets coupled to the adjacent guide.

If the waveguides are identical in terms of phase propagation constants ($\beta_m = k_0^2 n_0^2 - (\frac{m\pi}{d})^2$ where m denotes the mode number, n_0 denotes the index of the medium of propagation), a complete transfer of wave happens over some length of the guide and then it transfers back to the original guide again. If the propagation constants of the waveguides are not identical then the transfer of the wave is not complete. In classical modulators, the electrodes are placed in specific arrangements near each guide such that, when the electric field is applied, the refractive index of the waveguides are changed leading to significant shift in propagation constants [38, 154]. Thus influencing the power transfer from one guide to another.

The directional coupler strategy to our proposed VO₂-based waveguide modulator consists of two silicon waveguides at close proximity of each other. One of the waveguide is hybrid, as it designed with a patch of VO₂ deposited on the top of the waveguide. We aim at designing its dimensions such that, when VO₂ is metallic, the hybrid waveguide is well index-matched with the Si bus waveguide, fulfilling the coupling conditions. Hence, the input light from the bus waveguide is coupled to the VO₂ hybrid waveguide. Owing to short coupling length and the high absorption of VO₂, the re-coupling of light back to the

bus waveguide is prevented. The figure 3.1 shows the architectural concept of the proposed VO₂ based waveguide modulator.

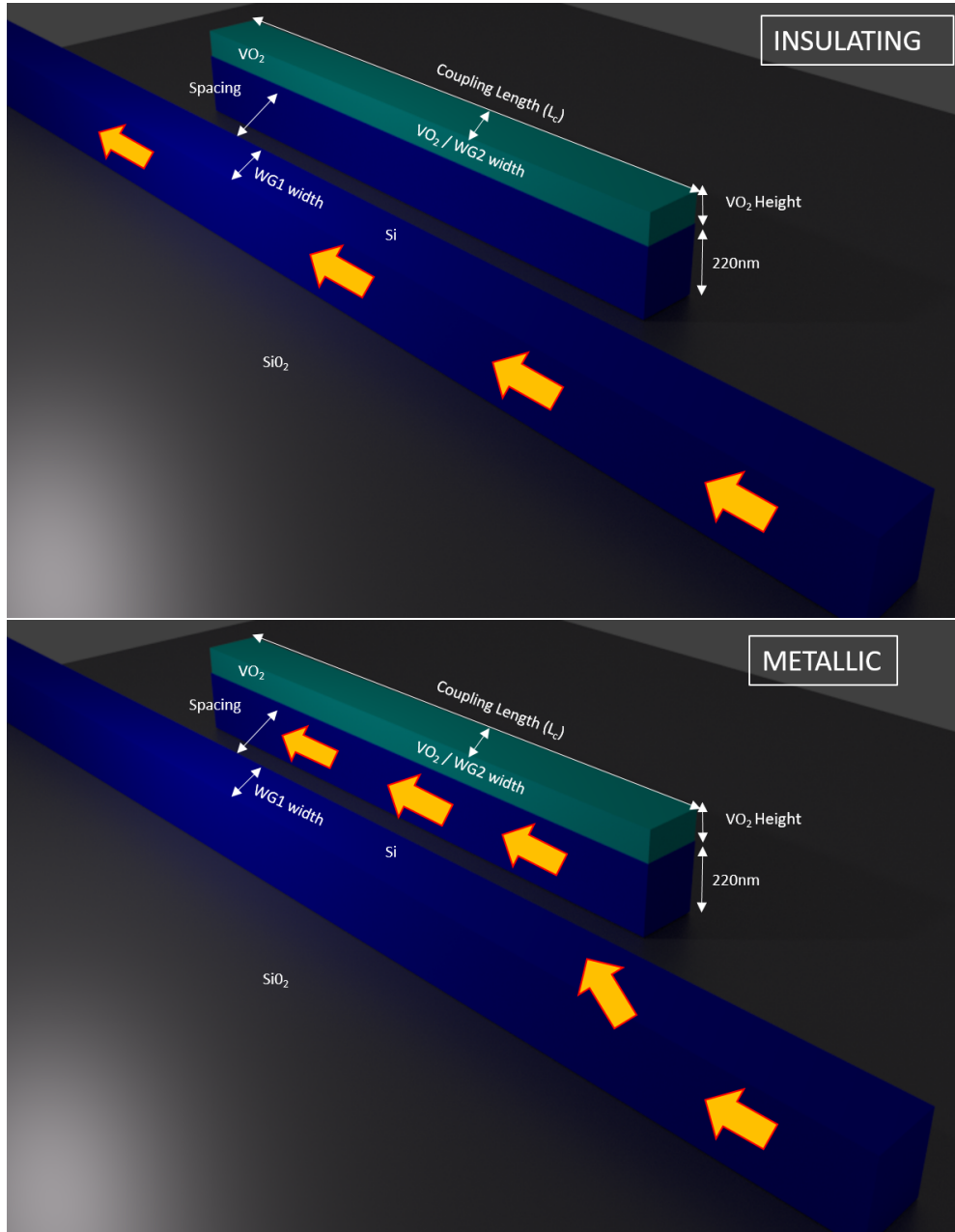


Figure 3.1: Schematic view of the active PCM modulator based on vanadium dioxide insulator-metal phase transition: Top Figure : VO₂ is insulating, wave propagation is unaltered. Figure below shows when VO₂ is metallic, the wave diverts its path of propagation into the adjacent waveguide leveraging the absorption of VO₂.

In order to find the right coupling conditions between the two proposed waveguides, we

plot evolution of the effective indices in the Si and Si/VO₂ waveguides versus the width of the Si/VO₂ waveguide (see fig. 3.2). The width of the Si bus waveguide is set at 0.52 μm. Thicknesses of the Si and VO₂ layer are respectively 0.22 and 0.12 μm. Calculation is performed at $\lambda = 1.55\mu\text{m}$ and with a spacing between the two waveguides of 0.4 μm. Refractive indices of Si, SiO₂ and VO₂ in metallic and insulator states are respectively of 3.4799, 1.4448, 2.0245 and 3.2430. The schematics for which are shown in figure 3.3. As a result we can observe the difference in the field and the effective refractive index, giving us an advantage to manipulate physical conditions for adequate coupling.

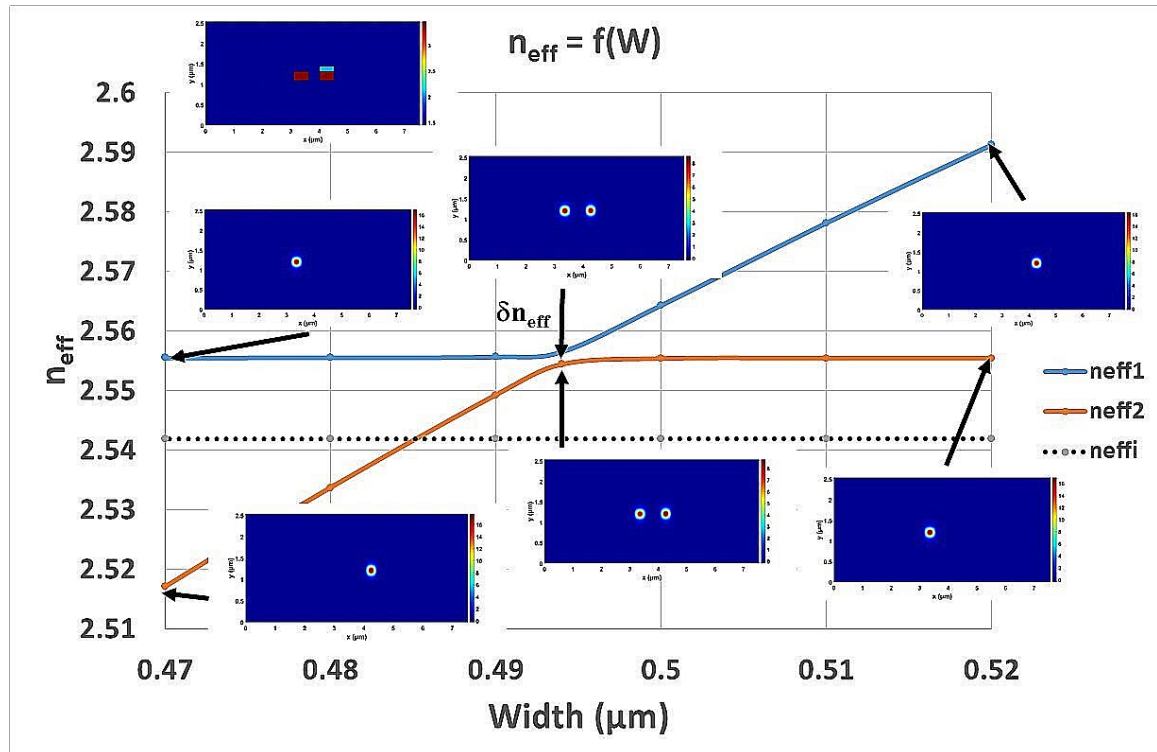
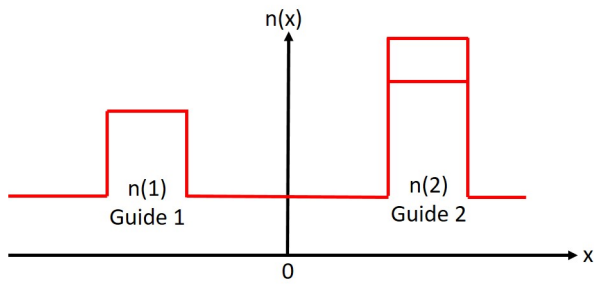
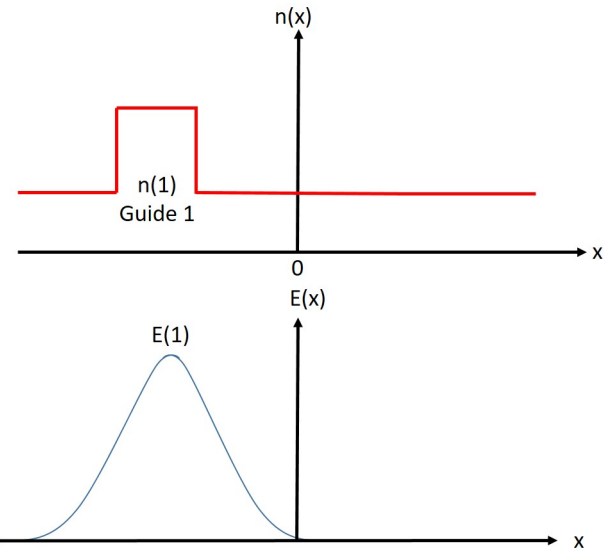


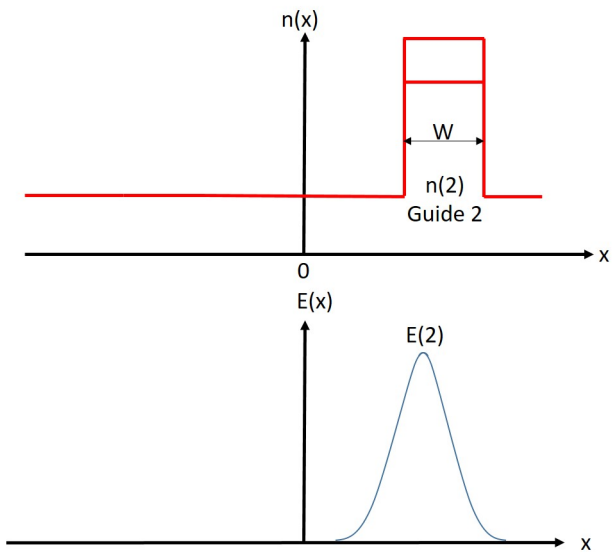
Figure 3.2: Evolution of the effective indices in the guide to guide coupler versus the width of the waveguide with the VO₂ layer.



(a) Bus waveguide and the hybrid waveguide sketch.



(b) Calculation of field propagation observed from waveguide 1



(c) Calculation of field propagation observed from waveguide 2

Figure 3.3: Refractive index distribution of the coupled waveguide and electric field of subsequent waveguides. The width of the VO₂/Si waveguide is adjusted to manipulate the effective index in order to match the bus waveguide effective index.

The advantage of our proposed design is the simple architecture employed and the scalability involved that can be considered as an add-on component for any linear waveguide system. And since, the VO₂ is deposited on top of the device rather than being embedded in the structure, the nanofabrication process is simpler. To design such a switchable directional coupler we need to match the propagation constant of bus waveguide β_1 to the propagation constant of waveguide with VO₂ patch on top β_2 at the condition when VO₂ is metallic. Where we see the supermode condition when $\beta_1 \approx \beta_2$.

The effective index of the mode in the strip Si waveguide is constant ($n_{eff,Si} = 2.5555$) for $\lambda = 1.5 \mu\text{m}$ as the width stay constant for all the modelling. For small width ($0.47 \mu\text{m}$) of the strip waveguide with VO₂, the effective index of the mode is lower ($n_{eff,2} = n_{eff,Si}/VO_2 = 2.5171$). Mode profiles of the two modes are given in the inset of figure 3.2. As the width of the waveguide with VO₂ increases, a phase matching occurs for $W = 0.494 \mu\text{m}$. In this case, the two modes are degenerated into odd and even modes (see the two insets in the middle of the figure 3.2) with effective indices respectively equal to $n_{eff,1} = 2.5565$ and $n_{eff,2} = 2.5544$. For larger widths, the effective index of the waveguide with VO₂ becomes higher than this of the Si waveguide ($n_{eff,1} = n_{eff,Si}/VO_2 = 2.5913$ for Width = $0.52 \mu\text{m}$). Close to the phase match condition, a power exchange between the two waveguides can be explained as follows.

3.3.1 Codirectional Coupling

Figure 3.4 represents co-directional coupling where at $z=0$, we assume that the entire power is in core 1 and as the wave propagates reaching a certain distance, the power is completely transferred to the adjacent waveguide.

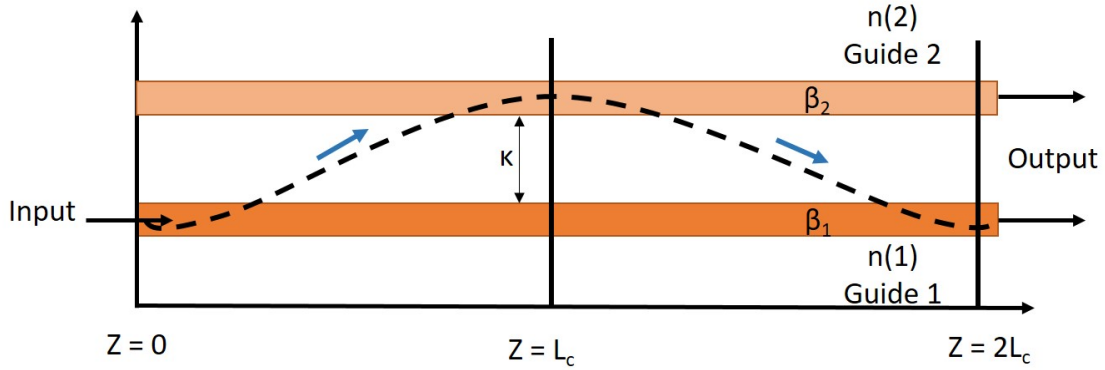


Figure 3.4: Schematics for mode coupling between two dissimilar waveguides.

Since both the modes in co-directional coupling are travelling in the same direction and usually with a same propagation constant ($\beta_1 > 0$ and $\beta_2 > 0$), the general solution for the coupled mode equation can be written as;

$$A(Z) = [a_1 e^{j\psi z} + a_2 e^{-j\psi z}] e^{-j\psi z} \quad (3.19)$$

$$B(Z) = [b_1 e^{j\psi z} + b_2 e^{-j\psi z}] e^{j\psi z} \quad (3.20)$$

Where the amplitude of mode propagating is given by the term $[a_1 e^{j\psi z} + a_2 e^{-j\psi z}]$, these terms are taken as a function of complex exponential because the power transfer between the guides follows a cosine pattern. Therefore with boundary conditions and acknowledging that in most case the power is injected to only one waveguide, then $A(0) = A_o$ and $B(0) = 0$. Hence, our equations are reduced to

$$A(Z) = A_o \left[\cos(\psi Z) + \frac{j \frac{\Delta\beta}{2}}{\psi} \sin(\psi z) \right] e^{-j \frac{\Delta\beta}{2} z} \quad (3.21)$$

$$B(Z) = -A_o \frac{j\kappa}{\psi} \sin(\psi z) e^{j \frac{\Delta\beta}{2} z} \quad (3.22)$$

Now we represent the above equations 3.21 and 3.22 in terms of the power in each

waveguide [155] and are given as;

$$P_1(z) = P_1(0) \left[1 - \frac{\kappa^2}{\psi^2} \sin^2 \psi \kappa \right] \quad (3.23)$$

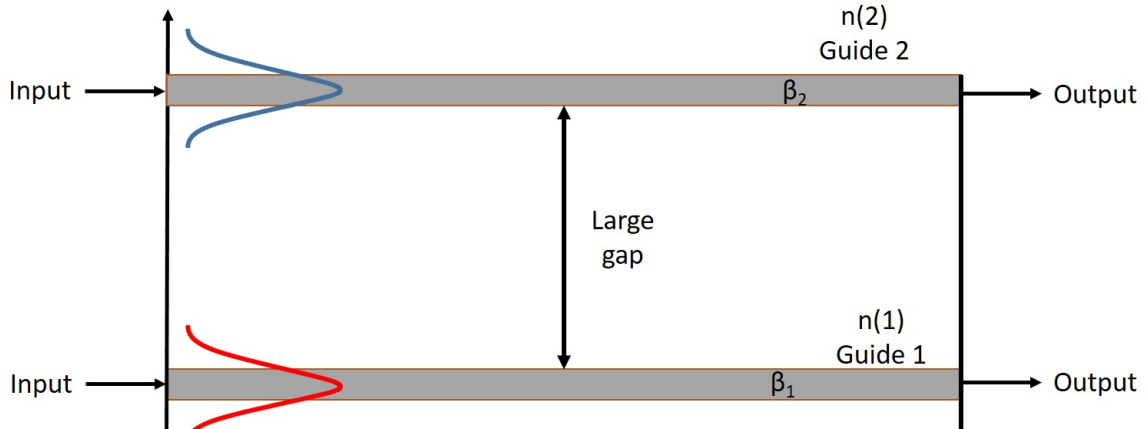
And the power variation in Core 2 can be represented as;

$$P_2(z) = P_1(0) \left[\frac{\kappa^2}{\psi^2} \sin^2 \psi \kappa \right] \quad (3.24)$$

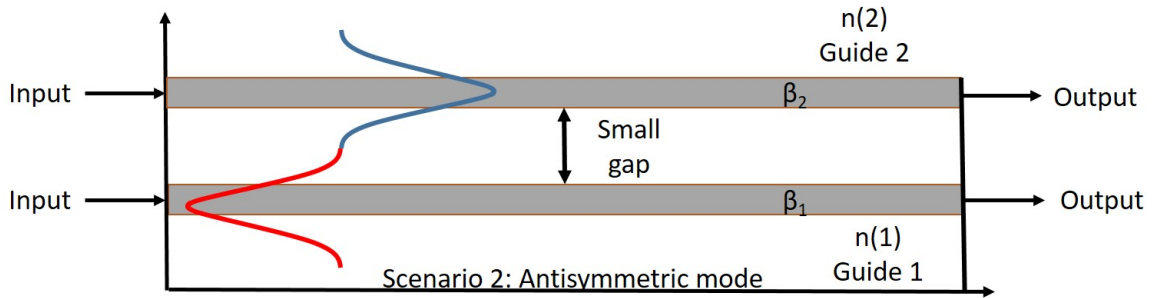
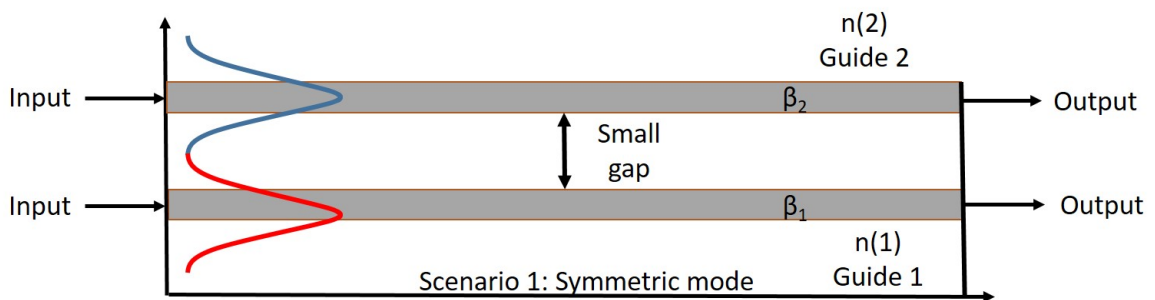
where $\psi^2 = \kappa^2 + \frac{\Delta\beta^2}{4}$ and $\Delta\beta = \beta_1 - \beta_2$ the phase mismatch. κ is the strength of interaction which depends on the waveguide parameters, core separation and wavelength. We observe that now the power follows a \sin^2 profile, which is close to cosine. We can express the maximum power-coupling efficiency as $F = (\frac{\kappa}{\psi})^2$. The coupling length is the maximum length over which the maximum power is transferred to the second waveguide. It is denoted by $L_c = \frac{\pi}{2\kappa}$, when $\beta_1 = \beta_2$ or $\Delta\beta = 0$.

3.3.2 Symmetric and Anti-symmetric field pattern

If we take two waveguides, such that they are well separated, the modes propagating in the waveguide will not interact. But if we bring closer both the waveguides, the modes in each waveguide start interacting, creating a new field or mode pattern for such composite system. This new field pattern corresponds to supermodes and they can be symmetric mode or asymmetric mode interaction. The schematics of which is shown below in figure 3.5b and 3.5.



(a) Well separated waveguide with isolated modes.



(b) Symmetric and anti-symmetric supermodes in the composite system when separation is less

Figure 3.5: Schematics for symmetric and anti-symmetric super modes in directional couplers

Now if we take the case for co-directional couplers, where we inject power in one waveguide, which is then later coupled to adjacent waveguide, the excited mode pattern for the input mode can be expressed in terms of symmetric and anti-symmetric field patterns (even and odd field patterns). Since they are mode patterns which remains the same throughout the propagation, therefore we can understand the propagation of mode in the composite system by understanding the propagation of symmetric and anti-symmetric mode.

Interestingly, as they propagate, since each mode has a different velocity and therefore a different effective index, they accumulate a phase shift between them. When the phase shift is π , the mode pattern are inverted such that the whole mode is transferred to the adjacent waveguide, this phenomenon explains the mode coupling as given by the equations below;

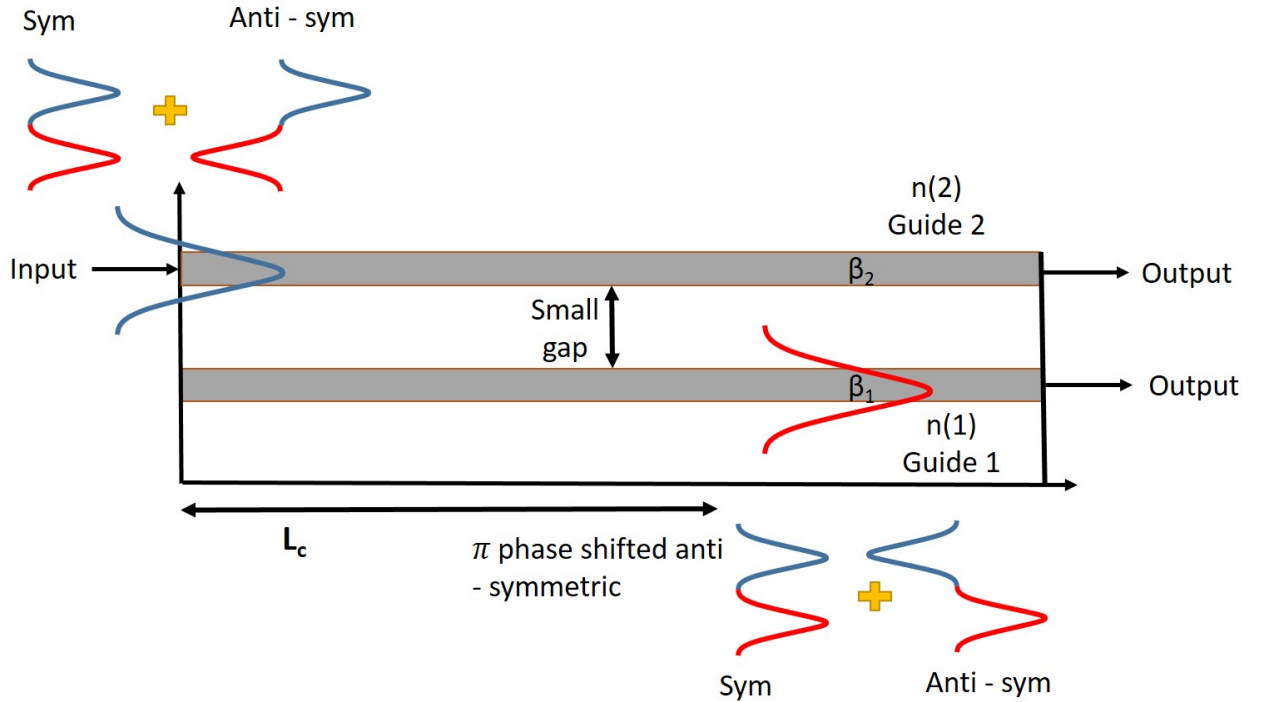


Figure 3.6: Schematics for π order phase between symmetric and anti-symmetric mode leading to co-directional mode coupling.

$$\text{At } Z = 0, \quad E(x) = E_{sym}(x) + E_{antisym}(x) \quad (3.25)$$

$$\text{At } Z = L, \quad E(x) = E_{sym}(x) + E_{antisym}(x)e^{[j(\beta_{sym} - \beta_{antisym})L]} \quad (3.26)$$

$$\text{When } (\beta_{sym} - \beta_{antisym})L = \pi, \quad E(x) = E_{sym}(x) - E_{antisym} \quad (3.27)$$

where $E(x)$ is the field of the mode propagating in the composite system, because of the phase shift, there is constructive and destructive interferences between the symmetric and

anti-symmetric modes which dictates the light transfer from one waveguide to the other. The length of the coupling can be written in terms of n_{eff} , as shown in equation 3.28. The variation of the coupling length with the inter-waveguide gap is shown in figure 3.7.

$$L_c = \frac{\lambda}{2.(n_{eff(sym)} - n_{eff(antisym)})} \quad (3.28)$$

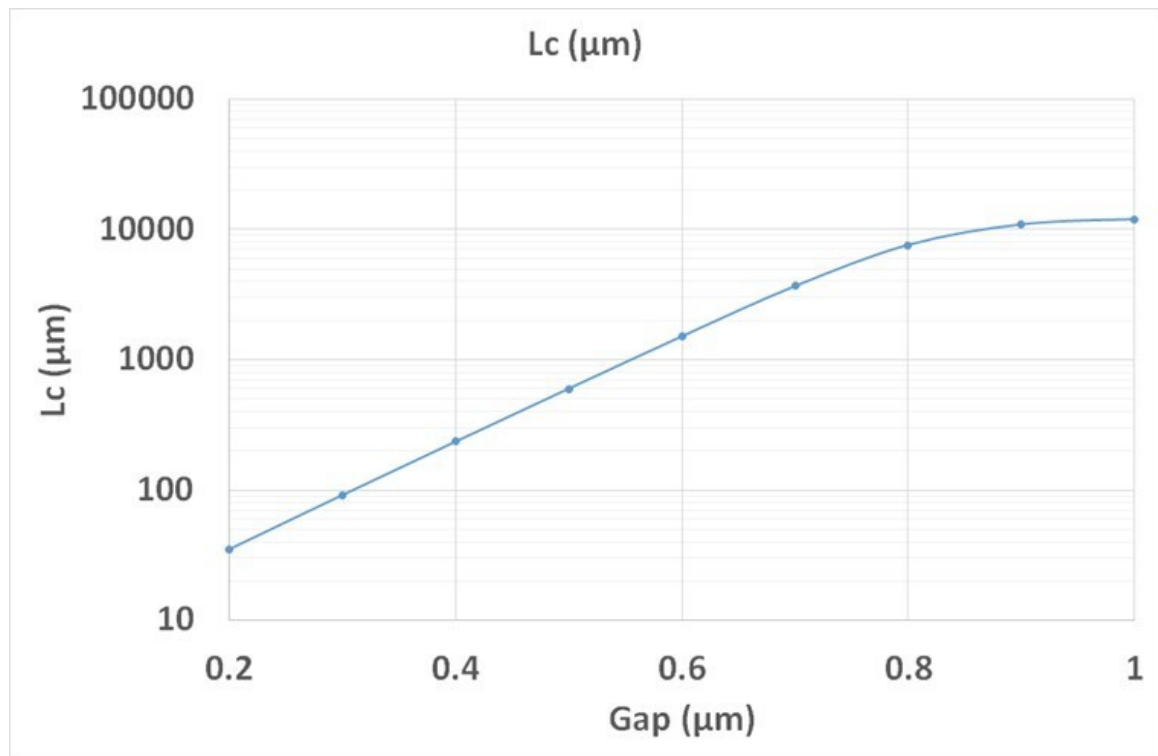


Figure 3.7: Variation of L_c versus the gap between the two coupled waveguides.

We can notice in figure 3.7 that for gap between 0.2 to 0.7 μm , variation of L_c in the logarithmic scale versus the gap is linear. This means that only with two points, it is possible to have an analytic expression of the coupling length versus the gap as:

$$L_c = 10^{(40.4771) \times \text{gap} + 7.454} \quad (3.29)$$

This linear behavior can be explained by the fact that the exponential evanescent part of the

fields of the two modes interact to create the even and the odd modes. Saturation effect for larger gap is due to the discretization of the modelling. The phase match condition is not strictly obtained. Following, in order to calculate the energy transfer of the input waveguide to the even and odd modes of the two coupled waveguides, we use the mode matching method (MMM). The intricate theory of MMM is explained in the appendix B.1. The theory involving the numerical analysis is explained in the next section and the figure 3.2 has been calculated employing the following numerical theory.

3.4 Simulation study and Numerical Analysis

3.4.1 2D Mode Solver

In a strip waveguide, the refractive index is a function of both transverse coordinates. In such a case, the analysis of the waveguide modes becomes a more complex task compared to slab guides as the dimensions for confinement increases. A starting point for the formulation of rigorous full-vectorial waveguide analysis are the Maxwell's equation, for the complex amplitudes and a time dependence in an anisotropic media.

$$\vec{\nabla} \times \vec{H} = j\omega\epsilon_0[\epsilon_r]\vec{E} \quad (3.30)$$

$$\vec{\nabla} \times \vec{E} = -j\omega\mu_0[\mu_r]\vec{H} \quad (3.31)$$

This equation can easily be converted into matrix format that makes the tensor aspect of μ and ϵ .

$$\begin{bmatrix} 0 & -\frac{\partial}{\partial z} & \frac{\partial}{\partial y} \\ \frac{\partial}{\partial z} & 0 & -\frac{\partial}{\partial x} \\ -\frac{\partial}{\partial y} & \frac{\partial}{\partial z} & 0 \end{bmatrix} \begin{bmatrix} H_x \\ H_y \\ H_z \end{bmatrix} = j\omega\epsilon_0 \begin{bmatrix} \epsilon_{xx} & \epsilon_{xy} & \epsilon_{xz} \\ \epsilon_{yx} & \epsilon_{yy} & \epsilon_{yz} \\ \epsilon_{xz} & \epsilon_{yz} & \epsilon_{zz} \end{bmatrix} \begin{bmatrix} E_x \\ E_y \\ E_z \end{bmatrix} \quad (3.32)$$

$$\begin{bmatrix} 0 & -\frac{\partial}{\partial z} & \frac{\partial}{\partial y} \\ \frac{\partial}{\partial z} & 0 & -\frac{\partial}{\partial x} \\ -\frac{\partial}{\partial y} & \frac{\partial}{\partial z} & 0 \end{bmatrix} \begin{bmatrix} E_x \\ E_y \\ E_z \end{bmatrix} = -j\omega\mu_0 \begin{bmatrix} \mu_{xx} & \mu_{xy} & \mu_{xz} \\ \mu_{yx} & \mu_{yy} & \mu_{yz} \\ \mu_{xz} & \mu_{yz} & \mu_{zz} \end{bmatrix} \begin{bmatrix} H_x \\ H_y \\ H_z \end{bmatrix} \quad (3.33)$$

We take only the diagonal values of the anisotropy because we can chose the axis that corresponds to the crystal axis of the anisotropic material. Which then reduces to only diagonal elements that arises when the tensor is rotated relative to the coordinate systems. These are the first few steps towards eigen value matrix equations that can be solved thanks to finite difference schemes. We also normalise the magnetic field H , such that $\tilde{H} = -j\omega\mu_0 H$ and also we normalise the matrix grid like $x' = j\omega\epsilon_0 x$, $y' = j\omega\epsilon_0 y$ and $z' = j\omega\epsilon_0 z$. Hence the modified matrix are:

$$\begin{bmatrix} 0 & -\frac{\partial}{\partial z'} & \frac{\partial}{\partial y'} \\ \frac{\partial}{\partial z'} & 0 & -\frac{\partial}{\partial x'} \\ -\frac{\partial}{\partial y'} & \frac{\partial}{\partial z'} & 0 \end{bmatrix} \begin{bmatrix} \tilde{H}_x \\ \tilde{H}_y \\ \tilde{H}_z \end{bmatrix} = \begin{bmatrix} \epsilon_{xx} & 0 & 0 \\ 0 & \epsilon_{yy} & 0 \\ 0 & 0 & \epsilon_{zz} \end{bmatrix} \begin{bmatrix} E_x \\ E_y \\ E_z \end{bmatrix} \quad (3.34)$$

$$\begin{bmatrix} 0 & -\frac{\partial}{\partial z'} & \frac{\partial}{\partial y'} \\ \frac{\partial}{\partial z'} & 0 & -\frac{\partial}{\partial x'} \\ -\frac{\partial}{\partial y'} & \frac{\partial}{\partial z'} & 0 \end{bmatrix} \begin{bmatrix} E_x \\ E_y \\ E_z \end{bmatrix} = \begin{bmatrix} \mu_{xx} & 0 & 0 \\ 0 & \mu_{yy} & 0 \\ 0 & 0 & \mu_{zz} \end{bmatrix} \begin{bmatrix} \tilde{H}_x \\ \tilde{H}_y \\ \tilde{H}_z \end{bmatrix} \quad (3.35)$$

Following, ignoring the loss, a mode in a waveguide has the following general mathematical form which is consistent with the Bloch theorem.

$$\vec{E}(x, y, z) = \vec{A}(x, y)e^{\gamma z} \quad (3.36)$$

unlike in previous section, here \vec{A} is the complex amplitude (mode shape) and γ represents the phase accumulation in -z direction ($\gamma = \alpha + j\beta$) which is complex propagation constant with oscillation and decay factor. For a perfect waveguide, the refractive index and the permeability are invariant versus the z axis, therefore a 3D waveguide problem can be

reduced to a 2D problem. And therefore, we normalise the modal equation to fit with the matrix grid and we have the following equation form;

$$\vec{E}(x', y', z') = \vec{A}(x', y') e^{\gamma z' / k_0} \quad (3.37)$$

$$\vec{H}(x', y', z') = \vec{B}(x', y') e^{\gamma z' / k_0} \quad (3.38)$$

Substituting the normalised to solution form of Maxwell's equations, like,

$$\frac{\partial E_z}{\partial y'} - \frac{\partial E_y}{\partial z'} = \mu_{xx} \tilde{H}_x \quad (3.39)$$

with some arithmetical calculation we get the following solution which are independent of E and H factors but with A and B which are the amplitude for the normalised mode equation and the z- component becomes $\tilde{\gamma}$ which is accumulation of phase.

$$\frac{\partial A_z}{\partial y'} - \frac{\gamma}{k_0} A_y = \mu_{xx} B_x \quad (3.40)$$

Following the similar analogy we can rewrite the matrix equations in the following form,

$$\begin{bmatrix} 0 & \tilde{\gamma} & \frac{\partial}{\partial y'} \\ \frac{\partial}{\partial z'} & 0 & \frac{-\partial}{\partial x'} \\ \frac{-\partial}{\partial y'} & \frac{\partial}{\partial z'} & 0 \end{bmatrix} \begin{bmatrix} B_x \\ B_y \\ B_z \end{bmatrix} = \begin{bmatrix} \epsilon_{xx} & 0 & 0 \\ 0 & \epsilon_{yy} & 0 \\ 0 & 0 & \epsilon_{zz} \end{bmatrix} \begin{bmatrix} A_x \\ A_y \\ A_z \end{bmatrix} \quad (3.41)$$

$$\begin{bmatrix} 0 & \tilde{\gamma} & \frac{\partial}{\partial y'} \\ \frac{\partial}{\partial z'} & 0 & \frac{-\partial}{\partial x'} \\ \frac{-\partial}{\partial y'} & \frac{\partial}{\partial z'} & 0 \end{bmatrix} \begin{bmatrix} A_x \\ A_y \\ A_z \end{bmatrix} = \begin{bmatrix} \mu_{xx} & 0 & 0 \\ 0 & \mu_{yy} & 0 \\ 0 & 0 & \mu_{zz} \end{bmatrix} \begin{bmatrix} B_x \\ B_y \\ B_z \end{bmatrix} \quad (3.42)$$

we normalise the propagation constant such as, $\tilde{\gamma} = \frac{\gamma}{k_0}$, $\tilde{\gamma} = jn_{eff}$, where $n_{eff} = n + jk$.

Following we convert the matrix into linear form so that we can discretize them using Dirichlet condition [156] and transform them into eigen value problems. So we can represent

the matrix equations in linear matrix form as,

$$D_y^e a_z - \tilde{\gamma} a_y = \mu_{xx} b_x \quad (3.43)$$

$$\tilde{\gamma} a_x - D_x^e a_z = \mu_{yy} b_y \quad (3.44)$$

$$D_x^e a_y - D_y^e a_x = \mu_{zz} b_z \quad (3.45)$$

$$D_y^h b_z - \tilde{\gamma} b_y = \epsilon_{xx} a_x \quad (3.46)$$

$$\tilde{\gamma} b_x - D_x^h b_z = \epsilon_{yy} a_y \quad (3.47)$$

$$D_x^h b_y - D_y^h b_x = \epsilon_{zz} a_z \quad (3.48)$$

We now solve equations 3.45 and 3.48 for the longitudinal components such that we can replace the E_z and H_z . After substituting and replacing, we now remain with equations that just contain the transverse field components E_x , E_y , H_x and H_y . These equations are then rearranged into common terms that are multiplying the field components, and are shown below,

$$-D_x^e, \epsilon_{zz}^{-1} D_y^h b_x + (D_x^e, \epsilon_{zz}^{-1} D_x^h + \mu_{yy}) b_y = \tilde{\gamma} a_x \quad (3.49)$$

$$-(D_y^e, \epsilon_{zz}^{-1} D_y^h + \mu_{xx}) b_x + D_y^e, \epsilon_{zz}^{-1} D_x^h, b_y = \tilde{\gamma} a_y \quad (3.50)$$

$$-D_x^h, \mu_{zz}^{-1} D_y^e a_x + (D_x^h, \mu_{zz}^{-1} D_x^e + \epsilon_{yy}) a_y = \tilde{\gamma} b_x \quad (3.51)$$

$$-(D_y^h, \mu_{zz}^{-1} D_y^e + \epsilon_{xx}) a_x + D_y^h, \mu_{zz}^{-1} D_y^e, a_y = \tilde{\gamma} b_y \quad (3.52)$$

we now convert the linear matrix equation into block matrix form as shown,

$$\begin{bmatrix} -D_x^e, \epsilon_{zz}^{-1} D_y^h & D_x^e, \epsilon_{zz}^{-1} D_x^h + \mu_{yy} \\ -(D_y^e, \epsilon_{zz}^{-1} D_y^h + \mu_{xx}) & D_y^e, \epsilon_{zz}^{-1} D_x^h, \end{bmatrix} \begin{bmatrix} b_x \\ b_y \end{bmatrix} = \tilde{\gamma} \begin{bmatrix} a_x \\ a_y \end{bmatrix} \quad (3.53)$$

$$\begin{bmatrix} -D_x^h, \mu_{zz}^{-1} D_y^e & D_x^h, \mu_{zz}^{-1} D_x^e + \epsilon_{yy} \\ -(D_y^h, \mu_{zz}^{-1} D_y^e + \epsilon_{xx}) & D_y^h, \mu_{zz}^{-1} D_y^e, \end{bmatrix} \begin{bmatrix} a_x \\ a_y \end{bmatrix} = \tilde{\gamma} \begin{bmatrix} b_x \\ b_y \end{bmatrix} \quad (3.54)$$

Where in we substitute,

$$\mathbf{P} = \begin{bmatrix} -D_x^e, \epsilon_{zz}^{-1} D_y^h & D_x^e, \epsilon_{zz}^{-1} D_x^h + \mu_{yy} \\ -(D_y^e, \epsilon_{zz}^{-1} D_y^h + \mu_{xx}) & D_y^e, \epsilon_{zz}^{-1} D_x^h, \end{bmatrix}$$

and

$$\mathbf{Q} = \begin{bmatrix} -D_x^h, \mu_{zz}^{-1} D_y^e & D_x^h, \mu_{zz}^{-1} D_x^e + \epsilon_{yy} \\ -(D_y^h, \mu_{zz}^{-1} D_y^e + \epsilon_{xx}) & D_y^h, \mu_{zz}^{-1} D_y^e, \end{bmatrix}$$

Therefore, we now can rewrite them as,

$$P \begin{bmatrix} b_x \\ b_y \end{bmatrix} = \tilde{\gamma} \begin{bmatrix} a_x \\ a_y \end{bmatrix} \quad (3.55)$$

$$Q \begin{bmatrix} a_x \\ a_y \end{bmatrix} = \tilde{\gamma} \begin{bmatrix} b_x \\ b_y \end{bmatrix} \quad (3.56)$$

For the final step to convert the equation into an eigen value problem we substitute b from equation 3.55 into the equation 3.56 and we get the following single matrix equation

as,

$$PQ \begin{bmatrix} a_x \\ a_y \end{bmatrix} = \tilde{\gamma}^2 \begin{bmatrix} a_x \\ a_y \end{bmatrix} \quad (3.57)$$

Where PQ can be replaced as some factor Ω^2 , therefore giving us the standard eigen value problem ($\lambda = \tilde{\gamma}^2$), that can be easily be solved using a simple function (eig() / eigs()) in matlab, in a manner such as $[V, D] = eig(A, B)$. Where V would provide with the eigenvectors that describes the mode of the amplitude profile and D describes the eigen-values representing phase accumulation. Eigs() function on the other hand helps to calculate all the modes with eigen-values close to the estimated effective refractive index.

3.4.2 Finite difference method

There are various numerical ways to analyse waveguides modes numerically. The most common technique used are Finite Element Method (FEM) and Finite Difference Method (FDM). Both these methods are equally powerful but the only difference is in their method of approach. Their main task is to solve complex differential equations. The FDM analyses the problem as a whole, solving the equation directly and reduces the complexity into a matrix form. Where as FEM lies more on a variation principle where it tries to minimize functions of the wave equation. In the scope of my thesis we will be focusing on FDM base mode matching method.

FDM was introduced by Stern in 1988 [157] with an idea of discretizing the wave equation (eigen value equations) into eigen value matrix equations. Where in the second order derivatives are approximated using three point difference scheme, where the discontinuity of the medium is matched by averaging the refractive index across the interface. As seen in the schematics of basic FDM strategy 3.8, we start with an equation having a continuous time derivative, where in store the function values at discrete points and we use finite differences to calculate derivatives, where we only know the functions at discrete points. The derivation

is found most commonly at the center of the two given points providing accuracy. The derivative of any order of a function at any given point can be approximated into a linear sum of known points of that function.

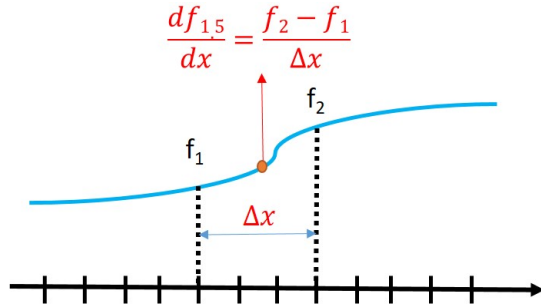


Figure 3.8: Basic Finite Difference Method

The finite difference [158] scheme can be applied to find the almost exact solution of mainly second order differentials and can be summarised graphically based on the various finite difference schemes.

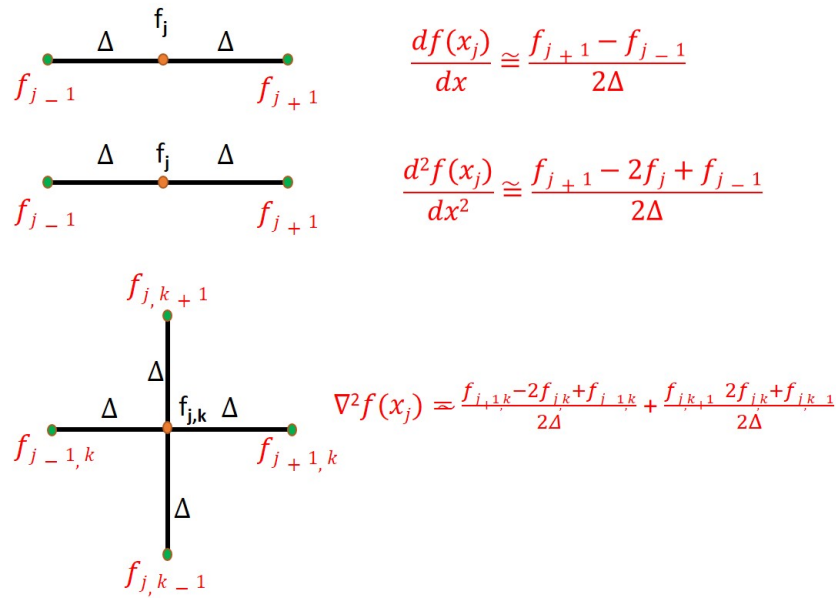


Figure 3.9: Finite Difference Method

We apply this technique in addition to Yee's grid [159], which discretize a given structure into finite cube blocks and adequately apply electric and magnetic components along the

vertices. These EM components are arranged in a manner such that it satisfies the Maxwell's divergence condition, follow the continuity and discontinuity of the EM components along the boundary conditions and provides an elegant arrangement to approximate Maxwell's curl equations. Together with these techniques we can accurately measure the EM field characteristics at each discrete points of the given photonic element structure. Following we show how using FDM and discretization using Yee's grid we can calculate modes of the waveguide numerically, thus getting a step closer toward realisation of the device.

In our case the grid mapping in terms of finite difference scheme have been performed such that we discretize the areas near the boundary of two interfaces and calculate more accurately the E and H fields, in contrast to commercially available mode solver which averages at the boundary. The schematics of which is given in the figure 3.10. The whole system is discretized into nine layers vertically along x axis and into six sections in horizontal y axis. This gives the accurate solution for effective refractive index and propagation constants on the order of 10^{-15} as opposed to an accuracy of 10^{-7} achieved by the commercial ones. The only down side is that the calculation is process intensive, hence it takes more time when imaginary part of the refractive index is added.

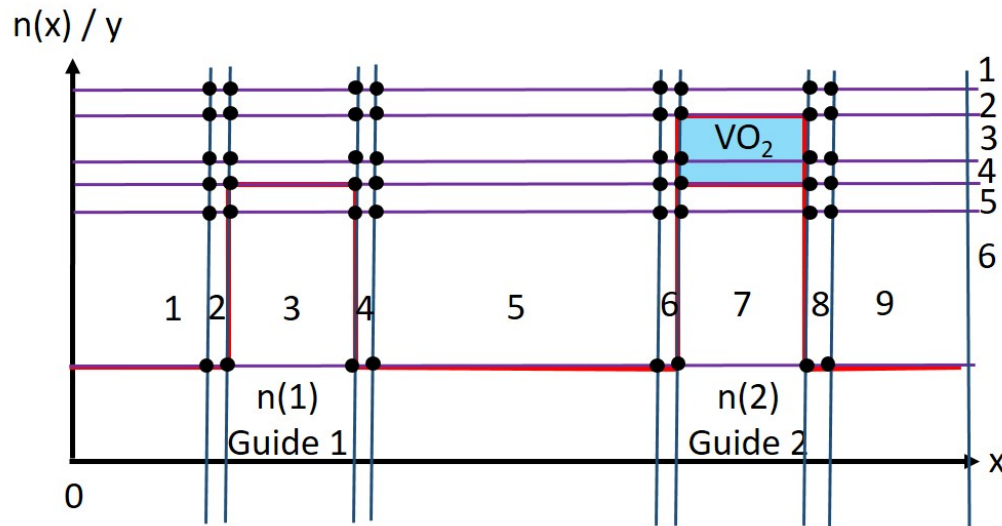


Figure 3.10: Finite difference scheme discretization of VO_2 waveguide modulator.

The eigen value problem in Matlab would return the following eigen values in the form $\lambda_i = \tilde{\gamma}_i^2$, which we solve for un-normalised γ_i , giving us $\gamma_i = k_o \sqrt{\tilde{\gamma}_i^2}$. Where in γ is represented as $\gamma_i = \alpha_i + j\beta_i$ such that, α ($\alpha_i = Re[\gamma_i]$) is the attenuation coefficient and β ($\beta_i = Im[\gamma_i]$) is propagation constant ($\beta = k_o n_{eff}$). Therefore we can finally calculate the effective refractive index as,

$$n_{eff} = \frac{\beta_i}{k_o} = Im[\sqrt{\tilde{\gamma}_i^2}] \quad (3.58)$$

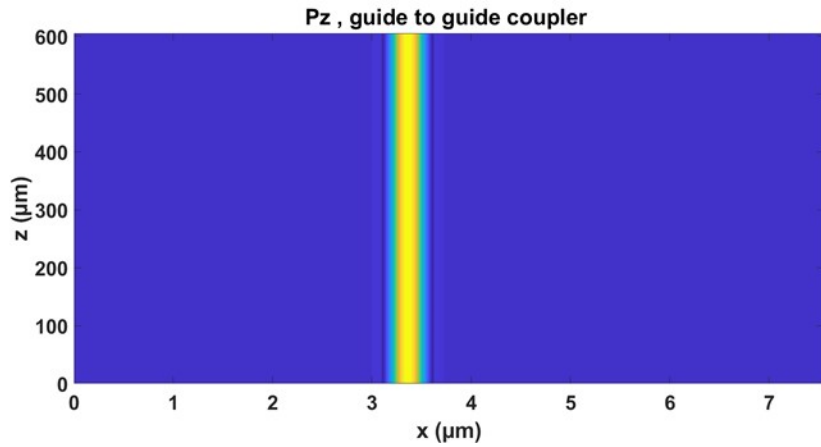
Thereafter, discretizing space and time so the electric and magnetic fields are separated in both space and time. We then solve the difference equations to obtain updated equations that express the unknown future fields in terms of known past fields. Using the updated equations enumerate future magnetic fields and future electric fields. We then keep repeating the steps until the result is acceptable. In our simulation, for defining the interfaces, we use the simplest method by overlapping orthogonal grids with different space steps [160]. For example, the space step around the nano-scale structure is small enough to describe its shape, whereas the space step in homogeneous space is bigger to obtain results in real time. The next section will focus on the simulations and the results thus obtained for the realization of the device followed by fabrication.

3.4.3 Simulation Results

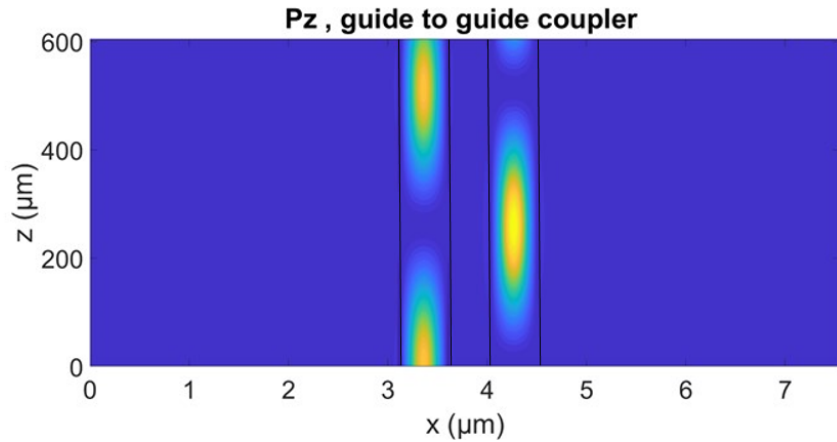
As stated before, when the propagation constants of the two waveguides are nearly the same, the Si waveguide and the VO₂ patched waveguide (VO₂ metallic state) satisfies the coupling condition and therefore an efficient optical power transfer between them takes place. Our task therefore consists in adjusting the dimensions of the two waveguides so their propagation constants match when VO₂ is metallic. Therefore, we calculate the effective refractive indices of the Si waveguide and VO₂ (at metallic state) patched waveguide at a wavelength of 1.55 μm by home made mode solver. The width and height of the bus Si waveguide were 530 nm and 220 nm, respectively. We set the height of VO₂ patch on top of

Si waveguide to 50 nm. In effectively making the height of VO₂-Si active hybrid waveguide to be (220 nm + 50nm) 270nm. The trick used here to quickly design the system and reduce computing time is that for the simulation, the *k* value of VO₂ is kept at 0. This was done such that the computational time for simulation is reduced.

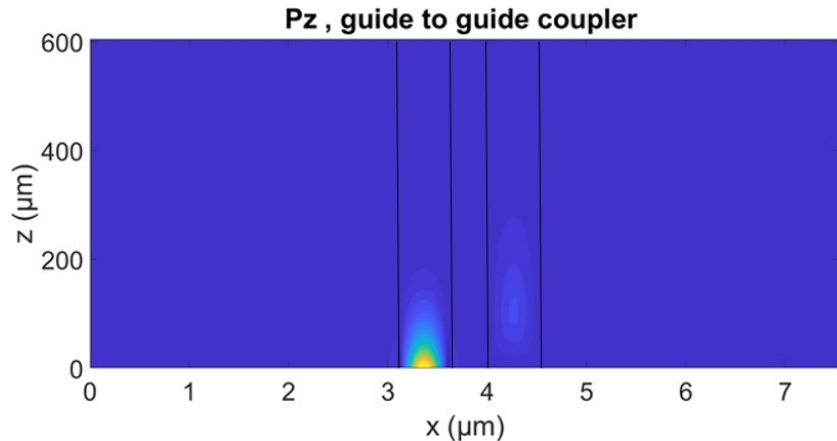
Following, in the figure 3.11, we see the synchronizing power transfer between two waveguides and the even and odd symmetric supermodes. In order to achieve the good coupling, the width of the VO₂ patched waveguide has to be determined such that the effective refractive indices of the two waveguides are nearly the same. The main complications involved with the correct width calculations for hybrid waveguide comes with high computational time when imaginary part of VO₂'s refractive index is included.



(a) *Simulation of wave propagation in bus waveguide when VO_2 is insulating.*



(b) *Co-directional coupling of wave in VO_2 patch waveguide when VO_2 is metallic without loss.*



(c) *Co-directional coupling of wave in VO_2 patch waveguide when VO_2 is metallic with loss.*

Figure 3.11: Top simulation view of wave propagation and modulation in the proposed device when VO_2 is insulating and when it is metallic (with and without loss).

In order to ensure good coupling condition, the width of the waveguide has to be

altered to match the perfect index condition. The high absorption value of VO_2 slowed the computational time, additionally the dimensions for best index match came at resolution of 1nm accuracy. This was beyond the scope of the fabrication facility available at the lab. After scores of the trials with cluster computations and reducing the computational step, we decided to create feasible device by keeping the imaginary part at 0. Such that, for experimental stand point we could dynamically change the input light properties and control the transition using the experimental setup to find the right working condition. Therefore the calculated width of the VO_2 patched waveguide is 510 nm at $k = 0$.

Efficiency of the modulation

In order to have an efficient modulation, as seen in figure 3.12 we need the Δn for optical switching between off/on states.

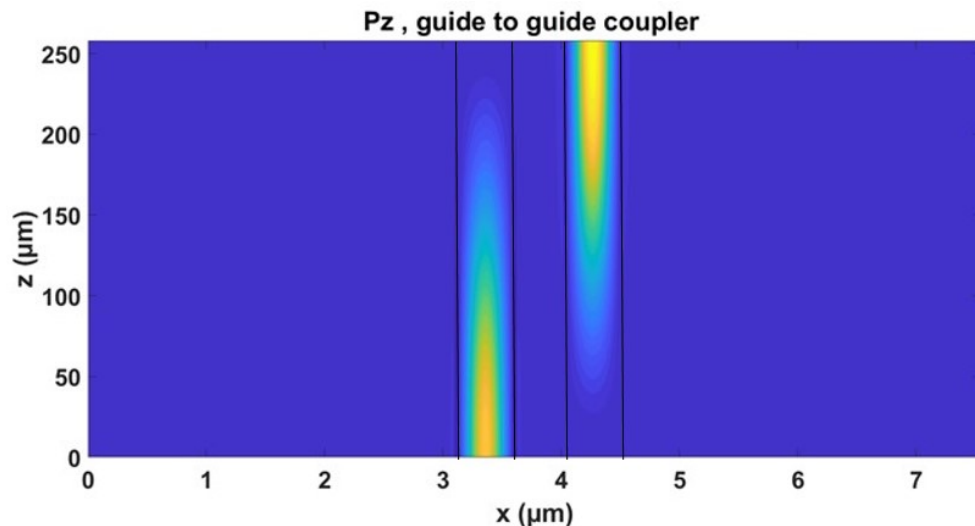


Figure 3.12: Efficient coupling of VO_2 waveguide modulator.

To obtain the switch efficiency and the spectral bandwidth of the modulator, we use a length of the modulator equal to L_c for a total transfer of light in the 2nd waveguide with VO_2 layer. The output power state of the output waveguide is 0. We change the refractive index of VO_2 in the metallic state, where the increase of $+\Delta n$ is required in order to simulate the

phase change material. The off/on switch variation versus Δn is obtained by plotting the power in the output waveguide versus Δn as seen in figure 3.13.

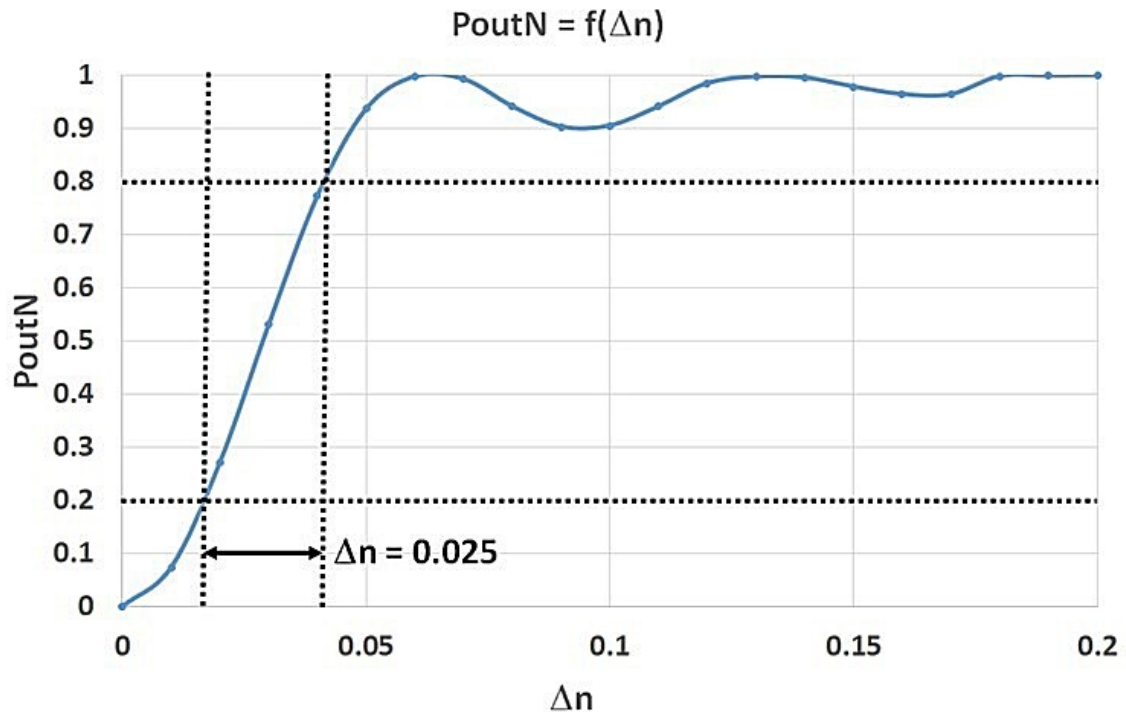


Figure 3.13: Evolution of the output power (P_{out}) versus the variation of the refractive index of the VO_2 layer.

Oscillations in the figure 3.13 are due to the fact that the coupling length changes when the refractive index of the VO_2 layer change. In the figure 3.14 we show the variation of the output power based on the variation in the wavelength. The curve is not symmetric because the coupling length changes with the wavelength as the effective indices and profiles of the modes change with the wavelength.

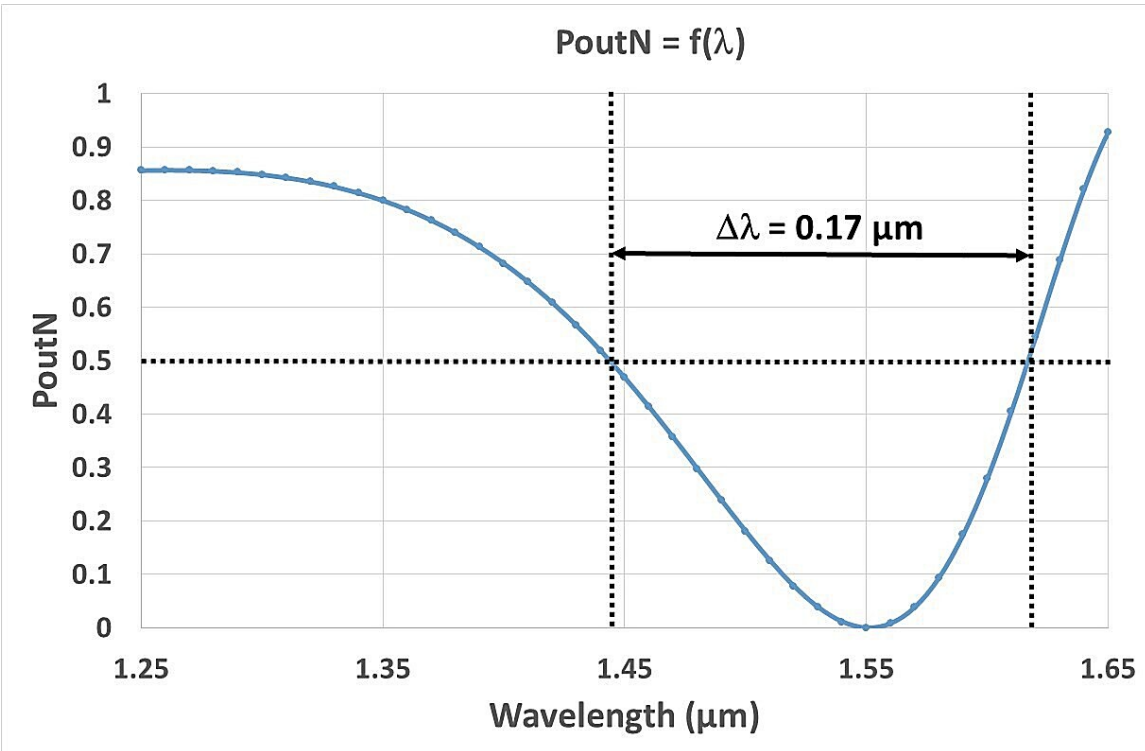
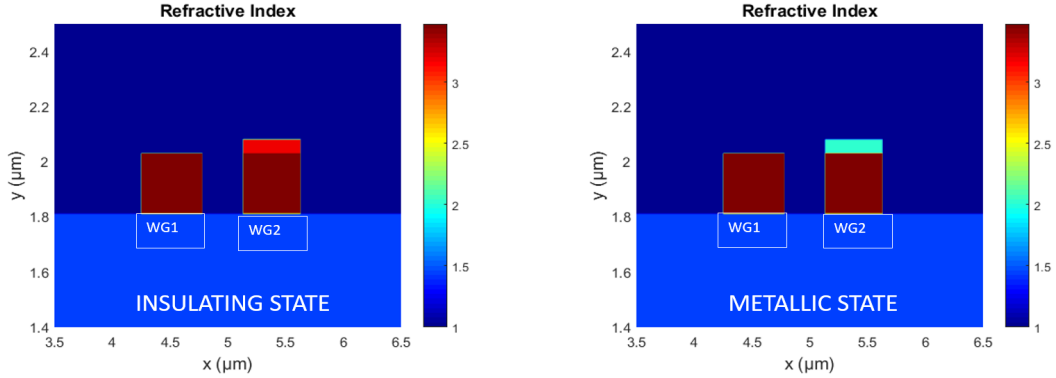
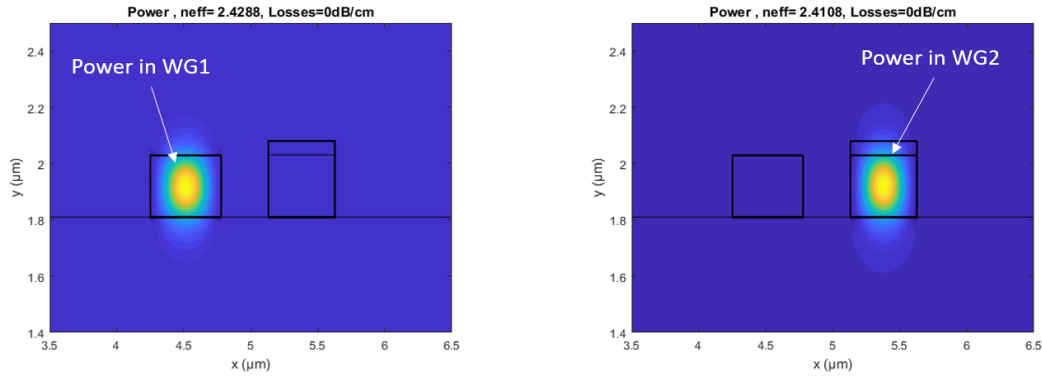


Figure 3.14: Evolution of the output power (P_{out}) versus the variation of the wavelength with losses.

In the following simulation figures 3.15, we see the schematic cross-sectional view of the coupler section and we observe the coupling of the wave in the VO_2 patch upon its insulator-metal transitions. We calculate the power in each waveguide thus simulated by mode matching and calculate the power transfer as a function of change of phase in VO_2 , table 3.1. The power calculation is an integration of all the field at an area close to the core of the waveguide.



(a) Device design when VO_2 patch is dielectric. (b) Device design when VO_2 patch is metallic.



(c) Simulated incident wave power in bus waveguide. (d) Simulated incident wave power in hybrid waveguide.

Figure 3.15: Schematic cross-sectional view of the coupler section in the optical device as simulated with light modulation as function of transition in VO_2 .

VO_2 state	Insulating	Metallic
Refractive Index	$3.243 + 0.25367i$	$2.02 + 2.9393i$
Power in bus waveguide	100%	0%
Power in hybrid waveguide	<1%	80%

Table 3.1: Power transfer simulation calculated around the core area of the waveguide. 80% of the input power is calculated at the central area of the core, rest is dissipated at the edges of the waveguide.

In the simulation, we observe a modulation depth of $9\text{dB} - 10\text{dB}$, similar to previous architecture [36]. With all the parameters thus obtained the only remaining value to be calculated is the coupling length which itself is proportional to the gap or the distance between the coupling waveguide. To isolate the optimized coupling length (L_c) which

provides maximum optical power transfer, the whole structure of the coupler section must be analyzed. L_c is a function of the difference between the propagation constants of the even and odd supermodes,

$$L_c = \frac{\pi}{(\beta_{even} - \beta_{odd})} = \frac{\lambda}{2(n_{even} - n_{odd})}$$

where λ is the wavelength, and n_{even} and n_{odd} are the effective refractive indices of the even and odd supermodes, respectively. Similarly L_c can also be highly dependent on the distance between the co-directional waveguides which are responsible for the coupling. As we see in figure:3.16, the couplers with a wider separation gap require a longer coupling length due to a slight propagation constant difference between the even and odd supermodes. For a much larger gap (>380 nm), the mode coupling between the two waveguides becomes weak, as we see below.

Parameters	Value Simulated
Height of Waveguide 1	220nm
Height of Waveguide 2	220nm
Height of VO_2 patch	50nm
Width of Waveguide 1	530nm
Width of Waveguide 2	510nm
Gap between the waveguides (Varying)	$350\mu m, 400\mu m, 450\mu m, 500\mu m$

Table 3.2: Geometric parameters for VO_2 waveguide modulator.

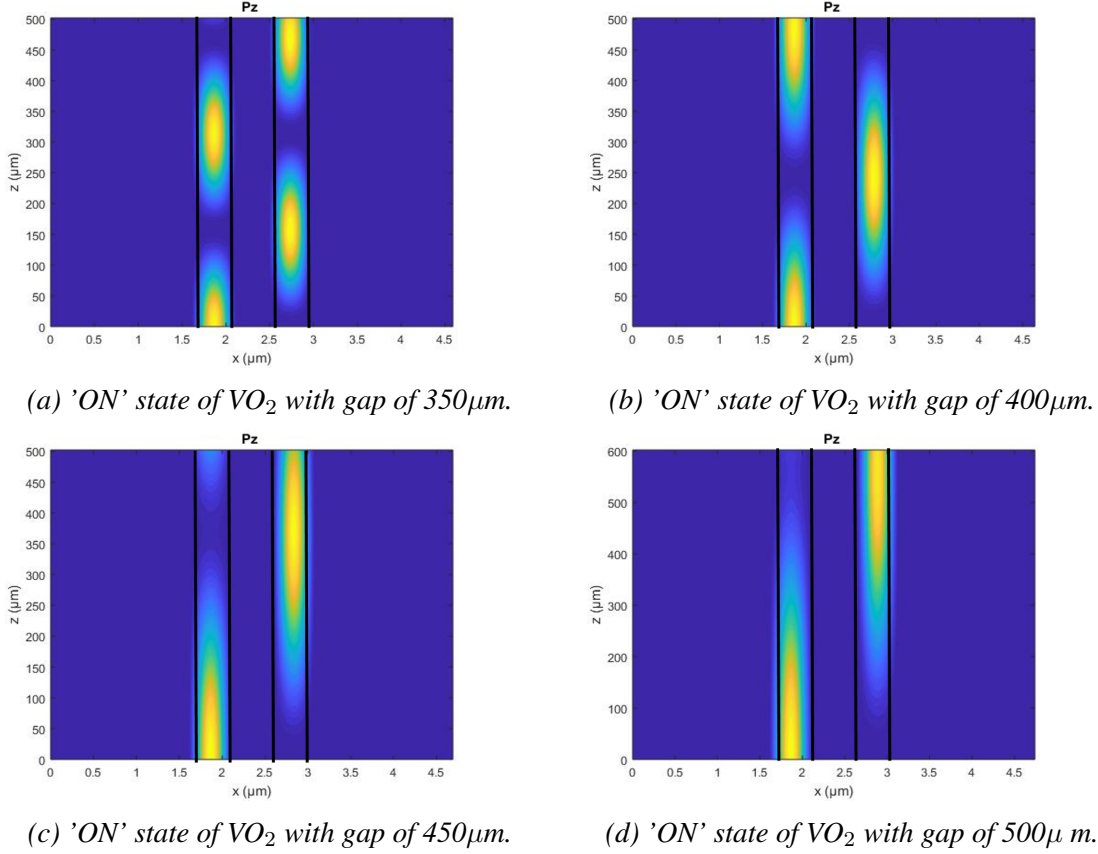


Figure 3.16: Intensity of the guided mode as a function of position along the device.

In figure 3.16 above, we see the changes in the coupling length parameters L_c as a function of distance or gap between them. Based on our simulations we plan to fabricate four different modulators with similar design parameters where the only varying parameter is the gap between the two waveguides. In the following, we will talk about the fabrication steps thus undertaken to achieve the device based on the simulated results.

3.5 Fabrication

As outlined before fig3.1, the initial sample consists of a VO_2 thin-film of 50nm deposited on a standard 220nm thick SOI substrate.

Following the steps of fabrication, the first lithography step defined both the waveguide structures. In order to define the structure, ZEP 520A resist was spun and pre-baked and

then the pattern was exposed using e-beam lithography system and then later developed. The mask was made in house and the whole lithography procedure was led by P. Romeo. After defining the patterns, we performed SEM imaging Fig3.18, in order to verify a successful pattern transfer and we observed a perfect pattern transfer and accurate waveguide gap distinction. The next step was to perform etching using RIE-ICP (Inductively Coupled Plasma Etching (ICP)) using a mixture of Ar and Cl₂ at room temperature. The formulation for etching recipe was done in house and the etching procedure was performed by C. Chevalier. After the etching procedure, we performed a SEM imaging in order to visualise the etched pattern. The SEM imaging revealed that contrary to the fabrication sketches, there were multiple imperfections following the fabrications.

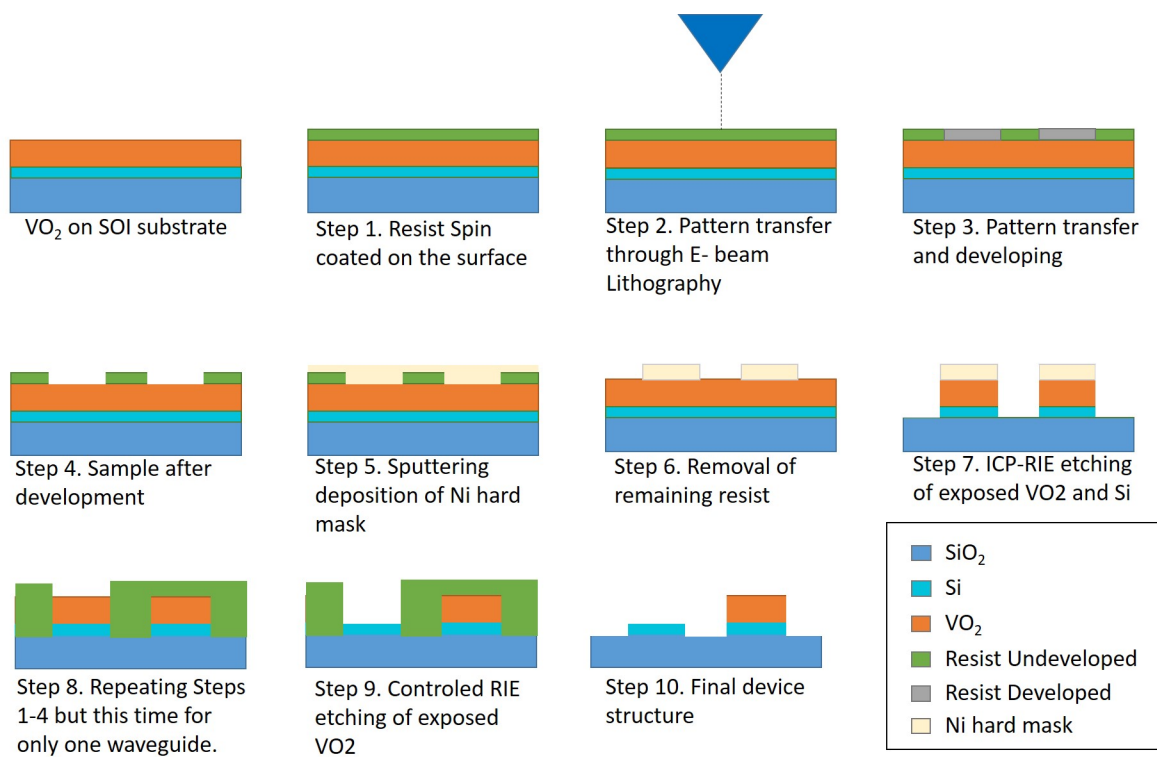


Figure 3.17: Fabrication steps involved for the realization of VO₂ modulator

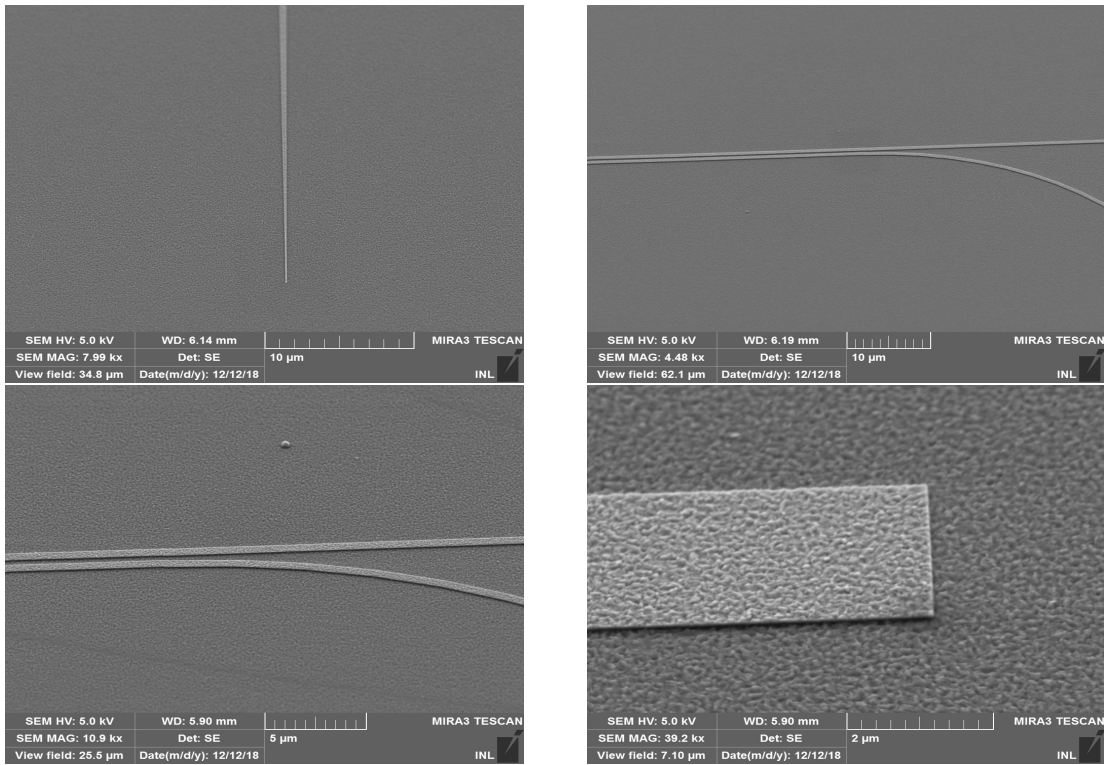


Figure 3.18: SEM image of patterned hard mask before the first ICP etching.

In direct comparison with before (fig:3.18) and after (fig:3.19) SEM imaging, we observe the inconsistency on the sample surface. Since we can almost distinguish the different waveguides, one can assume that the inconsistency could be either due to resists or mask residues on the top surface of the patterned waveguides. Indicating that the process must have been incomplete, leading to resist residue or the etching might have etched the metallic mask (reaching the VO₂) contrary to what was expected due to the low etch rate in the hard mask covered region.

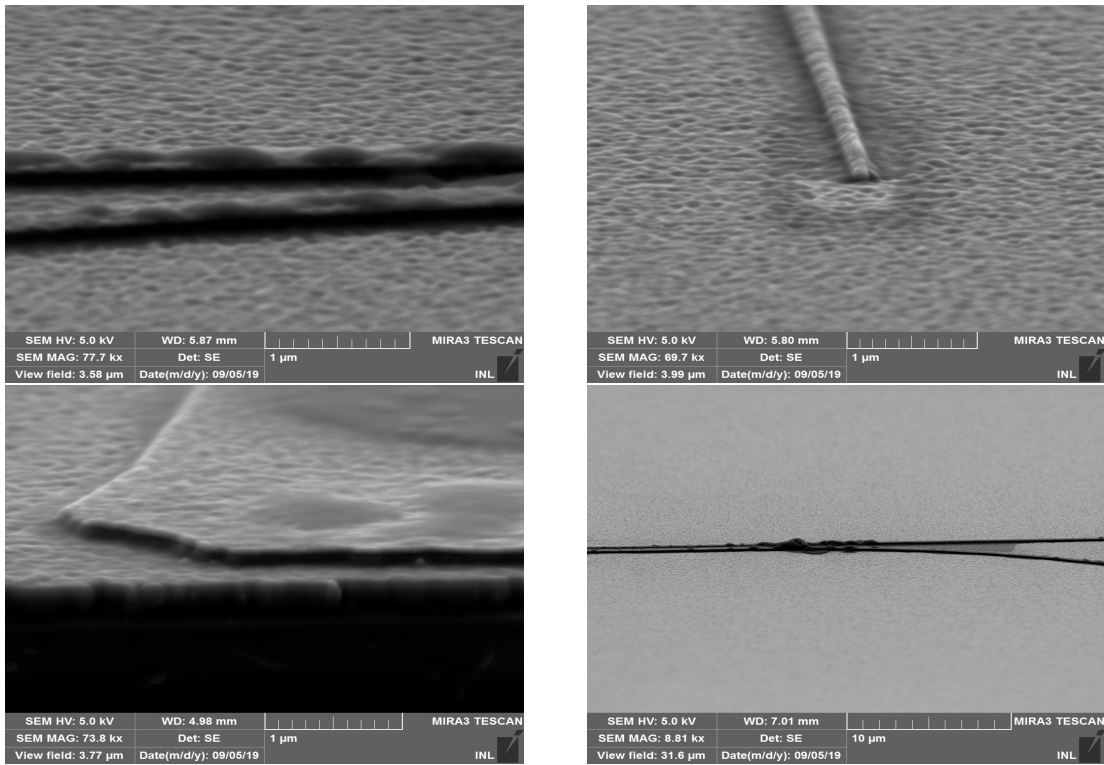


Figure 3.19: SEM image of patterned hard mask after ICP etching.

3.5.1 Discussion

The primary results of the fabrication can be considered as clearly not optimized. Contrary to what was expected, the metallic mask and the resist either got completely etched thus leading to residual effect on the surface. In order to recuperate the device, it is necessary to analyse the sample thoroughly and understand the chemical composition on the surface topography. This would pinpoint the material composition which would help us understand the etching failure stage. Secondly, performing a topographical study by AFM could give information about the roughness. Following the characterisation, we could proceed in caution with further etching and cleaning process in the hope of recovering the device. While on the other hand, we could rely on in house deposition technique to grow VO₂ and re-fabricate with bottom-up approach, where in VO₂ patch is directly grown on already designed Si waveguide.

3.5.2 Use of this modulator as a partial power transfer

The emergence of machine learning and artificial intelligence has opened up a new avenue for optical modulators. In that field, VO₂ could play a major role, leveraging its multi-level stages of phase transition. Following additional simulations as shown below fig:3.20, we could see its potential applications as a partial power filter using intermediate stages of VO₂ state transition as shown in figure 3.21. Power in core 1 denotes the original wave power being transferred in the bus waveguide. As we slowly switch the VO₂ on the hybrid waveguide, the refractive index of the material at dielectric state gradually switches towards metallic value, thus affecting the coupled power transfer efficiency [36]. The transition at later stages will be electrically assisted thus having finer control of the transitions.

We foresee that this dynamically controlled power transfer can act as a weight bank, which is one of the main functions performed by an algorithm in a neural network. And neural network is the core for the development of machine learning technologies and artificial intelligence. The optical modulation supported by our modulator design could aid in realising an all-optical neural network, propelling the computation capacity bottle-necked by our current transistors.

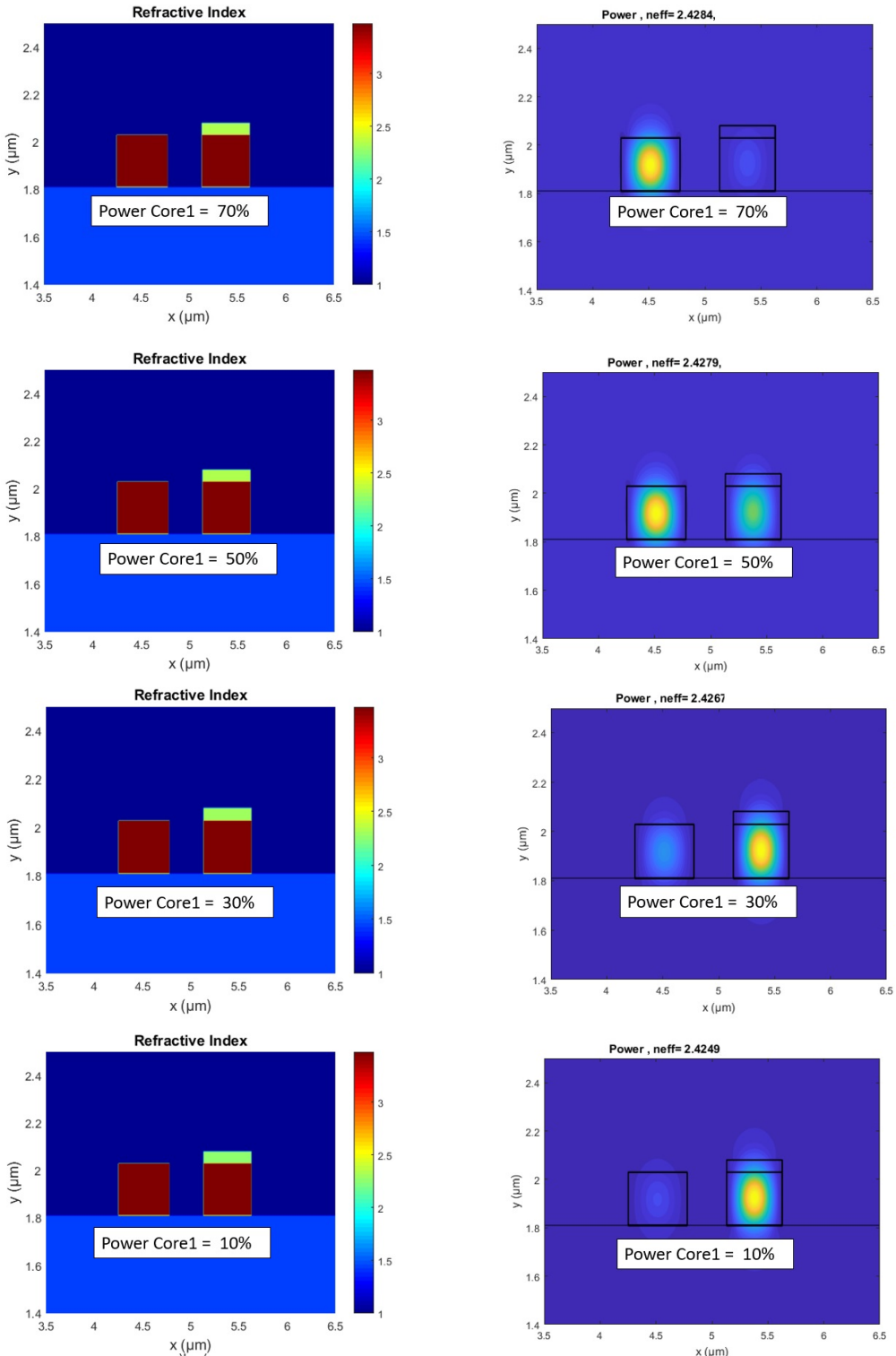


Figure 3.20: Simulation for VO_2 waveguide modulator as partial power filter using the intermediate state of VO_2 transitions.

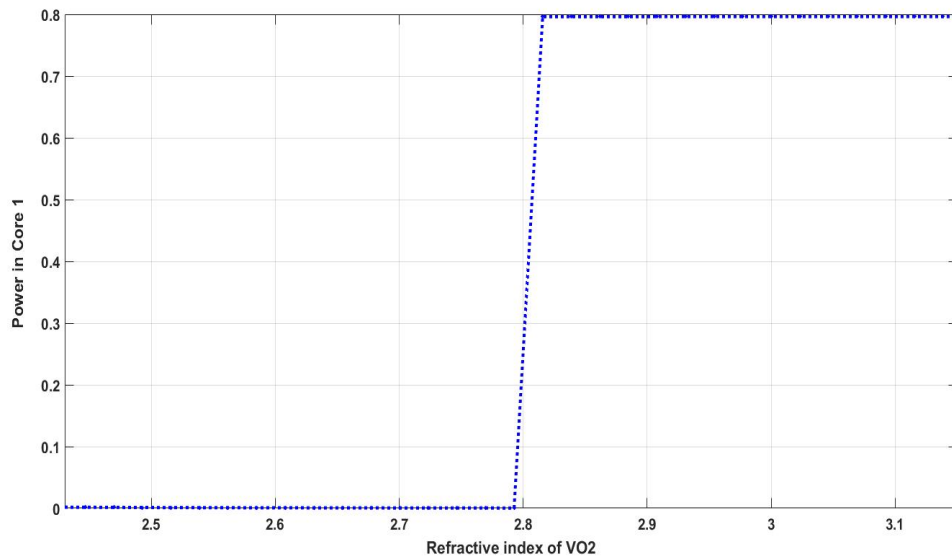


Figure 3.21: Gradual power variation in the bus waveguide (Core 1) as function of changing refractive index.

3.6 Conclusion

Our presented VO_2 based waveguide modulator, if fabricated successfully can be a great component for future integrated systems. The simulations for the modulators show that, compared to classical modulators, a simple trigger (optical, electrical or thermal) can have a profound impact on the transmission values in the bus waveguide. In opposition to the high absorption based VO_2 devices, this device architecture is compatible with CMOS technology and can be cascaded with low absorption loss. In future works, we plan to realise the device, overcoming the fabrication hurdles and obtain experimentally the modulation performance of the device.

Furthermore, in regard to the controlled power transfer filter, it find its usefulness in the creation of artificial all-optic neural networks (AONN), specifically as a weight bank. It is an emerging field with groundbreaking applications in improving Machine learning circuit and in sense for Artificial Intelligence (A.I) advancements [161]. In the previous decade the Neural network technology were dependent on electrical circuit / transistors for logic

operation. Followed by increased demand, the neural training networks are systematically switched to optical circuits, component by component. One of the most important of them are the weight banks. The electrical circuits used resistance as a weight to change the current in a electrical circuit. Optical weight banks depend on the absorption of an input light and amount of non-absorbed light that is detected is considered as weight.

The optical neural network system currently uses classic MZI passive modulators [162, 163] which are larger in size and limited tunability. Thus VO₂ seems to a hopeful replacement and efficient candidate, and also since the VO₂ tunability can be triggered in multiple ways, therefore future devices can use electrical or optical stimulus to trigger the transition states of VO₂ performing at much shorter timescales. Our modulator is quite broadband compared to the ring resonators in these linear modulators, which requires extremely precise wavelengths to function

CHAPTER 4

MULTIPOLAR RESONANCES WITH DESIGNER TUNABILITY USING VO₂

PHASE-CHANGE MATERIALS

4.1 Introduction

Engineering materials to accurately manipulate light has been the forefront of most of the recent technological advancement in optics. Light interaction and propagation within finite-size particles has been a topic of research for decades and is still the basis for a wealth of interesting new physical phenomena. Indeed, the most unusual fact is that such a classical topic is still the foundation for many fundamentally new and unexpected scientific and technological advances like loss-free negative-index metamaterials [164, 165], zero-index materials [45, 46, 47], invisibility cloaking [48, 49]. With the advancement in nano-science and nano fabrication techniques, new nano-objects are now available for the enhancement and control of light-matter interaction at the nanoscale [84, 85, 66].

The unique optical properties of metamaterials are derived from engineering their multipolar resonances in subwavelength structures. Therefore, knowledge of the underlying behavior of these multipolar resonances is essential for a variety of metamaterial applications [88, 89]. In dielectric metamaterials [78], supported resonances are a combination of electric and magnetic dipoles. Mie [39] in 1908 formulated the solutions for radiating and internal fields supported by the dielectric medium. These solutions were useful to understand and calculate the exact contribution of each modes of the nanostructure and to calculate the field distribution inside it.

These man-made Mie-resonance based metamaterials are static devices, with properties fixed after the fabrication process. It is therefore currently a great challenge to find efficient means to dynamically modulate such photonic devices at the nanoscale [166, 167]. One

such approach to induce tunability is to use phase transition materials like VO₂ [73, 168, 169, 74]. Recently similar strategies have been used to demonstrate phase modulation [170], tunable optical absorption [171, 172] or switchable dielectric-plasmonic regimes [173] in nanophotonic devices.

The starting idea of this chapter is to reduce the dimensions of VO₂ structures down to sizes comparable to the wavelength of operation, in order to tailor the electric dipole (ED) and magnetic dipole (MD) Mie resonances supported by these crystals. The IMT of VO₂ could then be used as an additional degree of freedom to dynamically tune the ED and MD resonances of this correlated system.

Here, we experimentally demonstrate the multipolar resonances supported by VO₂ nanocrystals (NCs) can be dynamically tuned and switched thanks to the IMT of VO₂. Using both Mie theory and Maxwell-Garnett effective medium theory, we retrieve the complex refractive index of the effective medium composed of a slab of VO₂ nanospheres embedded in SiO₂ and show that such a resulting metamaterial presents distinct optical tunability compared to unpatterned VO₂. But more importantly, we show in the following that this metamaterial approach enables designing tunable composite metamaterials presenting a refractive index modulation without induced extinction, or in other words a zero-induced extinction phase-change metamaterial. The following section explains the theory and concepts and is followed by a section explaining the fabrication and characterization techniques involved with the VO₂ NCs.

4.2 Mie theory for wavelength-scale particles

When an object is illuminated by an electromagnetic wave, it reradiates parts of the energy while being lost from the original wave. The nature, shape and the size of an object highly influences the quantity and the direction of light that is scattered [174]. The complexity of scattering analysis increases substantially when the size of the object approaches the wavelength of the incident wave. In such a situation, we can no longer assume the field to

be constant within the object and therefore the so-called "long-wavelength approximation" ceases to apply, and retardation effects must be considered. Accordingly, in order to compute the scattered field for such an arbitrary object, one would require a numerical approach. Such a complex problem can however be simplified if the object is a sphere. In 1908, Mie found an exact solution to the problem, by calculating the scattered field as a series solution [39]. The idea was to expand the electric and magnetic fields in terms of vector spherical harmonics. Then the field functions can be represented in a linear combination of terms that are products of separable functions of the three spherical coordinates.

Mie scattering theory indicates that light scattered by small (relative to the incident wavelength of light) spherical particles can be considered to consist of partial waves radiated by constituent electric charges of the spherical particle. The amplitude of these partial waves are central to Mie's solution and the coefficients terms are given by a_n and b_n . Where a_n denotes the amplitude of the n^{th} electric partial wave and b_n is the amplitude of the n^{th} magnetic partial wave. They are expressed numerically in the form of [175, 78, 176]:

$$a_n = \frac{\psi_n(x)\psi'_n(mx) - m\psi'_n(x)\psi_n(mx)}{\xi_n^{(1)'}\psi'_n(mx) - m\xi_n^{(1)'}(x)\psi_n(mx)} \quad (4.1)$$

$$b_n = \frac{\psi'_n(x)\psi_n(mx) - m\psi_n(x)\psi'_n(mx)}{\xi_n^{(1)'}\psi_n(mx) - m\xi_n^{(1)}(x)\psi'_n(mx)} \quad (4.2)$$

Where m is the complex refractive index, x is the size parameter ($x=\frac{2\pi mR}{\lambda}$) and the prime symbol ('') represents the derivatives in terms of the arguments of the function. And $\psi_n(z)$ and $\xi_n^{(1)}(z)$ are the Riccati-Bessel functions defined in terms of the spherical Bessel functions (z) [176, 177].

The electromagnetic interaction of light with spheres can then be modeled following the Lorenz-Mie formalism for scattering and absorption of light by small particles [40]. Within this formalism, the extinction, scattering and absorption efficiencies are given by:

$$Q_{sca} = \frac{2}{x^2} \sum_{n=1}^{\infty} (2n+1)(|a_n|^2 + |b_n|^2) \quad (4.3)$$

$$Q_{ext} = \frac{2}{x^2} \sum_{n=1}^{\infty} (2n+1)Re(a_n + b_n) \quad (4.4)$$

$$Q_{abs} = Q_{ext} - Q_{sca} \quad (4.5)$$

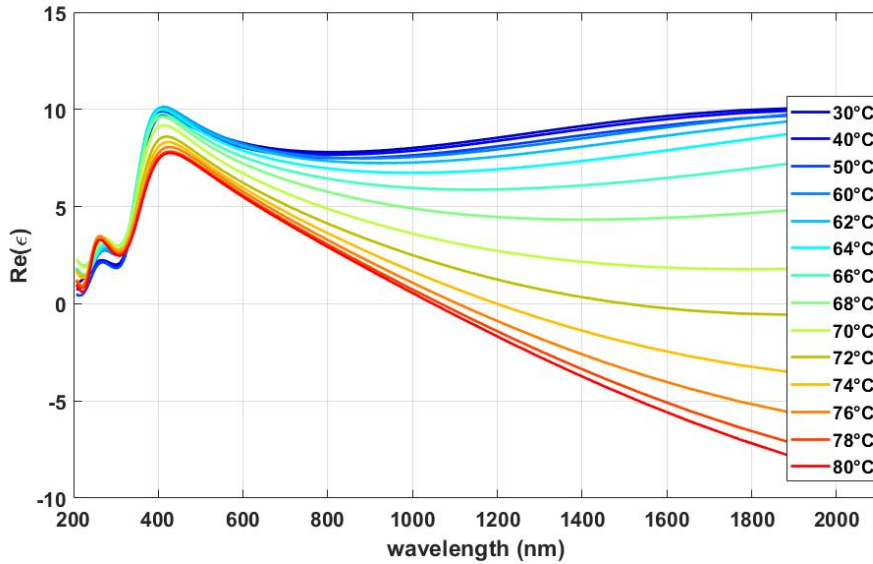
where a_n and b_n are the so-called scattering coefficients [40]. These depend on both the particle optical properties (relative to its surrounding medium) and size. Whereas the size parameter x is defined as

$$x = \frac{2\pi m_{med} R}{\lambda}$$

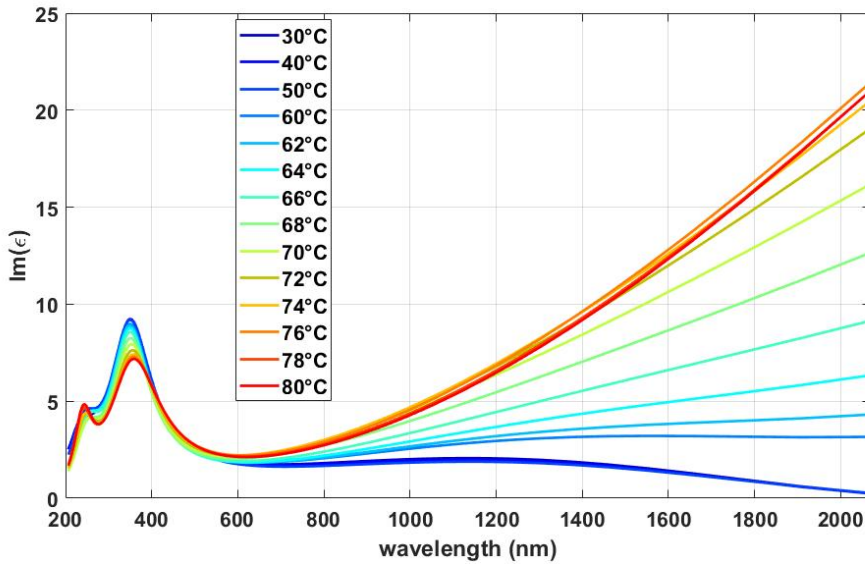
wherein m_{med} is the refractive index of the surrounding medium, λ the wavelength of the incident light in vacuum and R the sphere's radius. Materially, a_n and b_n are the weighting factors of the different excited electric and magnetic multipolar contributions. For example, a_1 and b_1 represent the electric and magnetic dipolar modes, and a_2 and b_2 correspond to the electric and magnetic quadrupolar modes, respectively.

4.3 VO₂ Nanocrystals: Theory

Figure 4.1 shows the real and imaginary part of the dielectric permittivity of a VO₂ thin-film in the Vis/NIR range as a function of temperature, as obtained by ellipsometry characterization and modelling of VO₂ thin film.



(a) Real part of the dielectric permittivity.



(b) Imaginary part of the dielectric permittivity.

Figure 4.1: Real and imaginary part of the dielectric permittivity ϵ of a VO_2 thin-film in the Vis/NIR range as a function of temperature.

Figure 4.2 shows the absorption cross section Q_{abs} of a VO_2 sphere of radius 50 nm in its insulating and metallic states embedded in fused silica ($m_{med} = 1.45$ for $\lambda = 1 \mu\text{m}$). The colored lines represent the contributions of dipolar electric a_1 , dipolar magnetic b_1 , quadrupolar electric a_2 and quadrupolar magnetic b_2 to Q_{abs} (absorption cross section).

We note that, regardless of the state of VO_2 , below 700 nm the electromagnetic response is dominated by the dipolar electric (ED) and magnetic response (MD), with a small contribution of the quadrupolar electric term (QE).

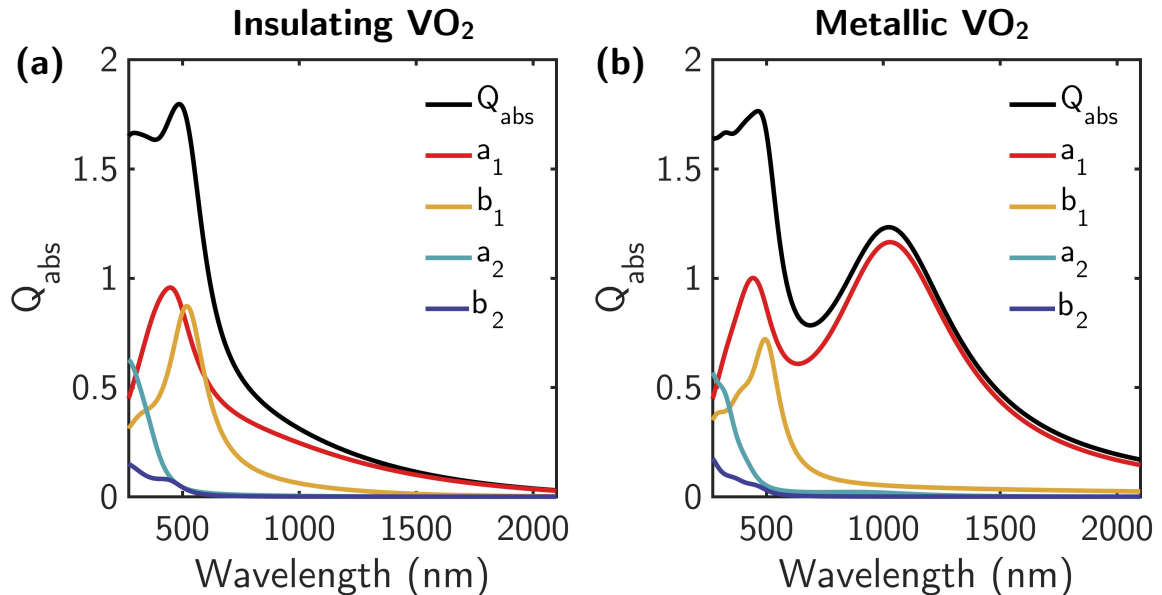


Figure 4.2: Calculated absorption efficiency of VO_2 spheres with radius 50 nm in their a) insulating and b) metallic states embedded in quartz. With colored lines are represented the dipolar electric a_1 (red), dipolar magnetic b_1 (yellow), quadrupolar electric a_2 (light blue) and quadrupolar magnetic b_2 (dark blue) contributions to Q_{abs} .

These resonances correspond to Whispering Gallery Modes (WGM) which resonate at the suitable wavelengths, the magnetic resonance redshifted with respect to the electric one [178]. On the other hand, when VO_2 is in its metallic phase, a DE resonance appears at a longer wavelength (1015 nm). The intensity of this resonance directly depends on the temperature, i.e. the higher the temperature, the more the metallic character and consequently the higher is the intensity of the resonance. This resonance is plasmonic and its physical origin is the negative value of the dielectric constant above 1000 nm in the metallic phase.

An ensemble of VO_2 nanospheres would therefore enable a dynamic tunability of multipolar resonances collectively [179] and to actively control the presence and the intensity of a plasmonic mode in the NIR.

4.4 VO₂ Nanocrystals: Fabrication and Characterization

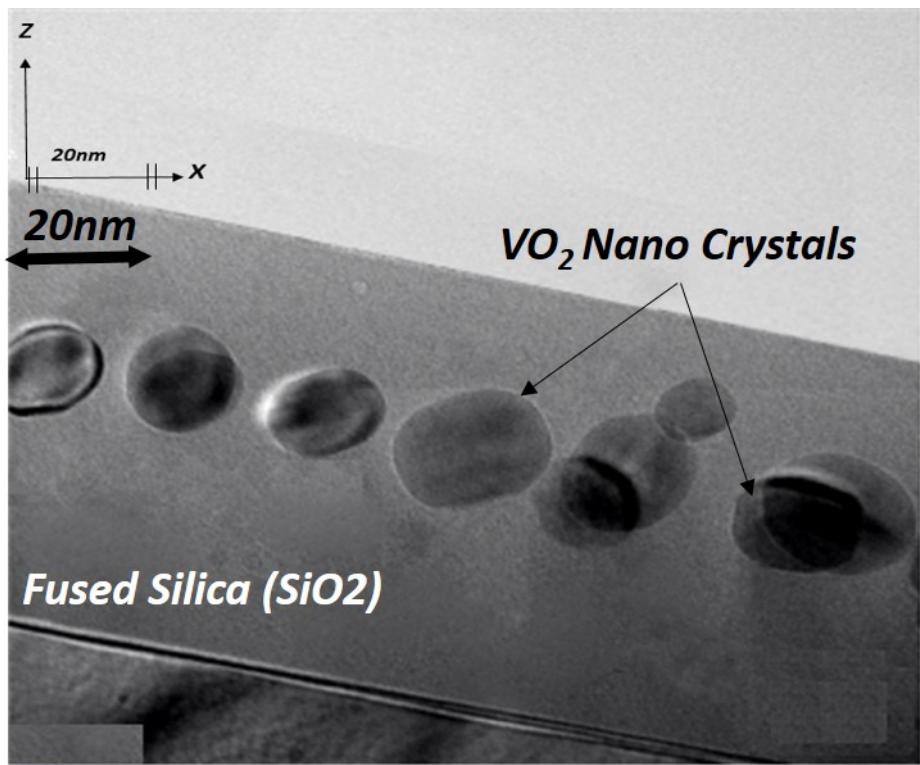
4.4.1 Fabrication

Reports on the synthesis and characterization of VO₂ NCs were first published in 2002 [180, 181], followed by studies on their nonlinear optical properties [182] in 2004 and their potential for ultra-fast modulation of optical transmission [183] in 2005.

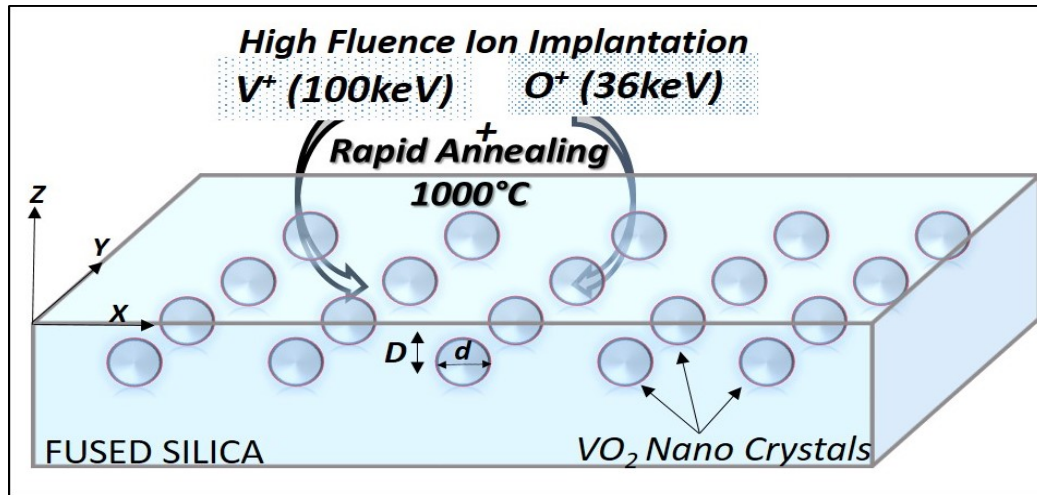
Here, the synthesis of a dense layer of isolated VO₂ nanocrystals embedded at about 100 nm depth below the surface began with a high fluence ion implantation of V⁺ and O⁺ with energies of 100 keV and 36 keV, respectively. These energies were chosen to produce overlapping concentration depth profiles of the elements. The formation of the VO₂ chemical compound was controlled by the fluence ratio of V to O (i.e. $8 \times 10^{16} \text{ cm}^{-2}$ to $1.6 \times 10^{17} \text{ cm}^{-2}$ and $4 \times 10^{16} \text{ cm}^{-2}$ to $8 \times 10^{16} \text{ cm}^{-2}$ for a ratio of 1:2). After ion implantation, nanocrystal growth was initiated by a rapid thermal annealing (RTA) step at 1000°C for 10 min in an inert gas at atmospheric pressure [184, 185]. The samples of VO₂ NCs were obtained from Prof. Dr. Helmut Karl, affiliated with Lehrstuhl für Experimentalphysik IV, Universität Augsburg (Germany). A 3D sketch representing a cross-sectional top view of the VO₂-NCs implanted in SiO₂, together with a TEM image of the VO₂-NCs layer is shown in figure 4.3b.

4.4.2 Characterization

We analysed the optical properties and the IMT of VO₂-NCs using a spectroscopic ellipsometer (UVISEL plus Horiba), ranging from 250 nm to 2100 nm. The system is coupled with a heating cell to thermally induce the IMT. The incident broadband light source is a Xenon lamp polarized at 45°. After reflection off the sample under study, the light is directed to a spectrometer, dispersed by appropriate gratings and measured with UV/Vis and NIR detectors. The acquired ellipsometric parameters *I_s* and *I_c* of the samples have been collected for varying angles 55° - 75° over a spectral range of 260 - 2100 nm. The



(a) TEM image of the VO₂-NCs in fused silica.

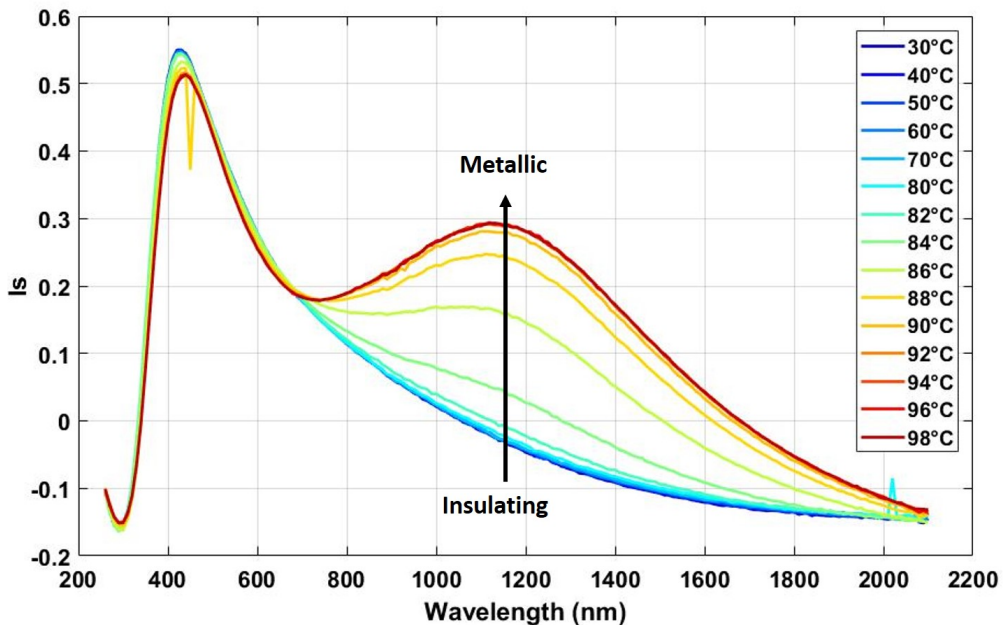


(b) 3D sketch representing a cross-sectional top view of the VO₂-NCs and deposition procedure.

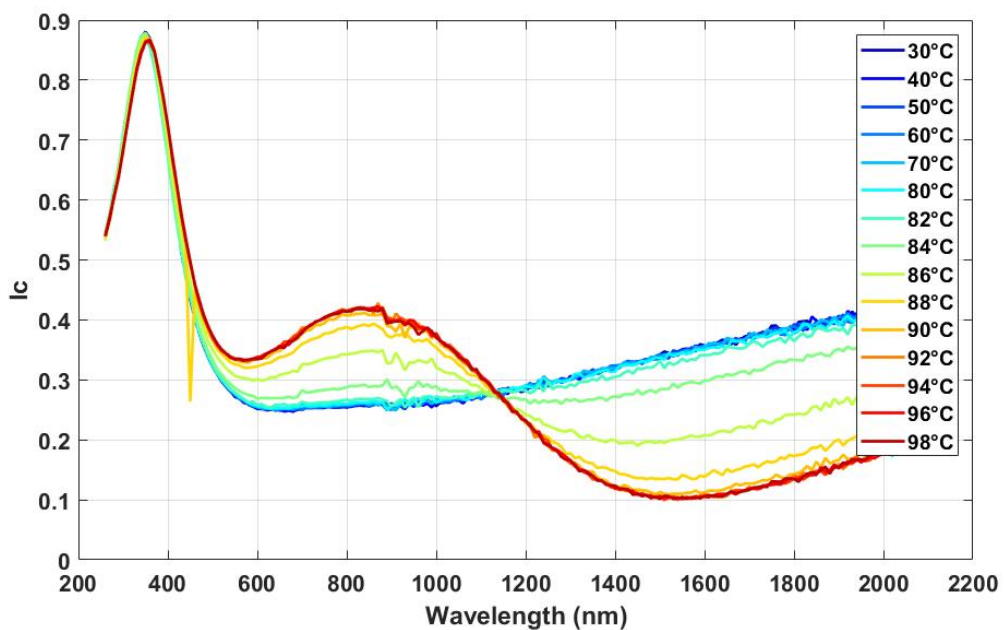
Figure 4.3: VO₂ NCs TEM image (top) and sketch (bottom)

acquisitions were carried out in a range of temperatures from 30°C to 80°C using a digitally controlled heat cell (Linkam THMSEL350V) in order to analyse the temperature-dependent optical properties of the sample under study.

Figure 4.4 shows the evolution of the I_s and I_c parameters of ellipsometry measurements



(a) I_s parameter.



(b) I_c parameter

Figure 4.4: Evolution of ellipsometric parameters I_s and I_c measured as a function of temperature. The acquisition was performed on VO_2 NC at an incident angle of 65°

as a function of temperature. The effect of the IMT of VO_2 -NCs is clearly observable on the raw ellipsometry measurements, with the appearance of a large peak in I_s whose intensity progressively increases around 1100 nm. This phenomenon is reversible, with a broad hysteresis behavior, as seen in Fig.4.5, and is a clear signature of the presence of stoichiometric VO_2 in the sample.

It is interesting to measure the real time dynamics of the IMT of VO_2 -NCs using the kinetic mode of our ellipsometer. In the kinetic mode, ellipsometric data are acquired every 200 ms at a fixed wavelength (in this case 1200 nm). Here, the kinetic data are shown (Fig: 4.6) during the evolution of phase change VO_2 -NCs by actively mapping the change in dielectric function (denoted by the component I_c). The heat cell is automatized to gradually increase the temperature at a given rate 1°C/min, the acquisition ranged from 23°C (room temperature) to 150°C. The hysteresis behavior as a function of temperature is shown in Fig.4.5, where the difference between the heating (red) and cooling (blue) cycles are put into evidence. The hysteresis loop is large, (differences in switching temperatures between heating and cooling 35°C), as expected from VO_2 -NCs, since it is an inherent property of VO_2 resulting from the structural changes during the transition.

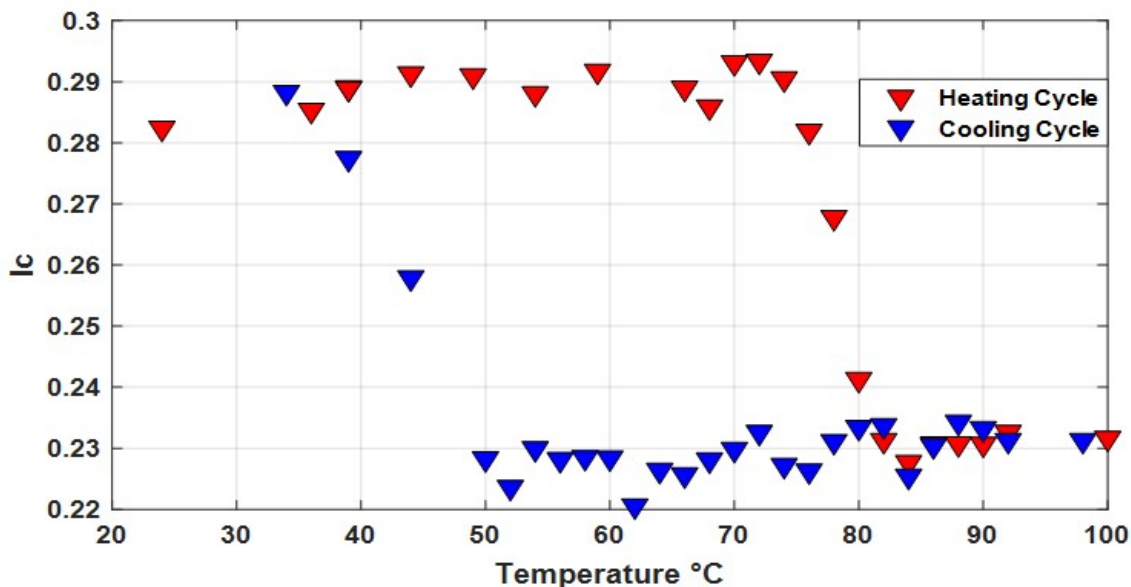


Figure 4.5: Thermal Hysteresis loop of VO_2 NCs.

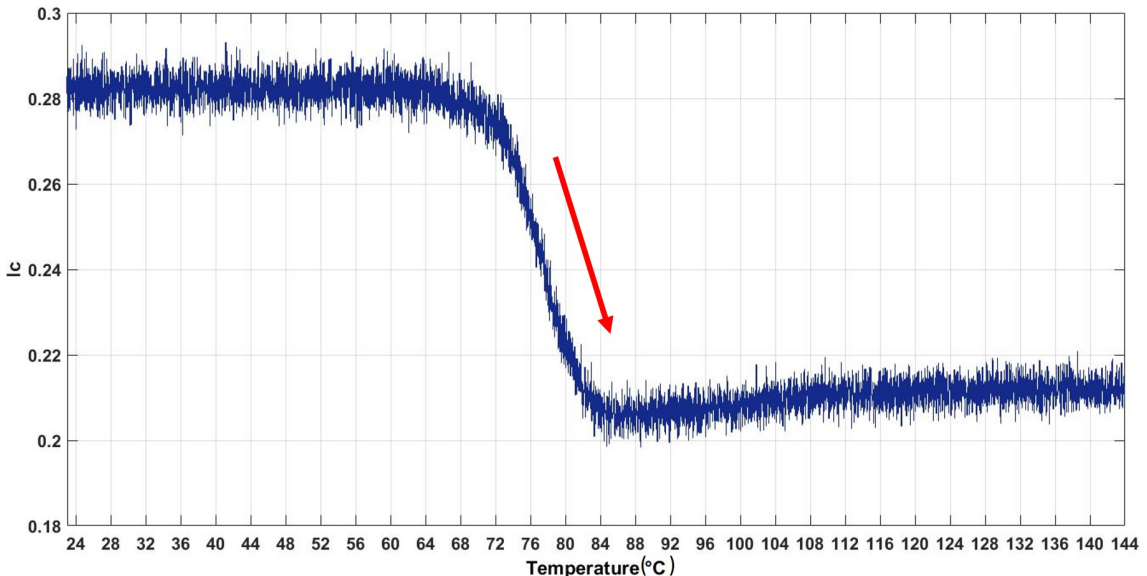


Figure 4.6: Dynamic optical measurements of the VO₂ NCs IMT. The rate of temperature ramp is 1° per minute. The initial starting temperature was 23°C

Through kinetic probing and hysteresis measurements, we observed a good optical modulation, typical from the VO₂-IMT. But in comparison with the bulk we observe a shift in transition temperature for NCs, as its initiation occurs later than that of the bulk. Following, we fit the experimental ellipsometry measurements with a multi-layer model composed of four layers as sketched in Figure 4.7 (i) a thin SiO₂ layer, (ii) the VO₂-NCs + SiO₂ effective layer, (iii) an intermediate layer containing vanadium inclusions and impurities and (iv) a semi-infinite SiO₂ substrate. This four-layer model is justified by TEM observations of the sample's cross sections. We use a reference dispersion file for SiO₂ (Palik: [41]).

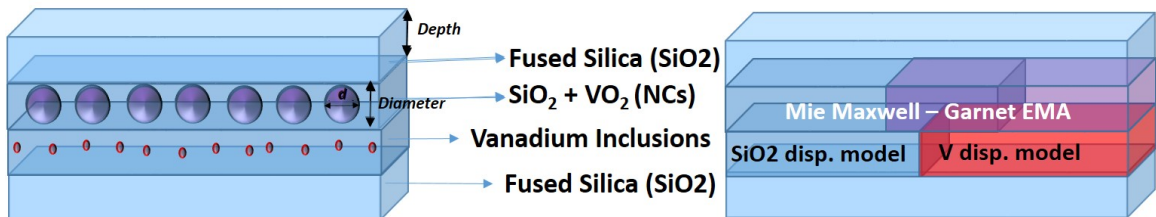


Figure 4.7: 3D representation of optical stacks for VO₂ NC embedded in fused silica.

4.5 Effective parameter retrieval of VO₂ Nanocrystals

In order to model the optical response of the slab composed of VO₂-NCs embedded in quartz, we have to calculate its effective refractive index m_{eff} . Because the conventional effective medium approximation is only valid for small inclusions compared to the wavelength, we therefore have to use a different framework to homogenize the medium as an effective medium. Here, to do so we use a Mie theory-based extension of Maxwell-Garnett effective medium approximation (EMA), as proposed by Doyle [186, 187]. Using the Mie extension of EMA, through the calculation of the Mie dipolar electric a_1 and magnetic b_1 dipolar coefficients we can take into account the size effects which are ignored by the electrostatic approximation in Maxwell-Garnett EMA.

4.5.1 Derivation of the expressions for effective permittivity and permeability

In order to numerically derive the effective dielectric permittivity (ϵ_{eff}) and magnetic permeability (μ_{eff}), we start with the Clausius - Mossotti equation, which describes the relation between the effective dielectric constant of suspended particle ($\bar{\epsilon}$) in a host medium (ϵ_h) as a function of the size (radius a), polarizability (α) and the volume fraction (f) of the embedded particles. The equation is given by:

$$\frac{\bar{\epsilon} - \epsilon_h}{\bar{\epsilon} + 2\epsilon_h} = \frac{f}{a^3}\alpha \quad (4.6)$$

Under the electrostatic approximation, the particle dipolar polarizability can be written as:

$$\alpha = \frac{\epsilon_i - \epsilon_h}{\bar{\epsilon} + 2\epsilon_h}a^3 \quad (4.7)$$

Where ϵ_i is the dielectric constant of the spherical material. Substituting and replacing the polarizability factor from the above two equations we get the classic Maxwell-Garnett

formula, given by:

$$\frac{\bar{\epsilon} - \epsilon_h}{\bar{\epsilon} + 2\epsilon_h} = f \frac{\epsilon_i - \epsilon_h}{\bar{\epsilon} + 2\epsilon_h} \quad (4.8)$$

Looking closely at Maxwell-Garnett formula, we notice that this equation is independent of the sphere radius a and is therefore only valid for sphere sizes much smaller than the illuminating wavelength λ . In our case, the light-matter interaction at play in the dielectric nanoparticles departs from the sole point-dipole approximation, due to the excitation of both electric and magnetic Mie resonances as well as the higher-order multipoles they can support. Therefore the electric dipole polarizability can be re-written in terms of the Mie coefficient a_1 by [188]:

$$\alpha_E = \frac{i3a^3}{2x^2}a_1 \quad (4.9)$$

Where the size parameter x is defined as:

$$x = \frac{2\pi a \sqrt{\epsilon_h}}{\lambda} \quad (4.10)$$

Now if we introduce the equations for α_E and x in the Clausius - Mossotti equation, we can derive the equation for ϵ_{eff} defined as:

$$\epsilon_{eff} = \frac{x^3 + 3ifa_1}{x^3 - \frac{3}{2}ifa_1} \quad (4.11)$$

Similarly for μ_{eff} , we define the magnetic dipole polarizability α_H in terms of dipolar magnetic Mie coefficient b_1 , shown as:

$$\alpha_H = \frac{i3a^3}{2x^2}b_1 \quad (4.12)$$

Now substituting α_H and x in Clausius - Mossotti equation we can derive the equation for

μ_{eff} defined as:

$$\mu_{eff} = \frac{x^3 + 3ifb_1}{x^3 - \frac{3}{2}ifb_1} \quad (4.13)$$

Relating to the sample values, x is the size parameter of the VO₂ spheres and f the volume filling fraction of the VO₂ spheres in the slab. And from the values of ϵ_{eff} and μ_{eff} the effective complex refractive index of the slab can be calculated as:

$$m_{eff} = n_{eff} + ik_{eff} = \sqrt{\epsilon_{eff} \cdot \mu_{eff}} \quad (4.14)$$

The dipolar coefficients are enough to model the response of the VO₂ particles since the quadrupolar terms are negligible, as seen in Figure 4.2.

Following the data fit procedure of experimental ellipsometry measurements, as mentioned in the last section, the respective thicknesses of SiO₂ top layer, VO₂-NC layer and V inclusion layer were set as free fit parameters, in multi-layer model shown in figure 4.7. None of the material's dispersion were fit, rather we modify the size and density of VO₂-NCs in our Mie-Maxwell Garnett model to adjust the fits to the measurements. Because there could exist correlations between thicknesses and permittivity in absorbing films, we simultaneously fit the two sets of measurements for VO₂ insulating and VO₂ metallic and we bind the different thicknesses. Meaning, the final fit will yield the same thicknesses for the different layers whatever is the phase of VO₂-NCs. The only difference between the two models lies in the dispersion of VO₂-NCs.

In Figure 4.8, we show the optimized fits together with the experimental data. We obtain an overall good correspondence between model and measurements for a VO₂-NCs size of $R = 35nm$ and a filling-factor $f = 0.18$. Especially, the fits are nearly perfect in the UV/Vis range but a slight discrepancy appears in the NIR.

The observed discrepancy in Fig.4.8 between the model and the experimental results is due to different effects which cannot be included without losing simplicity in the proposed

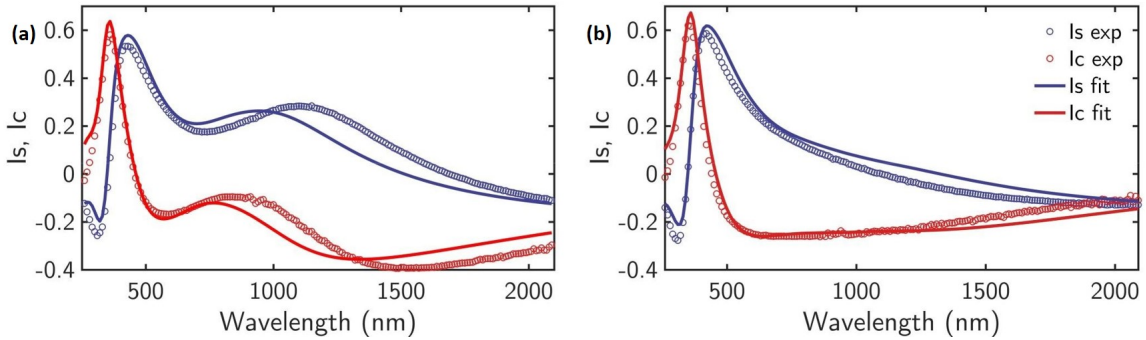


Figure 4.8: Fitting (solid line) and experimental measurements(circles) of the ellipsometric parameters I_s (blue) and I_c (red) for both states of VO_2 -NCs: a) metallic and b) insulating for a VO_2 -NCs for size of $R = 35\text{nm}$ and a filling-factor $f = 0.18$. (incident angle: 55°).

model. Two of the most probable important interactions could be the electromagnetic interaction between the particles and a potentially non-negligible degree of polydispersity in the size distribution of the VO_2 -NCs. The electromagnetic interaction between nanoparticles has a long standing history and a nice work on this effect can be found in Rechberger et al. [189]. We have applied the results of this research to our case and the details can be found in the following section.

4.5.2 Modelling the effect of interactions between nanoparticles

The Mie theory-based extension of Maxwell-Garnett effective medium approximation doesn't take into account the possible interaction between nanocrystals (NCs). In principle, given the mean separation of the NCs [190], interaction effects are expected to be small. However, to have a better estimation of how interaction effects may affect the plasmonic response of the NCs, we have calculated the absorption cross-section C_{abs} of dimers made of insulating and metallic VO_2 spherical NCs for different inter-particle distances (gaps) embedded in quartz. The spheres that were used for the calculation of the effective optical properties have a size of 70 nm ($R = 35\text{nm}$) and the considered gaps range between 10 and 150 nm. These calculations have been performed for three polarizations, as shown in figure 4.9: x-polarization (i.e. along the dimer axis), y-polarization (i.e. perpendicular to the dimer axis) and at 45° (This angle is chosen because the incident polarization used in the

ellipsometry experiments is linear at 45° with the incidence plane).

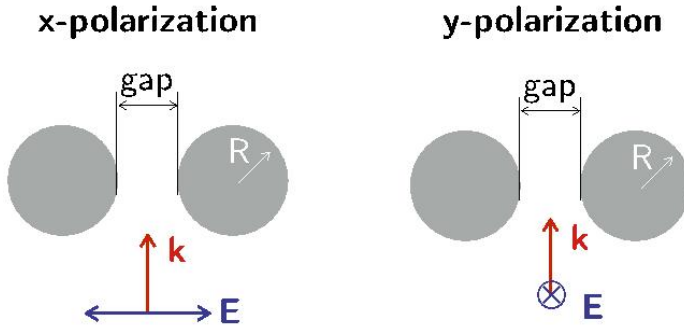


Figure 4.9: Scheme of the analyzed system: dimer formed by spheres ($R = 25\text{nm}$) separated by a gap and illuminated with x - (left) and y -polarized beams (right). With arrows are represented the polarization of the illuminating beam (E , blue arrow) and the wave vector (k , red arrow).

All the following calculations involving interparticle interactions were performed by Yael Gutierrez and Fernando Moreno from Department of Applied Physics, Universidad de Cantabria, Santander, Spain. These calculations have been performed using commercial software FDTD solutions (Version 8.16) from Lumerical Inc. Total field/scattered field light source conditions were used in all simulations and an illuminating linearly polarized plane-wave was set to propagate perpendicular to the dimer axis. The wavelength spectral range analyzed was from 260 to 1500 nm to mimic experimental conditions. A non-uniform mesh was used in the simulation region and a finer mesh was defined in the vicinity of the NPs. In this region, the mesh step was fixed at $d_x = d_y = d_z = 2\text{nm}$. The absorption cross-section was calculated within the total-field/scattered-field formalism.

VO₂ dimers in its metallic phase

The Figure below(4.10) shows how the different interparticle distances (gaps) effect the overall Localized Surface Plasmon Resonance (LSPR) peaks that appears in the absorption cross-section (C_{abs}) of a dimer made of metallic VO₂ nanospheres. Focusing on the figure, the dashed black lines represent the peak positions for a system of two non-interacting spheres (the two most left lines correspond to the electric and magnetic dipole resonances, respectively). Particularly, we pay attention to the LSPR peak appearing at 1176 nm which

has a pure dipolar electric character. Figure 4.10(a) shows how, for the dimer illuminated with x-polarized light, the LSPR peak is red-shifted as the gap becomes smaller, reaching a maximum shift of 110 nm for a gap of 5 nm. On the contrary, Figure 4.10(b) shows that the LSPR peak is blue-shifted when the dimer is illuminated with an y-polarized beam. The maximum blue-shift is 30 nm for a gap of 10 nm. These results are consistent with those reported by Rechberger et al [189].

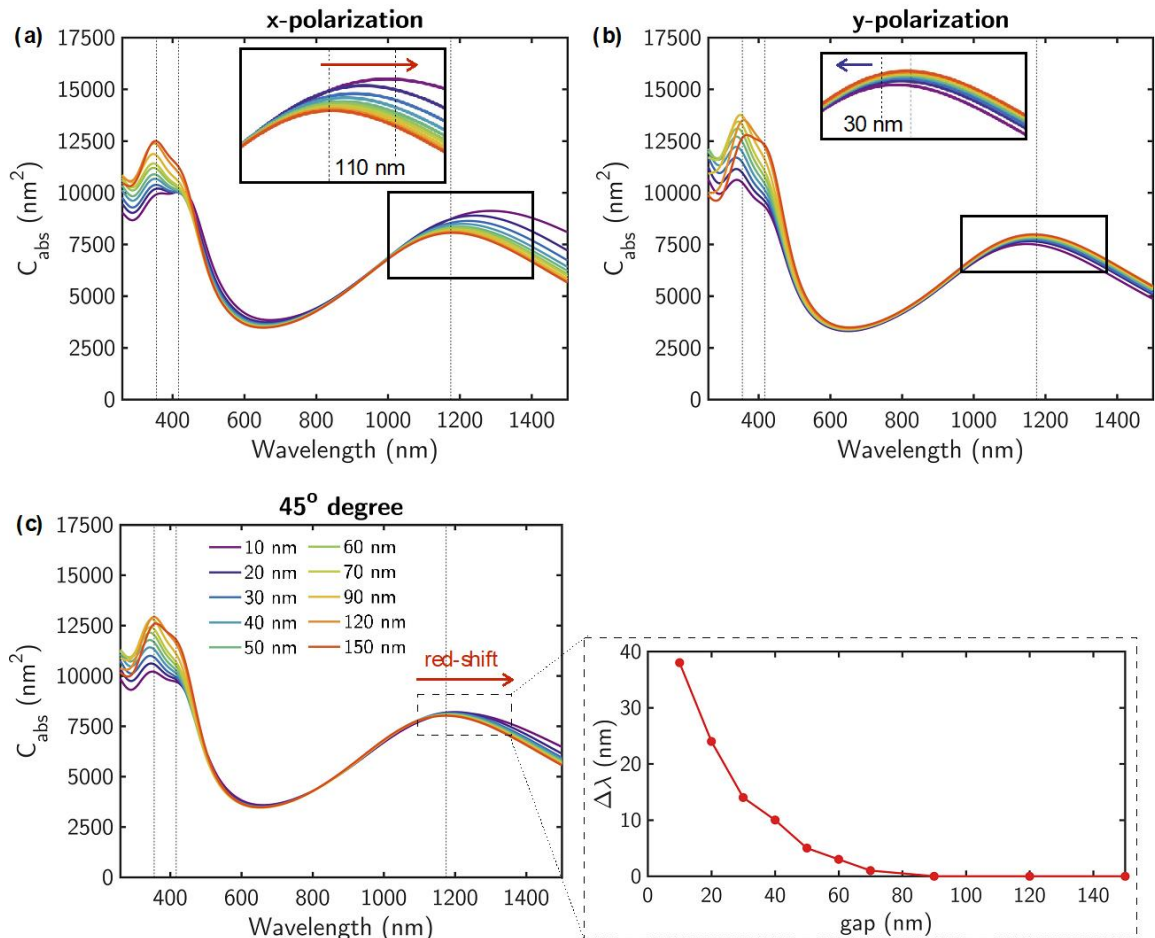


Figure 4.10: Absorption cross-section C_{abs} of VO_2 dimers in its metallic phase ($R = 35 \text{ nm}$) when illuminated with (a) x- (b) y- and (c) 45° polarizations (4.9) for different interparticle distances (gaps). As an inset in (a) and (b) is indicated the maximum spectral shift between the interacting and non-interacting (dashed black lines) dimer. In (c) the spectral shift $\Delta\lambda$ is represented as a function of the gap.

Therefore, when we consider our sample under study, we know that the NCs are randomly distributed inside the fused silica substrate, we can on average consider, the effect of the

interaction has an intermediate effect between the two extreme situations: x-polarization and y-polarization. Similarly from Figure 4.10(c) we can observe how the absorption cross-section (C_{abs}) of the dimer is affected for different gaps when it is illuminated with 45° linearly polarized light. As the gap decreases, the LSPR peak is redshifted of approximately about 40 nm and it is produced for the smallest gap.

VO₂ dimers in its insulating phase

Similarly like above, the Figure below(4.11) shows how the different interparticle distances (gaps) affects the overall Localized Surface Plasmon Resonance (LSPR) peaks that appear in the absorption cross-section (C_{abs}) of a dimer made of insulating VO₂ nanospheres. And again dashed black lines represent the spectral peak positions for a system of two non-interacting spheres (as in the previous case, they correspond to a coherent mixture of dipole resonances, of both electric and magnetic character). But in this case we look at resonance at 381nm rather than at 1176nm, whose origin is the superposition of a dipolar electric and a dipolar magnetic resonance. We study this resonance in the insulating phase in order to remove any parasitic effect coming from the dipolar electric resonance appearing at longer wavelengths in the metallic phase.

Figure (4.11) below shows how the resonance peak is shifted with decreasing the interparticle gap for (a) x- (b) y- and (c) 45° polarizations, respectively. For the three studied polarizations the overall effect is the same. For the largest gap (150 nm), the resonance is slightly blueshifted with respect to the non-interacting system. With decreasing interparticle distances the resonance peak further blueshifts reaching a maximum spectral shift for an intermediate gap of 60 nm approximately.

For smaller gaps the resonance peak comes back to the starting point. In this case, the resonance has two dipole contributions, one electric and one magnetic. The dimer electromagnetic interaction shifts the electric to the red part of the spectrum whilst the magnetic one is blue shifted [191]. In this case, the blue shift dominates for intermediate

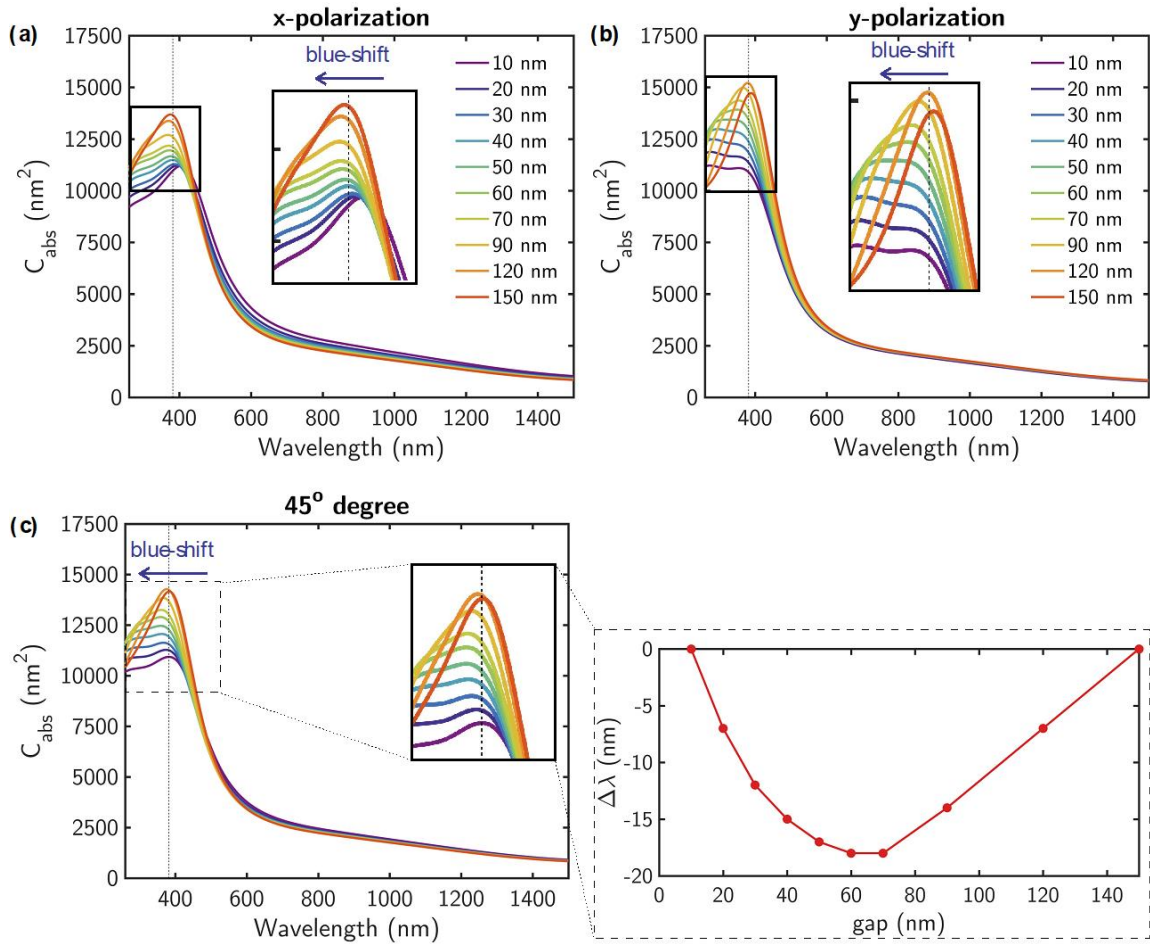


Figure 4.11: Absorption cross-section C_{abs} of VO_2 dimers in its insulating phase ($R = 35 \text{ nm}$) when illuminated with (a) x- (b) y- and (c) 45° polarizations (4.9) for different interparticle distances (gaps). As an inset in (a) and (b) is indicated the maximum spectral shift between the interacting and non-interacting (dashed black lines) dimer. In (c) the spectral shift $\Delta\lambda$ is represented as a function of the gap.

gap distances (60-100 nm) whilst for strong interaction (gaps smaller than 50 nm) the dipole electric resonance redshift compensates that of the magnetic one to the blue.

In the next section we will tackle the second important discrepancy, which is the possible polydispersity in the size distribution of the VO_2 -NCs.

4.5.3 Modelling the polydispersity in size distribution of nanoparticles

In this approach we calculate the effect of the potential polydispersity of the NCs in the sample. Fig. 4.12 shows the difference in the absorption cross-section spectra (C_{abs}) between

the reference system ($R = 35$ nm) and two other systems with well-defined polydispersities. The first has a symmetric size distribution centered on the reference size. The other system has an asymmetric size distribution, having a majority of NCs with the reference size, but others with larger sizes. For this study we will focus on the resonance (LSPR) appearing at ≈ 1176 nm in the VO_2 -NCs in their metallic phase. For example Fig.4.12(a) shows the C_{abs} spectra for the reference system and the one with the symmetric NCs size distribution Fig.4.12(b). In this case, there is no significant difference between both systems. On the contrary, in the case of the asymmetric NCs size distribution (Fig.4.12(c)) there are significant differences. The LSPR appearing in the C_{abs} spectrum of the polydisperse sample, as shown in Fig.4.12(c), is redshifted (20 nm) and also broader than the reference system.

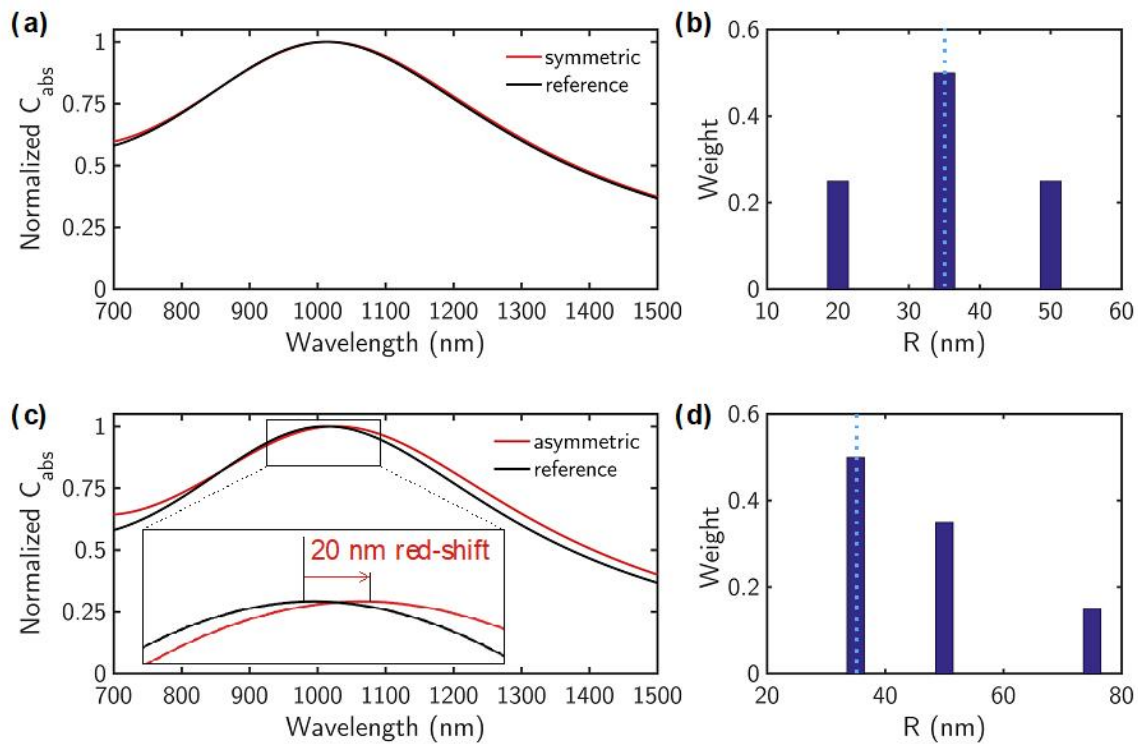


Figure 4.12: Absorption cross-section C_{abs} spectra for the reference monodisperse system ($R = 35$ nm, black line) and others with (a) symmetric and (c) asymmetric distribution of NC sizes. Size distribution of the (b) symmetric and (d) asymmetric systems. With the light dotted line is represented the size of the monodisperse distribution.

4.5.4 Discussion on the results and parameter retrieval of the system

Apart from the two important discrepancies that we have addressed, there could be other effects that could present minor contributions to the discrepancies observed in Figure 4.8. For example, we assume that VO₂-NCs is composed of purely stoichiometric VO₂ and we neglected the presence of suboxides such as V₂O₅ at the NCs surface. Furthermore, we directly used the dispersion as extracted from VO₂ thin films measurements to compute the different Mie coefficients. By doing so, we made the hypothesis that the complex permittivity of VO₂ inside the NCs has the exact same dispersion as VO₂ thin films, what could be subject to discussions [192].

Even though we have made all these approximations, we find a remarkably good qualitative agreement between measurements and calculations. We emphasize that this simple Mie-Maxwell-Garnett effective medium model is able to reproduce well the prominent features of the optical response for both states of VO₂ by simply changing the dispersion of VO₂ from insulating to metallic. Indeed, the calculations nicely reproduce the first peak in the visible, which is a combination of electric and magnetic dipole resonances and the second peak in the NIR which is a plasmonic resonance. This latter is only present when the VO₂ is metallic, e.g. when the real part of the permittivity is negative and is therefore a dynamically tunable resonance.

These calculations enable us to retrieve the effective permittivity of the active VO₂-NCs layer and homogenize it as an effective metamaterial medium. Figure 4.13 a-d shows the calculated ϵ_{eff} , μ_{eff} and m_{eff} for a slab with VO₂ spheres with radius $R = 35$ nm and a filling fraction $f = 0.18$ in their insulating (low temperature) and metallic (high temperature) states.

We see the clear differences in the optical dispersion as compared to un-patterned VO₂ layer. In particular, there are ranges of wavelength for which the IMT of VO₂ produces a large modulation of n_{eff} with a simultaneously low k_{eff} that is much lower than in bulk VO₂. This is especially true in the NIR range, for which k_{eff} remains lower than 0.1.

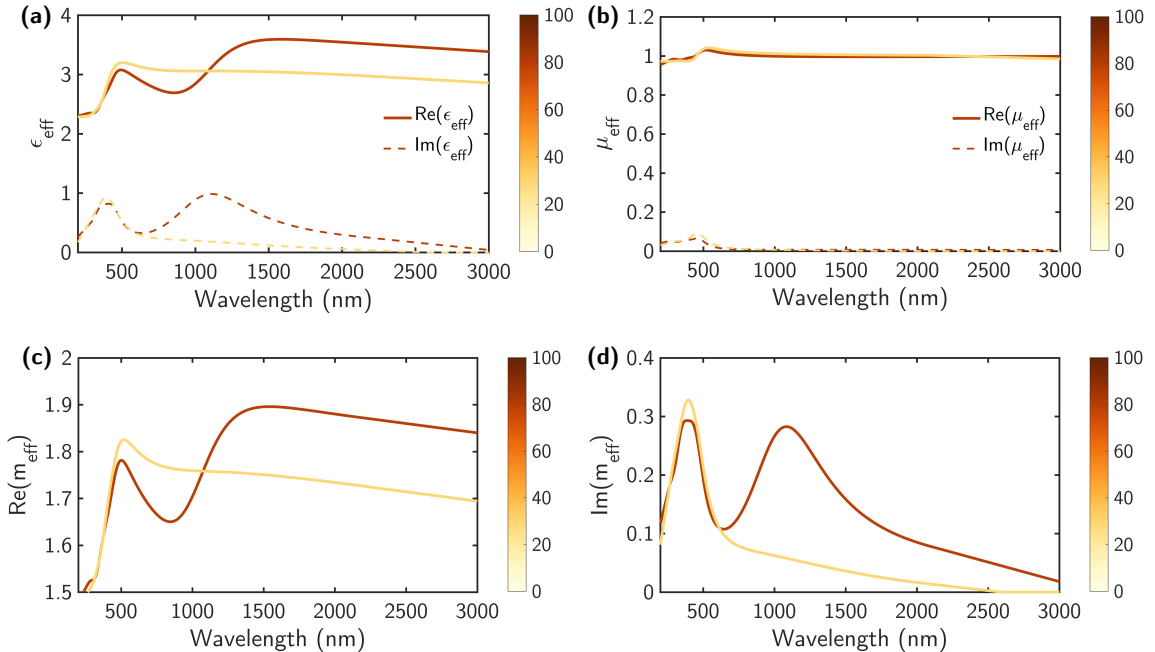


Figure 4.13: a) Effective dielectric function (ϵ_{eff}), b) magnetic permeability (μ_{eff}), and c) real and d) imaginary parts of the effective refractive index ($m_{\text{eff}} = n_{\text{eff}} + ik_{\text{eff}}$) of a slab of quartz with VO_2 spheres with radius $R = 35 \text{ nm}$ and a filling fraction $f = 0.18$ in their insulating (low temperature) and metallic (high temperature) states.

4.6 Tunable multipolar resonances based on VO_2 -NCs system: Future Perspective

4.6.1 Discussion

In the previous section, we calculated the main spectral characteristics of VO_2 -NCs based metamaterials using a combination of Mie theory and Maxwell-Garnett effective medium. This has enabled us to predict the expected optical properties of VO_2 -NCs of arbitrary sizes. Following, we show how this framework can be used to design tunable metamaterials with tailored properties in desired wavelength ranges. Figure 4.14 shows the calculated evolution of the n_{eff} and k_{eff} values of VO_2 -NCs in both their insulating and metallic states for different radius of NCs.

Comparing both the states, we see that at the insulating state the absorption peaks are controlled by the Mie resonances while in the metallic state they are dominated by the plasmonic resonance. Therefore by controlling the size parameter of NCs, we can control

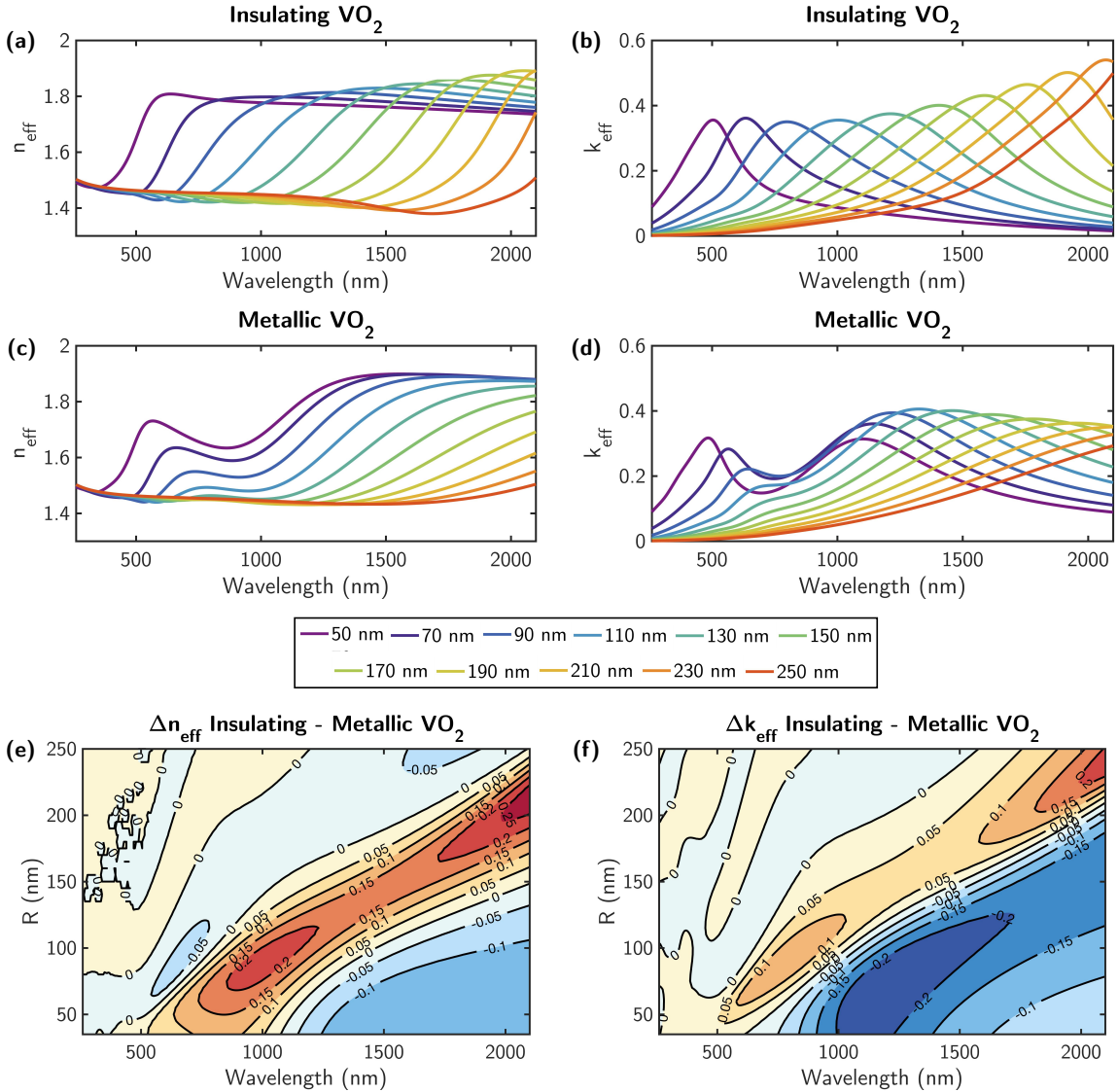


Figure 4.14: Variation of effective optical parameters for different sizes of nanocrystals in both states of VO_2 a) and b) n_{eff} and k_{eff} for insulating VO_2 with a filling fraction $f = 0.18$. c) and d) n_{eff} and k_{eff} for metallic VO_2 . e) and f) represent the amplitude of modulation of the effective refractive index of the metamaterial as a function of NCs size. e) Δn_{eff} and f) Δk_{eff} .

the spectral position of the absorption peaks in both the insulating and metallic states (see figure 4.14 b) and d)). The size of the VO_2 -NCs therefore enables tailoring the spectral distribution of the multipolar resonances hosted by this metamaterial.

In order to have a general view about different regimes of tunability that we can obtain with this system, Figure 4.14 e-f displays the amplitude of refractive index modulation produced by the IMT of VO_2 as a function of NCs size. To do so, we plot Δn_{eff} and

Δk_{eff} , which are defined as $\Delta n_{eff} = n_{eff,insulating} - n_{eff,metallic}$ and $\Delta k_{eff} = k_{eff,insulating} - k_{eff,metallic}$ and which represent the amplitude of modulation of the effective refractive index and extinction coefficient, respectively. With this figure, we can pinpoint specific regions of the size versus wavelength map in which the switching of VO₂ either translates into a tunable refractive index or a tunable extinction coefficient.

Interestingly, by plotting the Δn_{eff} and Δk_{eff} values calculated for a few selected VO₂-NCs sizes (as displayed in Figure 4.15), we immediately see that around the maximum Δn_{eff} reached for each NCs size, we simultaneously have $\Delta k_{eff}=0$. Furthermore, the wavelength at which this effect is obtained is directly governed by the size of VO₂-NCs. In other words, this phase-change metamaterial platform enables tailoring a dynamical tuning of refractive index without modifying the optical absorption. As displayed in Figure 4.15, this 'zero-induced-extinction' refractive index tuning occur in a designer wavelength range via selecting an appropriate size of NCs.

Said otherwise, by plotting the figure of merit (FOM) $\Delta n_{eff}/\Delta k_{eff}$ for different sizes of NCs and comparing the obtained FOM to the corresponding one for VO₂ thin films, we immediately see that not only the FOM is enhanced by more than two orders of magnitude but we can design the system to select the wavelength at which the FOM is boosted via the size of VO₂-NCs. This designer high FOM is much larger than in any other existing 'unpatterned' PCMs [193], and highlights the usefulness of our metamaterial approach. We also note that the opposite effect can be exploited, namely, close to the maximum Δk_{eff} , we can simultaneously have negligible Δn_{eff} . So this platform can be used to actively control the absorption without modifying the refractive index of the medium (e.g. for R=95nm at $\lambda=1500$ nm we get $\Delta k_{eff}=-0.2$ and $\Delta n_{eff}=0$).

4.6.2 Perspective towards designer metamaterial

Another exciting opportunity that can be envisioned for this metamaterial is to be used as an active platform to control scattering properties and directional beaming of light. Indeed,

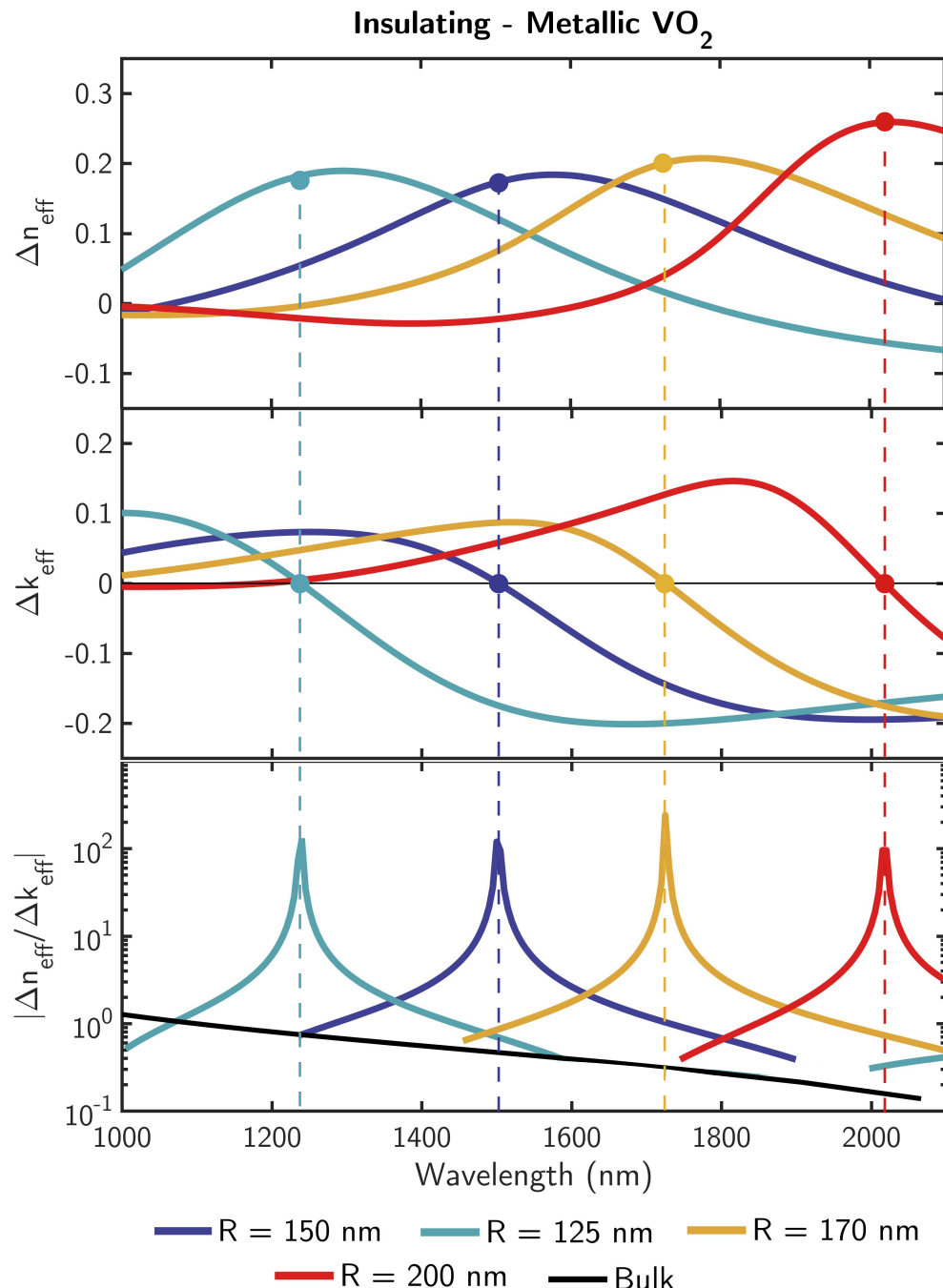


Figure 4.15: Spectral variation of the amplitude of modulation of the effective refractive index (Δn_{eff}) and extinction coefficient (Δk_{eff}) of the metamaterial for selected NCs size. Bottom graph: Figure of Merit ($FOM = \Delta n_{\text{eff}} / \Delta k_{\text{eff}}$) of the VO₂-NCs platform for different sizes of nanocrystals and compared to the FOM for a VO₂ thin-film.

when multipolar resonances are spectrally overlapping in nanoparticles, the scattered fields can interfere and produce directional scattering. In particular, spectrally overlapping ED and

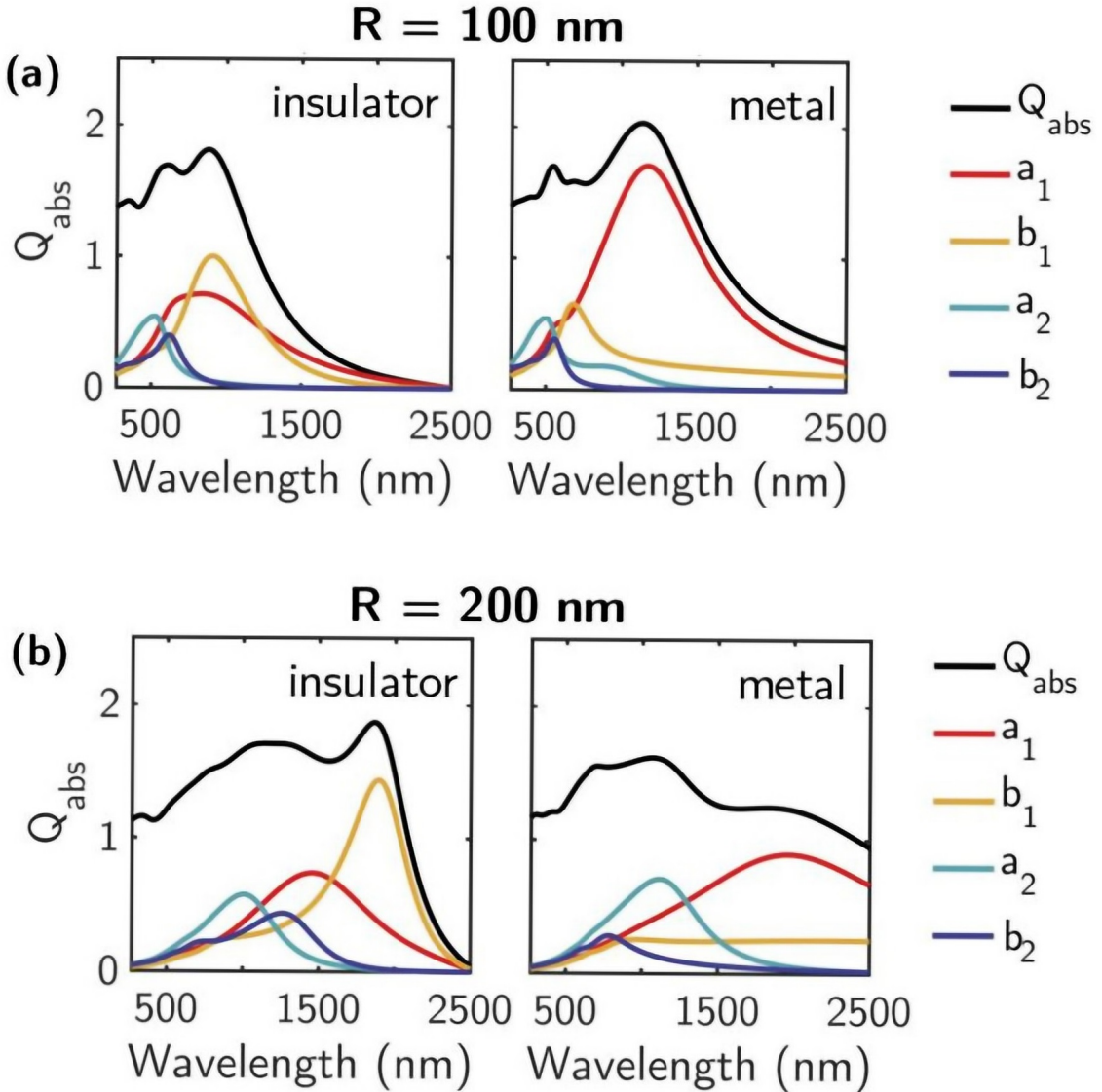


Figure 4.16: Calculated absorption cross-section efficiency Q_{abs} of NCs of different sizes in their insulator and metallic states embedded in quartz. With colored lines are represented the dipolar electric a_1 (red), dipolar magnetic b_1 (yellow), quadrupolar electric a_2 (light blue) and quadrupolar magnetic b_2 (dark blue) contributions to Q_{abs} .

MD resonances yield the so-called Kerker conditions that either suppress the forward or the backward scattering of light [194, 178]. Figure 4.16 displays the multipolar decomposition of light fields within VO₂-NCs as a function of size and VO₂ phase, either insulating or metallic. We see that each size of NCs produces overlapping ED and MD resonances which would coherently interfere at specific wavelengths. Then, when the VO₂ is switched from

its insulating phase to the metallic one, we can suppress the DM contribution associated to the b_1 coefficient and strongly enhance the DE contribution associated to the a_1 coefficient.

Simply put, at specific wavelengths we switch from a dielectric MD resonance to a plasmonic ED resonance. This implies that this hybrid metamaterial enables an active and dynamical control of the Kerker conditions [194]. From that perspective, we foresee a dynamic modulation of the directionality of light scattering as well as actively tunable perfect reflection or absorption. We also note the presence of tunable quadrupolar modes (a_2 and b_2 coefficients, figure 4.16) that may be used for complex tunable interference phenomena between different multipoles, hence opening a wealth of different possibilities of spatially distributing the scattered light for directionality control purposes (see [179, 195] for more details). This tunable multipoles could also find an interest in the recently proposed framework of spontaneous emission engineering through interferences between higher-order multipoles [196].

4.6.3 Conclusions

In conclusion, we have demonstrated an active platform using VO₂-NCs that can be integrated in SiO₂ as spherical nano-inclusions that enable exploiting the VO₂ IMT to tune and switch multipolar modes in the visible and near-infrared ranges. Particularly, the presence of a plasmonic mode in the NIR whose gradual appearance and intensity are directly controlled by the VO₂ state. The presence of two simultaneous dipole resonances in two different spectral regions, Vis and NIR, could open the possibility of new multiplexing based techniques for SERS applications.

Contrary to bulk and thin-films VO₂, such a metamaterial approach provides means to tailor the complex refractive index and tunability of phase-change materials. Indeed, we have shown that, by adjusting the VO₂-NCs size, this system can be exploited as a designer phase-change metamaterial with adjustable refractive index modulation and absorption modulation. Especially, we can design the system to have a large refractive index tunability

without inducing modulation of the extinction coefficient at specific wavelengths, or in other words a zero-induced-loss refractive index modulation. Furthermore, such VO₂-NCs can be optically switched at femto-seconds timescale (~ 150 fs) [183] and present very large hysteresis (see [184] and the supplementary information). We can therefore envision this platform to be used for ultra-fast all-optical integrated systems with memory effects.

We emphasize that the resulting metamaterial presents several benefits from a practical point of view, and most notably the nanostructures are embedded in a dielectric host that protects them from the environment and consequent processes that can affect its optical response (protection from oxidization [197], chemical reaction [198], mechanical scratches, etc.). This makes such a platform extremely easy to handle and to integrate in various environments, contrary to thin-films of phase-change materials that are very sensitive. The samples presented here were fabricated by ion implantation, a technique that is widely used in the microelectronics industry and could therefore be exploited for large-scale fabrication of samples. Furthermore, the size, density and depth of NCs in the host could be controlled through adjustment of implantation parameters and annealing process. This implantation process can be carried out in many different CMOS-compatible platforms such as thermal SiO₂ on silicon substrate and results in a flat surface that does not require any complex post-process step such as CMP to planarize the device. A next logical step could be to integrate nanophotonic devices on top of this metamaterial for a wealth of tunable functionalities such as an active control of spontaneous light emission [199, 196, 200] or dynamically tunable Huygen's metasurfaces [201].

From a broader scientific perspective, the results presented in this chapter help define a new system with which to study tunable interactions between nanoparticles and tunable interferences between multipolar resonances. We envision it to serve as a testbed for dynamical modulation of light scattering, tunable Kerker effects and active control of light directionality.

CHAPTER 5

VO₂ BASED METASURFACES FOR TUNABLE FREE-SPACE NANOPHOTONICS

Many modern day conveniences, which we take for granted, has been possible through the understanding of light as an electromagnetic wave. Devices like radio, lasers and more recent things such as wireless communication, flat-screen color displays and LEDs were achievable because we understood and controlled electromagnetic waves. The breakthrough in wireless technology has been one of the turning point in the human civilization. This made the world a smaller place as it enabled instantaneous communications affecting the global trade and economics. The credit for the development goes to the decades of research in the field of transmission and detection of electromagnetic waves through the study of antennas. The scaling of these antennas down to lengths comparable or even smaller than the wavelength of light as well as the periodic arrangements of these antennas has led to great advantages in terms of scalability and efficiency compared to isolated antennas.

The light-matter interactions in natural materials are governed by the complex refractive index and not the structure. The interaction and control of light is produced through the modification of its polarisation, phase and amplitude. There are only a few exceptions for which the micro-structure in natural materials comes into play, the most well-known being the blue wings of the morpho-butterfly [54]. These natural microstructures became an inspiration for controlling light-matter interactions through engineering the structure and arrangement of matter. Such artificially engineered materials are also known as Metamaterials, which were created to go beyond what is naturally existing (meta means 'beyond' in greek). In order to achieve the desired interactions with light, the constituents of these metamaterials, called meta-atoms (usually smaller than the wavelength of light), are user defined and are designed and arranged such that an averaged effect is encountered in terms of scattering

and interference with light waves. The overall property or response of the metamaterials depend on the individual unit structures as well as the arrangement and orientation of the meta-atoms. Therefore, by adjusting those properties, one can take advantage to develop new materials, possessing unique properties that are not naturally available in nature. Such works have led to the development of negative index materials [42, 43, 44], zero-index materials [45, 46, 47], invisibility cloaking [48, 49] and sub-diffraction imaging [50, 51].

Recently, there is a growing interest for 2D planar metamaterials, namely metasurfaces. These metasurfaces provide similar exotic properties as metamaterials, but their thickness are only a fraction of the wavelength and are therefore easier to fabricate and to integrate. While standard bulk components such as lenses rely on phase accumulation during propagation and therefore require to be curved, metasurfaces are flat components that can be integrated easily into most of the on-chip devices. This dramatically reduce the dimensions of the optical components. The physics behind metasurfaces is to locally control the electromagnetic fields through the abrupt modification of the phase and/or amplitude using nano-resonators. By spatially arranging these elements, one can mold the wavefront of light by design [202, 203]. And it is made possible using arrays of nano antennas with designed spacing and varying geometric parameters like shape, size, material type, orientation and their arrangement.

Unlike in conventional optics, where light travels through a medium of a particular refractive index to alter its path, metamaterials enable manipulating the effective complex refractive index of the medium achieving desired wavefront control. So far most of the experimentally demonstrated metasurfaces are static post-fabrication, which means that their optical functionalities are encoded into their design permanently after the fabrication. The potential application of these metasurfaces (all dielectric or plasmonic) can be increased exponentially if their optical response can be dynamically and reversibly modified.[52, 53].

The type of metasurfaces that is based on metallic nano-structures or nano-resonators leverage surface plasmons (SP) [58] to drive the optical response of the devices; hence known as plasmonic metasurfaces [59, 60]. Researchers have demonstrated that plasmonic

metasurfaces can enable controlling polarization, amplitude and phase of electromagnetic radiation [61, 62] for applications as flat lenses [63], holograms [64] or directional couplers [65]. On the other hand, dielectric metamaterials and metasurfaces can support multipolar resonances such as electric and magnetic dipoles as well as higher-order modes. Mie theory as discussed in Chapter 4 is therefore useful to understand and calculate the exact contribution of each modes of the nanostructure and to calculate fields distribution inside it.

Despite the growth in static Mie resonance based metasurfaces, making them tunable remains a major issue. In recent years, considerable efforts have been made towards tunable nanophotonic devices made of metallic nanostructures coupled to various phase-change materials such as GeSbTe and VO₂ [73, 74, 75]. However, all-dielectric tunable nanostructures remain largely unexplored. In this chapter we show that the IMT of VO₂ can be exploited to dynamically tune the resonances of sub-wavelength scattering structures and the overall optical properties of dielectric metasurfaces. This concept is used for two different targeted applications: first we propose a platform for tunable structural coloration based on TiO₂ nanostructures on VO₂ thin-film. Second, we experimentally demonstrate a VO₂-assisted modulation of electric and magnetic Mie resonances supported by amorphous silicon nano-pillars, achieving tunable perfect absorption or transmission modulation depth of about three orders of magnitude at $\lambda = 1555\text{nm}$.

5.1 VO₂ metasurface for tunable structural color.

5.1.1 Introduction

Sci-fi movies and comics have shaped the way we see the future and are sometimes precursors to innovations, e.g. the giant touch-screen transparent displays. The past few decades have seen exponential advancement in color display technologies which are crucial for devices ranging from televisions to smartphones. As the current trend is moving from high contrast 2D displays to 3D or heads-up displays, it is crucial for the pixel technology to keep up the pace. But the majority of these technologies uses either LCD's (Liquid Crystal

Displays) or LED's (Light emitting diodes) which are larger in dimension compared to wavelength of operation, therefore it limits the boundaries for scaling down the device size.

Additionally, the majority of the time when we want to produce color we use pigments for visual display both static (posters, paints, printers etc,) and some in dynamic displays like LCD's. Synthetic colorants are expensive to produce, harder to recycle and environmentally damaging. Furthermore they decay and are not stable, they lack resolution what further limits their range of applications. Therefore, in search for suitable replacement, researchers have given considerable attention to structural coloration. As previously mentionned, a famous example of structural color can be seen in nature: the metallic blue color of Morpho butterfly wings. Morpho butterfly helped us realize that there is an alternative way of producing colors without any colorants or pigments, by simply arranging transparent materials in a periodic structure [54] shaping the interference between the incident and reflected light. However, the high quality of structural colors exhibited by nature requires complicated and bulky structures [55, 56] which makes the size of the structure much larger than the wavelength [57].

In this regard, utilizing the artificial structures of 2D metasurface appears favourable for the generation of high resolution structural color beyond the diffraction limit. Structural color generation can be achieved in various number of ways. The phenomenon revolves around the interaction of nanostructures with the incident light to the reflected or transmitted light [204, 205, 206].

In the field of plasmonic structural color reproduction, the plasmonic resonance has shown tremendous ability to selectively filter visible colors in transmission and reflection modes by coupling SP with the incident light. Additionally, the ease of fabrication and high flexibility at nano scale have further propelled its applications in creating high resolution structural color filters beyond the diffraction limit [207, 208, 209, 210]. Alternatively, using high-index dielectric materials as meta-structures generates electric and magnetic dipole resonances [59] that can induce novel optical phenomenon [211, 87]. The application and

further explanation regarding the structural color production using dielectric metamaterial will be discussed in a later section.

5.1.2 Color perception

First, it is important to understand that the color of an object, as we see it, depends both on the light source and on the human perception of color. Indeed, the human eye has a limited spectral bandwidth and only detects the values of wavelength that lie in the range of 0.38-0.78 μm . There are two receptors in human eyes, rod cells and cone cells and it is the cone cells that are responsible for color vision. Cone cells are further divided into 3 types, on the basis of which wavelength of color they are more sensitive to: namely, the short (S, short wavelength (blue)), medium (M, greenish yellow), and long (L, yellowish red) cone types [212]. Additionally, human eye is able to distinguish up to a few hundred of hue, i.e. it can detect a change of 1nm in the blue-green and yellow wavelength ranges up to 10nm and more in longer red wavelengths.

Second it is important to understand how we scientifically classify different colors. For that, we usually use CIE diagrams. CIE stand for Commission internationale de l'éclairage, which is a 100 years old organization that creates international standards related to light and color. CIE 1931 is a Color Matching System. Color matching does not try to explain how colors look to humans, color matching teaches us how to determine a color calculated numerically, and then accurately replicate the color measured (e.g. in print or digital displays). To reiterate the concept, Color Matching Systems are not based on explaining color with attributes such as hue or intensity, they simply tell us what light configurations seem to be the same color to most people (they "match"). Color matching helps to provide us with a simple color reproduction system. In order to give them some mathematically useful properties, the 1931 XYZ Color Matching Functions (CMFs) are a linear transformation of the 1931 RGB Color Matching Functions. You can plot the primaries of other color spaces onto the XYZ chromaticity diagram to see the triangles they form. The area inside

a primary triangle is known as a color gamut. The figure 5.1, displays the sensitivity of different types of cone and the figure 5.2 shows a CIE graph of all the colors that human eye can perceive and also the sRGB chromaticity triangle showing the colors of our monitor displays. Therefore, for future structural color-based displays employing metasurfaces it is desirable to create or filter distinct colors as human eyes are quite sensitive to the accuracy of the colors.

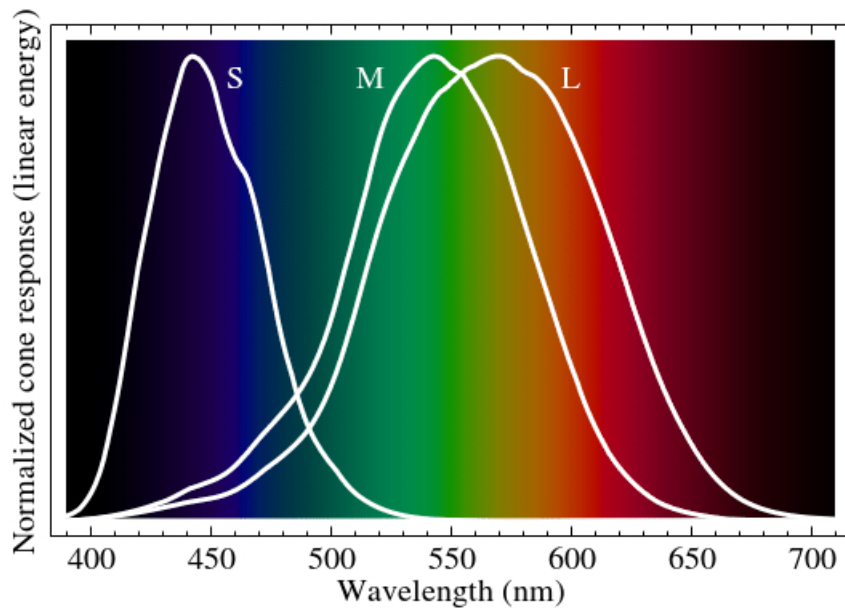


Figure 5.1: Normalized response spectra of human cones, to monochromatic spectral stimuli, with wavelength given in nanometers [213].

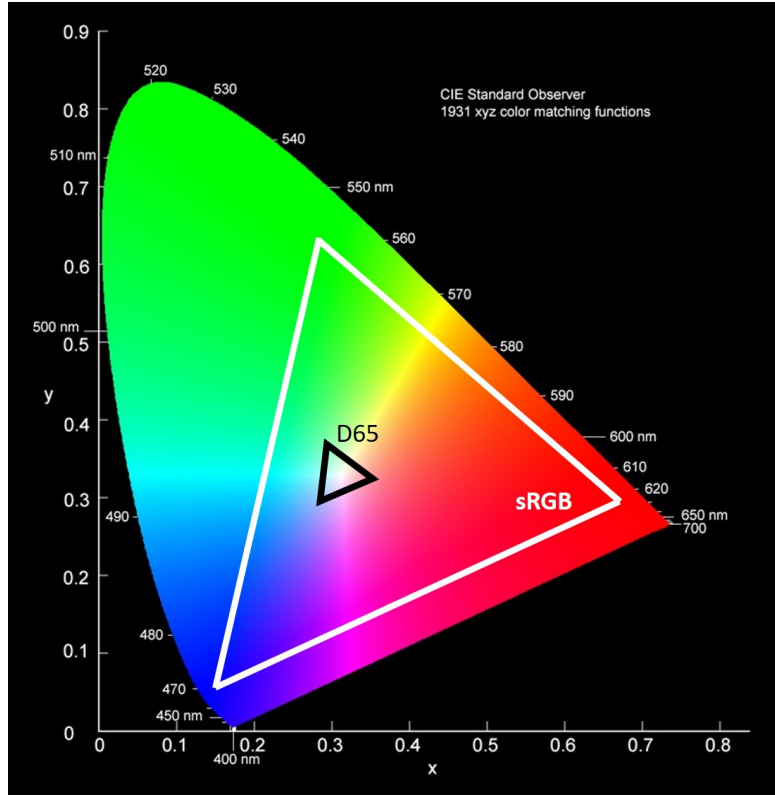


Figure 5.2: The chromaticity diagram of the CIE 1931 color space. The curved outer limit is the spectral locus, with wavelengths shown in nanometers. The colors your monitor displays in this image are specified using sRGB, so colors outside the sRGB range are not displayed correctly. This diagram shows the maximum saturated vivid colors that can be perceived by human eyes.

5.1.3 RGB color space

Most displays generate colors using a combination of red, green and blue pixels, which are primary colors defining the RGB color space. This is the most traditional way for defining colors of pixels in LDR (Light Dependent Photo Resistor) images. However, the definition for red, green and blue can vary from devices to devices, and are thus called device-dependent. In reality, the RGB need not be defined by their spectral power distribution but four chromatic points in the CIE-xy 5.2 diagram are sufficient. Three of which corresponds to RGB colors but the fourth point is white and it is obtained when we mix equal intensities of red green and blue (i.e. when R=G=B). The most common white point in CIE standard is illuminant D65 [214] and it is used extensively in industries for the simulation of natural daylight for visually demanding applications like digital art, film, photography, colorimetry

etc. The idea behind the D65 is for industrial standardisation of lighting. D65 is a particular embodiment of the D series of illuminants defined by the CIE and attempt to simulate the spectral power distribution of natural daylight represented in figure 5.3.

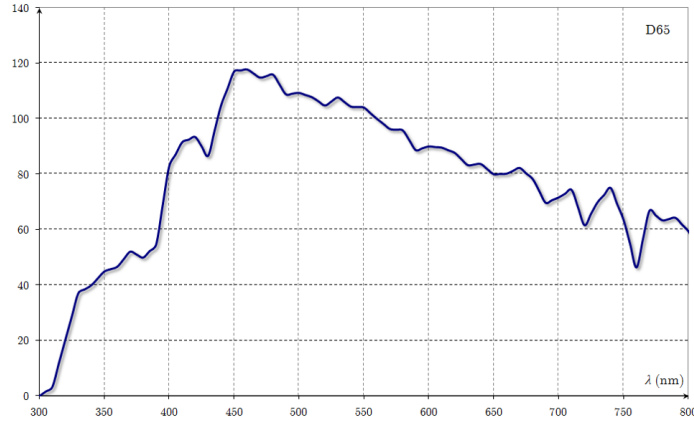


Figure 5.3: This the D65 sunlight spectrum simulated by D series daylight simulator by CIE standard. It cover the whole visible spectrum and the roughness shows the various points of absorption and diffusion by earth's atmosphere. This figure is taken from [215]

The spectral power distribution shown in figure 5.3 is similar to a core of the light source - it provides the fundamental data about a light from which color temperature, chromaticity and other photo-metrics are calculated from. Therefore, in color representation, the D65 white illuminant for each structure is crucial, as the RGB color produced will be a function of the white color the structure can represent.

Structural coloration has proven to generate bright colors with transparent nanostructures. One could therefore imagine this technology to replace conventional color paint that uses toxic or non-recyclable chemicals. So far, it is however difficult to envision this structural coloration to be the basis for new color displays because this would require to dynamically tune each color pixels. Research into tunability of structural coloring is increasing thanks to its practical applications such as dynamic displays, cryptography and camouflage. In the following, we investigate how VO₂ could be used to dynamically modulate structural colored pixels.

5.1.4 All dielectric tunable structural color generation

Structural color generation by metallic nanostructures can operate beyond the diffraction limit but it has drawbacks [216] like restrained compactness of the functional elements and high resolution is backed by high loss, leading to peak broadening, implying limited number of distinctive colors. Whereas dielectric structures overcome these optical loss by exploiting Mie resonances. As explained in chapter 4, under some specific conditions, the resonances hosted by high refractive index dielectric nanoparticles is a combination of both magnetic and electric dipolar modes. The enhancement of magnetic response caused when incident light interacts with particles of size similar to the wavelength can provide an opportunity to design color filters that uses Mie resonance with higher order multipoles [66].

In addition we can further adjust the optical properties of metasurfaces using collective effects through coupling between resonators with a more general resonance category called Fano resonance [67] that is based on the constructive/destructive interferences between the radiated and reflected fields [68]. This kind of resonance can be used as another degree of freedom to engineer the structural color generation by interference between the directly reflected light and the guided resonances mode on a surface structure. This type of resonance gives us the flexibility in material choice, scalability for large scale fabrication and angular dependency.

Hence, in recent years, all dielectric nano-materials have been extensively used to realise a broad range of effects and functionalities [201, 217]. However, in the field of color filters, the application of dielectric materials was quite challenging because of the high loss in the visible range for standard high refractive index materials (ex: a-Si) which limited the higher saturation attainable by the dielectric metasurface. To overcome this limitation, TiO₂ appears as a promising alternative dielectric material with negligible visible range losses [218, 219].

Therefore, we studied square lattice of nano-rods of TiO₂ for structural coloration, as shown in figure 5.4a [220, 219]. TiO₂ is a material of interest because it is transparent in

the visible range, but compared to Silicon it has a lower refractive index and the resonant response of each nano-pillar is therefore weaker. But this situation can be altered by fabricating arrays of multiple resonators together. Furthermore, using a periodic arrangement of TiO_2 unit cells we can enhance Mie resonances by overlapping through phase matching the radiated Fano and Mie scattering resonances. Therefore with the following arrangements, it is possible to generate a collective enhanced structural color, that can be tuned by design, through adjusting the geometry of arrangement. The simulation relating to the following work was aided by my fellow doctorate colleague Raphaël Mermet-Lyaudoz.

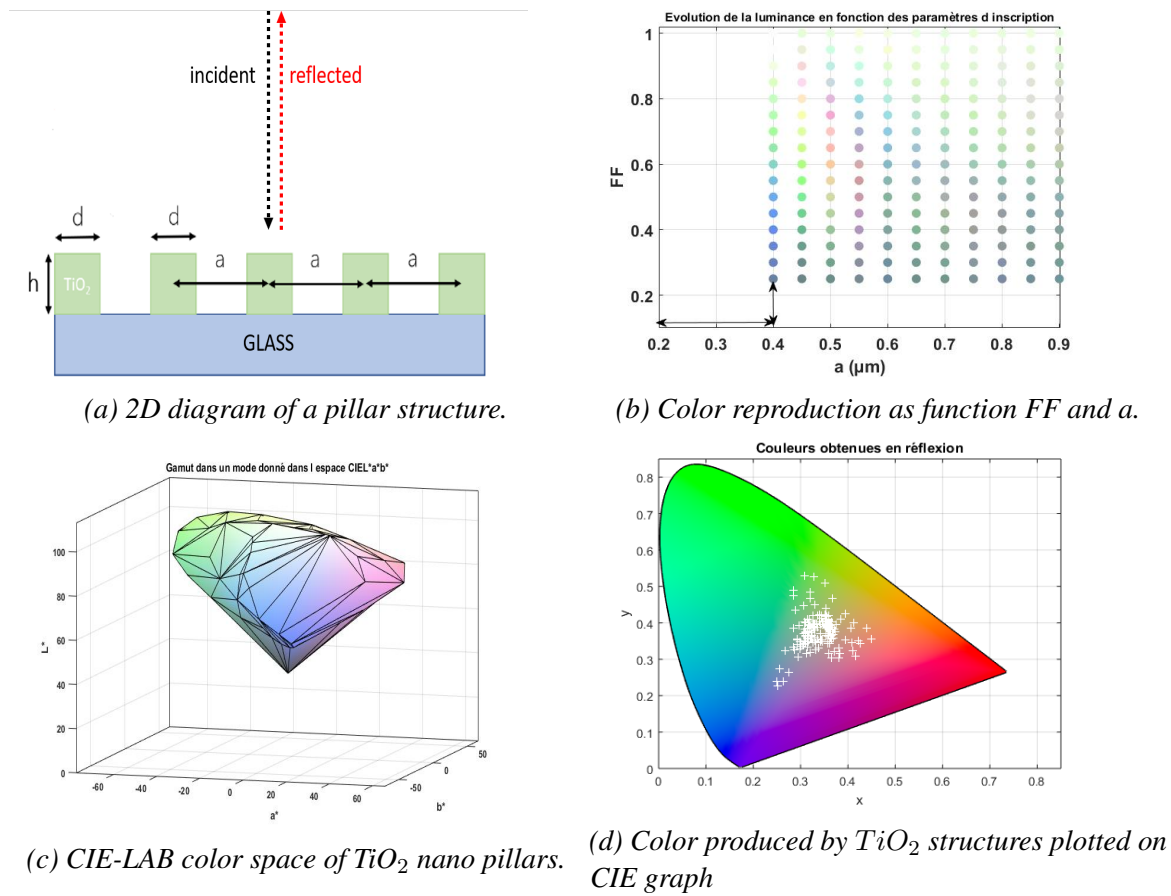


Figure 5.4: TiO_2 nanostructures and the constituent color reproduction with varying dimensional parameters .

We chose to simulate the structure such that, keeping the thickness h constant at 100nm, we vary the period a and the filling factor FF ($FF = \frac{d}{a}$, where d is the diameter) and map out the color thus obtained on a CIE diagram, as shown in the figure 5.2. The reflectance

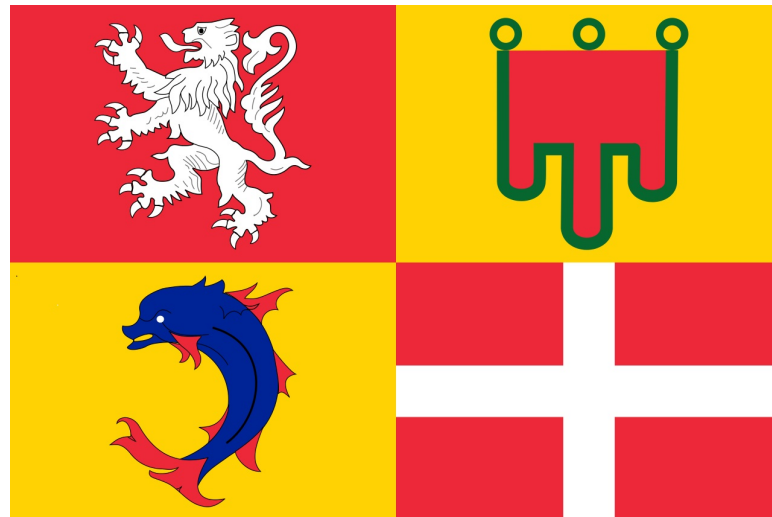
spectra for structures with different period a and different filling factor FF are computed with the rigorous coupled wave analysis method. On the other hand, to avoid complications related to representing colors in a 2D plot, we represent them in terms of CIE-LAB color space values [221, 222]¹.

In the above figure 5.4 we display the range of colors obtained by simulating variation in the FF and the period (a). This variation influences the Fano resonance and thus simulates the variation in interference leading to the destined color change. The resultant variation in the color is shown in the figure 5.4b. The 3D color gamut on CIE-LAB color space represents the overall range of the colors with their respective contrast coordinates, figure: 5.4c. This is similar to the 2D representation shown in the figure 5.4d, where we observe the clustering of the color values near the white reference of the TiO_2 nano-pillars. For a higher L value, we can expect faded colors. In order to correctly interpret CIE color values, it is important to state the correct white reference, for the case of TiO_2 , it is shown in figure 5.6a. With respect to a given white point, the CIE-LAB model is device-independent—it defines colors independently of how they are created or displayed. In addition, we also observe in figure 5.4b that for a given height (h) of 100nm the TiO_2 nanopillars simulates colors at $FF > 0.2$ and at $a > 0.4\mu m$, meaning the overall diameter of the pillars are large. In next section, keeping the same dimensional condition, we observe the color reproduction of VO_2 nano-pillars.

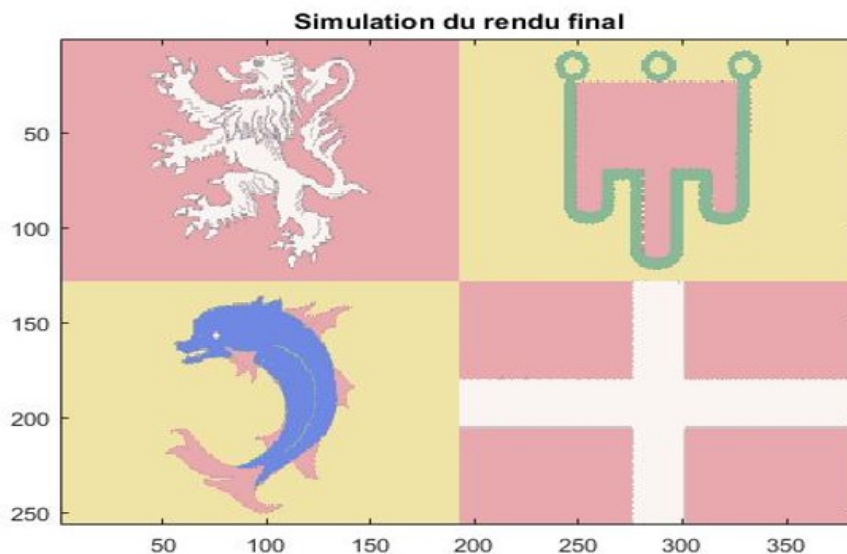
Following, we now reproduce a colored picture using the previously defined TiO_2 structures arranged in a pixel array. As shown in figure 5.5, we can observe that the colors of the picture represented are overpowered by white hue because the structural colors reproduced by TiO_2 nano pillars are close to white reference region. As we see from the figure 5.4c the color gamut L^* value ranges between 40 - 100, which indicates the contrast of the color compared to white illuminant. From the above observations we can conclude that,

¹CIE-LAB stands for CIE $L^*a^*b^*$, where L^* for the lightness from black (0) to white (100), a^* from green (-) to red (+), and b^* from blue (-) to yellow (+). International Commission on Illumination (CIE) in 1976 defined the color space so that the same amount of numerical change in these values corresponds to roughly the same amount of visually perceived change.

given the size of TiO_2 nano pillars, the color reproduction is weak in terms of its contrast. Following, in the coming section we evaluate and compare similar dimension but different composition material for the nano-pillars and understand better the color reproduction technique with possible tunability.

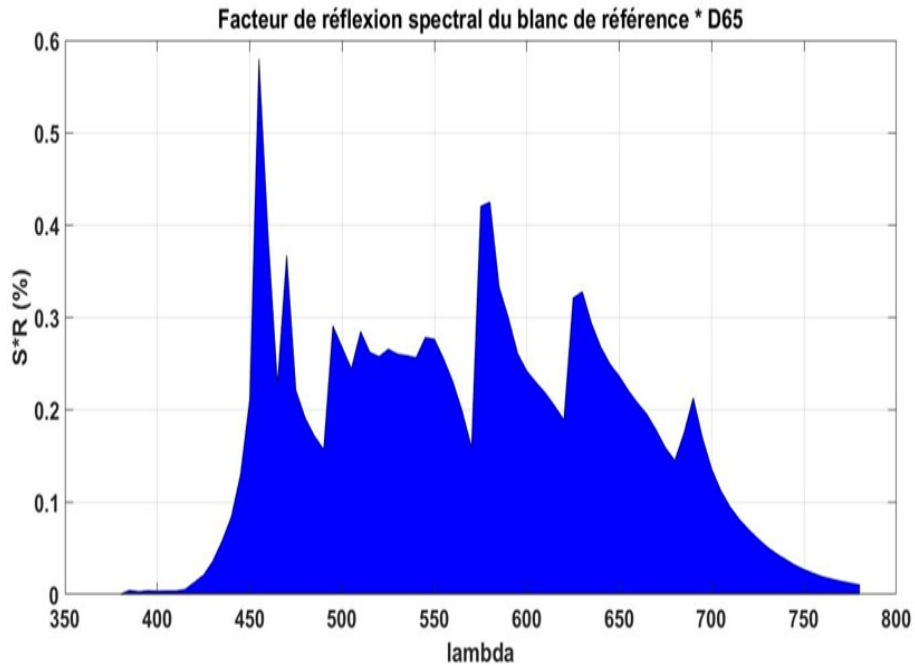


(a) The original image depicting the flag of Auvergne-Rhône-Alpes region

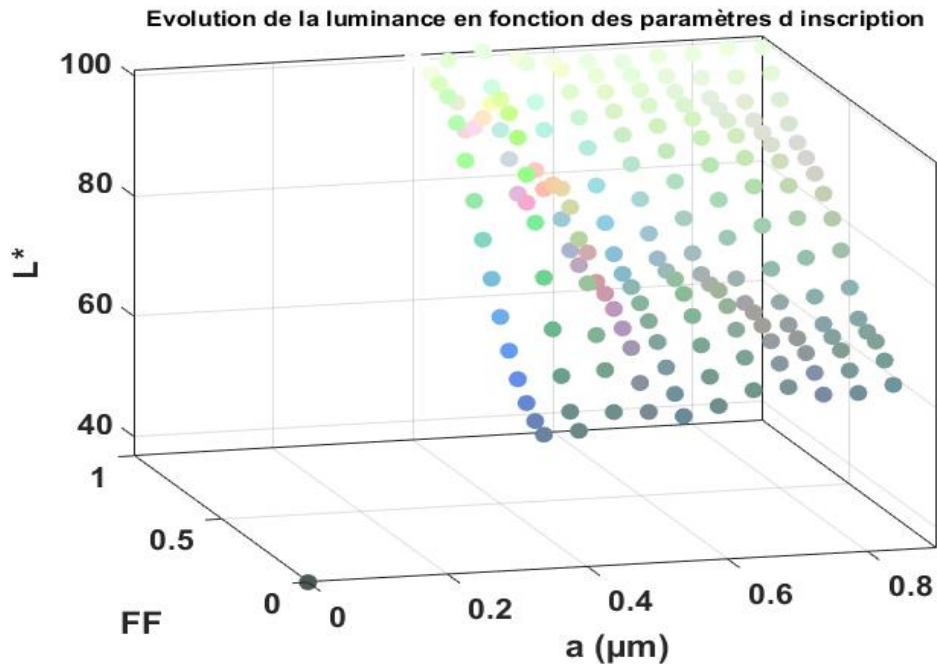


(b) The replicated image using the TiO_2 nano pillars.

Figure 5.5: Real and simulated image based on structural color of TiO_2 .



(a) CIE white illuminant D65 spectra of TiO_2 nano pillars. We observe that the D65 spectrum is not smooth and the peaks denotes absorption influenced by the structure.



(b) Variation Lightness (L^*) as a function FF and a

Figure 5.6: TiO_2 D65 white reference and the variation of color and L value as the function FF and a.

In the next section we discuss design strategy for dynamic tunability of the nano pillars,

where we replace the TiO_2 nano-pillars with VO_2 nano-pillars in a similar pixel array arrangement.

5.1.5 Tunable color generation using VO_2

Traditional transmissive and reflective displays typically have three sub-pixel regions with static red, green and blue color filters. These sub-pixels control the intensity of each basic color transmitted or absorbed to create arbitrary colors through a process called color mixing. On the contrary, a display built from a dynamic color changing surface can eliminate the need for individual sub-pixels, increasing resolution without reducing pixel dimensions. While all displays are based on light emission, here the display would be a reflective or transmissive one. And would therefore only require daylight or ambient lighting, reflected off the device [223]. Another possibility is to use it as a transmissive device for augmented reality.

The need for tunable structural color arises from the limitations faced by the current industry. Apart from larger pixel size, most of the tunable pixels in displays industry uses liquid crystal's (LCs), which are big (hundreds micron-scale), have a slow response time to dynamic color switch and are difficult to recycle. The tunability of structural color has been previously studied and demonstrated but they involved liquid crystal's (LCs) [224] or chemical transformation [225] or mechanical changes [226]. In our case we demonstrate through simulation the tuning of structural color using VO_2 as the tuning element and we further discuss two different ways for achieving the tunability using VO_2 in different arrangement.

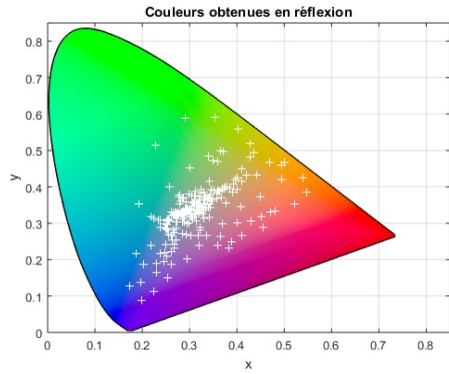
VO_2 nanostructures

Similar to previous nano-pillars structure of TiO_2 , we simulate the reflectivity of VO_2 nano-pillars on silica for structural color generation and leverage the IMT of VO_2 to dynamically tune these structural colors. The idea behind is that, in addition to the transition property,

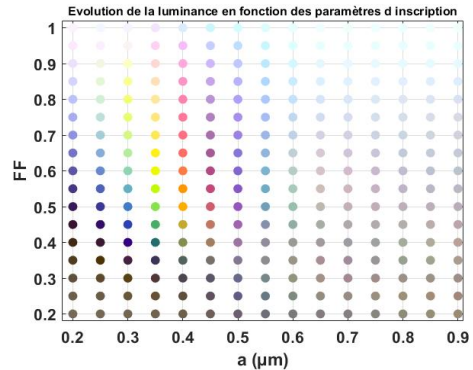
compared to TiO_2 , the complex refractive index of VO_2 is larger in the visible range with lower absorption value. As a result we can achieve good index contrast compared to external environment. Secondly, at the transitioned metallic state, the refractive index of VO_2 is changed along with the absorption value, affecting Mie resonance by shifting the electric and magnetic dipole hosted by dielectric VO_2 . Additionally, the radiated field is highly influenced by the increasing absorption during IMT for metallic VO_2 , thus altering Fano resonance value. And therefore we expect to see some variation in the color.

The variation in the structural reproduction by each state of VO_2 nano-pillars can be observed in Figure: 5.7b and Figure: 5.8b, comparing the simulated color palettes. As displayed in Figure 5.7, the variation in FF and period of the nano-pillars, produces a significant range of colors. Even at the natural insulating state we observe sharp contrast in the colors produced by the VO_2 nano-pillars when compared to TiO_2 . The dimensions of the structures were kept the same and we observe that VO_2 nano-pillars simulate colors at lower values of FF and a , meaning smaller diameter for the nano-pillars. Therefore in addition to bright colors and the transition, we have the size advantage. Because VO_2 has a higher refractive index compared to TiO_2 , the color thus produced by VO_2 nanostructures are more dispersed, covering larger area in CIE diagram compared to the TiO_2 structures.

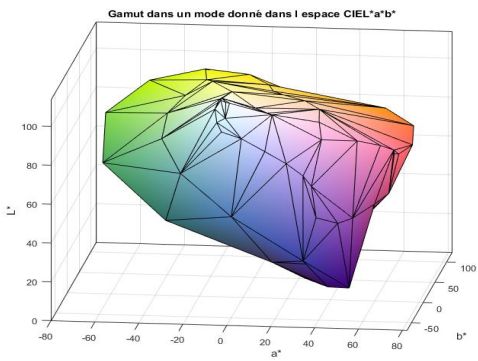
Comparing the color production in insulating (5.7) and metallic (5.8), we observe a minor shift in the chromaticity of the reproduced colors. It could be clearly observed in figure 5.9, where the white dots represents the colors reproduced when VO_2 is metallic and black when it is insulating. We see that, the points covered when VO_2 is insulating is much far spread as when it is metallic. This change in chromaticity can be owed to the change in optical properties during the transition, affecting both Mie and Fano resonances. In figure 2.18 in Chapter 2, we see the evolution of n and k of VO_2 thin-film. We observe greater index contrast at higher wavelengths than at visible range. Therefore, this shows a promising direction for the advancements in dynamic color tunability exploiting VO_2 material's properties as foundation rather than involving additional gases or chemicals for



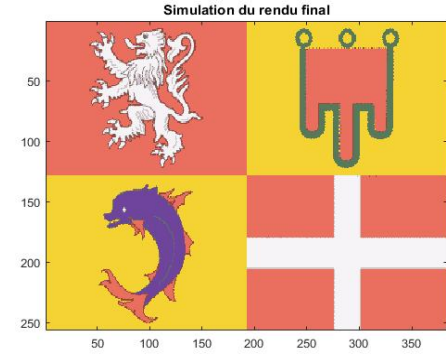
(a) VO_2 colors on CIE map



(b) Color reproduction as function FF and a



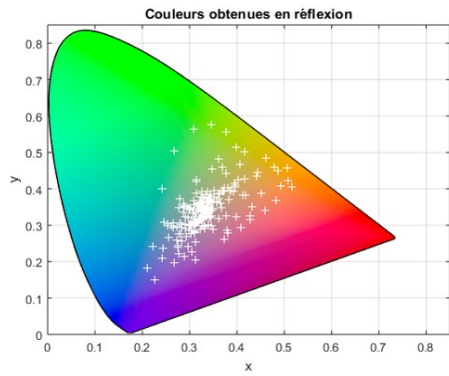
(c) CIE-LAB color space of VO_2 nanowires.



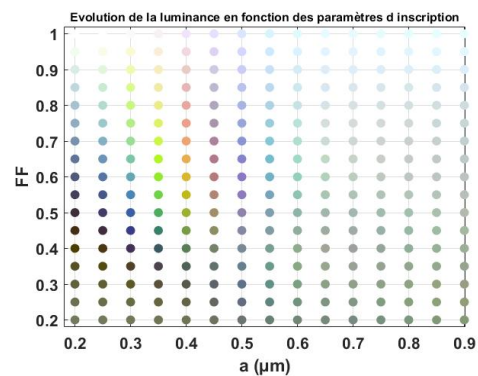
(d) The replicated image.

Figure 5.7: The structural color reproduction by VO_2 in semiconductor state.

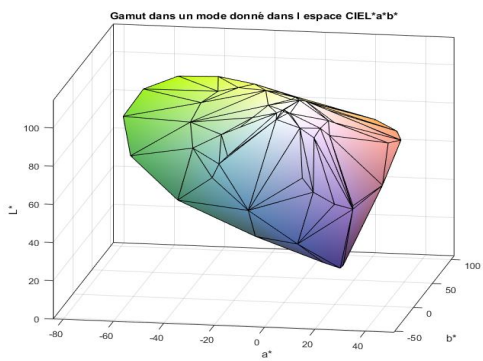
color reaction such as in recent studies [227, 228, 229, 230, 231, 232, 233].



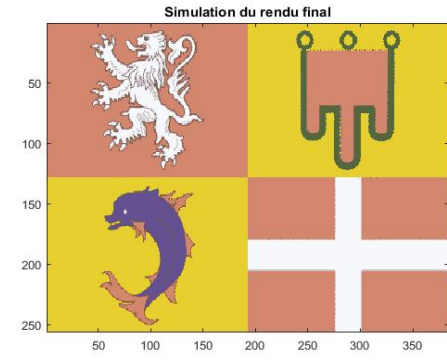
(a) VO_2 colors on CIE map



(b) Color reproduction as function FF and a



(c) CIE-LAB color space of VO_2 nanopillars.



(d) The replicated image.

Figure 5.8: The structural color reproduction by VO_2 in metallic state.

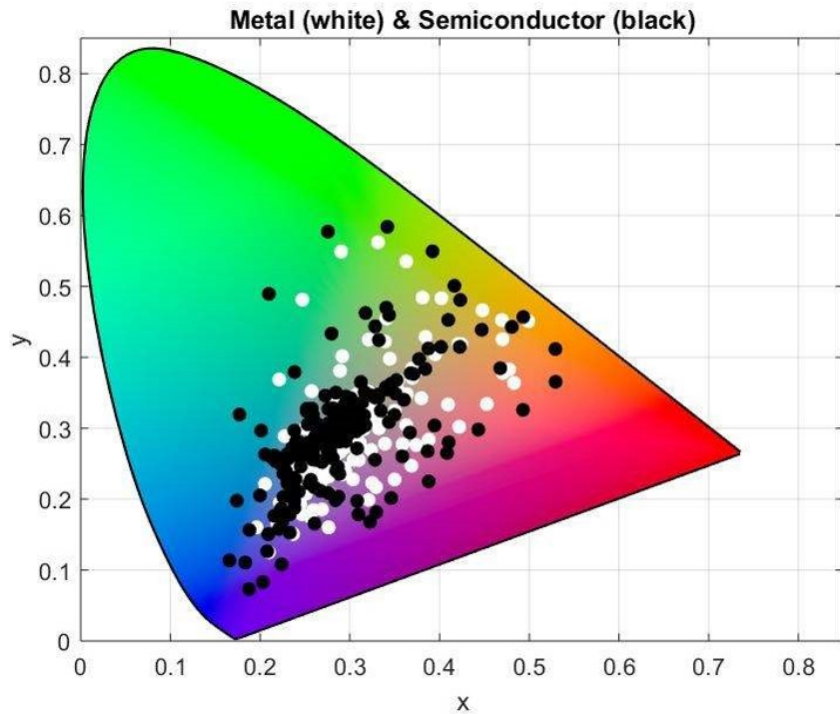


Figure 5.9: VO_2 nano structure color gamut comparison

TiO₂ nanostructures on VO₂

We now discuss an alternative structure composed of the following layers; (1) Substrate (SiO₂), (2) VO₂ layer, (3) TiO₂ nano-pillars and the external medium (4) air. The color reproduction initiating Fano resonance [234] depends on the interference between the directly reflected light and the local guided resonances mode on a surface structure. When this localized guided mode interferes with reflected light from the surface at same phase, the constructive interference produces a sharp reflectance peak. The concept behind this structure with VO₂ thin-film is that, for Fano resonance, the guided modes that propagate in the planar structure of the TiO₂ layer "feels" an equivalent index (n_{eff}). The evanescent part (tail) of the mode should lie in the vicinity of the boundary of VO₂ layer or lie in the VO₂ layer, so that during the transition the optical change in the VO₂ layer would affect the overall effective index (n_{eff}) and thus affecting the interference.

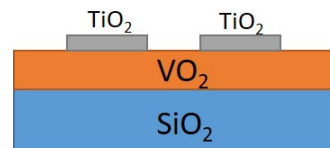
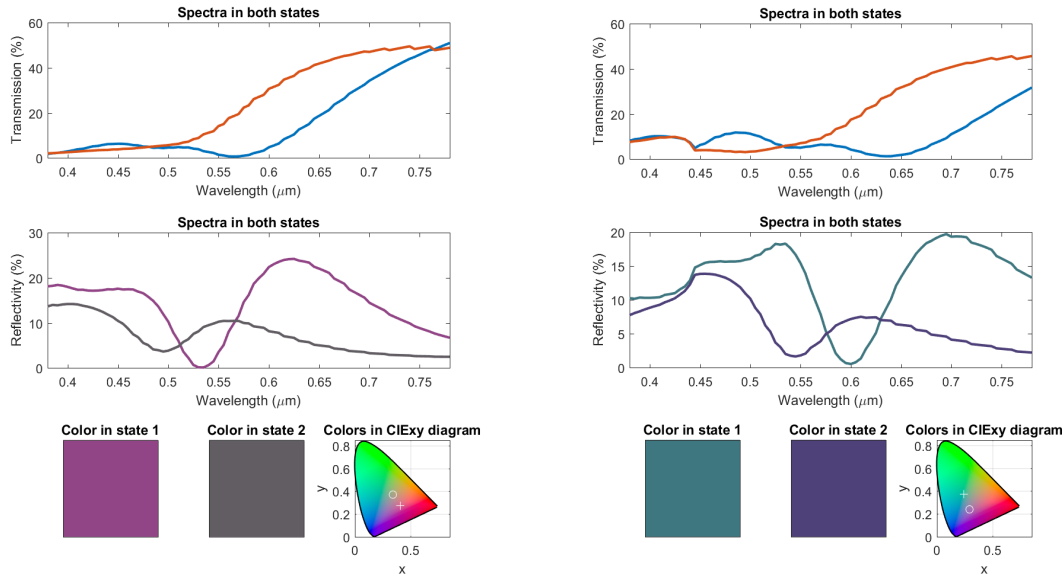
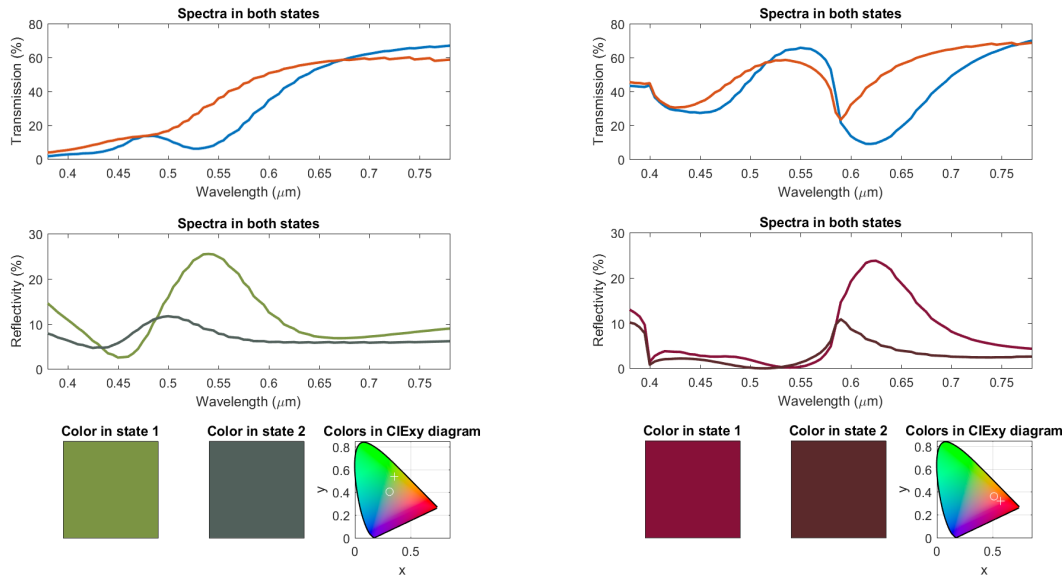


Figure 5.10: TiO₂ metasurface fabricated on VO₂ thin film deposited on SiO₂



(a) $\text{FF} = 0.11, P = 0.25 \mu\text{m}, \text{VO}_2 \text{ thick} = 0.19 \mu\text{m}$ (b) $\text{FF} = 0.11, P = 0.3 \mu\text{m}, \text{VO}_2 \text{ thick} = 0.23 \mu\text{m}$



(c) $\text{FF} = 0.12, P = 0.25 \mu\text{m}, \text{VO}_2 \text{ thick} = 0.12 \mu\text{m}$. (d) $\text{FF} = 0.1, P = 0.4 \mu\text{m}, \text{VO}_2 \text{ thick} = 0.13 \mu\text{m}$

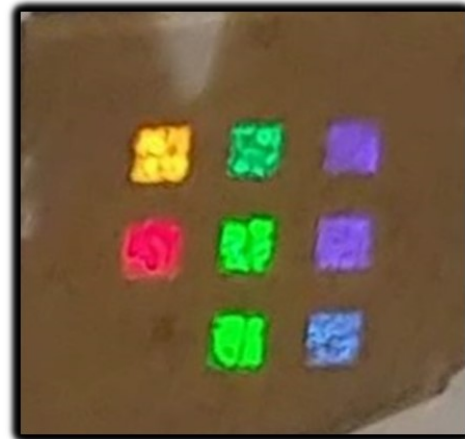
Figure 5.11: TiO_2 nanostructures on VO_2 , the color switch observed at both the states of VO_2 .

The resultant reflected color produced was simulated for both the states of VO_2 . The interesting color switches thus observed are given in the figure below 5.11. The transition of VO_2 affects the Fano resonance resulting from interference between the radiation waves of Mie resonance and directly reflected waves in a way that we observe the color change. This shows the flexibility and possibility of using VO_2 to induce tunability property for the

structural color production. Following, we deposited TiO_2 nano-pillars on the surface of a VO_2 thin-film, as shown in the figure: 5.12. This technological step was done by Marco Abbarchi and his team at University Aix-Marseille.



(a) TiO_2 nanopillars arrays on VO_2 thin film.



(b) Different viewing angles showed variation of colors for different pixel arrays.



(c) Structural color observed at an undefined angle 1.



(d) Structural color observed at an undefined angle 2.

Figure 5.12: Photographs of TiO_2 nano pillars viewed at (a) normal incident and (b) at an angle. For the images (c) and (d) we observe the different structural colors at different angles, as they are highly sensitive to angle.

We observe zero reflection from the nanostructures at normal incidence from the figure 5.12a and when observed from certain angles we see vibrant structural colors, represented in figure 5.12b. The structural colors in the figures 5.12c and figure 5.12d can be observed with perfect distinction from each pixel, even though the experiment was done to measure the temperature dependence of the color switching but we observed stronger angle dependence

compared to temperature dependence. Therefore it might seem the color switching is due to IMT but it is mainly due to the angle of observation. We need to further evaluate the temperature dependency of the sample with help of a steadier camera observation setup.

5.1.6 Discussion and future perspectives

In summary, Mie resonances supported by dielectric nanostructures can be used to create highly saturated structural colors. Additionally, we have presented two different approaches for achieving tunable structural color generation with VO₂ as a tunable element. By tuning the VO₂ transition state, the recorded color switch were presented in a CIE diagram. Based on the properties of Fano resonances as well as Mie resonances, the reflected colors have also been achieved from VO₂ metasurface and thus can generate bright, high-contrast, and high resolution structural colors and even colorful images. Even though these preliminary results are promising, there is still challenge of achieving perfect tunability in color reproduction. The ultra-thin size of the color filters has the potential to be integrated on-chip. We believe this research will be important for the realization of optical display, imaging, data storage. And have potential applications like in cryptography, security, imaging, optical data storage and further optical devices that rely on efficient and simple color tuning mechanisms. Although, mass production remains still a challenge and, there is still a large space to explore in relation to structural colors before commercialization. We believe colors generated from metasurfaces can be extensively used to take the place of chemical pigments, and dramatically improve quality and sustainability of the environment in the future.

5.2 VO₂ metasurface for tunable perfect absorption

Metamaterial based perfect absorbers have gained quite a traction in the recent years [235, 236]. An electromagnetic (EM) perfect absorber is a device in which all the incident radiation is absorbed at the operating frequency. The initial applications for absorbers were in stealth operation in range of RADAR or microwave/ radio wave operations, reducing radar cross section [69, 70]. More recently EM absorbers are used to reduce EM interference by absorbing spurious EM radiations. The control of light absorbance plays a major role in our current photonic industries and can have strong impact in the solar energy harvesting [71, 72], bolometers, chemical and biological sensors. Metamaterials are designed to modify the permeability (μ) and the permittivity (ϵ) such that their impedance match the free space impedance, creating reflection-free artificial medium. This can be highly useful in creating perfect filters with limited losses. In this section we design and experimentally demonstrate design strategy for a VO₂ based tunable metasurface perfect absorber, composed of Si resonators, supporting both electric and magnetic Mie mode.

5.2.1 Concept

As explained in the previous chapter, in some specific cases, dielectric nano-particles can support both electric and magnetic resonances [76, 77]. In a dielectric nano-particle, a Mie magnetic resonance originates from an excitation of a particular electromagnetic mode in the particle. This excitation occurs when the effective wavelength of light inside the particle becomes comparable to the particle's size, exhibiting a circular displacement current of electric field [78, 79]. The capability of exciting both electric and magnetic responses is of great interest, but simultaneously exciting them gives an additional advantage for accurate light manipulation. Moreover, the spectral positions of electric and magnetic dipole resonances can be tuned by varying the geometry of a dielectric resonator so that desired scattering properties are achieved. This could be key as it gives another degree of freedom

to engineer a metamaterial's response by design [80, 78]. More importantly, constructive or destructive interferences between the fields of electric and magnetic dipole resonances, can affect the particle's scattering properties [237]. This phenomenon was studied by Milton Kerker in 1983, his study revealed that one can achieve an asymmetric field radiation with zero backward scattering or zero forward scattering under proper combinations of electric and magnetic dipoles in subwavelength magneto-dielectric particles. According to Kerker's first condition, when $\mu = \epsilon$, the incident wave experiences a zero backward scattering or in other words, no reflection. The second Kerker condition produces a zero forward scattering (i.e. no transmission) when, μ and ϵ satisfy the condition $\epsilon = \frac{(4-\mu)}{2\mu-1}$.

Kerker's conditions could occur in small high-index dielectric nano structures by enabling the spectral overlap between the electric dipole (ED) and magnetic dipole (MD) sustained by Mie resonances. It has been shown that silicon nano-particles can support electric and magnetic dipole [238, 239] and it has also been demonstrated that using cylinders rather than spheres allows for tuning of the spectral spacing between the electric and magnetic lowest order resonances [240, 241]. A full overlap between the ED-lattice resonance and MD resonances of nanoparticles in certain spectral range realize the resonant lattice Kerker effect (resonant suppression of the scattering or reflection) [242, 243]. Where a strong suppression of reflected light is observed due to the destructive interferences between EM waves scattered by the ED and MD of every nanostructures [244, 240].

In our work, we assemble specifically designed Si nano-resonators into two dimensional periodic arrays fabricated on VO₂ thin-film. The principle is as follows: when VO₂ is insulating, the ED and MD resonances overlap and we thus fulfill the Kerker conditions and obtain a zero backward scattering. As VO₂ is lossy even in its insulating state, most of the light is absorbed and we therefore obtain a near-perfect absorber. On the other hand, when VO₂ becomes metallic, the MD resonance disappears and the Kerker condition is no longer fulfilled. However, as the absorption of VO₂ largely increases, we still maintain a near-perfect absorption regime, but spectrally shifted due to the refractive index modulation of

VO_2 . The phase state of the VO_2 layer therefore defines the interaction between the incident light and two resonant modes and control the spectral position of the perfect absorption. We further demonstrate experimentally that, leveraging the reversible tuning of VO_2 we measure a regime of tunable coherent perfect absorption reducing metasurface reflection by more than two orders of magnitude at 1555nm wavelength. The proposed design concept is shown in figure: 5.13.

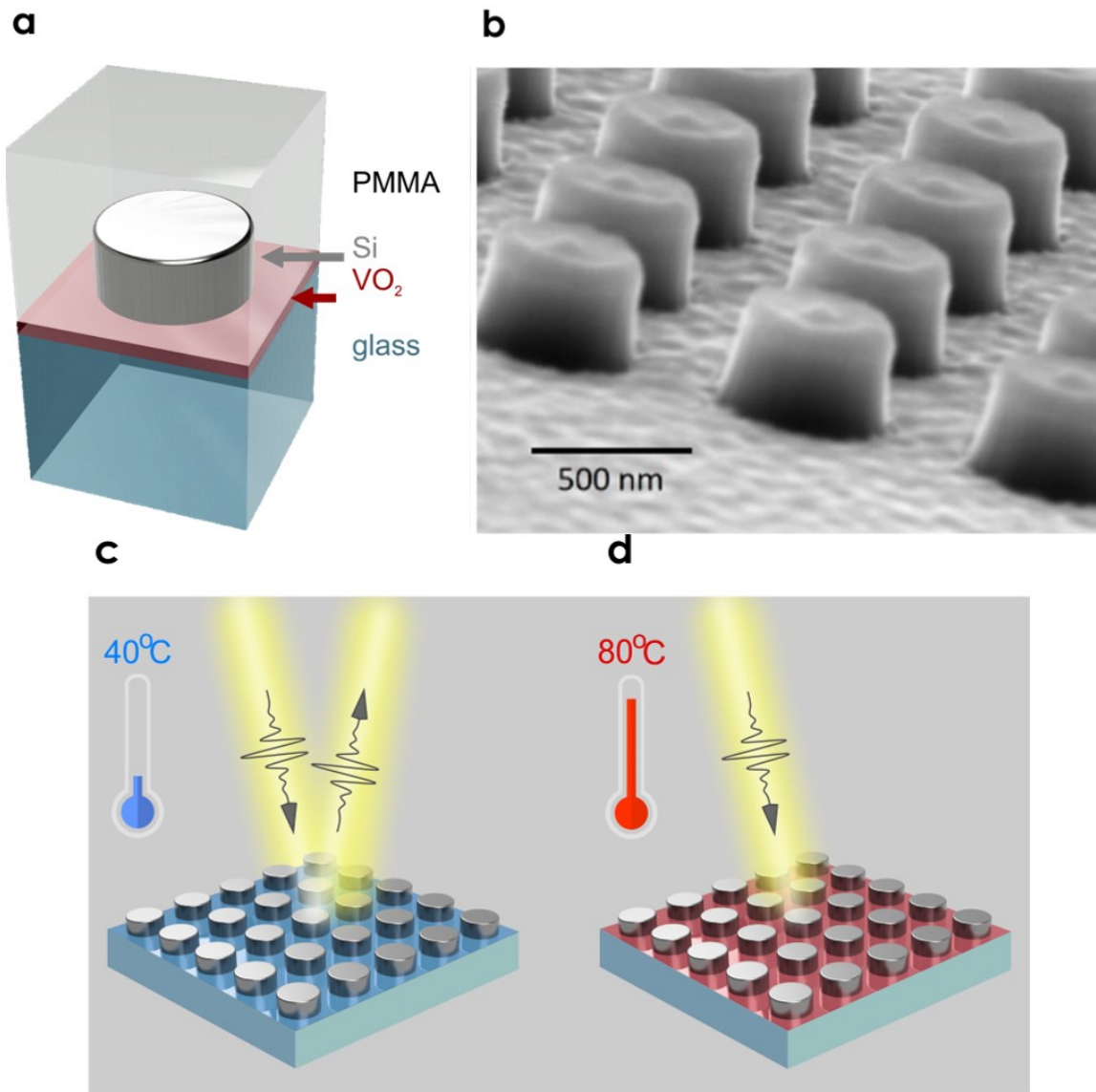


Figure 5.13: a) Design concept: a silicon meta-atom is embedded into glass/PMMA surrounding with a buried thin VO₂ layer. VO₂ thickness: 25 nm, Si disk height: 240 nm, disk radius: 270 nm, square lattice period: 800 nm, PMMA layer thickness: 400 nm and b) Electron microscope image of the fabricated Si-VO₂ metasurface prior to the PMMA coating. c) Functionality concept: at low temperatures, the metasurface reflects light at a designed wavelength, and d) at high temperature the light is absorbed by the metasurface.

Supporting numerical calculation related to metasurfaces were performed in CST Microwave Studio. This work was done in collaboration with Yuri Kivshar's team from Australian national university and Shriram Ramanathan's team from Purdue University, US.

5.2.2 Metasurface Design and Simulation

Design

The silicon nano-disks were designed on the basis of EM simulation study on absorption, transmission and reflection as a function of Si nano-disk diameter. The simulation was rendered with Si nano-disks fabricated on VO_2 thin-film with SiO_2 as substrate. As shown in the figure 5.14, we see a perfect absorption region in the telecom range.

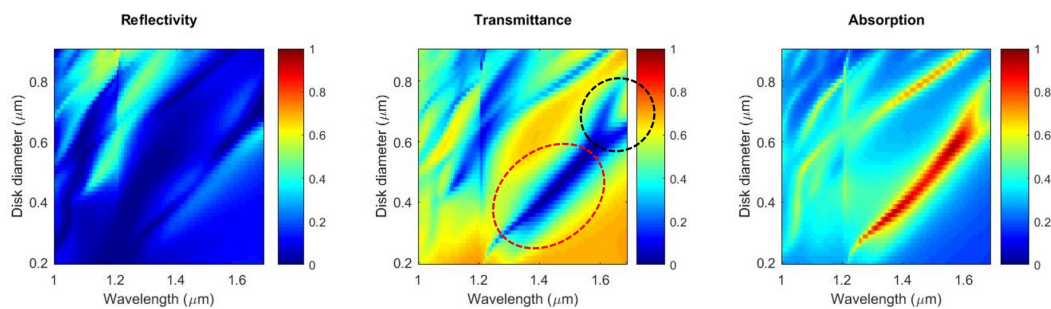


Figure 5.14: EM simulation study on absorption, transmission and reflection as a function of Si nano disk diameter, with a period of 830nm and VO_2 is insulating. The red dotted circle shows perfect absorption (transmission is near 0) region due ED and MD overlap and black dotted circle shows the split in the dipole overlap.

Consequently we simulated the similar disk diameter dependency on the absorption, reflection and transmission when VO_2 is metallic. And we observe in figure: 5.15, contrary to the previous result, only one resonance (ED) when VO_2 becomes metallic but we keep a strong absorption. We also scanned the dependency of absorption, reflection and transmission on temperature variance in VO_2 , as displayed in figure:5.16. For a disk diameter of 540 nm and a period of 830 nm we see a large shift in the perfect absorption region as a function of the change in absorption strength upon the IMT of VO_2 as the temperature is increased.

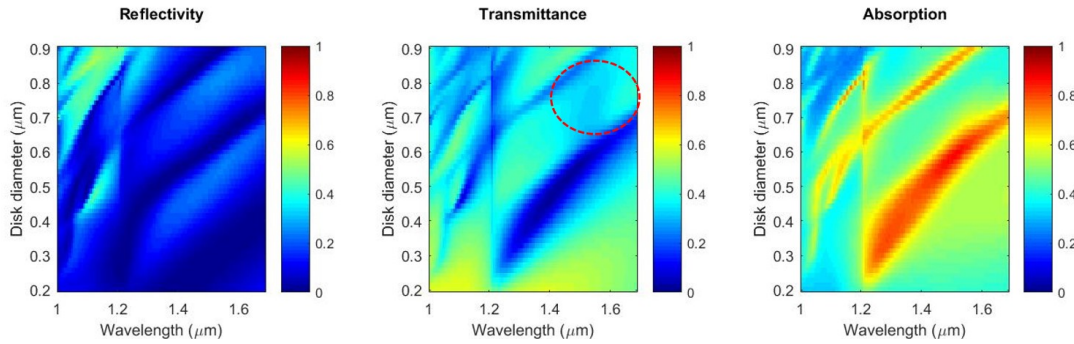


Figure 5.15: EM simulation study on absorption, transmission and reflection as function of Si nano disk diameter, with a period of 830nm and VO₂ is Metallic. The red dotted circle shows disappearance of the MD when VO₂ becomes metallic but we keep a strong absorption.

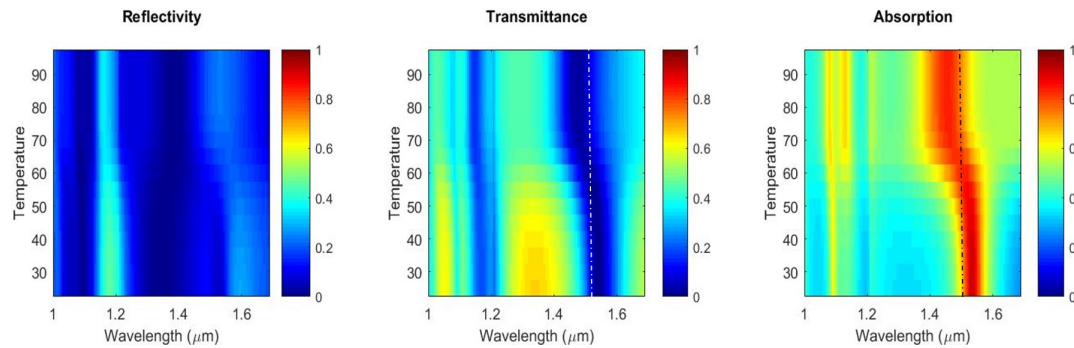


Figure 5.16: EM simulation study on absorption, transmission and reflection of Si nano disk diameter 540nm scanned as function of temperature, with a period of 830nm. The dotted line shows the wavelength of interest 1.55 μm, for our tunable near-perfect absorption device.

5.2.3 Metasurface Fabrication

The fabrication of the Si resonator metasurface starts with a 25 nm thin VO₂ layer deposited on quartz by magnetron sputtering from a V₂O₅ target under Ar/O₂ partial pressure, similar to the conditions and techniques discussed in Chapter 2. The deposition was performed at an elevated temperature of 750°C, in order to maintain the crystalline growth of VO₂. After a thin layer of SiO₂ is deposited to protect the VO₂ layer. Following, a 240 nm thick layer of amorphous silicon (a-Si) was deposited by PECVD (plasma-enhanced chemical vapor deposition). The precursor gas used is SiH₄ at a temperature 300°C. figure: 5.17.

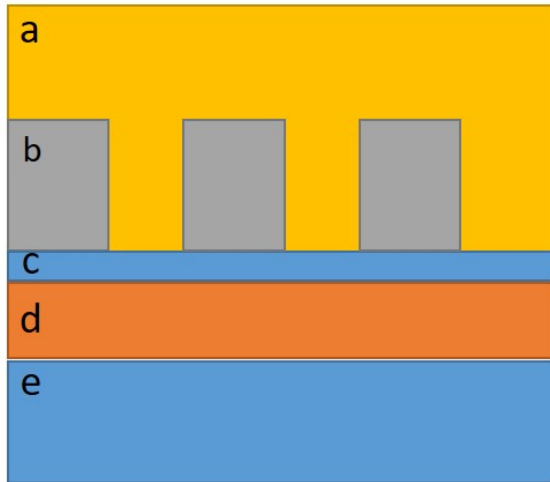


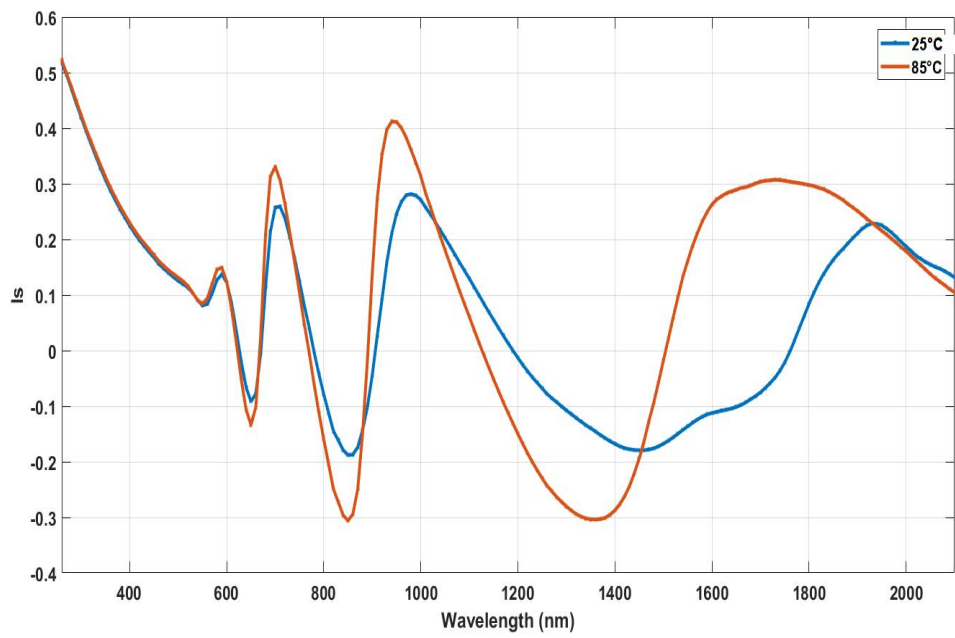
Figure 5.17: Device sketch of the a-Si metasurface on VO₂ thin films. The layers are defined as: a. PMMA, b. a-Si nano disks, c. SiO₂ protective layer, d. VO₂ thin film and e. SiO₂ substrate layer

The next step involves e-beam lithography for patterning the metasurface; Hydrogen Silsesquioxane (HSQ) resist is spun on the sample and patterned using E-beam lithography. Subsequently, TMAH developer is used to develop the HSQ resist which is then used as a hard mask to transfer the patterns into a-Si via ICP-RIE (plasma) dry etching with Cl₂/Ar. Finally, a 400-nm-thick layer of PMMA is spun on the sample, in order to provide an appropriate index contrast and protective layer. Finally, a small part of the sample is covered by a 200-nm-thick gold layer serving as a reference layer for the reflection measurements.

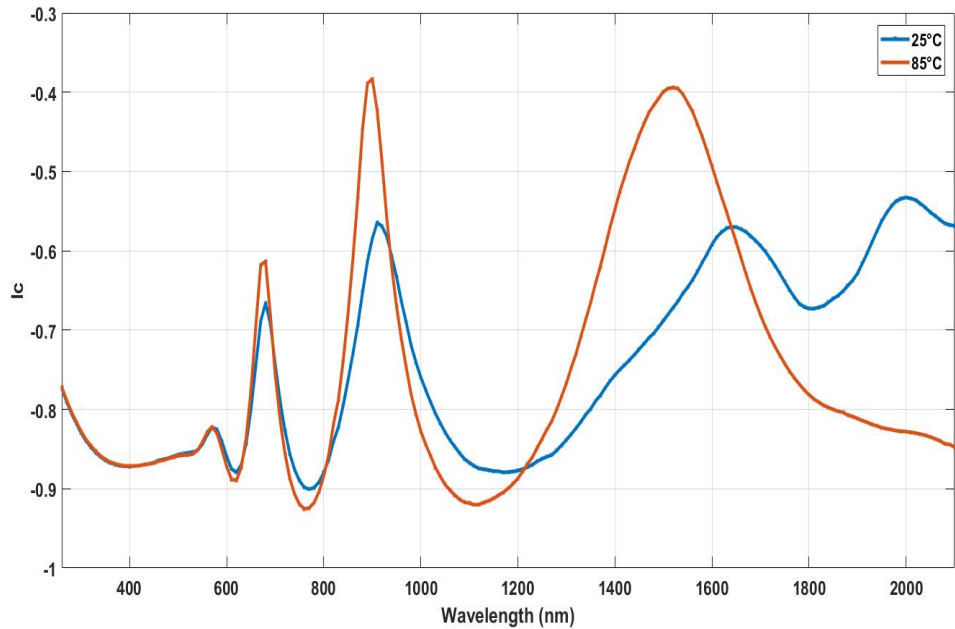
5.2.4 Metasurface Characterization

The first step for characterization was done on 25nm VO₂ on SiO₂, prior to the fabrication of metasurface. The results of which are mentioned in Chapter 2. Spectroscopic measurement were performed at various stage of deposition as to analyse the effect of the fabrication process on the VO₂ thin-film's transition properties. It was observed that direct deposition of a-Si on VO₂ thin-film, inhibits the IMT, therefore we chose to modify the fabrication process to add a protective layer of SiO₂ circumventing the effect of a-Si deposition on the transition. Following the deposition of metasurface and the subsequent lithography, temperature controlled spectroscopic ellipsometry was performed at 25°C and 85°C to check

the VO₂ switch quality after each technological steps. Figure 5.18: shows the I_s and I_c parameters as a function of temperature. This measurement was conducted on the final stage of device fabrication, after multiple stages of etching and deposition. From the figure 5.18 we can clearly observe the variation in I_s and I_c parameters, owing to the transition of the VO₂ indicating that the VO₂ haven't been damaged by the different technological steps.



(a) I_s values as a function of temperature



(b) I_c values as a function of temperature

Figure 5.18: I_s and I_c values as a function of temperature at the final stage of the fabrication of the metasurfaces. Analysing the figure, we see the effect of VO_2 transition, suggesting successful completion of all the stages of fabrication.

To measure the VO_2 -induced optical tunability of the metasurface, the sample was

placed on a heat cell enabling $\pm 0.1^\circ\text{C}$ temperature control. A broadband light source (halogen lamp) is focused on the devices through a 10x objective and the reflection from the metasurface is collected with the same objective. Reflected light is then dispersed in a spectrometer and detected with an InGaAs IR camera. The setup response is calibrated using the gold reference layer deposited on the sample. To measure the reversible tunability, the temperature is raised from 23°C to 90°C and back to room temperature. The heating-cooling cycle is repeated 10 times with no noticeable changes in the sample performance. A spectrum is collected every 2°C as shown in the figure 5.19.

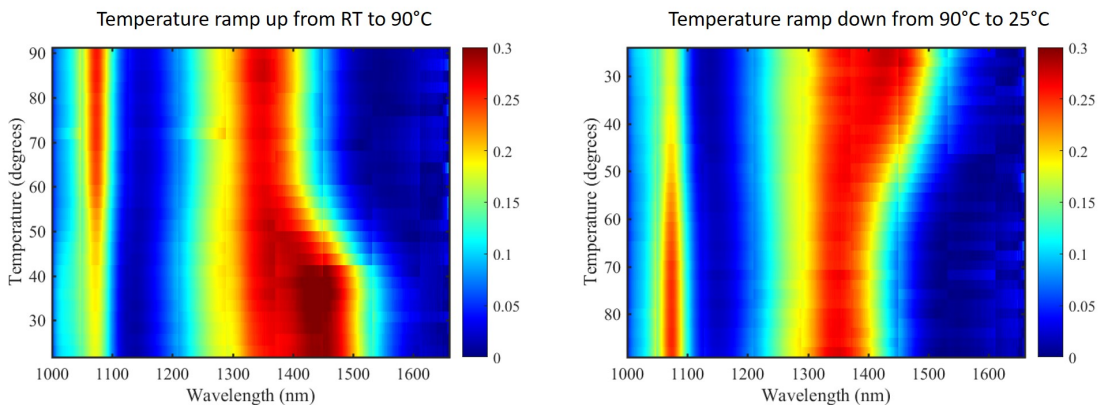


Figure 5.19: Reflection measurements versus temperature of the metasurface. We observe a perfect absorption at 1550 nm when the phase of VO_2 is metallic. And we also observe the tunability and reversibility as due to temperature induced phase modulation of VO_2 .

In Fig.5.20(a), we show two reflection spectra corresponding to insulator (40°C) and metal (80°C) phases of VO_2 layer. Fig. 5.20(b) emphasizes the experimentally observed reflection contrast between the two states. At the wavelength 1555 nm that corresponds to the fiber communication C-band, the modulation depth in reflection exceeds two orders of magnitude. Finally, in Fig.5.20(c) we trace the reflection at 1555 nm and observe a hysteresis behavior of reflection versus temperature. In the region $30^\circ\text{C} - 70^\circ\text{C}$ the metasurface reflection can be in one of the two states depending on the history of heating-cooling cycles and therefore presents an interesting memory effect.

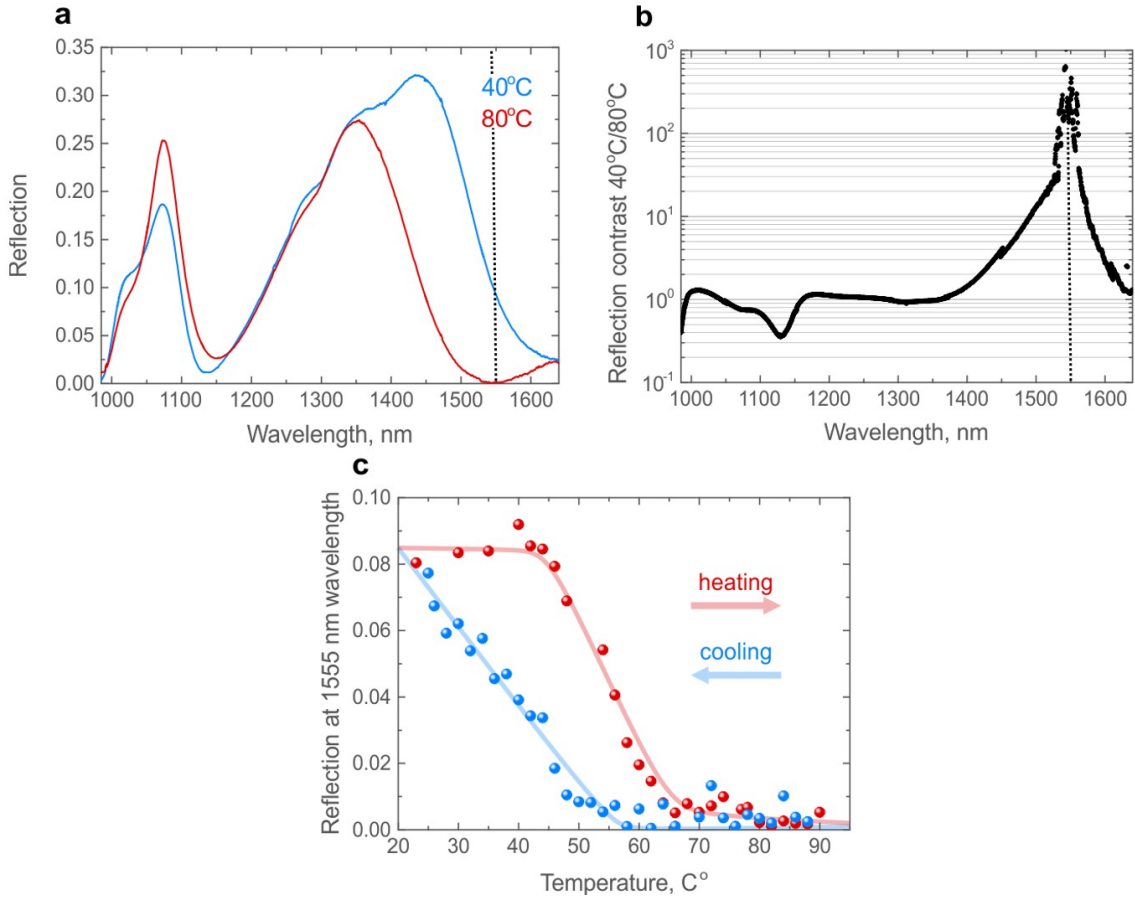


Figure 5.20: Experimental results on the tunable reflection of the Si-VO₂ metasurface. (a) Reflection spectra for two temperature points: 40°C (a dielectric phase of VO₂) and 80°C (a metallic phase of VO₂). (b) Reflection contrast between the two temperature points. (c) Reversible temperature tuning of the metasurface reflection at 1550 nm wavelength exhibiting a hysteresis-like behavior.

5.2.5 Conclusions and outlook

We have demonstrated, for the first time to our knowledge, tunable Mie-resonant silicon metasurfaces leveraging the transition of VO₂ to control the spectral overlap between the ED and MD resonances. This dynamic tuning was shown to produce a two-order-of-magnitude modulation of the metasurface reflection. We have also demonstrated the metasurface optical response further features a hysteresis behavior, hinting towards the possibility of memory state devices. Although we faced some fabrication issues with the IMT of VO₂, which we believed were caused by the deposition procedure of the amorphous-silicon, we were able to overcome this issue, by carefully fabricating a protective layer of SiO₂ on VO₂ and evaluated

the switching of VO₂ at each steps of fabrication. Therefore the successful fabrication of this device, paves the way to nanoscale optical switches, modulators, and sensors based on all-dielectric resonant metasurfaces.

CHAPTER 6

CONCLUSION AND FUTURE PERSPECTIVES

Nanophotonics have an incredible potential that should play an important role in the coming technological revolution. With the growth in the artificial intelligence and neural computing fields, the demand for on-chip computation and autonomy has propelled the nano-designing to improve the computing efficiency per unit area for the current architecture. In lieu for such revolution, the microelectronics industry is currently facing a strong bottleneck, due to the intrinsic limitations of electronic interconnects. Nanophotonics is one of the possible solution to improve the overall performance of microelectronic systems e.g. by using photonic links as an on-chip information carrier. If we consider the hardware standards, Silicon plays a major role in both the microelectronics and the photonics sector, but the electro-optical modulation properties are inherently weak in Silicon. Therefore, the majority of demonstrated devices in Silicon photonics are passive and numerous researches are now focusing on hybrid technologies. The aim of my thesis was to tackle this problem by introducing active materials in hybrid platforms to design and demonstrate dynamically reconfigurable nanophotonic devices.

VO_2 has been at the forefront of active research for understanding the physics behind its phase change properties and its adaptability to modulation devices for various application. Even though VO_2 has intriguing physics and extraordinary properties it also presents drawbacks for photonics. The high inherent absorption of VO_2 in the telecommunication range represents a major disadvantage for its application in integrated or cascaded nano/micro devices. My task in this thesis aimed at investigating the potential of VO_2 for nanophotonics, with a specific emphasis on how to circumvent these drawbacks and to design and demonstrate efficient integrated devices. Chapter 1 and 2 are dedicated to understand the phase transition in VO_2 and its associated physical mechanisms. Following this study, we were

able to create an optical model which successfully describes the permittivity dispersion of VO₂ in all of its states, ranging from insulating to fully metallic as well as all the mixed metal-insulator partial states in between.

Even though VO₂ has been widely studied, its full potential has not really been exploited due to its high inherent optical absorption losses. Through the design strategy in Chapter 3, we try to leverage the inherent absorption of VO₂ as an advantage to create an efficient optical modulator. The theoretical studies performed in Chapter 1 and Chapter 2 have been fundamental in designing such a device. The electromagnetic simulation has helped us designing optimal dimensions and geometries for the proposed modulator. Despite the un-optimized fabrication process, we have seen that it is possible to realise an active modulator leveraging the transition properties of VO₂. While most VO₂-based modulators proposed so far rely on the end states of VO₂, which means either ON or OFF state, we propose an optional advantage of such a tunable modulator device in the field of neural network computing, wherein the intermediate states of VO₂ plays a major role in controlling the power coupling, creating a power filter. Seen in terms of Neural computing, this filter can act as a weight bank, which is an essential component for realising a machine learning algorithm in an all-optical system.

In chapter 4, we manipulate the material dimensions influencing the ED and MD resonances sustained by the material. Contrary to the previous chapter, where tunability depends on the states of VO₂, here, additional external dimensional control over ED and MD along with the inherent IMT of VO₂, give us a better control over the manipulation of light. And thus demonstrating that, by creating a composite metamaterial of VO₂ nanocrystals (NCs), one can tailor the multipolar resonances hosted by VO₂ NCs and dynamically tune them by leveraging the insulator-to-metal transition of VO₂. In addition to that, we retrieve the complex refractive index of the effective medium composed of a slab of VO₂-NCs embedded in SiO₂, using Mie theory and Maxwell Garnett effective medium theory. Showing, that such a resulting metamaterial presents distinct optical tunability compared

to unpatterned VO₂ and can indeed be exploited as a designer phase-change metamaterial with adjustable refractive index modulation and absorption modulation. This provides us the ability to design a system having large refractive index tunability without inducing modulation of the extinction coefficient at specific wavelengths. Hence paving the way for low-loss tunable metamaterials.

Finally, in the last chapter, we explore the use of VO₂ as a means to create tunable metasurfaces in two important domains of application: tunable structural coloration and tunable perfect absorption. In the field of color generation technologies, we are expected to move past our current generation of stack displays and pigment dependencies to more simple surface displays aiming for more power efficient, ecological and vibrant display technology. One solution is to use structural color generation. Initial structural colors were created using designed TiO₂ dielectric nanostructures invoking Mie resonances and Fano resonances, but most nano-based devices studied so far are passive [245]. My preliminary simulations results show us the potential of VO₂ to induce dynamic tunability for the structural color generation. We try to achieve the tunability in mainly two ways; First, imprinting TiO₂ nanostructures on VO₂ thin films, manipulating the Fano resonance via the IMT transition of VO₂, thus promoting a tunable color. The second way is to construct directly VO₂ nano-structures designed specifically to support Mie resonances such that by controlling the state of VO₂, we could achieve an original color switching paradigm. These results indicate that the IMT of VO₂ may have a future in tunable color displays.

The second section of this chapter is focused on Mie-resonant silicon metasurfaces tunable by VO₂. Using arrays of a-Si nano-pillars, specifically designed to sustain overlapping ED and MD resonances, we have experimentally demonstrated that the reversible tuning of the VO₂ state enables switching the Kerker condition and introduces a two-order-of-magnitude modulation of the reflection at telecom wavelength ranges. The metasurface optical response further features a hysteresis behavior due to the IMT of VO₂, thus adding an interesting possibility for a non-volatile memory of its state. We believe that our work

uncovers a great potential for tunable dielectric metasurfaces, paving the way for nanoscale optical switches, modulators, and sensors based on all-dielectric resonant metasurfaces.

The majority of the work in this thesis was focused on incorporating an additional tunable degree of freedom leveraging VO₂ for different passive nanostructure devices, ranging from integrated guided optics to free-space metasurfaces. Many different adaptations, tests, and experiments have been left for the future due to lack of time (i.e. the experimental demonstration of the modulator device and the tunable structural color). Future works concern better implementation of VO₂ for its tunability, because in order to beat the virtue of electronics, i.e. integrability and re-programmability, it is necessary for photonics to evolve into next generation miniaturized systems, that can incorporate reconfigurable platforms with adjustable properties and are able to completely manipulate the key features of the information carrier (photons).

Additionally, future work also concerns with adapting the designer VO₂ NCs: to harness the advantage of optics in realization of on-demand adaptive functionalities, design of dynamically reconfigurable meta-surface based tunable devices having unprecedented performance is indispensable. Keeping in mind the energy, the robustness, the memory and the endurance of multi-cycle performance of the photonic device in order to outperform its electronic counterparts, we may also have to look into new design paradigm and use new material approaches [246, 247]. In order to achieve such a grand feat we might also take into account the emerging field of Deep Learning as powerful platform for designing, intelligent analysis and optimisation of meta-surfaces leveraging VO₂ tunable properties or any adaptable PCMs by reducing computational loads and solving multi dimensional EM simulation problems and thus helping us to find optimized solutions for each applications.

Appendices

APPENDIX A

ADDITIONAL WAVEGUIDE THEORY

A.1 Boundary Conditions

After we have defined the characteristics of the EM wave properties in the main text. We now try to understand the EM field behaviour at the boundary edges of the propagating medium. It is important because the modern devices are not composed of only one medium but several, stacked in a manner necessary for its application. Hence it is required to understand the behaviour of EM wave at the interfaces of the different medium and the environment. To do so we hypothesize two mediums with ϵ_1 and ϵ_2 and then solve the Maxwell's equation to equate a relation between the wave characteristics between the two mediums. Therefore, by solving Maxwell's equation based on the wave characteristics we observe the boundary conditions, as follows;

- The tangential components of the electric field should be continuous across the boundary.

$$E_{1t} = E_{2t} \quad (\text{A.1})$$

- If there are no current flowing on the surface of the boundary then, tangential magnetic components are continuous, that is

$$H_{1t} = H_{2t} \quad (\text{A.2})$$

But if the current flows on the surface, then the magnetic fields are discontinuous and are related by current density on the surface J_s ,

$$H_{1t} - H_{2t} = J_s \quad (\text{A.3})$$

- The normal components of the electric flux densities are continuous if there are no charge on the surface,

$$D_{1n} = D_{2n} \quad (\text{A.4})$$

But if there are charge on the surface then the flux densities are discontinuous and related to charge density ρ_s

$$D_{1n} - D_{2n} = \rho_s \quad (\text{A.5})$$

- Normal components of the magnetic flux densities are continuous, such that

$$B_{1n} = B_{2n} \quad (\text{A.6})$$

So in a summary, these boundary conditions, where the tangential components of E and H must be equal and continuous and normal components of D and B must be equal or continuous, must be followed whenever we encounter an interface between two dielectric media provided there are no free charges at the interface.

A.2 Total internal Reflection

We are well versed from ray theory that, when light is incident on an interface between two medium, at a given angle the light will be totally reflected internally. The conditions being that medium of propagation should have refractive index n_1 greater than n_2 , the outside medium. The schematic of which is shown in figure A.1. In terms of wave theory, the question thus arises, the existences of a transmitted wave and its nature.

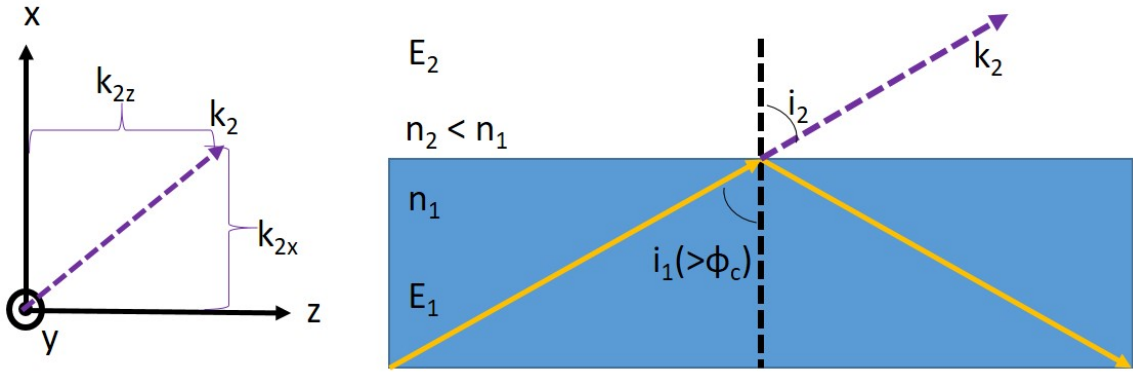


Figure A.1: Transmitted wave characteristics in total internal reflection (TIR), the direction of propagation in z direction.

Therefore in order to find the wave characteristics of transmitted wave, we assume an existence of transmitted wave at an angle i_2 with respect to normal n_2 having a propagation constant k_2 , then the electric field associated with the wave is given by;

$$\vec{E}_2 = E_{20} \exp[i(k_{2x}x + k_{2z}z - \omega t)] = E_{20} \exp[i(k_2 x \cos i_2 + k_2 z \sin i_2 - \omega t)] \quad (\text{A.7})$$

Now if we apply Snell's law of refraction, we know see that,

$$\sin i_2 = \frac{n_1}{n_2} \sin i_1 \quad (\text{A.8})$$

$$\cos i_2 = \frac{n_1}{n_2} \sqrt{\frac{n_2^2}{n_1^2} - \sin^2 i_2} \quad (\text{A.9})$$

Since, i_1 is greater than ϕ_c , which is the critical angle, then equation A.11 become imaginary.

$$\sin i_1 > \frac{n_1}{n_2} \quad (\text{A.10})$$

$$\cos i_2 = i\gamma \frac{n_1}{n_2} (\text{imaginary}) \quad (\text{A.11})$$

Following we equate equation A.7 with values from equation A.11 and A.10, we get the

following equation,

$$\vec{E}_2 = E_{20} e^{-\alpha x} \exp[i(k_2 z \frac{n_1}{n_2} \sin i_1 - \omega t)] \quad (\text{A.12})$$

where $\alpha = k_2 \frac{n_1}{n_2} \gamma$. Which means with TIR, there is an associated transmitted wave in the region with lower index medium, whose amplitude decreases exponentially w.r.t to x and this wave is known as evanescent wave. Later we'll show that this evanescent wave will play a major role in realization of photonic devices.

A.3 Optical Waveguide and transmission analysis

We have understood the wave characteristics inside a medium and also at interface of an medium. These conditions were an ideal since there was no restriction in direction for wave propagation and the medium was homogeneous. For practical applications, this not the case, hence we try to derive the equation for an in-homogeneous medium. Therefore we solve the Maxwell's equation like before, but this time the constitutive relation will be, as follows;

$$D = \epsilon \cdot \vec{E}; \epsilon(x, y, z) = \epsilon_0 n^2(x, y, z) \quad (\text{A.13})$$

$$B = \mu \cdot \vec{H} = \mu_0 \cdot \vec{H} \quad (\text{A.14})$$

Solving for wave equation, we take curl of equation 3.1 but contrary to previous calculation, we don't assume $\vec{\nabla} \cdot \vec{E} \neq 0$ since ϵ depends on the x, y, z direction. Therefore we derive the wave equation in an inhomogeneous medium as;

$$\nabla^2 \cdot \vec{E} + \vec{\nabla} \left(\frac{1}{n^2} \vec{\nabla} n^2 \cdot \vec{E} \right) - \mu_0 \epsilon_0 n^2 \frac{\partial^2 \vec{E}}{\partial t^2} \quad (\text{A.15})$$

Considering a general case similar to classical waveguide where there is an index discontinuity in both x and y direction, i.e. $n^2(x, y)$, eg: optical fiber or rectangular slab

waveguide. Then the z- part (longitudinal component) of the wave equation and t- part of the wave equation can be separated out, and equations can be separated written as;

$$\vec{E}(x, y, z, t) = \vec{E}_o(x, y) \exp[i(\omega t - \beta z)] \quad (\text{A.16})$$

$$\vec{H}(x, y, z, t) = \vec{H}_o(x, y) \exp[i(\omega t - \beta z)] \quad (\text{A.17})$$

The aim is to understand the field values as function of x and y and their respective propagation constants. In order to understand the concepts, we again, try to simplify the conditions by taking a planar waveguide rather than classical waveguide, as the index discontinuity is only in one direction for the slab.

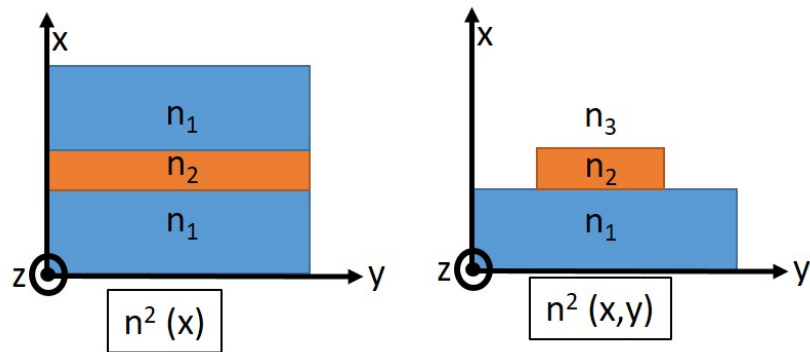


Figure A.2: Schematics of 1-D planar waveguide and 2-D rectangular planar waveguide .

In order to understand the characteristics of field functions based on index discontinuity, we try to simplify, by considering the case where the refractive index only varies in one transverse direction i.e. $n^2(x)$ as shown in figure A.2. Now since the discontinuity of the index is only in x direction therefore the y- part of the wave equation can also be separated out, such that if the direction of propagation is z- direction, then propagation constant in y- direction is zero..

$$E_j = E_j(x) \exp[i(\omega t - \beta z)] \quad (\text{A.18})$$

$$H_j = H_j(x) \exp[i(\omega t - \beta z)] \quad (\text{A.19})$$

where $j = x, y, z$. Solving for equations 3.1 and 3.2, we get in total 6 resultant equations corresponding to x, y and z . These equations relate the E and H components corresponding x, y, z directions and are function of $n(x)$, these equations are as shown;

•

$$i\beta E_y = -i\omega \mu_0 H_x \quad (\text{A.20})$$

•

$$i\beta E_x - \frac{\partial E_x}{\partial x} = -i\omega \mu_0 H_y \quad (\text{A.21})$$

•

$$\frac{\partial E_x}{\partial x} = -i\omega \mu_0 H_z \quad (\text{A.22})$$

•

$$i\beta H_y = -i\omega \epsilon_0 n^2(x) H_x \quad (\text{A.23})$$

•

$$-i\beta H_x - \frac{\partial H_z}{\partial x} = i\omega \epsilon_0 n^2(x) H_y \quad (\text{A.24})$$

•

$$\frac{\partial H_y}{\partial x} = i\omega \epsilon_0 n^2(x) H_x \quad (\text{A.25})$$

These six equation can be further simplified based on the type of polarization of the light, we can characterize them into TE and TM mode.

A.4 TE mode

If we assume the form of a mode where the electric field is not in the longitudinal direction, i.e. $E_y \neq 0$ and $E_x = 0$. Then we invoke equations A.20, A.22 and A.24, where E_y, H_x

and H_z are non vanishing components. They are known as transverse electric (TE) modes because on E_y component of electric field is present and it is transverse in y-direction.

Following we try to rearrange the TE equations in terms for E_y , we get,

$$\frac{d^2 E_y}{dx^2} + [k_o^2 n^2(x) - \beta^2] E_y = 0 \quad (\text{A.26})$$

Where $k_o = \frac{\omega}{c} = \frac{2\pi}{\lambda_o}$, λ_o free space wavelength. In order to gain the perspective, we observe a simple case for planar mirror waveguide, the schematic for which is shown in figure A.3.

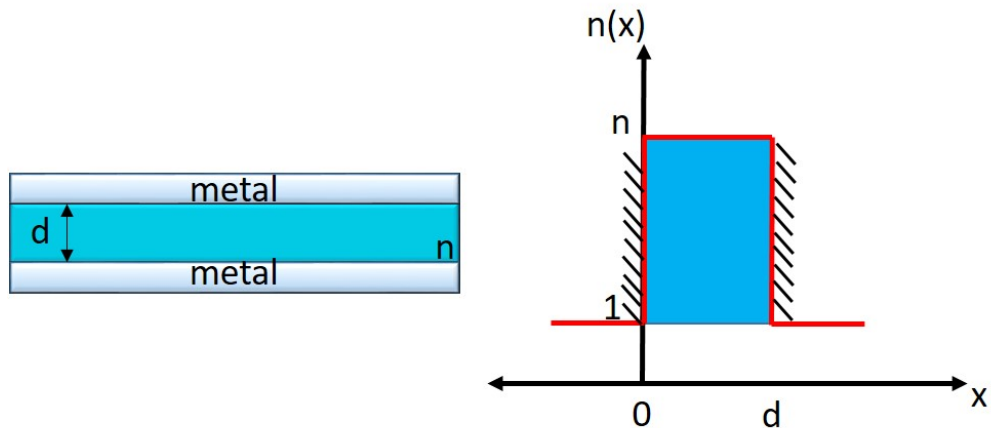


Figure A.3: Planar mirror waveguide with reflective metal surface on the boundary and the index variation map as function of x-axis value.

Based on the schematic, we can define the wave equation in the region $0 < x < d$ as,

$$\frac{d^2 E_y}{dx^2} + [k_o^2 n^2 - \beta^2] E_y = 0 \quad (\text{A.27})$$

where we define $[k_o^2 n^2 - \beta^2] = \kappa^2$. For the region where light is confined $0 < x < d$, the $\beta < k_o n$, then $\kappa^2 > 0$. Therefore the wave equation can be represented as,

$$E_y = A \sin \kappa x + B \cos \kappa x \quad (\text{A.28})$$

Applying boundary conditions, i.e. $E_y = 0$ at $x=0$ and at $x=d$. Therefore, $B=0$ and $\kappa d = m\pi$, we get the TE (E_y) modes;

$$E_y = A \sin \frac{m\pi x}{d}; m = 1, 2, 3 \quad (\text{A.29})$$

The propagation constant β can be then calculated from $[k_o^2 n^2 - \beta^2] = \kappa^2$, therefore, we get,

$$\beta_m^2 = k_o^2 n^2 - \frac{m\pi^2}{d}; m = 1, 2, 3 \quad (\text{A.30})$$

We can observe from the equation A.30 that it can sustain only discrete modes or it can entertain certain sets of values. Further evaluating the TE mode propagation we can discretize it into two constituent plane waves propagating in $+xz$ and $-xz$ direction make an angle θ_m with z axis, similar to TIR plane wave. From which we can evaluate the effective index of the material as observed by various TE modes can be represented as;

$$n_{eff,m} = \frac{\beta_m}{k_o} = n \cos \theta_m \quad (\text{A.31})$$

This shows the relationship between mode number, β and n_{eff} .

Although using planar mirror waveguide is useful for understanding, it is more practical to understand and evaluate the TE modes for step index dielectric waveguide as it is closer to objective of the thesis. Therefore, we evaluate TE modes for the schematics as shown in the figure A.4.

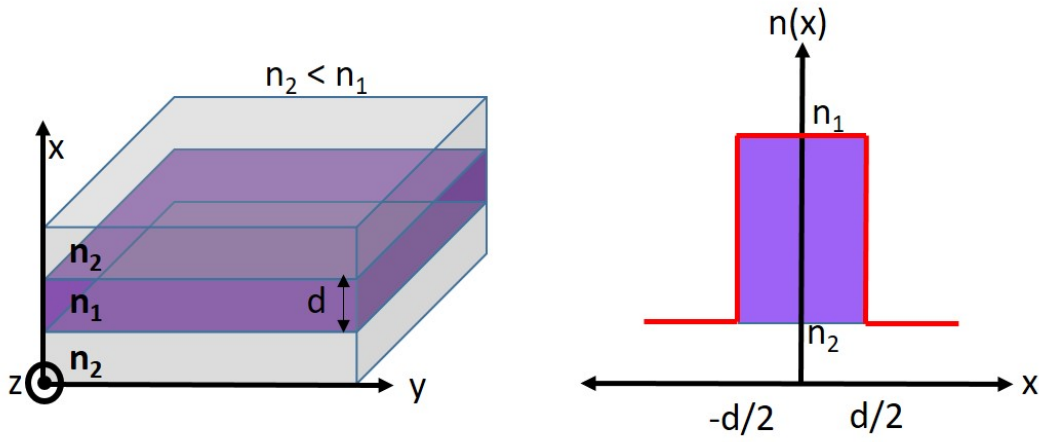


Figure A.4: Symmetric step-index planar waveguide structure and the index variation map as function of x-axis value.

The variation of refractive as a function of x can be written as; $n(x) = \begin{cases} n_1; |x| < d/2 \\ n_2; |x| > d/2 \end{cases}$

Based on the above schematics, we can write the E_y equations as,

$$\text{For } |x| < d/2, \frac{d^2 E_y}{dx^2} + \kappa^2 E_y = 0 \quad (\text{A.32})$$

$$\text{For } |x| > d/2, \frac{d^2 E_y}{dx^2} - \gamma^2 E_y = 0 \quad (\text{A.33})$$

Where $[k_o^2 n^2 - \beta^2] = \kappa^2$ and $[\beta^2 - k_o^2 n^2] = \gamma^2$. The solution for the E_y are as follows;

$$E_y = A \sin \kappa x + B \cos \kappa x; |x| < d/2, \quad (\text{A.34})$$

$$E_y(x) = \begin{cases} C e^{-\gamma x}; & |x| < d/2 \\ D e^{\gamma x}; & |x| > d/2 \end{cases} \quad (\text{A.35})$$

Where A, B, C and D are values determined by the boundary conditions, in our case it is $x = \pm d/2$. And the guided mode condition is $n_2 < \frac{\beta}{k_o} < n_1$. Each modes have a transmitted evanescent wave at the boundaries, whose field (E_y) decays at the rate of $\frac{1}{e}$ outside the

boundary. The penetration depth is measured as $d_p = \frac{1}{\gamma}$.

A.5 TM mode

Similar to TE mode description, the non vanishing components of TM mode are H_y , E_x and E_z , which are given by the equations A.21, A.23 and A.25. In order to find solutions for the TM modes we solve for H_y , and we get the following equation;

$$\frac{d^2H_y}{dx^2} - \left[\frac{1}{n^2(x)} \frac{dn^2(x)}{dx} \right] \frac{dH_y}{dx} + [k_o^2 n^2(x) - \beta^2] H_y = 0 \quad (\text{A.36})$$

We solve this equation A.36 of given $n^2(x)$ based on the symmetric planar waveguide as shown in figure A.4, where the refractive index varies as shown;

$$n(x) = \begin{cases} n_1; |x| < d/2 \\ n_2; |x| > d/2 \end{cases}$$

Therefore by solving the equation A.36, we get the following H_y equations;

$$\text{For } |x| < d/2, \frac{d^2H_y}{dx^2} + \kappa^2 H_y = 0 \quad (\text{A.37})$$

$$\text{For } |x| > d/2, \frac{d^2H_y}{dx^2} - \gamma^2 H_y = 0 \quad (\text{A.38})$$

Where $[k_o^2 n^2 - \beta^2] = \kappa^2$ and $[\beta^2 - k_o^2 n^2] = \gamma^2$. As we see that these equations are similar to the solutions we have got for TE modes. And therefore the solutions are also similar, as shown below;

$$H_y = A \sin \kappa x + B \cos \kappa x; |x| < d/2, \quad (\text{A.39})$$

$$H_y(x) = \begin{cases} C e^{-\gamma x}; & |x| < d/2 \\ D e^{\gamma x}; & |x| > d/2 \end{cases} \quad (\text{A.40})$$

Where A, B, C and D are values again determined by the boundary conditions,

A.6 Coupled mode theory

Until now, we have concerned our self in understanding the properties of EM waves in an confined medium and its properties while propagating in the medium. Based on this understanding we have developed the concept of modes, its associated power and its propagation properties. One of the most important property of an optical waveguide is its ability to share power with 100 % when certain condition are fulfilled. This sharing of power is ubiquitous and are known as mode coupling. This is one of a common physical principle that underpins the behaviour nearly all perturbed waveguide structures; like waveguide tapers, bends, grating and beam couplers [155]. The principle of coupled mode theory can easily be understood with one of the most profound and versatile device in integrated optics, i.e. the directional coupler. The directional coupler works by coupling two modes traveling in the same direction such there is a power redistribution between the two cores of the waveguide and after a certain distance, there is complete transfer of power.

Based on our previous section, we know that, there is a evanescent field extending outside any dielectric waveguide, whose field is exponentially decaying. If we bring two similar and symmetric parallel waveguides sufficiently close together, the evanescent part overlap spatially. Usually, the inter-waveguide gap required for this overlap to be significant is of the order of the width of the waveguide, the schematics of which is shown in figure A.5.

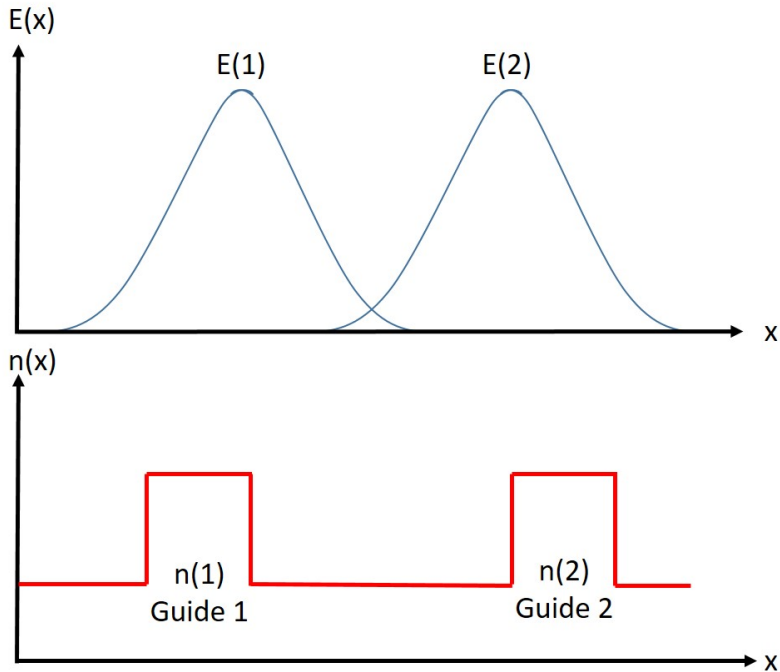


Figure A.5: Overlap of transverse evanescent field between two adjacent parallel symmetric slab waveguide structure and the index variation map of guide as function of x-axis value.

To understand the coupling power transfer mechanism, rather than using similar waveguide, we take 2 waveguides such that the propagation constant (β) is different for each waveguide, as shown in the schematic figure 3.4. This case is similar to the scope this thesis. We start with the following solutions;

$$\vec{E} = A(z)\vec{E}_1 + B(z)\vec{E}_2 \quad (\text{A.41})$$

$$\vec{H} = A(z)\vec{H}_1 + B(z)\vec{H}_2 \quad (\text{A.42})$$

Here A and B are the amplitude of the wave propagating in the waveguide 1 and 2 respectively, where as E and H are the electric and magnetic field of the light wave. In co-directional coupling

We then compute the equations A.41 and A.42 by substituting them in to Maxwell's curl equations (3.2 and 3.1), which is followed by substituting the enforced Maxwell's equation

into general integral equations describing orthogonality in lossless isotropic waveguides to obtain generalised coupled-mode equations, as shown;

$$\frac{dA}{dz} + c_{12} \frac{dB}{dz} e^{-j(\beta_2 - \beta_1)z} + j\chi_1 A + j\kappa_{12} B e^{-j(\beta_2 - \beta_1)z} = 0 \quad (\text{A.43})$$

$$\frac{dB}{dz} + c_{21} \frac{dA}{dz} e^{-j(\beta_2 - \beta_1)z} + j\chi_2 A + j\kappa_{21} A e^{-j(\beta_2 - \beta_1)z} = 0 \quad (\text{A.44})$$

Here, unlike previous section κ represents mode coupling coefficient, c represents butt coupling coefficient and χ propagation constant. These generalised coupled-mode solutions are further solved to describe the coupling between two waveguides, irrespective of their shape. These equations are important as we can further evaluate them to calculate coupling coefficient like, butt coupling coefficient, mode coupling coefficient and change in average propagation constant [248]. The coupling mechanism usually entails the transfer of power from one waveguide to another. This transfer also influences the mode in the adjacent waveguide modifying its shape. This interaction can happen in one of the two ways, either evanescent waves of symmetric modes interact or asymmetric modes interact. This interaction creates a new mode pattern and are called supermodes. The power transfer in super modes can be calculated using the power equation for the waveguide (waveguide 1) which is given by,

$$P = \frac{1}{2} \int_{-\infty}^{\infty} \int_{-\infty}^{\infty} (\vec{E} \times \vec{H}) \hat{z} dx dy \quad (\text{A.45})$$

Solving the above equations we get;

$$P = \frac{1}{2} \left[|A|^2 + |B|^2 + A^* B c_{21} e^{-j2\delta z} + A B^* c_{21}^* e^{-j2\delta z} \right] \quad (\text{A.46})$$

With assumption of complex conjugate symmetry of $c_{21} = c_{12}$ and $\chi_1 = \chi_2^*$, where $\delta = \frac{\beta_2 - \beta_1}{2}$.

Following we now try to analyse the power transfer that takes place during mode coupling.

In order to do that we assume that there is no loss of power along the propagation direction ($\frac{dP}{dz} = 0$) but only a transfer of power from one guide to another happens. So we can rewrite the equation as;

$$jA^*B(\kappa_{21}^* - \kappa_{12} - 2\delta c_{21})e^{-j2\delta z} - jAB^*(\kappa_{21}^* - \kappa_{12} - 2\delta c_{21}^*)e^{j2\delta z} = 0 \quad (\text{A.47})$$

In order to make the power independent of Z- direction, we must have $\kappa_{21}^* = \kappa_{12} + 2\delta c_{21}^*$. Keeping it in mind, we can simply write the reviewed coupled mode equations, assuming that $c_{12} = \chi = 0$;

$$\frac{dA}{dz} = -j\kappa_{12}Be^{-j(\beta_2 - \beta_1)z} \quad (\text{A.48})$$

$$\frac{dB}{dz} = +j\kappa_{21}Ae^{j(\beta_2 - \beta_1)z} \quad (\text{A.49})$$

APPENDIX B

ENERGY TRANSFER AND MODE MATCHING METHOD

B.1 Mode Matching Method

Mode matching method (MMM) is computational electromagnetic technique [249, 158] formulated in a Cartesian coordinate to simulate the evolution of the light wave which propagates in a guiding structure, by expanding the EM field into eigen modes in local area cross section, which varies according to the axis of propagation figure B.1. This method consists in replacing the structure to be modeled by an equivalent structure made up of a succession of elementary straight guides of variable sections.

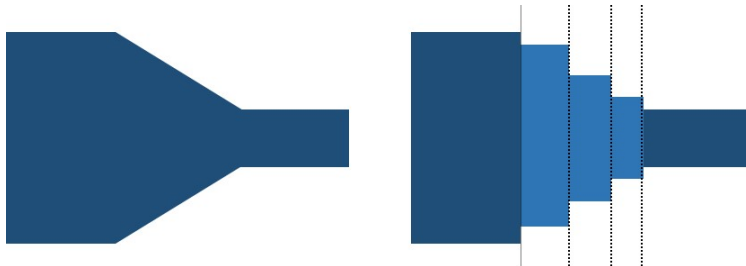


Figure B.1: a) Structure to model. b) Decomposition of the structure to be modeled into elementary straight wave guides.

In MMM, the optical structure is discretized in to various sections along the propagation direction and replacing the structure to be modeled by an equivalent structure made up of a succession of elementary straight guides of variable sections. The advantage of this equivalent structure is that we know how to calculate the guided and radiated modes of each straight portion. These modes will be called local modes of the portion considered. In our case for 3D structure, the effective indices and the profiles of the various components of the electromagnetic field of the local modes are calculated using matlab modeling tools, whose the simulation numerical theory was discussed earlier in this chapter was developed in the

laboratory.

B.1.1 Mode matching at an Interface

The propagation of the light wave in the equivalent structure shown in figure B.1b is calculated from interface matrices which is expressed by boundary conditions. Considering the continuity of the tangential components of the electric field E and of the magnetic induction H on either side of the interface between two straight guides and propagation matrices P which represents the phase shift introduced by the propagation of the modes in the equivalent straight guide portion. It should be noted that the method gives a rigorous solution of the problem when the thicknesses of the different portions of straight guide converge towards 0.

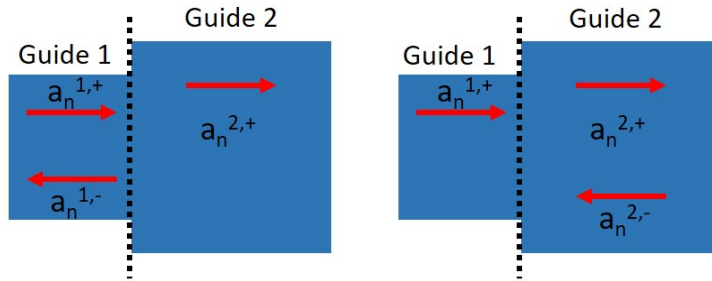


Figure B.2: Schematic diagram of the calculation of reflection and transmission coefficients at an interface in the case of an incident wave equal to (a). $a_n^{1,+}$ and (b) $a_n^{2,-}$.

For our case, we consider a plane interface between two portions of straight guides denoted 1 and 2 in $z = 0$, as shown in figure B.2. We seek to calculate the field reflected and transmitted to this interface when it is lit by a guided mode of index p in guide 1, as shown in figure 2. Based on the boundary conditions we obtain the following relations:

$$a_p^{1,+} E_{p,t}^{1,+} + \sum_{i=1}^n a_i^{1,-} E_{i,t}^{1,+} = \sum_{j=1}^m a_j^{2,+} E_{j,t}^2 \quad (\text{B.1})$$

$$a_p^{1,+} H_{p,t}^{1,+} - \sum_{i=1}^n a_i^{1,-} H_{i,t}^{1,+} = \sum_{j=1}^m a_j^{2,+} H_{j,t}^2 \quad (\text{B.2})$$

The negative sign (-) for the tangential components of magnetic induction is imposed by the conservation of the Lorentz reciprocity principle for a counter-propagating wave. Therefore in order to calculate the reflection coefficients $R_{i,p}$ and transmission $T_{j,p}$ of the interface, we construct a vector products between the fields E and H so as to obtain the energy transferred to each mode. For equation B.1, we represent it with respect to the magnetic field with modes k propagating in guide 1, whereas for equation B.1, we represent the electric field with modes l propagating in the guide 2. We thus obtain the relations:

$$a_p^{1,+} \langle E_p^1, H_k^1 \rangle + \sum_{i=1}^n a_i^{1,-} \langle E_i^1, H_k^1 \rangle = \sum_{j=1}^m a_j^{2,+} \langle E_j^2, H_k^1 \rangle \quad (\text{B.3})$$

$$a_p^{1,+} \langle E_l^1, H_p^1 \rangle - \sum_{i=1}^n a_i^{1,-} \langle E_l^2, H_i^1 \rangle = \sum_{j=1}^m a_j^{2,+} \langle E_l^2, H_2^j \rangle \quad (\text{B.4})$$

With $P_{i,j}^{a,b} = \langle E_i^a, H_j^b \rangle = \int \int_S (E_{i,x}^a \cdot H_{j,y}^b - E_{i,y}^a \cdot H_{j,x}^b) dx dy$, where i and j represent the indices of the modes considered, a and b the numbers of the layers and n and m the total numbers of modes considered in the 2 guides. The coefficients $a_i^{1,-}$ and $a_j^{2,+}$ are obtained by solving the linear system by equating $a_p^{1,+} = 1$. We can thus represent the equations in matrix form and can be represented as;

$$\begin{bmatrix} -\sum_{i=1}^n \langle E_i^1, H_k^1 \rangle & \sum_{j=1}^m \langle E_j^2, H_k^1 \rangle \\ \sum_{i=1}^n \langle E_l^2, H_i^1 \rangle & \sum_{j=1}^m \langle E_l^2, H_2^j \rangle \end{bmatrix} \begin{pmatrix} a_i^{1,-} \\ a_j^{2,+} \end{pmatrix} = \begin{pmatrix} \langle E_p^1, H_k^1 \rangle \\ \langle E_l^2, H_p^1 \rangle \end{pmatrix} \quad (\text{B.5})$$

Which can be written in term of Power P is shown as;

$$\begin{bmatrix} -\sum_{i=1}^n PEH_{i,k}^{1,1} & \sum_{j=1}^m PEH_{j,k}^{2,1} \\ \sum_{i=1}^n PHE_{i,l}^{2,1} & \sum_{j=1}^m PHE_{j,l}^{2,2} \end{bmatrix} \begin{pmatrix} a_i^{1,-} \\ a_j^{2,+} \end{pmatrix} = \begin{pmatrix} PEH_{p,k}^{1,1} \\ PHE_{l,p}^{2,1} \end{pmatrix} \quad (\text{B.6})$$

where k varies from 1 to n, and l varies from 1 to m. And thus we obtain a square matrix of dimension n + m. The resolution of this system makes it possible to obtain the coefficients $a_i^{1,-}$ and $a_j^{2,+}$ corresponding to the excitement of p mode. The PEH and PHE conventions are

used when the variable indices i or j are applied respectively to the field E or H. It is to note that we can represent $\sum_{i=1}^n PEH_{i,k}^{1,1} = \delta_{i,k}.PEH_{k,k}^{1,1}$ and $\sum_{j=1}^m PHE_{j,l}^{2,2} = \delta_{j,l}.PHE_{l,l}^{2,2}$ are the diagonal matrix. And $PEH_{p,k}^{1,1} = \delta_{p,k}.PEH_{p,p}^{1,1}$ vector containing a single non-zero element at index p.

The reflection coefficient $r_{i,p}^{1,2}$ and $t_{j,p}^{2,1}$ are obtained by the relations;

$$r_i^{1,2} = a_i^{1,-} \quad (\text{B.7})$$

$$t_j^{2,1} = a_j^{2,+} \quad (\text{B.8})$$

With

$$\begin{pmatrix} a_i^{1,-} \\ a_j^{2,+} \end{pmatrix} = \begin{bmatrix} -\sum_{i=1}^n \langle E_i^1, H_k^1 \rangle & \sum_{j=1}^m \langle E_j^2, H_k^1 \rangle \\ \sum_{i=1}^n \langle E_l^2, H_i^1 \rangle & \sum_{j=1}^m \langle E_l^2, H_j^2 \rangle \end{bmatrix}^{-1} \begin{pmatrix} \langle E_p^1, H_k^1 \rangle \\ \langle E_l^2, H_p^1 \rangle \end{pmatrix}$$

By varying the index p of the incident field in the medium 1, we obtain the set of reflection and transmission coefficients of the structure when the incident field is one of the modes of the guide for region 1. We can notice the set of reflection coefficients constitutes a square matrix of dimension $n \times n$, while the transmission coefficients form a rectangular matrix of dimension $n \times m$. Similarly, it should be noted that the same reasoning can be used when the incident field comes from region 2. Therefore we obtain the coefficients $a_i^{1,-}$ and $a_j^{2,+}$ as,

$$\begin{bmatrix} -\sum_{j=1}^m \langle E_j^2, H_k^2 \rangle & \sum_{i=1}^n \langle E_i^1, H_k^2 \rangle \\ \sum_{j=1}^m \langle E_l^1, H_j^2 \rangle & \sum_{n=1}^l \langle E_l^1, H_1^2 \rangle \end{bmatrix} \begin{pmatrix} a_j^{2,+} \\ a_i^{1,-} \end{pmatrix} = \begin{pmatrix} \langle E_p^2, H_k^2 \rangle \\ \langle E_l^1, H_p^2 \rangle \end{pmatrix} \quad (\text{B.9})$$

In term of Power P is shown as;

$$\begin{bmatrix} -\sum_{j=1}^m P_{j,k}^{2,2} & \sum_{i=1}^n P_{i,k}^{1,2} \\ \sum_{j=1}^m P_{l,j}^{1,2} & \sum_{i=1}^n P_{l,j}^{1,1} \end{bmatrix} \begin{pmatrix} a_j^{2,+} \\ a_i^{1,-} \end{pmatrix} = \begin{pmatrix} P_{p,k}^{2,2} \\ P_{l,p}^{1,2} \end{pmatrix} \quad (\text{B.10})$$

The reflection coefficient $r_j^{2,1}$ and $t_j^{1,2}$ are obtained by the relations;

$$r_j^{2,1} = a_j^{2,+} \quad (\text{B.11})$$

$$t_i^{2,1} = a_i^{1,-} \quad (\text{B.12})$$

With

$$\begin{pmatrix} a_i^{2,+} \\ a_j^{1,-} \end{pmatrix} = \begin{bmatrix} -\sum_{j=1}^m \langle E_j^2, H_k^2 \rangle & \sum_{i=1}^n \langle E_i^1, H_k^2 \rangle \\ \sum_{j=1}^m \langle E_l^1, H_j^2 \rangle & \sum_{i=1}^n \langle E_l^1, H_1^i \rangle \end{bmatrix}^{-1} \begin{pmatrix} \langle E_p^1, H_k^1 \rangle \\ \langle E_l^2, H_p^1 \rangle \end{pmatrix}$$

By varying the index p of the incident field in the medium 2, we obtain all the reflection and transmission coefficients of the structure when the incident field is one of the modes of the guide for region 2. We can notice the reflection coefficients constitutes a square matrix of dimension $m \times m$, while the transmission coefficients form a rectangular matrix of dimension $m \times n$.

B.1.2 Interface matrix

To obtain the interface matrix of refractive index i, it is necessary to obtain a matrix relation which connects the propagating and counter-propagating waves propagating in the guide of refractive index $i-1$ with those propagating in the guide of refractive index i.

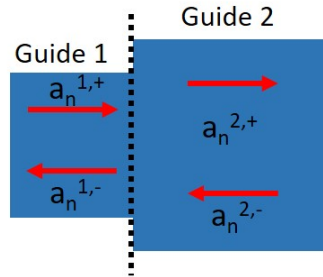


Figure B.3: Relationship between the amplitudes of electromagnetic waves at an interface.

When we try to express the relationships between the reflection and transmission of light at an interface, we consider the case shown in figure B.3 for which, we must determine the link between propagating waves and counter-propagating in both media. For this, we determine the link between the two incoming waves $a^{1,-}$ and $a^{2,+}$, which were not taken into account in the above figures.

$$a^{1,-} = r_{1,2}a^{1,+} + t_{2,1}a^{2,-} \quad (\text{B.13})$$

$$a^{2,+} = t_{1,2}a^{1,+} + r_{2,1}a^{2,-} \quad (\text{B.14})$$

Equations B.13 and B.14 make it possible to obtain the interface transfer matrix:

$$\begin{pmatrix} a^{1,-} \\ a^{2,+} \end{pmatrix} = \begin{bmatrix} r_{1,2} & t_{2,1} \\ t_{1,2} & r_{2,1} \end{bmatrix} \begin{pmatrix} a^{1,+} \\ a^{2,-} \end{pmatrix} \quad (\text{B.15})$$

B.2 Layer Matrix

The layer matrix simply describes the propagation of the light wave in the homogeneous guide of layer with refractive index i. It is simply expressed as a function of the phase shift

of the light wave:

$$\begin{pmatrix} a_i^+ e^{j\beta_i z_{i-1}} \\ a_i^- e^{-j\beta_i z_{i-1}} \end{pmatrix} = \begin{bmatrix} e^{j\beta_i d_i} & 0 \\ 0 & e^{-j\beta_i d_i} \end{bmatrix} \begin{pmatrix} a_i^+ & e^{j\beta_i z_i} \\ a_i^- & e^{-j\beta_i z_i} \end{pmatrix} \quad (\text{B.16})$$

B.2.1 Generalization for N interfaces

We are trying to calculate the reflection and transmission coefficients in Figure B.1 which consists of a large number of interfaces. The calculation begins by describing the boundary conditions of the last interface. By applying the Sommerfeld radiation conditions [250] which says that in the presence of an excitation coming from the first medium, the wave $a^{n,-} = 0$. By referring on the conditions in equation B.15 to the interface, we obtain the following relations:

$$a^{n-1,-}(z_{n-1}) = r_{n_1,n} a^{n-1,+}(z_{n-1}) \quad (\text{B.17})$$

$$a^{n-1,+}(z_{n-1}) = t_{n_1,n} a^{n-1,+}(z_{n-1}) \quad (\text{B.18})$$

By adding the propagation constant to the interface z_{n-1} , we can rewrite the equation B.17 as;

$$a^{n-1,-}(z_{n-2}) = I_{n-1}^r a^{n-1,+}(z_{n-2}) \quad (\text{B.19})$$

where,

$$I_{n-1,n}^r = [e^{-j\beta_i^{n-1} e^{n-i}}] \cdot [r_{n-1,n}] \cdot [e^{-j\beta_i^{n-1} e^{n-i}}] \quad (\text{B.20})$$

$$a^{n,+}(z_{n-1}) = I_{n-1}^t a^{n-1,+}(z_{n-2}) \quad (\text{B.21})$$

With,

$$I_{n-1,n}^t = [e^{-j\beta_i^{n-1} e^{n-i}}] \cdot [t_{n-1,n}] \quad (\text{B.22})$$

We perform this iterative process up to interface 1, which allows us to obtain the relationship:

$$a^{1,-}(z_1) = I_1^r a^{1,+}(z_1) \quad (\text{B.23})$$

From the equations B.13 and B.14, we can calculate the amplitudes for $i + 1$ in different layers using the equations:

$$a^{i+1,+}(z_{i+1}) = T_i a^{1,+}(z_i) \quad (\text{B.24})$$

where,

$$T_i = [[I_d] - [r_{i+1,i}] \cdot [I_{i+1}^r]]^{-1} \cdot [t_{i,i+1}] \cdot [e^{-j\beta_{i+1} e_{i+1}}] \quad (\text{B.25})$$

$$a^{i+1,-}(z_i) = I_{i+1}^r a^{1,+}(z_i) \quad (\text{B.26})$$

The reflection and transmission coefficients at the different interfaces are obtained by solving a linear system comprising a number of equations equal to the number of unknowns, which ensures the uniqueness of the solution. In the end, we can obtain the reflection and transmission coefficients using the relations B.23 and B.24:

$$r = \frac{a^{1,-}(z_1)}{a^{1,+}(z_1)} = I_1^r \quad (\text{B.27})$$

$$t = \frac{a^{1,-}(z_n)}{a^{1,+}(z_1)} = \prod_{i=1}^{n-1} T_i \quad (\text{B.28})$$

With the calculation for the reflection and transmission coefficient for the mode matching method, we have laid the foundation for the theory for all the numerical calculation that

would enable us to simulate and fabricate the novel modulator.

Therefore, if the optical modulator is properly designed, when VO₂ is semiconducting, the propagation constant doesn't match with the bus waveguide, consequently, light from the input Si waveguide propagates through without coupling to the VO₂ patched waveguide. However, when the phase of VO₂ is changed from dielectric to metal, the wave changes direction and couples into the VO₂ patched waveguide. The propagation loss of the hybrid VO₂ patched waveguide abruptly increases due to the VO₂ lossy metallic characteristics. As a result, the light amplitude at the output Si waveguide decreases after being absorbed along the hybrid VO₂ waveguide. By repeating this operation back and forth, we can modulate the optical signals at the output of the Si bus waveguide. This simple architecture has shown to be a promising solution for on-off operations. When the device is "ON" there is not a single photon that is lost in the device, as no light is coupled in the VO₂-based WG. On the contrary, in the "OFF" state, we could potentially absorb all of the incoming light.

In order to implement this design strategy, we have to compute the light propagation and its interaction with the strip waveguide structure and its confinement. So to understand that wave, we have to perform numerical analysis for the E and H components in terms of material properties, design and boundary conditions. Theory involving the numerical analysis is explained in the main text section and the figure 3.2 has been calculated employing the following the numerical theory.

REFERENCE

- [1] Ghavam G Shahidi. “Chip Power Scaling in Recent CMOS Technology Nodes”. In: *IEEE Access* 7 (2018), pp. 851–856.
- [2] Takasumi Tanabe et al. “All-optical switches on a silicon chip realized using photonic crystal nanocavities”. In: *Applied Physics Letters* 87.15 (2005), p. 151112. eprint: <https://doi.org/10.1063/1.2089185>.
- [3] Qianfan Xu et al. “Micrometre-scale silicon electro-optic modulator”. In: *Nature* 435 (2005), 325 EP –.
- [4] William M. J. Green et al. “Ultra-compact, low RF power, 10 Gb/s silicon Mach-Zehnder modulator”. In: *Opt. Express* 15.25 (2007), pp. 17106–17113.
- [5] G Stefanovich, A Pergament, and D Stefanovich. “Electrical switching and Mott transition in VO₂”. In: *Journal of Physics: Condensed Matter* 12.41 (2000), pp. 8837–8845.
- [6] A. Cavalleri et al. “Femtosecond Structural Dynamics in VO₂ during an Ultrafast Solid-Solid Phase Transition”. In: *Phys. Rev. Lett.* 87 (23 2001), p. 237401.
- [7] Mengkun Liu et al. “Terahertz-field-induced insulator-to-metal transition in vanadium dioxide metamaterial”. In: *Nature* 487 (2012), 345 EP –.
- [8] FJ Morin. “Oxides which show a metal-to-insulator transition at the Neel temperature”. In: *Physical review letters* 3.1 (1959), p. 34.
- [9] Y Muraoka, Y Ueda, and Z Hiroi. “Large modification of the metal–insulator transition temperature in strained VO₂ films grown on TiO₂ substrates”. In: *Journal of Physics and Chemistry of Solids - J PHYS CHEM SOLIDS* 63 (2002), pp. 965–967.
- [10] C. N. Berglund and A. Jayaraman. “Hydrostatic-Pressure Dependence of the Electronic Properties of VO₂ Near the Semiconductor-Metal Transition Temperature”. In: *Phys. Rev.* 185 (3 1969), pp. 1034–1039.
- [11] F. J. Morin. “Oxides Which Show a Metal-to-Insulator Transition at the Neel Temperature”. In: *Phys. Rev. Lett.* 3 (1 1959), pp. 34–36.
- [12] Frederick Seitz. *The modern theory of solids*. Vol. 548. McGraw-Hill New York, 1940.
- [13] Shinbum Lee et al. “Epitaxial stabilization and phase instability of VO₂ polymorphs”. In: *Scientific reports* 6 (2016), p. 19621.

- [14] John B Goodenough. “The two components of the crystallographic transition in VO₂”. In: *Journal of Solid State Chemistry* 3.4 (1971), pp. 490–500.
- [15] Francesco Grandi, Adriano Amaricci, and Michele Fabrizio. “Unraveling the Mott-Peierls intrigue in Vanadium dioxide”. In: *arXiv preprint arXiv:1906.10632* (2019).
- [16] Rudolf Ernst Peierls and Rudolf Peierls. *Surprises in theoretical physics*. Princeton University Press, 1979.
- [17] Tiegui Lin and Yufen Zhang. “Metal-insulator transition of monoclinic VO₂ thin film without Peierls distortion”. In: *Vacuum* 163 (2019), pp. 338–341.
- [18] Gabriel Kotliar and Dieter Vollhardt. “Strongly correlated materials: Insights from dynamical mean-field theory”. In: *Physics today* 57.3 (2004), pp. 53–60.
- [19] Jan M Tomczak and Silke Biermann. “Effective band structure of correlated materials: the case of VO₂”. In: *Journal of Physics: Condensed Matter* 19.36 (2007), p. 365206.
- [20] MW Haverkort et al. “Orbital-assisted metal-insulator transition in VO₂”. In: *Physical Review Letters* 95.19 (2005), p. 196404.
- [21] M. M. Qazilbash et al. “Mott Transition in VO₂ Revealed by Infrared Spectroscopy and Nano-Imaging”. In: *Science* 318.5857 (2007), pp. 1750–1753. eprint: <http://science.sciencemag.org/content/318/5857/1750.full.pdf>.
- [22] JP Pouget et al. “Dimerization of a linear Heisenberg chain in the insulating phases of V 1-x Cr x O 2”. In: *Physical Review B* 10.5 (1974), p. 1801.
- [23] M Ghedira et al. “Structural aspects of the metal-insulator transitions in V0.985Al0.015O₂”. In: *Journal of Solid State Chemistry* 22.4 (1977), pp. 423–438.
- [24] A Tselev et al. “Symmetry relationship and strain-induced transitions between insulating M1 and M2 and metallic R phases of vanadium dioxide”. In: *Nano letters* 10.11 (2010), pp. 4409–4416.
- [25] Hans W. Verleur, A. S. Barker, and C. N. Berglund. “Optical Properties of VO₂ between 0.25 and 5 eV”. In: *Phys. Rev.* 172 (3 1968), pp. 788–798.
- [26] Hui Chen and W Z Shen. “Perspectives in the characteristics and applications of Tauc-Lorentz dielectric function model”. In: *European Physical Journal B* 43 (2005), pp. 503–507.
- [27] Anibal Gavini and Clarence C. Y. Kwan. “Optical Properties of Semiconducting VO₂ Films”. In: *Phys. Rev. B* 5 (8 1972), pp. 3138–3143.

- [28] G. E. Jellison and F. A. Modine. “Parameterization of the optical functions of amorphous materials in the interband region”. In: *Applied Physics Letters* 69.3 (1996), pp. 371–373. eprint: <https://doi.org/10.1063/1.118064>.
- [29] Cheng Wang et al. “Nanophotonic lithium niobate electro-optic modulators”. In: *Optics express* 26.2 (2018), pp. 1547–1555.
- [30] Xi Xiao et al. “High speed silicon photonic modulators”. In: *2017 Optical Fiber Communications Conference and Exhibition (OFC)*. IEEE. 2017, pp. 1–3.
- [31] Hao Feng et al. “40 Gb/s electro-absorption-modulator-integrated DFB laser with optimized design”. In: *Optical Fiber Communication Conference and Exhibit*. IEEE. 2002, pp. 340–341.
- [32] Changhyun Ko and Shriram Ramanathan. “Observation of electric field-assisted phase transition in thin film vanadium oxide in a metal-oxide-semiconductor device geometry”. In: *Applied Physics Letters* 93.25 (2008), p. 252101.
- [33] Matthew Jerry et al. “Dynamics of electrically driven sub-nanosecond switching in vanadium dioxide”. In: *2016 IEEE Silicon Nanoelectronics Workshop (SNW)*. IEEE. 2016, pp. 26–27.
- [34] S Chen et al. “A novel structural VO₂ micro-optical switch”. In: *Optical and quantum electronics* 35.15 (2003), pp. 1351–1355.
- [35] Lijun Jiang and William N Carr. “Design, fabrication and testing of a micromachined thermo-optical light modulator based on a vanadium dioxide array”. In: *Journal of Micromechanics and Microengineering* 14.7 (2004), p. 833.
- [36] Jin Tae Kim. “CMOS-compatible hybrid plasmonic modulator based on vanadium dioxide insulator-metal phase transition”. In: *Optics letters* 39.13 (2014), pp. 3997–4000.
- [37] Kelvin JA Ooi et al. “Ultracompact vanadium dioxide dual-mode plasmonic waveguide electroabsorption modulator”. In: *Nanophotonics* 2.1 (2013), pp. 13–19.
- [38] Ryan M Briggs, Imogen M Pryce, and Harry A Atwater. “Compact silicon photonic waveguide modulator based on the vanadium dioxide metal-insulator phase transition”. In: *Optics express* 18.11 (2010), pp. 11192–11201.
- [39] Gustav Mie. “Beiträge zur Optik trüber Medien, speziell kolloidaler Metallösungen”. In: *Ann. Phys.* 330.3 (1908), pp. 377–445.
- [40] Craig F Bohren and Donald R Huffman. *Absorption and scattering of light by small particles*. John Wiley & Sons, 2008.
- [41] Edward D. Palik. *Handbook of Optical Constants of Solids*. Academic Press, 1998.

- [42] John Brian Pendry. “Negative refraction makes a perfect lens”. In: *Physical review letters* 85.18 (2000), p. 3966.
- [43] Richard A Shelby, David R Smith, and Seldon Schultz. “Experimental verification of a negative index of refraction”. In: *science* 292.5514 (2001), pp. 77–79.
- [44] Shuang Zhang et al. “Experimental demonstration of near-infrared negative-index metamaterials”. In: *Physical review letters* 95.13 (2005), p. 137404.
- [45] Mário Silveirinha and Nader Engheta. “Tunneling of electromagnetic energy through sub-wavelength channels and bends using ε -near-zero materials”. In: *Physical review letters* 97.15 (2006), p. 157403.
- [46] Andrea Alu et al. “Epsilon-near-zero metamaterials and electromagnetic sources: Tailoring the radiation phase pattern”. In: *Physical review B* 75.15 (2007), p. 155410.
- [47] Iñigo Liberal and Nader Engheta. “Near-zero refractive index photonics”. In: *Nature Photonics* 11.3 (2017), p. 149.
- [48] David Schurig et al. “Metamaterial electromagnetic cloak at microwave frequencies”. In: *Science* 314.5801 (2006), pp. 977–980.
- [49] Wenshan Cai et al. “Optical cloaking with metamaterials”. In: *Nature photonics* 1.4 (2007), p. 224.
- [50] Nicholas Fang et al. “Sub-diffraction-limited optical imaging with a silver superlens”. In: *Science* 308.5721 (2005), pp. 534–537.
- [51] Zhaowei Liu et al. “Far-field optical hyperlens magnifying sub-diffraction-limited objects”. In: *science* 315.5819 (2007), pp. 1686–1686.
- [52] Yunuen Montelongo et al. “Plasmonic nanoparticle scattering for color holograms”. In: *Proceedings of the National Academy of Sciences* 111.35 (2014), pp. 12679–12683.
- [53] Yao-Wei Huang et al. “Aluminum plasmonic multicolor meta-hologram”. In: *Nano letters* 15.5 (2015), pp. 3122–3127.
- [54] Boris Gralak, Gérard Tayeb, and Stefan Enoch. “Morpho butterflies wings color modeled with lamellar grating theory”. In: *Optics express* 9.11 (2001), pp. 567–578.
- [55] Naoki Okada et al. “Rendering Morpho butterflies based on high accuracy nano-optical simulation”. In: *Journal of Optics* 42.1 (2013), pp. 25–36.
- [56] Ting Xu et al. “Structural colors: from plasmonic to carbon nanostructures”. In: *Small* 7.22 (2011), pp. 3128–3136.

- [57] Yinghong Gu et al. “Color generation via subwavelength plasmonic nanostructures”. In: *Nanoscale* 7.15 (2015), pp. 6409–6419.
- [58] Alexander V Kildishev, Alexandra Boltasseva, and Vladimir M Shalaev. “Planar photonics with metasurfaces”. In: *Science* 339.6125 (2013), p. 1232009.
- [59] Patrice Genevet et al. “Recent advances in planar optics: from plasmonic to dielectric metasurfaces”. In: *Optica* 4.1 (2017), pp. 139–152.
- [60] Hou-Tong Chen, Antoinette J Taylor, and Nanfang Yu. “A review of metasurfaces: physics and applications”. In: *Reports on progress in physics* 79.7 (2016), p. 076401.
- [61] Yang Zhao and Andrea Alù. “Manipulating light polarization with ultrathin plasmonic metasurfaces”. In: *Physical Review B* 84.20 (2011), p. 205428.
- [62] Xingjie Ni, Alexander V Kildishev, and Vladimir M Shalaev. “Metasurface holograms for visible light”. In: *Nature communications* 4 (2013), p. 2807.
- [63] Anders Pors et al. “Broadband focusing flat mirrors based on plasmonic gradient metasurfaces”. In: *Nano letters* 13.2 (2013), pp. 829–834.
- [64] Guoxing Zheng et al. “Metasurface holograms reaching 80% efficiency”. In: *Nature nanotechnology* 10.4 (2015), p. 308.
- [65] Alexander A High et al. “Visible-frequency hyperbolic metasurface”. In: *Nature* 522.7555 (2015), p. 192.
- [66] Yuri Kivshar and Andrey Miroshnichenko. “Meta-optics with Mie resonances”. In: *OPN* 28.1 (2017), pp. 24–31.
- [67] Andrey E Miroshnichenko, Sergej Flach, and Yuri S Kivshar. “Fano resonances in nanoscale structures”. In: *Reviews of Modern Physics* 82.3 (2010), p. 2257.
- [68] Shanhui Fan and John D Joannopoulos. “Analysis of guided resonances in photonic crystal slabs”. In: *Physical Review B* 65.23 (2002), p. 235112.
- [69] Ben A Munk. *Frequency selective surfaces: theory and design*. John Wiley & Sons, 2005.
- [70] Ronald L Fante and Michael T McCormack. “Reflection properties of the Salisbury screen”. In: *IEEE transactions on antennas and propagation* 36.10 (1988), pp. 1443–1454.
- [71] Harry A Atwater and Albert Polman. “Plasmonics for improved photovoltaic devices”. In: *Materials For Sustainable Energy: A Collection of Peer-Reviewed Research and Review Articles from Nature Publishing Group*. World Scientific, 2011, pp. 1–11.

- [72] Stéphane Collin. “Nanostructure arrays in free-space: optical properties and applications”. In: *Reports on Progress in Physics* 77.12 (2014), p. 126402.
- [73] M Wuttig, H Bhaskaran, and T Taubner. “Phase-change materials for non-volatile photonic applications”. In: *Nat. Photonics* 11.8 (2017), p. 465.
- [74] Sébastien Cueff et al. “Dynamic control of light emission faster than the lifetime limit using VO₂ phase-change”. In: *Nat. Commun.* 6 (2015), p. 8636.
- [75] Yonghwi Kim et al. “Phase Modulation with Electrically Tunable Vanadium Dioxide Phase-Change Metasurfaces”. In: *Nano letters* (2019).
- [76] A García-Etxarri et al. “Strong magnetic response of submicron Silicon particles in the infrared”. In: *Opt. Express* 19.6 (2011), p. 4815.
- [77] Andrey B Evlyukhin et al. “Demonstration of magnetic dipole resonances of dielectric nanospheres in the visible region”. In: *Nano letters* 12.7 (2012), pp. 3749–3755.
- [78] Qian Zhao et al. “Mie resonance-based dielectric metamaterials”. In: *Materials today* 12.12 (2009), pp. 60–69.
- [79] Akram Ahmadi and Hossein Mosallaei. “Physical configuration and performance modeling of all-dielectric metamaterials”. In: *Physical Review B* 77.4 (2008), p. 045104.
- [80] Andrey E Miroshnichenko et al. “Optically induced interaction of magnetic moments in hybrid metamaterials”. In: *Acs Nano* 6.1 (2011), pp. 837–842.
- [81] Jayant Baliga et al. “Energy Consumption in Optical IP Networks”. In: *J. Lightwave Technol.* 27.13 (2009), pp. 2391–2403.
- [82] David Miller. “Miller, D.: Device requirements for optical interconnects to silicon chips. Proc. IEEE 97, 1166-1185”. In: *Proceedings of the IEEE* 97 (2009), pp. 1166 –1185.
- [83] Randolph Kirchain and Lionel Kimerling. “A roadmap for nanophotonics”. In: *Nature Photonics* 1 (2007), 303 EP –.
- [84] Lukas Novotny and Bert Hecht. *Principles of nano-optics*. Cambridge university press, 2012.
- [85] A Femius Koenderink, Andrea Alu, and Albert Polman. “Nanophotonics: shrinking light-based technology”. In: *Science* 348.6234 (2015), pp. 516–521.
- [86] Kai Liu et al. “Recent progresses on physics and applications of vanadium dioxide”. In: *Materials Today* 21.8 (2018), pp. 875 –896.

- [87] Arseniy I Kuznetsov et al. “Optically resonant dielectric nanostructures”. In: *Science* 354.6314 (2016), aag2472.
- [88] Toon Coenen et al. “Directional emission from a single plasmonic scatterer”. In: *Nature communications* 5 (2014), p. 3250.
- [89] Andrea Alù and Nader Engheta. “Cloaking and transparency for collections of particles with metamaterial and plasmonic covers”. In: *Optics Express* 15.12 (2007), pp. 7578–7590.
- [90] N F Mott. “The Basis of the Electron Theory of Metals, with Special Reference to the Transition Metals”. In: *Proceedings of the Physical Society. Section A* 62.7 (1949), pp. 416–422.
- [91] John B. Goodenough. “The two components of the crystallographic transition in VO₂”. In: *Journal of Solid State Chemistry* 3.4 (1971), pp. 490 –500.
- [92] Max Born and Robert Oppenheimer. “Zur quantentheorie der moleküle”. In: *Annalen der physik* 389.20 (1927), pp. 457–484.
- [93] George A Hagedorn. “A time dependent Born-Oppenheimer approximation”. In: *Communications in Mathematical Physics* 77.1 (1980), pp. 1–19.
- [94] Arthur K Kerman and Abraham Klein. “Generalized hartree-fock approximation for the calculation of collective states of a finite many-particle system”. In: *Physical Review* 132.3 (1963), p. 1326.
- [95] Paul AM Dirac. “Note on exchange phenomena in the Thomas atom”. In: *Mathematical Proceedings of the Cambridge Philosophical Society*. Vol. 26. 3. Cambridge University Press. 1930, pp. 376–385.
- [96] J. Hubbard and Brian Hilton Flowers. “Electron correlations in narrow energy bands. II. The degenerate band case”. In: *Proceedings of the Royal Society of London. Series A. Mathematical and Physical Sciences* 277.1369 (1964), pp. 237–259. eprint: <https://royalsocietypublishing.org/doi/pdf/10.1098/rspa.1964.0019>.
- [97] M Taguchi et al. “Bulk screening in core-level photoemission from Mott-Hubbard and charge-transfer systems”. In: *Physical Review B* 71.15 (2005), p. 155102.
- [98] J. Zaanen, G.A. Sawatzky, and J.W. Allen. “The electronic structure and band gaps in transition metal compounds”. In: *Journal of Magnetism and Magnetic Materials* 54-57 (1986), pp. 607 –611.
- [99] George Grüner. “The dynamics of charge-density waves”. In: *Reviews of modern physics* 60.4 (1988), p. 1129.
- [100] John M Longo, Peder Kierkegaard, et al. “A refinement of the structure of VO₂”. In: *Acta Chem. Scand* 24.2 (1970), pp. 420–426.

- [101] M. Marezio et al. “Structural Aspects of the Metal-Insulator Transitions in Cr-Doped VO₂”. In: 5 (1972), pp. 2541–2551.
- [102] Masatoshi Imada, Atsushi Fujimori, and Yoshinori Tokura. “Metal-insulator transitions”. In: *Reviews of modern physics* 70.4 (1998), p. 1039.
- [103] Masatoshi Imada, Atsushi Fujimori, and Yoshinori Tokura. “Metal-insulator transitions”. In: *Rev. Mod. Phys.* 70 (4 1998), pp. 1039–1263.
- [104] Wei Li et al. “Ultrafast All-Optical Graphene Modulator”. In: *Nano letters* 14 (2014).
- [105] Dmitry Ruzmetov et al. “Hall carrier density and magnetoresistance measurements in thin-film vanadium dioxide across the metal-insulator transition”. In: *Physical Review B* 79 (2010).
- [106] A. Zylbersztein and N. F. Mott. “Metal-insulator transition in vanadium dioxide”. In: *Phys. Rev. B* 11 (11 1975), pp. 4383–4395.
- [107] T. M. Rice, H. Launois, and J. P. Pouget. “Comment on “VO₂: Peierls or Mott-Hubbard\? A view from band theory””. In: *Physical Review Letters* 73 (1994), p. 3042.
- [108] Volker Eyert. “The metal-insulator transitions of VO₂: A band theoretical approach”. In: *Annalen der Physik* 11.9 (2002), pp. 650–704.
- [109] S. Biermann et al. “Dynamical Singlets and Correlation-Assisted Peierls Transition in VO₂”. In: *Phys. Rev. Lett.* 94 (2 2005), p. 026404.
- [110] M W Haverkort et al. “Orbital-Assisted Metal-Insulator Transition in VO₂”. In: *Physical review letters* 95 (2005), p. 196404.
- [111] T Koethe et al. “Transfer of Spectral Weight and Symmetry across the Metal-Insulator Transition in VO₂”. In: *Physical Review Letters - PHYS REV LETT* 97 (2006).
- [112] A S. Belozerov and Poteryaev Alexander. “Monoclinic M1 phase of VO₂: Mott-Hubbard versus band insulator”. In: *Physical Review B* 85 (2012).
- [113] S. Kim et al. “Correlation-assisted phonon softening and the orbital-selective Peierls transition in VO₂”. In: *Physical Review Letters* 87.19, 195106 (2013), p. 195106. arXiv: 1207.1770 [cond-mat.str-el].
- [114] J. P. Pouget et al. “Dimerization of a linear Heisenberg chain in the insulating phases of V_{1-x}Cr_xO₂”. In: *Physical Review Letters* 10 (1974), pp. 1801–1815.
- [115] J. P. Pouget et al. “Electron Localization Induced by Uniaxial Stress in Pure VO₂”. In: *Physical Review Letters* 35 (1975), pp. 873–875.

- [116] H Katzke, P Tolédano, and W Depmeier. “Theory of morphotropic transformations in vanadium oxides”. In: *Physical Review B* 68.2 (2003), p. 024109.
- [117] Zheng Yang, Changhyun Ko, and Shriram Ramanathan. “Oxide electronics utilizing ultrafast metal-insulator transitions”. In: *Annual Review of Materials Research* 41 (2011), pp. 337–367.
- [118] Byung-Gyu Chae et al. “Highly Oriented VO₂ Thin Films Prepared by Sol-Gel Deposition”. In: *Electrochemical and Solid State Letters - ELECTROCHEM SOLID STATE LETT* 9 (2006).
- [119] J. W. Tashman et al. “Epitaxial growth of VO₂ by periodic annealing”. In: *Applied Physics Letters* 104.6 (2014), p. 063104. eprint: <https://doi.org/10.1063/1.4864404>.
- [120] T. Maruyama and Y. Ikuta. “Vanadium dioxide thin films prepared by chemical vapour deposition from vanadium(III) acetylacetone”. In: *Journal of Materials Science* 28.18 (1993), pp. 5073–5078.
- [121] Ping Jin and Sakae Tanemura. “Formation and Thermochromism of VO₂Films Deposited by RF Magnetron Sputtering at Low Substrate Temperature”. In: *Japanese Journal of Applied Physics* 33.Part 1, No. 3A (1994), pp. 1478–1483.
- [122] E. N. Fuls, D. H. Hensler, and A. R. Ross. “REACTIVELY SPUTTERED VANADIUM DIOXIDE THIN FILMS”. In: *Applied Physics Letters* 10.7 (1967), pp. 199–201. eprint: <https://doi.org/10.1063/1.1754909>.
- [123] Yuzo Shigesato, Mikiko Enomoto, and Hidehumi Odaka. “Thermochromic VO₂ films deposited by RF magnetron sputtering using V₂O₃ or V₂O₅ targets”. In: *Japanese Journal of Applied Physics* 39.10R (2000), p. 6016.
- [124] Merve Ertas Uslu, I Burc Misirlioglu, and Kursat Sendur. “Selective IR response of highly textured phase change VO₂ nanostructures obtained via oxidation of electron beam deposited metallic V films”. In: *Optical Materials Express* 8.8 (2018), pp. 2035–2049.
- [125] PJ Fillingham. “Domain structure and twinning in crystals of vanadium dioxide”. In: *Journal of Applied Physics* 38.12 (1967), pp. 4823–4829.
- [126] Xiong-Bang Wei et al. “Growth mode and texture study in vanadium dioxide thin films deposited by magnetron sputtering”. In: *Journal of Physics D: Applied Physics* 41.5 (2008), p. 055303.
- [127] Hyojin Yoon et al. “Reversible phase modulation and hydrogen storage in multivalent VO₂ epitaxial thin films”. In: *Nature materials* 15.10 (2016), p. 1113.
- [128] Josef Humlincek. “1 - Polarized Light and Ellipsometry”. In: *Handbook of Ellipsometry*. Ed. by Harland G. Tompkins and Eugene A. Irene. Norwich, NY: William Andrew Publishing, 2005, pp. 3 –91. ISBN: 978-0-8155-1499-2.

- [129] I. H. Malitson. “Interspecimen Comparison of the Refractive Index of Fused Silica*,†”. In: *J. Opt. Soc. Am.* 55.10 (1965), pp. 1205–1209.
- [130] H. Fujiwara et al. “Assessment of effective-medium theories in the analysis of nucleation and microscopic surface roughness evolution for semiconductor thin films”. In: *Phys. Rev. B* 61 (16 2000), pp. 10832–10844.
- [131] Yong Jai Cho et al. “Spectroscopic ellipsometry characterization of high-k dielectric HfO₂ thin films and the high-temperature annealing effects on their optical properties”. In: *Applied Physics Letters* 80.7 (2002), pp. 1249–1251. eprint: <https://doi.org/10.1063/1.1448384>.
- [132] Jian Li and Joonghoe Dho. “Anomalous optical switching and thermal hysteresis behaviors of VO₂ films on glass substrate”. In: *Applied Physics Letters* 99.23 (2011), p. 231909. eprint: <https://doi.org/10.1063/1.3668089>.
- [133] Christian Wagner and Noreen Harned. “EUV lithography: Lithography gets extreme”. In: *Nature Photonics* 4.1 (2010), p. 24.
- [134] Yurii A Vlasov and Sharee J McNab. “Losses in single-mode silicon-on-insulator strip waveguides and bends”. In: *Optics express* 12.8 (2004), pp. 1622–1631.
- [135] C Doerr et al. “Single-chip silicon photonics 100-Gb/s coherent transceiver”. In: *Optical Fiber Communication Conference*. Optical Society of America. 2014, Th5C–1.
- [136] Kyle Preston et al. “Waveguide-integrated telecom-wavelength photodiode in deposited silicon”. In: *Optics letters* 36.1 (2011), pp. 52–54.
- [137] Ansheng Liu et al. “A high-speed silicon optical modulator based on a metal–oxide–semiconductor capacitor”. In: *Nature* 427.6975 (2004), p. 615.
- [138] Qianfan Xu et al. “12.5 Gbit/s carrier-injection-based silicon micro-ring silicon modulators”. In: *Optics express* 15.2 (2007), pp. 430–436.
- [139] Aya O Zaki, Khaled Kirah, and Mohamed A Swillam. “Hybrid plasmonic electro-optical modulator”. In: *Applied Physics A* 122.4 (2016), p. 473.
- [140] Shashank Pandey, Barun Gupta, and Ajay Nahata. “Terahertz plasmonic waveguides created via 3D printing”. In: *Optics express* 21.21 (2013), pp. 24422–24430.
- [141] Feiying Sun et al. “Experiment and modelling study of the modulation performance in the graphene-Si heterojunction waveguide”. In: *Fifth Symposium on Novel Optoelectronic Detection Technology and Application*. Vol. 11023. International Society for Optics and Photonics. 2019, p. 1102307.
- [142] Tom Baehr-Jones et al. “Optical modulation and detection in slotted silicon waveguides”. In: *Optics Express* 13.14 (2005), pp. 5216–5226.

- [143] Luis David Sánchez et al. “Experimental demonstration of a tunable transverse electric pass polarizer based on hybrid VO₂/silicon technology”. In: *Optics letters* 43.15 (2018), pp. 3650–3653.
- [144] Graham T. Reed et al. “Recent breakthroughs in carrier depletion based silicon optical modulators”. In: *Nanophotonics* 3.4-5 (2013), pp. 229–245.
- [145] W H. Rosevear and W Paul. “Hall Effect in VO₂ near the Semiconductor-to-Metal Transition”. In: *Physical Review B - PHYS REV B* 7 (1973), pp. 2109–2111.
- [146] Arash Joushaghani et al. “Sub-volt broadband hybrid plasmonic-vanadium dioxide switches”. In: *Applied Physics Letters* 102.6 (2013), p. 061101. eprint: <https://doi.org/10.1063/1.4790834>.
- [147] Arash Joushaghani et al. “Wavelength-size hybrid Si-VO₂ waveguide electroabsorption optical switches and photodetectors”. In: *Opt. Express* 23.3 (2015), pp. 3657–3668.
- [148] Julien Macario et al. “Full spectrum millimeter-wave modulation”. In: *Optics express* 20.21 (2012), pp. 23623–23629.
- [149] Irene Olivares et al. “Optical switching in hybrid VO₂/Si waveguides thermally triggered by lateral microheaters”. In: *Optics express* 26.10 (2018), pp. 12387–12395.
- [150] Bahaa EA Saleh and Malvin Carl Teich. *Fundamentals of photonics*. John Wiley & Sons, 2019.
- [151] Dietrich Marcuse. *Theory of dielectric optical waveguides*. Elsevier, 2013.
- [152] James Clerk Maxwell. “VIII. A dynamical theory of the electromagnetic field”. In: *Philosophical transactions of the Royal Society of London* 155 (1865), pp. 459–512.
- [153] John Henry Poynting. “XV. On the transfer of energy in the electromagnetic field”. In: *Philosophical Transactions of the Royal Society of London* 175 (1884), pp. 343–361.
- [154] Graham T Reed et al. “Silicon optical modulators”. In: *Nature photonics* 4.8 (2010), p. 518.
- [155] Amnon Yariv. “Coupled-mode theory for guided-wave optics”. In: *IEEE Journal of Quantum Electronics* 9.9 (1973), pp. 919–933.
- [156] Wangtao Lu and Ya Yan Lu. “Waveguide mode solver based on Neumann-to-Dirichlet operators and boundary integral equations”. In: *Journal of Computational Physics* 231.4 (2012), pp. 1360–1371.
- [157] MS Stern. “Semivectorial polarised finite difference method for optical waveguides with arbitrary index profiles”. In: *IEE Proceedings J (Optoelectronics)* 135.1 (1988), pp. 56–63.

- [158] Kai Jiang and Wei-Ping Huang. “Finite-difference-based mode-matching method for 3-D waveguide structures under semivectorial approximation”. In: *Journal of lightwave technology* 23.12 (2005), p. 4239.
- [159] Kane Yee. “Numerical solution of initial boundary value problems involving Maxwell’s equations in isotropic media”. In: *IEEE Transactions on antennas and propagation* 14.3 (1966), pp. 302–307.
- [160] Ardavan F. Oskooi et al. “Meep: A flexible free-software package for electromagnetic simulations by the FDTD method”. In: *Computer Physics Communications* 181.3 (2010), pp. 687 –702.
- [161] Yichen Shen et al. “Deep learning with coherent nanophotonic circuits”. In: *Nature Photonics* 11.7 (2017), p. 441.
- [162] Damien Woods and Thomas J Naughton. “Optical computing: Photonic neural networks”. In: *Nature Physics* 8.4 (2012), p. 257.
- [163] David AB Miller. “Silicon photonics: Meshing optics with applications”. In: *Nature Photonics* 11.7 (2017), p. 403.
- [164] SeokJae Yoo, Suyeon Lee, and Q-Han Park. “Loss-free negative-index metamaterials using forward light scattering in dielectric meta-atoms”. In: *ACS Photonics* 5.4 (2018), pp. 1370–1374.
- [165] Behrad Gholipour et al. “Reconfigurable ultraviolet and high-energy visible dielectric metamaterials”. In: *Nano letters* 19.3 (2019), pp. 1643–1648.
- [166] 03cello Ferrera et al. “Dynamic nanophotonics”. In: *JOSA B* 34.1 (2017), pp. 95–103.
- [167] Nikolay I Zheludev. “Obtaining optical properties on demand”. In: *Science* 348.6238 (2015), pp. 973–974.
- [168] Yujie Ke et al. “Vanadium dioxide: The multistimuli responsive material and its applications”. In: *Small* 14.39 (2018), p. 1802025.
- [169] Run Shi et al. “Recent advances in fabrication strategies, phase transition modulation, and advanced applications of vanadium dioxide”. In: *Appl. Phys. Rev.* 6.1 (2019), p. 011312.
- [170] Yonghwi Kim et al. “Phase Modulation with Electrically Tunable Vanadium Dioxide Phase-Change Metasurfaces”. In: *Nano Lett.* (2019).
- [171] Zhihua Zhu et al. “Dynamically reconfigurable metadevice employing nanostructured phase-change materials”. In: *Nano Lett.* 17.8 (2017), pp. 4881–4885.
- [172] Jura Rensberg et al. “Active optical metasurfaces based on defect-engineered phase-transition materials”. In: *Nano Lett.* 16.2 (2016), pp. 1050–1055.

- [173] Nikita A Butakov et al. “Switchable plasmonic–dielectric resonators with metal–insulator transitions”. In: *ACS Photonics* 5.2 (2017), pp. 371–377.
- [174] Cecilia Noguez. “Surface plasmons on metal nanoparticles: The influence of shape and physical environment”. In: *J. Phys. Chem. C* 111.10 (2007), pp. 3606–3619.
- [175] Roy G Grainger et al. “Calculation of Mie derivatives”. In: *Applied Optics* 43.28 (2004), pp. 5386–5393.
- [176] Hendrik Christoffel Hulst and Hendrik C van de Hulst. *Light scattering by small particles*. Courier Corporation, 1981.
- [177] Milton Abramowitz and Irene A Stegun. *Handbook of mathematical functions with formulas, graphs, and mathematical tables*. Vol. 55. US Government printing office, 1948.
- [178] J.M. Geffrin et al. “Magnetic and electric coherence in forward- and back-scattered electromagnetic waves by a single dielectric subwavelength sphere”. In: *Nat. Commun.* 3.1 (2012), p. 1171.
- [179] Michael I. Tribelsky et al. “Small Dielectric Spheres with High Refractive Index as New Multifunctional Elements for Optical Devices”. In: *Sci. Rep.* 5.1 (2015), p. 12288.
- [180] R Lopez et al. “Synthesis and characterization of size-controlled vanadium dioxide nanocrystals in a fused silica matrix”. In: *J. Appl. Phys.* 92.7 (2002), pp. 4031–4036.
- [181] Rene Lopez et al. “Size effects in the structural phase transition of VO₂ nanoparticles”. In: *Phys. Rev. B* 65.22 (2002), p. 224113.
- [182] Rene Lopez et al. “Optical nonlinearities in VO₂ nanoparticles and thin films”. In: *Appl. Phys. Lett.* 85.22 (2004), pp. 5191–5193.
- [183] Matteo Rini et al. “Photoinduced phase transition in VO₂ nanocrystals: ultrafast control of surface-plasmon resonance”. In: *Opt. Lett.* 30.5 (2005), pp. 558–560.
- [184] Thorben Jostmeier et al. “Optically imprinted reconfigurable photonic elements in a VO₂ nanocomposite”. In: *Appl. Phys. Lett.* 105.7 (2014), p. 071107.
- [185] Thorben Jostmeier et al. “Optically imprinted reconfigurable photonic elements in a VO₂ nanocomposite”. In: *Appl. Phys. Lett.* 105.7 (2014), p. 071107.
- [186] R Ruppin. “Evaluation of extended Maxwell-Garnett theories”. In: *Opt. Commun.* 182.4-6 (2000), pp. 273–279.
- [187] William T Doyle. “Optical properties of a suspension of metal spheres”. In: *Physical review B* 39.14 (1989), p. 9852.

- [188] George W. Mulholland, Craig F. Bohren, and Kirk A. Fuller. “Light Scattering by Ag-gglomerates: Coupled Electric and Magnetic Dipole Method”. In: *Langmuir* 10.8 (1994), pp. 2533–2546. eprint: <https://doi.org/10.1021/la00020a009>.
- [189] W Rechberger et al. “Optical properties of two interacting gold nanoparticles”. In: *Opt. Commun.* 220.1-3 (2003), pp. 137–141.
- [190] Fernando Moreno and Francisco González. *Light Scattering from Microstructures*. Vol. 534. 2000.
- [191] Pablo Albella et al. “Low-Loss Electric and Magnetic Field-Enhanced Spectroscopy with Subwavelength Silicon Dimers”. In: *The Journal of Physical Chemistry C* 117.26 (2013), pp. 13573–13584. eprint: <https://doi.org/10.1021/jp4027018>.
- [192] Luisa Whittaker, Christopher J Patridge, and Sarbajit Banerjee. “Microscopic and nanoscale perspective of the metal- insulator phase transitions of VO₂: some new twists to an old tale”. In: *J. Phys. Chem. Lett* 2.7 (2011), pp. 745–758.
- [193] Sajjad Abdollahramezani et al. “Tunable nanophotonics enabled by chalcogenide phase-change materials”. In: *arXiv preprint arXiv:2001.06335* (2020).
- [194] Milton Kerker, D-S Wang, and CL Giles. “Electromagnetic scattering by magnetic spheres”. In: *JOSA* 73.6 (1983), pp. 765–767.
- [195] Wei Liu and Yuri S Kivshar. “Generalized Kerker effects in nanophotonics and meta-optics”. In: *Opt. Express* 26.10 (2018), pp. 13085–13105.
- [196] Evgenia Rusak et al. “Tailoring the Enhancement of and Interference among Higher Order Multipole Transitions in Molecules with a Plasmonic Nanoantenna”. In: *arXiv preprint arXiv:1905.08482* (2019).
- [197] Yael Gutierrez et al. “How an oxide shell affects the ultraviolet plasmonic behavior of Ga, Mg, and Al nanostructures”. In: *Opt. Express* 24.18 (2016), p. 20621.
- [198] T. W H Oates et al. “The effect of atmospheric tarnishing on the optical and structural properties of silver nanoparticles”. In: *J. Phys. D: Appl. Phys.* 46.14 (2013), p. 145308.
- [199] Sébastien Bidault, Mathieu Mivelle, and Nicolas Bonod. “Dielectric nanoantennas to manipulate solid-state light emission”. In: *J. Appl. Phys.* 126.9 (2019), p. 094104.
- [200] Sébastien Cueff et al. “Tailoring the Local Density of Optical States and Directionality of Light Emission by Symmetry Breaking”. In: *IEEE J. Sel. Topics Quantum Electron.* 25.3 (2019), pp. 1–7.
- [201] Manuel Decker et al. “High-efficiency dielectric Huygens’ surfaces”. In: *Adv. Opt. Mater.* 3.6 (2015), pp. 813–820.

- [202] Nanfang Yu et al. “Light propagation with phase discontinuities: generalized laws of reflection and refraction”. In: *science* 334.6054 (2011), pp. 333–337.
- [203] Nanfang Yu and Federico Capasso. “Flat optics with designer metasurfaces”. In: *Nature materials* 13.2 (2014), p. 139.
- [204] Daisuke Inoue et al. “Polarization independent visible color filter comprising an aluminum film with surface-plasmon enhanced transmission through a subwavelength array of holes”. In: *Applied Physics Letters* 98.9 (2011), p. 093113.
- [205] Masashi Miyata, Hideaki Hatada, and Junichi Takahara. “Full-color subwavelength printing with gap-plasmonic optical antennas”. In: *Nano letters* 16.5 (2016), pp. 3166–3172.
- [206] Xiaoyang Duan, Simon Kamin, and Na Liu. “Dynamic plasmonic colour display”. In: *Nature communications* 8 (2017), p. 14606.
- [207] Qin Chen and David RS Cumming. “High transmission and low color cross-talk plasmonic color filters using triangular-lattice hole arrays in aluminum films”. In: *Optics express* 18.13 (2010), pp. 14056–14062.
- [208] Alexander S Roberts et al. “Subwavelength plasmonic color printing protected for ambient use”. In: *Nano letters* 14.2 (2014), pp. 783–787.
- [209] Zhigang Li et al. “All-metal structural color printing based on aluminum plasmonic metasurfaces”. In: *Optics express* 24.18 (2016), pp. 20472–20480.
- [210] Luc Duempelmann et al. “Four-fold color filter based on plasmonic phase retarder”. In: *ACS Photonics* 3.2 (2015), pp. 190–196.
- [211] Alexander Krasnok et al. “Towards all-dielectric metamaterials and nanophotonics”. In: *Metamaterials X*. Vol. 9502. International Society for Optics and Photonics. 2015, p. 950203.
- [212] János Schanda. *Colorimetry: understanding the CIE system*. John Wiley & Sons, 2007.
- [213] Vladimir Riabov. “The Role of Linguistics, Psychology, and Physiology in Various Computing Applications”. In: *Rivier Academic Journal* 13 (2017), pp. 1–10.
- [214] TM Goodman. “International standards for colour”. In: *Colour Design*. Elsevier, 2012, pp. 177–218.
- [215] Noboru Ohta and Alan Robertson. *Colorimetry: fundamentals and applications*. John Wiley & Sons, 2006.
- [216] Amir Arbabi and Andrei Faraon. “Fundamental limits of ultrathin metasurfaces”. In: *Scientific reports* 7 (2017), p. 43722.

- [217] Chihhui Wu et al. “Spectrally selective chiral silicon metasurfaces based on infrared Fano resonances”. In: *Nature communications* 5 (2014), p. 3892.
- [218] Mohammadreza Khorasaninejad et al. “Achromatic metalens over 60 nm bandwidth in the visible and metalens with reverse chromatic dispersion”. In: *Nano letters* 17.3 (2017), pp. 1819–1824.
- [219] Shang Sun et al. “All-dielectric full-color printing with TiO₂ metasurfaces”. In: *ACS nano* 11.5 (2017), pp. 4445–4452.
- [220] JH Lee, GE Jang, and YH Jun. “Investigation and evaluation of structural color of TiO₂ coating on stainless steel”. In: *Ceramics International* 38 (2012), S661–S664.
- [221] X. ZHANG. “A Spatial Extension of CIELAB for Digital Color Image Reproduction”. In: *SID Technical Digest*, 1996 27 (1996), pp. 731–734.
- [222] C. Connolly and T. Fleiss. “A study of efficiency and accuracy in the transformation from RGB to CIELAB color space”. In: *IEEE Transactions on Image Processing* 6.7 (1997), pp. 1046–1048.
- [223] Jie Sun et al. “Large-scale nanophotonic phased array”. In: *Nature* 493.7431 (2013), p. 195.
- [224] Daniel Franklin et al. “Polarization-independent actively tunable colour generation on imprinted plasmonic surfaces”. In: *Nature communications* 6 (2015), p. 7337.
- [225] Daniel Franklin et al. “Actively addressed single pixel full-colour plasmonic display”. In: *Nature communications* 8 (2017), p. 15209.
- [226] Philipp Gutruf et al. “Mechanically tunable dielectric resonator metasurfaces at visible frequencies”. In: *ACS nano* 10.1 (2015), pp. 133–141.
- [227] Yisheng Gao et al. “Lead halide perovskite nanostructures for dynamic color display”. In: *ACS nano* 12.9 (2018), pp. 8847–8854.
- [228] Guoping Wang et al. “Mechanical chameleon through dynamic real-time plasmonic tuning”. In: *ACS nano* 10.2 (2016), pp. 1788–1794.
- [229] Zile Li et al. “Dielectric meta-holograms enabled with dual magnetic resonances in visible light”. In: *ACS nano* 11.9 (2017), pp. 9382–9389.
- [230] Shang Sun et al. “Real-time tunable colors from microfluidic reconfigurable all-dielectric metasurfaces”. In: *ACS nano* 12.3 (2018), pp. 2151–2159.
- [231] Julien Proust et al. “All-dielectric colored metasurfaces with silicon Mie resonators”. In: *Acs Nano* 10.8 (2016), pp. 7761–7767.

- [232] Jiao-Rong Fan et al. “Plasmonic Metasurfaces Based on Nanopin-Cavity Resonator for Quantitative Colorimetric Ricin Sensing”. In: *Small* 13.1 (2017), p. 1601710.
- [233] Ruggero Verre et al. “Polarization conversion-based molecular sensing using anisotropic plasmonic metasurfaces”. In: *Nanoscale* 8.20 (2016), pp. 10576–10581.
- [234] Björn CP Sturmberg et al. “Fano resonances of dielectric gratings: symmetries and broadband filtering”. In: *Optics express* 23.24 (2015), A1672–A1686.
- [235] JY Rhee et al. “Metamaterial-based perfect absorbers”. In: *Journal of Electromagnetic Waves and Applications* 28.13 (2014), pp. 1541–1580.
- [236] MA Baqir and Pankaj Kumar Choudhury. “Hyperbolic metamaterial-based UV absorber”. In: *IEEE Photonics Technology Letters* 29.18 (2017), pp. 1548–1551.
- [237] Braulio García-Cámara et al. “Light scattering by an array of electric and magnetic nanoparticles”. In: *Optics express* 18.10 (2010), pp. 10001–10015.
- [238] Aitzol García-Etxarri et al. “Strong magnetic response of submicron silicon particles in the infrared”. In: *Optics express* 19.6 (2011), pp. 4815–4826.
- [239] Andrey B Evlyukhin et al. “Optical response features of Si-nanoparticle arrays”. In: *Physical Review B* 82.4 (2010), p. 045404.
- [240] Isabelle Staude et al. “Tailoring directional scattering through magnetic and electric resonances in subwavelength silicon nanodisks”. In: *ACS nano* 7.9 (2013), pp. 7824–7832.
- [241] Andrey B Evlyukhin, Carsten Reinhardt, and Boris N Chichkov. “Multipole light scattering by nonspherical nanoparticles in the discrete dipole approximation”. In: *Physical Review B* 84.23 (2011), p. 235429.
- [242] Viktoriia E Babicheva and Andrey B Evlyukhin. “Resonant lattice Kerker effect in metasurfaces with electric and magnetic optical responses”. In: *Laser & Photonics Reviews* 11.6 (2017), p. 1700132.
- [243] Jean-Michel Geffrin et al. “Magnetic and electric coherence in forward-and back-scattered electromagnetic waves by a single dielectric subwavelength sphere”. In: *Nature communications* 3.1 (2012), pp. 1–8.
- [244] J Van de Groep and A Polman. “Designing dielectric resonators on substrates: Combining magnetic and electric resonances”. In: *Optics express* 21.22 (2013), pp. 26285–26302.
- [245] Bo Yang et al. “Structural colors in metasurfaces: principle, design and applications”. In: *Materials Chemistry Frontiers* 3.5 (2019), pp. 750–761.
- [246] Martin Salinga et al. “Monatomic phase change memory”. In: *Nature materials* 17.8 (2018), pp. 681–685.

- [247] Wei Zhang and Evan Ma. “Single-element glass to record data”. In: *Nature materials* 17.8 (2018), pp. 654–655.
- [248] SE Miller. “Coupled wave theory and waveguide applications”. In: *Bell System Technical Journal* 33.3 (1954), pp. 661–719.
- [249] M Reed et al. “Efficient propagation algorithm for 3D optical waveguides”. In: *IEE Proceedings-Optoelectronics* 145.1 (1998), pp. 53–58.
- [250] William H Raymond and HL Kuo. “A radiation boundary condition for multi-dimensional flows”. In: *Quarterly Journal of the Royal Meteorological Society* 110.464 (1984), pp. 535–551.